



HAL
open science

Towards greener thermosets: cardanol-based polybenzoxazines and dialdehyde cellulose based composites

Rime Ganfoud

► **To cite this version:**

Rime Ganfoud. Towards greener thermosets: cardanol-based polybenzoxazines and dialdehyde cellulose based composites. Other. COMUE Université Côte d'Azur (2015 - 2019), 2018. English. NNT : 2018AZUR4209 . tel-02570341

HAL Id: tel-02570341

<https://theses.hal.science/tel-02570341v1>

Submitted on 12 May 2020

HAL is a multi-disciplinary open access archive for the deposit and dissemination of scientific research documents, whether they are published or not. The documents may come from teaching and research institutions in France or abroad, or from public or private research centers.

L'archive ouverte pluridisciplinaire **HAL**, est destinée au dépôt et à la diffusion de documents scientifiques de niveau recherche, publiés ou non, émanant des établissements d'enseignement et de recherche français ou étrangers, des laboratoires publics ou privés.



$$\rho \left(\frac{\partial v}{\partial t} + v \cdot \nabla v \right) = -\nabla p + \nabla \cdot T + f$$

$$e^{i\pi} + 1 = 0$$

THÈSE DE DOCTORAT

Towards greener thermosets: Cardanol-based polybenzoxazines and dialdehyde cellulose-based composites



Vers des thermodurcissables bio-sourcés :
Polybenzoxazines à partir de cardanol et composites à
base de dialdéhyde cellulose

Rime GANFOUD

Institut de Chimie de Nice

Présentée en vue de l'obtention
du grade de docteur en Chimie
de l'Université Côte d'Azur

Dirigée par : Pr Nicolas Sbirrazzuoli
Co-encadrée par : Dr Nathanael Guigo
Soutenue le : 10 décembre 2018

Devant le jury, composé de :

Pr Mohamed Naceur Belgacem, Grenoble-INP
Pagora, France. *Rapporteur*

Pr Rosa Marià Sebastià Pérez, UAB,
Espagne. *Rapporteur*

Dr Laurent Heux, Directeur de recherche,
CERMAV, France. *Examineur*

Dr Pierre Verge, Ingénieur de recherche, LIST,
Luxembourg. *Examineur*

Université Côte D'azur – UFR Sciences
Ecole Doctorale Sciences Fondamentales et Appliquées

THESE

Pour obtenir le titre de
Docteur en Sciences
de l'Université Côte d'Azur

Discipline : Chimie
Présentée et soutenue par

Rime GANFOUD

Towards greener thermosets: Cardanol-based polybenzoxazines and
dialdehyde cellulose-based composites



Vers des thermodurcissables biosourcés : Polybenzoxazines à partir
de cardanol et composites à base de dialdehyde cellulose

Thèse dirigée par le Professeur Nicolas SBIRRAZZUOLI

Soutenance : 10 décembre 2018

Jury :

Rapporteurs

Mohamed Naceur Belgacem, Professeur Grenoble-INP Pagora, France

Rosa Maria Sebastián Pérez, Professeur, Département de chimie, Université Autonome de
Barcelone, Espagne

Examineurs

Laurent Heux, Directeur de Recherche, CERMAV, France

Pierre Verge, Ingénieur de Recherche, LIST, Luxembourg

Nathanael Guigo, Maitre de conférences, ICN, Université Côte d'Azur, France

Nicolas Sbirrazzuoli, Professeur, ICN, Université Côte d'Azur, France

ABSTRACT:

To reduce the use of finite petroleum-based resources, interest has grown regarding the valorization of renewable resources in chemistry. The work presented in this thesis focused on two bio-based resources: plant oil and lignocellulosic biomass, for the preparation of greener thermoset materials. The first part discussed about polybenzoxazine thermosets. The bio-based content was gradually increased through substitution of petro-based phenol by bio-based cardanol. Cardanol is a natural phenolic derivative extracted from the cashew nutshell liquid. A first study focused on the effect of this aliphatic side chain and how it can tune the reactivity and the final thermo-mechanical properties of the materials. In the following study the reactivity of polymerization of di-phenol monomer was investigated using advanced isoconversional analyses and thermo-mechanical analyses for a better understanding of the polymerization reaction. The second part discussed about the preparation of fully bio-based composites using modified cellulose microfibrils (MFC). Poly(furfuryl alcohol) (PFA) is a bio-based matrix obtained after polymerization of furfuryl alcohol (FA) with maleic anhydride, both obtained from HMF. The PFA properties can be modified by the introduction of cellulose as a filler. MFC was modified by oxidation to lead to reactive dialdehyde functions. By varying the degree of oxidation (DO), the properties of different composites were studied to determine the most adequate DO for the better PFA/MFC compatibility and the most adequate PFA/MFC ratio. Finally, the last study of this thesis focused on the concept of “all cellulose composites” (ACC), and particularly how to reduce the moisture sensitivity of these materials. Two different furanic compounds were used as cross-linkers to increase the hydrophobicity: a first compound with one furan ring and a second with two furan rings.

Key words: Benzoxazine, bio-based polymers, cardanol, cellulose microfibrils, composites, dialdehyde cellulose, furfuryl alcohol, thermosets

RÉSUMÉ :

L'utilisation et la valorisation de ressources renouvelables dans le domaine de la chimie connaît un intérêt grandissant pour remplacer les ressources fossiles. Le travail présenté dans ce manuscrit de thèse est axé sur deux ressources bio-sourcées utilisées pour la préparation de thermoset bio-sourcés : huile végétale et biomasse lignocellulosique. La première partie concerne les polybenzoxazines. A partir d'un monomère à base de phénol, le caractère bio-sourcé est progressivement augmenté par substitution du phénol par du cardanol. Le cardanol est un dérivé phénolique bio-sourcé extrait de l'huile de coque de noix de cajou. Une première étude se concentre sur les effets apportés par cette chaîne alkyle sur la réactivité et les propriétés finales du matériau. Par la suite, la réaction de polymérisation du composé de référence est évaluée par des études cinétiques, corrélées aux analyses thermo-mécaniques pour une meilleure compréhension de la réaction de polymérisation. La seconde partie de cette thèse se concentre sur la préparation de composites totalement bio-sourcés, avec des microfibrilles de cellulose (MFC) modifiées pour obtenir des dialdéhyde cellulose (DAC). Le poly(alcool furfurylique) (PFA) est une matrice bio-sourcée polymérisée à partir d'alcool furfurylique (FA) et d'anhydride maléique, tous deux obtenus à partir du HMF. Les propriétés du PFA peuvent être modifiées en y incorporant un renfort, tel que la cellulose. La modification de MFC par oxydation génère des fonctions aldéhydes réactives qui améliorent la compatibilité avec la matrice. Cette étude compare différents composites préparés à partir de MFC oxydée à différents DO pour déterminer quel DO entraîne une meilleure compatibilité. Pour finir, des matériaux préparés à partir d'une unique source de cellulose, les « all cellulose composites », ont fait l'objet de la dernière étude. Deux différents renforts furaniques ont été utilisés pour contrer les problèmes de sensibilité à l'humidité de la cellulose, et donc augmenter l'hydrophobicité.

Mots clés : Alcool furfurylique, benzoxazine, cardanol, composites, dialdéhyde cellulose, microfibrilles de cellulose, polymères bio-sourcés, thermoset

Remerciements

J'adresse mes sincères remerciements au Professeur Nicolas Sbirrazzuoli, directeur de l'équipe Matériaux et Polymères Eco-Compatible, pour son accueil au sein de son équipe afin de réaliser mes travaux de thèse, ainsi que pour son encadrement au cours de ces trois années. Je remercie aussi le Docteur Nathanael Guigo pour son aide et son suivi au cours de cette thèse.

Je souhaite également exprimer ma reconnaissance aux membres du jury de thèse, Pr. Mohamed Naceur Belgacem, Pr. Rosa Maria Sebastiàn, Dr. Laurent Heux, et Dr. Pierre Verge, d'avoir accepté d'évaluer ce travail.

Je souhaite remercier tous les membres du laboratoire de l'Institut de Chimie de Nice, passés et présents, pour l'aide et le soutien qu'ils m'ont apporté. Je remercie également, les doctorants de l'équipe, ainsi que les anciens pour leur bonne humeur et les moments agréables passés avec eux aussi bien au laboratoire qu'en dehors.

Enfin, je remercie tout particulièrement mes amis, et ma famille pour leur soutien durant ces années.

List of abbreviations

A	Pre-exponential factor	
Ac₂O	Acetic anhydride	
ACC	All Cellulose Composite	
AGU	Anhydroglucose Unit	
ATR	Attenuated Total Reflectance	
BHMF	2,5-bis(hydroxymethyl)furan	
BMI	Bismaleimide	
BZ	Benzoxazine	
CHCA	α -cyano-4-hydroxycinnamic acid	
CHCl₃ / CDCl₃	Chloroform / deuterated	
CNSL	Cashew Nutshell Liquid	
C_p	Heat capacity	J.g ⁻¹ .K ⁻¹
DAC	Dialdehyde cellulose	
DCM	Dichloromethane	
DGEBA	Diglycidylether of bisphenol A	
DHMF	5,5'-dihydroxymethyl furoin	
di-BZ	Di-benzoxazine monomer	
DMA	Dynamic Mechanical Analysis	
DMSO d₆	Dimethylsulfoxide <i>deuterated</i>	
DO	Degree of oxidation	
DSC	Differential Scanning Calorimetry	
E' / G'	Storage modulus	Pa
E'' / G''	Loss modulus	Pa
E_a	Apparent activation energy	J.mol ⁻¹
EDA	Ethylenediamine	
EDX	Dispersive X-ray spectroscopy	
Et₃N	Triethylamine	
f(α)	Mathematical function associated to the reactional mechanism	
FA	Furfuryl alcohol	
FTIR	Fourier-Transform Infrared Spectroscopy	
H	Enthalpy of reaction	J.g ⁻¹

H_i	Partial enthalpy of reaction	J.g^{-1}
HMTA	Hexamethylenetetramine	
HOAc	Acetic acid	
HRMS	High Resolution Mass Spectrometry	
k(T)	Rate constant	S.I.
LiCl/DMAc	Lithium chloride/N,N-dimehtylacetamide	
MA	Maleic anhydride	
MALDI	Matrix-Assisted Laser Desorption/Ionization	
MCC	Microcrystalline cellulose	
mCPBA	<i>Meta</i> -perchlorobenzoic acid	
MFC	Microfibrillar cellulose	
mono-BZ	Mono-benzoxazine monomer	
MS	Mass Spectrometry	
NaOMe	Sodium methanolate	
NCC	Nanocrystalline	
NFC	Nanofibrillar cellulose	
PBZ	Polybenzoxazine	
PFA	Poly(furfuryl alcohol)	
PTFE	Polytetrafluoroethylene	
NMR	Nuclear Magnetic Resonance spectroscopy	
R	Gas constant	$\text{J.mol}^{-1}.\text{K}^{-1}$
ROP	Ring-opening polymerization	
RT	Room Temperature	
SEM	Scanning Electron Microscopy	
SOCl₂	Thionyl chloride	
tan δ	Damping factor	
TEM	Transmission Electron Microscopy	
TEMPO	2,2,6,6-tetramethylpiperidine-N-oxyl	
TGA	Thermogravimetric Analysis	
TLC	Thin Layer Chromatography	
TOF	Time-Of-Flight	
TPT-OMe	5-Methoxy-1,3,4-triphenyl-4,5-dihydro-1H-1,2,4-triazoline	
TTT	Time-Temperature-Transformation	

$T_{5\%}$	5 wt% loss temperature	°C
$T_{10\%}$	10 wt% loss temperature	°C
T_{α}	Temperature of α relaxation	°C
T_{β}	Temperature of β relaxation	°C
T_{γ}	Temperature of γ relaxation	°C
T_g	Glass transition temperature	°C
$T_{g\infty}$	Infinite glass transition temperature	°C
T_m	Melting temperature	°C
T_p	Polymerization temperature	°C
T_r	Reaction temperature	°C
T_v	Temperature of vitrification	°C
α	Extent of conversion	
α_i	Extent of conversion at time t_i	
β	Heating rate	K.min ⁻¹
ΔH_i	Heat released at time t_i	J.g ⁻¹
ΔH_{tot}	Total heat released	J.g ⁻¹
ϕ	Heat flow	W.g ⁻¹
θ	Contact angle	°

Table of content

General Introduction	15
Part I – Polybenzoxazine thermosets	21
Chapter I: From petrobased to bio-based thermosets – State of the art	23
I. History of thermosets engineering	25
II. General characteristics of thermosets	26
II.1. Gelation	26
II.2. Glass transition and vitrification	26
III. Main classes of thermosets	28
III.1. Phenol-Formaldehyde resins	29
III.1.1. Properties of phenolic resins	31
III.1.2. Drawbacks of phenol-formaldehyde resins	31
III.2. Epoxy resins	32
III.2.1. Polymerization process	33
III.2.2. Properties and applications of epoxy resins	34
III.3. Polybenzoxazine resins – A new generation of phenolics	35
III.3.1. Commercialization of polybenzoxazine resins	37
III.3.2. Synthesis of the monomer	41
III.3.3. Ring-opening polymerization and cure mechanism	43
III.3.4. Di-functional benzoxazine monomers	44
III.3.4.1. Synthesis and properties of diamine bridging groups	45
III.3.5. Benzoxazine monomers from renewable phenolic derivatives	48
IV. References	55
Chapter II: Cardanol-based benzoxazine resins: structure-to-properties relationship	63
I. Introduction	65
II. Materials and methods	69
II.1. Materials	69
II.2. Liquid state NMR characterization	69
II.3. Mass analysis	69
II.4. FT-IR analysis	69
II.5. Differential Scanning Calorimetry (DSC)	70
II.6. Rheological analysis	70
II.7. Dynamical Mechanical Analysis (DMA)	70
II.8. Thermogravimetric Analysis (TGA)	70
III. Results and Discussions	72
III.1. Monomers synthesis and structural characterization	72
III.1.1. Symmetric benzoxazines synthesis	72
III.1.1.1. ¹ H NMR characterization	73
III.1.1.2. Mass characterization	76

III.1.2. Asymmetric benzoxazines synthesis	79
III.1.1.1. ¹ H NMR characterization	79
III.1.1.2. Mass characterization	81
III.1.3. Purification process	82
III.1.4. FT-IR characterization of benzoxazine monomers	83
III.2. Thermo-analytical follow-up of ring opening and cross-linking reactions	84
III.2.1. Characterization by DSC	84
III.2.2. DSC vs TGA correlation	89
III.2.3. Chemorheology of polymerization	90
III.3. After cure completion, characterization and final properties of the polybenzoxazine resins	92
III.3.1. Material preparation	92
III.3.2. FT-IR characterization of the polymers	93
III.3.3. Thermo-mechanical characterization by DMA	94
III.3.4. Thermal stability of the cured products	97
IV. Conclusion	100
V. References	101
VI. Supplementary Information	107

Chapter III: Physico-chemical aspect of phenol-based benzoxazine polymerization

	109
I. Introduction	111
II. Thermokinetic analysis	113
II.1. Extent of conversion and apparent activation energy	113
II.2. Isoconversional methods: Principle and Advanced kinetic methods	114
II.3. Advanced isoconversional analysis	115
III. Results and Discussions	116
III.1. Non-isothermal kinetic analysis of di-phenol benzoxazine polymerization reaction	116
III.2. Apparent activation energy	117
III.3. Thermal and thermomechanical analyses and kinetic studies	120
III.4. Chemorheological analysis and kinetic study	121
III.5. Evolution of glass transition temperature (T _g) over curing	122
IV. Isothermal analysis	124
IV.1. DSC measurements	124
IV.2. Isoconversional analysis in isothermal mode of di-phenol BZ	125
V. Conclusion	127
VI. References	128

Part II – Dialdehyde cellulose-based composites _____ 133

Chapter IV: From lignocellulosic biomass to bio-based thermosets – State of the art _____ 135

I. Vegetable biomass _____	137
I.1. The complex architecture of plant cell wall _____	137
I.2. Composition of plants _____	138
I.2.1. Cellulose _____	138
I.2.1.1. Molecular structure _____	139
I.2.1.2. Cellulose biosynthesis _____	140
I.2.2. Hemicellulose _____	140
I.2.3. Lignin _____	142
I.2.4. Other compounds _____	143
II. From in situ cellulose to cellulosic raw materials _____	143
II.1. The different sources of cellulose _____	143
II.2. Extraction of cellulose from biomass _____	144
II.2.1. Mechanical pulp _____	144
II.2.2. Chemical pulp _____	144
II.2.3. Chemi-(thermo)mechanical pulp _____	144
II.3. The different forms of isolated cellulose _____	144
II.3.1. Thermo-mechanical properties _____	146
II.4. Surface modification of cellulose _____	147
II.4.1. Substitution: cellulose esterification _____	148
II.4.2. Substitution: cellulose etherification _____	148
II.4.3. Cellulose oxidation _____	149
III. From lignocellulosic biomass to furanic building blocks and polymers _____	152
III.1. Furfuryl alcohol _____	155
III.1.1. Synthesis of furfuryl alcohol _____	155
III.1.2. Properties, reactivity, and applications _____	156
III.1.3. From furfuryl alcohol to poly(furfuryl alcohol): polymerization mechanism _____	157
IV. References _____	161

Chapter V: Microfibrillar cellulose: a suitable filler for bio-based composites within a poly(furfuryl alcohol) matrix _____ 171

I. Introduction _____	173
II. Experimental section _____	175
II.1. Chemical materials _____	175
II.2. FTIR Spectroscopy _____	175
II.3. Transmission Electronic Microscopy (TEM) _____	175
II.4. Differential Scanning Calorimetry (DSC) _____	175
II.5. Dynamic Mechanical Analysis (DMA) _____	176

II.6. Thermogravimetric Analysis (TGA)	176
II.7. Cellulose oxidation	176
II.8. Determination of the degree of oxidation (DO)	176
II.9. Material preparation	177
III. Results and Discussion	179
III.1. FTIR analysis	179
III.2. DSC measurements of FA polymerization in presence of MFC	180
III.3. Microscopic morphology characterization by TEM	182
III.4. Thermo-mechanical properties investigation by DMA	184
III.5. Thermal properties investigated by TGA	188
IV. Conclusion	189
V. References	191
VI. Supplementary Information	194

Chapter VI: Hydrophobization of thermoset-like all cellulose composites **195**

I. Introduction	197
II. Experimental section	200
II.1. Characterization techniques	200
II.1.1 Liquid state NMR	200
II.1.2. FT-IR spectroscopy	200
II.1.3. Scanning electron microscopy (SEM)	200
II.1.4. Water contact angle	200
II.1.5. Dynamic mechanical analysis (DMA)	200
II.2. Chemical materials	201
II.3. Preparation of 5,5'-dihydroxymethyl furoin (DHMF)	201
II.3.1. Characterization by ¹ H NMR	202
II.3.2. Characterization by FT-IR	203
II.4. Processing of the all cellulose composites	204
III. Results and Discussions	206
III.1. Structural characterization	206
III.1.1. FT-IR characterization	206
III.1.2. Macroscopic and microscopic morphologies of the thermosets ACCs	208
III.2. Moisture sensitivity	211
III.3. Thermo-mechanical properties of the composites by DMA	215
IV. Conclusion	219
V. References	220
VI. Supplementary Information	222
General Conclusion	231

General Introduction

In the last two decades, the chemistry of renewable resources and related bio-based materials got the attention of scientists, from both the academy and the industry. Nowadays, the petroleum dominance in Chemistry for the synthesis of synthons is almost total, including the field of polymers and advanced materials. The world production of plastic is continually increasing reaching 335 million tonnes in 2016 (against 322 in 2015 and 311 million tonnes in 2014). This production applies for a wide range of applications such as packaging (39.9 %), building and construction (19.7 %), automotive (10 %), electrical and electronics (6.2 %), and agriculture (3.3 %)¹. However, the rarefaction of this resource impacts directly on the world economy as it is not renewable on a human scale, and the immoderate use of petroleum by-products leads to important environmental damages. To accommodate the needs of a growing world population with the resulting impact on our environment is one of the biggest challenges of today's society.

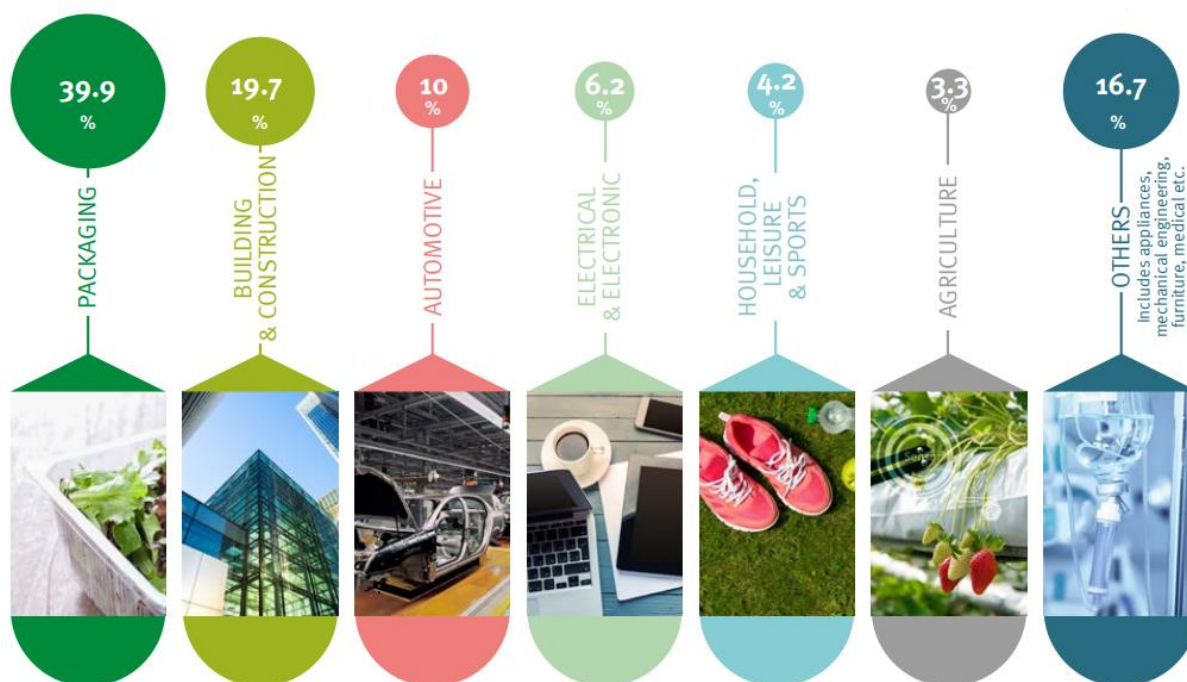


Figure 1. Plastic world production in 2016. Source: *PlasticsEurope Market Research Group (PEMREG) and Conversion Market & Strategy GmbH.*

To regulate this man-made disruption on the environment, a common agreement has been endorsed through the Kyoto protocol in 1997 in order to reduce the greenhouses gas emissions. Ten years later, the REACH directive (Registration, Evaluation, and Authorization of Chemicals) entered into force in 2007 to increase the legislation on safety and chemical management, according to the principles of Green Chemistry. This concept has been defined in the 90's by Paul Anastas and John Warner². From 12 principles, they encourage “invention,

conception, and application of chemical products and processes that aim at reducing the utilization and production of dangerous compounds". Thus, the scientific community started to develop for the last two decades processes for polymers from renewable resources, motivated by the 7th principle.

Crude oil, coal, natural gas, and biomass are sustainable resources of carbon. Vegetable biomass is a good candidate for sustainable raw materials for the preparation of polymers. It is estimated to 10,000 billion of tons. Research is mainly based on this resource to create new synthesis processes, both ecologic and sustainable, and lead to more eco-friendly materials. Following this idea, researchers could extract molecules used for chemical syntheses and polymers preparation essentially from agricultural waste and bio-refinery by-products. The use of natural resources from non-food crops and non-edible by-products allows a valorization of these second and third generation feedstocks, which were stocked or burnt until a few years ago, and are still mainly burnt. The re-use of these materials is part of the circular economy. In addition, when these materials are bio-based we talk about bio-economy. Among the possible raw renewable materials available from vegetable biomass, two bio-resources present a high potential to replace petroleum: plant oil and lignocellulosic biomass.

Cardanol is a natural oil extracted from the Cashew Nutshell Liquid (CNSL), and is an economical and abundant non-edible agricultural by-product used in many applications in research and industry³. More than a sustainable, available, and at an advantageous price, cardanol presents an aromatic structure with a 15 carbons aliphatic side chain which makes it an interesting and promising natural phenol derivative.

The lignocellulosic biomass is composed, among other things, of hemicellulose. After chemical treatment and acid hydrolysis, furfuryl alcohol (FA) is extracted from the hemicellulose. The FA is a bio-based monomer that can be polymerized with an acid catalyst to form a bio-based thermoset. Moreover, the cellulose is the most abundant natural polymer present in plant biomass. It remains the most explored and exploited as it is very promising for new material applications since its physico-chemical properties offers a wide potential for innovation. Cellulose is often used as a reinforcement compound but can also be chemically modified for the preparation of new types of bio-based thermosets.

Thus, the work presented in this thesis is based on the preparation of greener thermosets and composites. The thesis is separated into two parts: the first part concerns the study of polybenzoxazine thermoset matrix. The interest for this class of polymer is growing under the polymer community. This work was performed in collaboration with the Luxembourg Institute

of Science and Technology. The second part is dedicated to the preparation of fully bio-based composites from the lignocellulosic biomass. This part of the work was performed in collaboration with the *Centre de Recherche sur les Macromolécules Végétales* in Grenoble.

After this general introduction and context of the work, **Chapter I** is dedicated to the bibliographic study of thermosets further centered on polybenzoxazines (PBZ) which is the first thermoset matrix studied here.

Chapter II presents the results and discussions on three systems of benzoxazine (BZ). As the cardanol gains more interest for the preparation of bio-based materials, this study aims at increasing the understanding of the effect of cardanol on the final polymer properties, and particularly the effect brought by the aliphatic side chain. For this purpose, di-functionalized BZ monomers were synthesized. The first was obtained using two phenols, then using one phenol and one cardanol, and finally with two cardanols.

Chapter III is dedicated to the kinetic analysis of polymerization of the first synthesized di-phenol monomer, using advanced isoconversional analysis.

Chapter IV introduces the second part with the bibliographic part of the lignocellulosic biomass presenting the main natural polymers and the different ways to modify cellulose. Then, a description of the obtention of FA from hemicellulose is followed by its detailed polymerization into poly(furfuryl alcohol) (PFA).

Chapter V is centered on the use of modified microfibrillar cellulose as a filler to reinforce the PFA and improve its stiffness.

Chapter VI focuses moisture sensitivity issue of cellulose, in the form of thermoset-like “all cellulose composites” (ACC). These ACC were reinforced by furanic cross-linkers to evaluate their effect of the moisture sensitivity, and thus their hydrophobicity.

Finally, a general conclusion summarizes the results obtained in this thesis and presents some outlooks.

- (1) *Plastics-the Facts 2017 An Analysis of European Plastics Production, Demand and Waste Data.*
- (2) Anastas, P. T.; Warner, J. C. *Green Chemistry: Theory and Practice*; New York, 8991.
- (3) Paramashivappa, R.; Phani Kumar, R.; Vithayathil, P. J.; Srinivasa Rao, A. Novel Method for Isolation of Major Phenolic Constituents from Cashew (*Anacardium Occidentale* L.) Nut Shell Liquid. *J. Agric. Food Chem.* **2001**, *49* (5), 2548–2551.

Part I

Polybenzoxazine thermosets

Chapter I

From petro-based to bio-based
thermosets – State of the art

I. History of thermosets engineering	25
II. General characteristics of thermosets	26
II.1. Gelation	26
II.2. Glass transition and vitrification	26
III. Main classes of thermosets	28
III.1. Phenol-Formaldehydes resins	29
III.1.1. Properties of phenolic resins	31
III.1.2. Drawbacks of phenol-formaldehyde resins	31
III.2. Epoxy resins	32
III.2.1. Polymerization process	33
III.2.2. Properties and applications of epoxy resins	34
III.3. Polybenzoxazine resins – A new generation of phenolics	35
III.3.1. Commercialization of polybenzoxazine resins	36
III.3.2. Synthesis of the monomer	39
III.3.3. Ring-opening polymerization and cure mechanism	41
III.3.4. Di-functional benzoxazine monomers	42
III.3.4.1. Synthesis and properties of diamine bridging groups	43
III.3.5. Benzoxazine monomers from renewable phenolic derivatives	45
IV. References	52

I. History of thermosets engineering

“Resin or plastic compounds which in their final state as finished articles are substantially infusible and insoluble. Thermosetting resins are often liquid at some stage in their manufacture or processing, which are cured by heat, catalysis, or other chemical means. After being fully cured, thermosets cannot be resoftened by heat. Some plastics which are normally thermoplastic can be made thermosetting by means of cross-linking with other materials.” This is the definition of thermosets found in Whittington’s Dictionary of Plastics¹.

A large variety of thermoset polymers has been developed during the years, essentially because of the economical commercialization of key precursor materials rather than a result of a chemist’s ability to adjust polymers for specific characteristics and properties. The notion of macromolecules of Staudinger² is relatively recent as it was proposed and accepted only in the late 1920’s. The concept of macromolecules was then in contrast with the micellar theory that describes big molecules as an aggregation of smaller molecules, kept together by non-covalent interactions.

Polymers can be classified considering various criteria (*e.g.* origin, structure, stereochemistry, number of monomers, connectivity, properties, applications, etc.). Within this classification can be found rubbers. Rubbers, naturals or synthetics, are widely used industrial products. It presents the main properties to be tough, elastic, water and chemical resistant, hard to tear, and resist to abrasions and impacts. These properties lead to their use in tires or gloves. The subcategory “Plastics” of the polymers can be differentiated into two main categories, thermoplastics and thermosets, depending on their response to temperature³. Thermoplastics are constituted of linear or branched polymer chains which are known to be re-moldable and recyclable. Thermosets are covalent cross-linked polymer forming a three-dimensional network. Due to this strong architecture, a thermoset is considered infusible, insoluble, and non-recyclable (they are sometimes re-used by grinding them to make composites). On the other hand, they possess very high thermo-mechanical properties. However, recent research focused on the recyclability of thermosets^{4,5}, particularly for a better environmental impact.

II. General characteristics of thermosets

II.1. Gelation

Thermosets are very interesting materials and widely used in the industry. For a better understanding of the material, it is important to understand their general characteristics. Among them, the gelation phenomenon is a transition occurring during curing where the molecular weight reaches nearly the maximum and is usually assumed to be infinite. At this point, all monomers are connected by at least one covalent bond, forming an insoluble macromolecule. Gelation is a microscopic transformation producing macroscopic changes. This phenomenon depends on the chemistry of the system and occurs at a specific degree of conversion⁶. The microscopic gelation itself is difficult to measure as the obtained network is insoluble with a molecular weight close to infinite. In contrast, the macroscopic effect is easier to detect. The macroscopic gel point can be identified by thermo-mechanical techniques such as rheological analysis or dynamic mechanical analysis (DMA). Above gelation, there is no more increase in the molecular weight, but the cross-link density increases and the free chain segment length decreases⁷. Gelation is important from an industrial processing point of view because when the viscosity is high, it affects the general processability of thermosets and composite prepregs. And depending at which stage of curing the gelation occur, it affects the final properties of the material such as the stiffness and adhesion. In general, thermosets cannot be processed above gelation. Gillham⁸ suggested to determine the gelation point as the peak in the tangent delta from a frequency depended isothermal DMA measurement. DMA transitions show frequency dependence; however, the gel point is defined as the point where the tangent delta becomes frequency independent. A common method is to use the crossover point between the storage and the loss moduli, and it can also be defined in term of viscosity as it is correlated with the maximum of viscosity⁹. The method proposed by Gilham is known to be the most reliable, even though it is more time consuming than other methods.

II.2. Glass transition and vitrification

The glass transition temperature (T_g) is an important characteristic of polymeric materials. This temperature correlates to a drastic variation of the heat capacity (C_p) and therefore, to the material's mechanical properties. Thus, it can be measured either by Differential Scanning Calorimetry (DSC) or by Dynamic Mechanical Analysis (DMA). Note that the transition measured by DMA is not strictly identical to the glass transition measured by DSC. DMA measure the α -relaxation (T_α) which corresponds to a mechanical relaxation, while DSC

measures the heat capacity variation that is associated to the transition from the glassy state to the rubbery state (T_g) or from the rubbery state to the glassy state (*i.e.* vitrification, T_v). The glass transition temperature is defined as a temperature domain of the transition from the glassy state to the viscoelastic or rubbery state during thermal treatment. The understanding of this critical feature is important for applications, because it determines the mechanical properties of the material at a given temperature. During the cross-linking, vitrification can occur if the T_g is equal or becomes higher than the reaction temperature (T_r). This phenomenon of vitrification corresponds to the transition from the liquid to the glassy state and induces a high decrease of the molecular motion. It can occur before or after gelation and can be observed for isothermal or non-isothermal curing processes. Vitrification is also important in term of processability as the kinetic of polymerization is highly decreased in the glassy state. It was shown that at this stage, the reaction is not chemically controlled but controlled by diffusion¹⁰. This effect becomes relevant with an increase of the difference between the glass transition temperature and the reaction temperature ($T_g - T_r$). When this difference reaches 20 – 40 °C¹¹, the reaction is considered as stopped. During the polymerization, the T_g value increases with conversion as the molar mass increases in the pre-gel state as well as the cross-link density in the post-gel state.

To summarize the concepts presented above, the Time-Temperature-Transformation (TTT) diagram developed by Gillham for thermosetting systems⁸ shows the transitions between the different states and phenomena taking place during the cross-linking (**Figure 1**). The TTT diagram presents the three critical temperatures of the glass transition noted T_{g0} , $T_{g\text{ gel}}$, and $T_{g\infty}$ which correspond to the glass transition temperature of precursors before any reaction, the temperature of coincidence between gelation and vitrification, and the glass transition temperature of the fully cross-linked system, respectively.

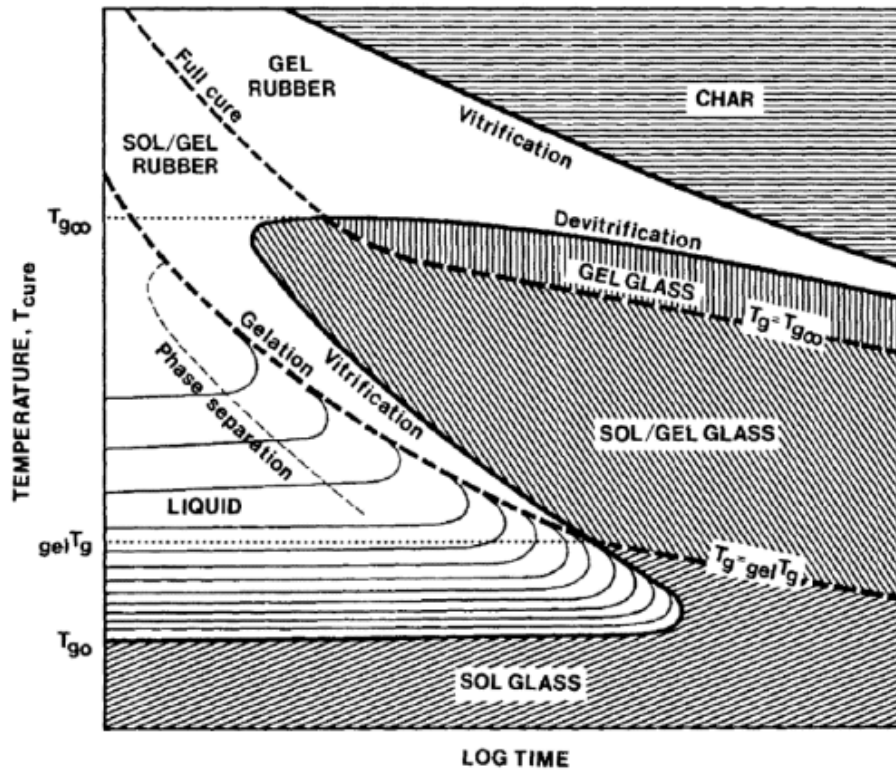


Figure 1. Time-Temperature-Transformation (TTT) diagram by Gillham⁸.

III. Main classes of thermosets

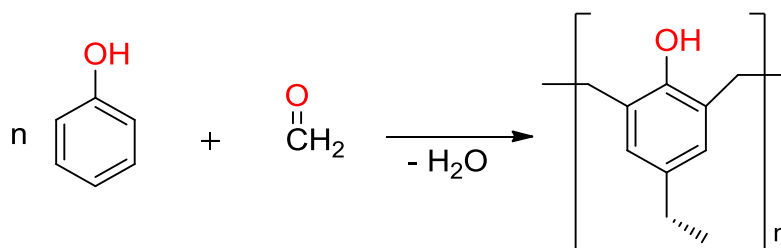
The first successful commercial venture based on polymers started when Charles Goodyear discovered the process of vulcanization of natural rubber in 1839¹². Plastics industry started with the world's first synthetic plastic, Bakelite, developed by Leo Baekeland in 1909¹³. Bakelite was dominant in the plastics technology for many years commonly used in the coating industry for protective purposes and in electrical and automobile industry for its low conductivity properties and high heat resistance. Nowadays, the advance of various milestones in thermosetting resin technology (**Table 1**) allows to progressively substitute Bakelite, either being easier to manufacture or at a lower cost. The main industrially used thermoset resins are described in the following sub-chapters.

Table 1. Historical milestones of thermosets⁹.

1839	Vulcanization of rubber by Goodyear
1909	'Heat and Pressure' patent for phenolic resins by Baekeland
1928	Commercial introduction of Urea-formaldehyde
1933	Patent on unsaturated polyester resins by Ellis
1937	1 st production of polyurethanes
1939	1 st patent on epoxy
1942	Industrialization of silicon by Dow Corning
1947	Commercialization of epoxy
1954	Polyurethanes introduced in the US
1964	Polyimides introduced as a fabricated product
1970s	1 st patent on cyanate esters by Mobay & Bayer
1970s	Polyimides thermosets expand into high-T adhesives and composites for aerospace applications
1980–1990s	Development of BMI & BMI copolymer commercial applications

III.1. Phenol-Formaldehydes resins

First developed in the beginning of the 20th century, resins based on the use of formaldehyde and obtained by polycondensation have found interest in many fields, like insulation, coatings, electrical devices, automotive parts, or adhesives and mainly in wood industry¹⁴. Phenol-formaldehyde resins are the first fully synthetic man-made resin, from the polycondensation reaction between phenol and formaldehyde (**Scheme 1**).

**Scheme 1.** Chemical reaction leading to phenol/formaldehyde resin.

The use of phenolic resins was promoted by the “heat and pressure” patent of Leo Baekeland in 1909. The patent involved the use of high pressure and closed mold, to avoid the problems of bubbles and the evolution of gases and steam. Fillers were used to avoid the problem of brittleness of polymerized phenolic resin by enhancing its properties^{13,15,16}. Depending on the

phenol/formaldehyde ratio and the used catalyst, these phenolic resins are differentiated in two types: resol phenolic resins and novolac phenolic resins^{9,17,18}.

- Resol phenolic resins

Resol phenolic resins are produced by the polymerization of phenol and formaldehyde solution, with an alkaline catalyst, at 100 °C for about 1 hour. The most usual conditions include 1.1 to 1.5 mole of formaldehyde for 1 mole of phenol. At this stage of polymerization, the product is an intermediate gel-like resin. To have a solid product, the intermediate is dried under vacuum for 3 to 4 hours. Under these conditions, resol phenolic resins belong to water-soluble thermoplastics. To reach the final thermoset material, heating above its gel point initiates the curing process. Resol resins have reactive methylol and hydroxyl groups which participate to the formation of larger molecules through methylene cross-linking reactions, without addition of a curing agent.

Resol phenolic resins have a short shelf life (less than 1 year) and have the advantage to not require curing agent but only heat to initiate the cross-linking reactions. However, its cross-linking occurs through a polycondensation reaction, leading to water as by-product.

- Novolac phenolic resins

In contrast to the resol phenolic resins, the polymerization for novolac phenolic resins requires the presence of an acid catalyst and present an infinite shelf life under usual storage conditions and require a hardener for the cross-linking. Usually, a pre-polymerization step is performed with a phenol-formaldehyde ratio of 1:0.8. After a polymerization of 2 to 4 hours at 160 °C for water removal, a low molecular weight molten intermediate is obtained. The corresponding glassy material is obtained after cooling and blended with powdered hexamethylene tetramine (HMTA). Upon heating, the HMTA provides the formaldehyde necessary for the final curing, giving to the resin a final phenol-formaldehyde ratio of 1:1.5.

Some differences between resol type and novolac type phenolic resins are listed in **Table 2** below.

Table 2. Main differences between resol and novolac phenolic resins.

Resol phenolic resins	Novolac phenolic resins
Alkaline catalyst	Acidic catalyst
Quench	Pre-polymerization
Methylol bearing resins	Non methylol bearing resins
Short shelf life	Infinite shelf life
By-product: water	By-product: ammonia
Liquid	Solid

III.1.1. Properties of phenolic resins

Phenolic resins are available in the forms of flaks, films, liquid, and powder. They are considered to be general-purpose thermosets and cost about 1.85 € per kilogram^{19–21}. Classical phenolic resins based on resol and novolac reach an annual worldwide production volume of approximately 4.7 million tons in 2014²². These resins offer attractive characteristics such as high mechanical strength, heat resistance and dimensional stability, high resistance against various solvents, acids and water. They are flame resistant materials and induce low smoke upon incineration. Their composites, through their good heat and flame resistance and low cost, find a major place in thermo-structural application in the aerospace industry^{14,23}. Moreover, phenolic resins can be easily molded into different shapes and present low volume shrinkage. Novolac-based resins are more dimensionally stable as they release ammonia upon curing, compared to resol-based resins which release water, as water molecules are larger than ammonia molecules, which can create more, or larger defects within the material⁹.

III.1.2. Drawbacks of phenol-formaldehyde resins

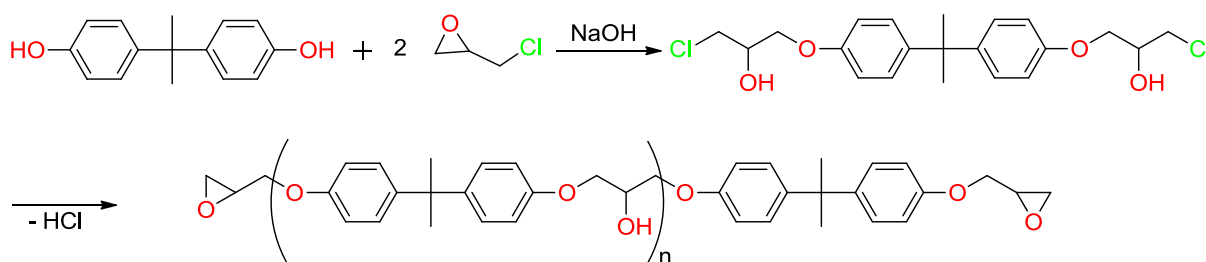
Phenolic resins present some major shortcomings. They cure at a relatively high temperature by a polycondensation reaction which releases by-products. This requires the application of pressure during molding and curing to avoid the formation of bubbles and form a void-free component. The curing reaction requires the use of a catalyst. The final resol type resins present a limited shelf-life at ambient conditions, while novolac type resins release ammonia during the process. Moreover, as for many neat matrices, phenolic resins are very brittle, due to their rigid aromatic units held by short methylene linkages.

To try to overcome these drawbacks, different strategies have been studied, *e.g.* either by incorporation of fillers^{24–28} or by modifying the chemistry with the concept of addition cure

phenolics²⁹⁻³¹. In this concept, a new chemistry is needed to modify the cure, particularly the cross-linking without the production of volatiles.

III.2. Epoxy resins

In 1943, Pierre Castan patented his process for the preparation of an artificial thermosetting resin³². The first commercially available and until today, the most popular epoxy resin, is synthesized from the reaction of bisphenol A with epichlorohydrin, resulting in diglycidyl ether of bisphenol A (DGEBA). This chemical reaction is described in **Scheme 2**. Epichlorohydrin is generally used in large excess or can also be used as solvent. Sodium hydroxide is added either in aqueous or alcoholic solution to form a phenolate intermediate³³. In general, the mechanism is described as two competitive reactions between a phenolate ion (Ar-O⁻) and epichlorohydrin. The first reaction is a one-step reaction of nucleophilic substitution with the cleavage of C-Cl bond; the second reaction is a two-step reaction associated with a ring-opening of the epichlorohydrin by the phenolate ion followed by an *intra*-molecular cyclization of the generated alcoholate which goes with a release of chlorate anion.



Scheme 2. Chemical reaction between bisphenol A and epichlorohydrin to form DGEBA monomeric resin. With n = number of repeating units, from 0 to 25 for typical commercial product.

This epoxidation strategy has the advantage of the possibility of tailoring the length and molecular weight of the pre-polymer. Thus, DGEBA characteristics depend mainly on the molar ratio epichlorohydrin/bisphenol A. Other strategies of epoxidation exist:

- *Oxidation of double bonds*: epoxidation is obtained by peroxidation of C=C double bonds. The use of hydrogen peroxide (H₂O₂) can be sufficient to generate oxiran rings. However, if an electron withdrawing group is present in β -position of the double bond, its oxidation will require a stronger oxidative agent (such as *m*-chloroperbenzoic acid

(*m*CPBA)). This strategy induces a complex purification process of the epoxy monomer, limiting its industrial development^{34,35}.

- *Via glycidyl (meth)acrylate*: the epoxidation is obtained through the reaction of a glycidyl (meth)acrylate with another co-monomer containing a vinyl or (meth)acrylic group by free radical polymerization³⁶.

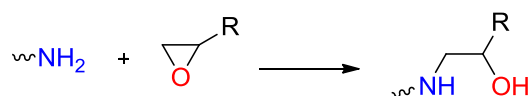
III.2.1. Polymerization process

DGEBA has a linear structure with a monomeric structure described in **Scheme 2**, and the cross-linking requires a curing agent, or hardener which can be either in liquid or solid state. An important feature of the curing process is that no volatile compounds are generated. This allows the formation of a void-free structure without application of pressure during forming or molding processing. Different pathways are possible to generate macromolecular networks of epoxy thermosets.

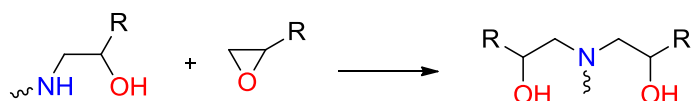
The step growth, or polyaddition pathway concerns the reaction of epoxy groups with a hardener (amine, alcohol, carboxylic acid...) to obtain the cross-linked 3D network. Amines are the most used curing agent for epoxies. The reaction consists of the oxiran ring opening by the primary amine nucleophilic attack leading to a hydroxyl group and a secondary amine which reacts with another oxiran ring. As shown by different authors^{37–39} the generation of hydroxyl function induces a catalytic effect on the epoxy-amine reaction. A side reaction of etherification can occur in excess of oxiran groups (**Scheme 3**).

Main reactivity: polyaddition

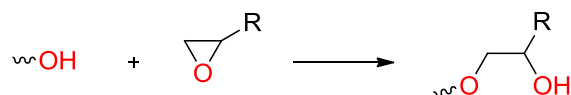
a) Reaction with primary amine



b) Reaction with secondary amine



Secondary reactivity: etherification



Scheme 3. Epoxy/amine main and side reactions of polymerization.

The chain-growth polymerization process includes homopolymerization and copolymerization. The *homopolymerization* is a self-reaction of epoxy groups that can also be induced by thermal or catalytic inductions of either nucleophilic or electrophilic species. The catalytic curing agent forms an active alkoxide which provokes the propagation. Such catalyzed chain propagations lead to relatively low molecular mass values due to several chain transfer and complex termination steps⁴⁰. *Copolymerization* of epoxies can occur with amines, cyclic anhydride or carboxylic acid catalyzed by Lewis bases. Previous authors pointed out a strictly alternant mechanism called “living anionic copolymerization” in analogy with biological system. This kind of polymerization is supposed to avoid all chain transfer and termination reactions^{41,42}.

III.2.2. Properties and applications of epoxy resins

Epoxies have high performance bonding ability, high mechanical strength, excellent dielectric properties, low curing shrinkage because of their high density, good chemical corrosion resistance and do not release volatiles upon curing. Epoxy resins can be cured at ambient temperature or at higher temperatures or even by exposition to UV light. Usually, epoxies cured under heat are more thermally and chemically resistant than those cured at room temperature⁴³. The properties can be modulated depending on the desired application, by modifying the components of the resin and/or the hardener. Thus, the final resin can be flexible or rigid, can possess a high or low modulus, can be filled or foamed, or can be conductive or insulative. These resins are used in a wide range of applications including adhesives⁴⁴, in electronics for encapsulation, potting and printed circuit boards⁴⁵, and in aerospace industries as matrices for composites with high performances⁴⁶. Epoxy resins are also widely used as floor coating. Flooring compositions were regularly developed, giving a hard, chemical resistant, smooth, and firmly adherent floor covering resin. What can be considered as a drawback for these resins is the requirement of a curing agent. Moreover, the resin and the hardener must be mixed right before utilization. The relatively high cost of epoxy resins systems (22.79 € to 89.01 € per square meter) restricts its use mainly for repairing or surfacing existing flooring substrates (*e.g.* concrete)⁴⁷. When used as coating, the rigidity of cured epoxies can be an important shortcoming, which can be counterbalanced by the use of a more appropriate and flexible curing agent and by controlling the stoichiometry between the resin and the hardener. Some specific properties can also be enhanced by addition of a resinous modifier (*e.g.* polyvinyl acetate, polystyrene...), then, the enhanced property is a characteristic property of the added resin, which has eventually a lower cost than the epoxy resin.

III.3. Polybenzoxazine resins – A new generation of phenolics

As previously mentioned, phenolic resins, in the family of high performance polymers, can find a wide range of applications such as aerospace and structural fields. Although classical phenolic resins cannot be substitutes for epoxy resins in many engineering areas, their composites still find a major market for thermo-structural applications essentially in the aerospace industry as they show good heat and flame resistance and low cost. However, as the polymerization occurs by a polycondensation process, small molecules are released causing void formation during the curing process which is the major drawback of this type of thermosets. In this context, a relatively new class of thermoset from the family of phenolic resins, polybenzoxazines, was developed to combine the thermal properties and flame retardance of phenolics and the mechanical performance and molecular design flexibility of epoxy systems⁴⁸. Polybenzoxazine (PBZ) resins succeeded to overcome several shortcomings of conventional novolac and resol-type phenolic resins, while retaining their beneficial properties. PBZ resins can be expected to replace traditional phenolic resins or epoxy resins. The opportunity of molecular design flexibility allows a control of the properties of the cured material for specific requirement. PBZ resins present some unique features^{49,50}:

- No catalyst or hardener required for curing
- No void formation
- Near zero volumetric change upon curing
- Low flammability
- Low water absorption
- Low coefficient of thermal expansion
- High char yield
- High UV and chemical stability
- Excellent static and dynamic mechanical properties
- T_g much higher than cure temperature
- Fast mechanical property build-up as a function of degree of polymerization.

The physical and mechanical properties of PBZ are shown to compare favorably with those of conventional phenolic and epoxy resins. The **Table 3** compares the properties between those three matrices.

Table 3. Comparative properties of high performance polymers²³.

Property	Epoxies	Phenolics	PBZ
Cure temperature (°C)	RT – 180	150 – 190	160 – 220
Max use temperature (°C)	180	200	130 – 280
Cure shrinkage (%)	>3	0.002	~0
Tensile strength (MPa)	90 – 120	24 – 45	100 – 125
Tensile modulus (GPa)	3.1 – 3.8	3.0 – 5.0	3.8 – 4.5
T_g (°C)	150 – 220	170	170 – 340
Elongation at break (%)	3.0 – 4.3	0.3	2.3 – 2.9
TGA onset (°C)	260 – 340	300 – 360	380 – 400
Dielectric constant (1 MHz)	3.8 – 4.5	4.0 – 10	3.0 – 3.5

PBZ resins show the highest tensile properties, the highest onset of thermal degradation, and a T_g which can be raised to as much as 340 °C with proper choice of the phenolic precursor. A remarkable feature of cross-linked PBZ resins is their strong hydrogen bonding network, as strong *intra*-molecular H-bonds between phenolic –OH and Mannich bridge may be responsible of the high onset temperature of thermal degradation²³. Due to their outstanding properties, PBZ resins can be appropriate substitutes for epoxies. However, PBZ resin shows its own shortcomings like high curing temperature which can be in a window range of 160 – 220 °C. The brittleness of this matrix is also a major concern. Thus, modifications are required to both improve the ductility of the final polymer and reduce the polymerization temperature for expanding its applications. Different strategies were employed to try to achieve desirable properties, such as addition of polymerizable groups, co-polymerization, blends, and composites^{51–53}.

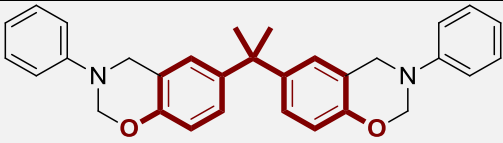
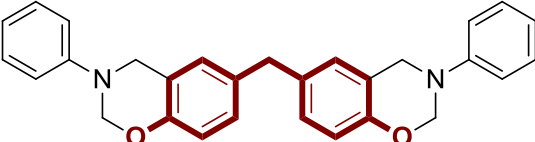
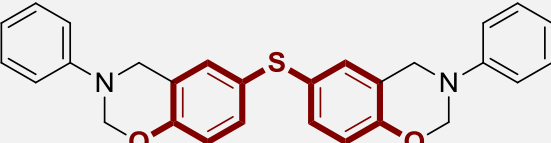
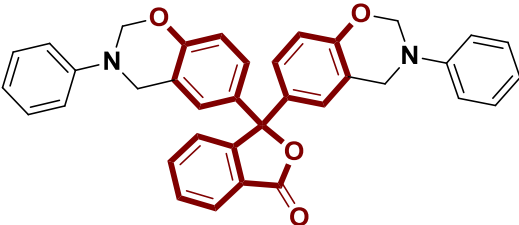
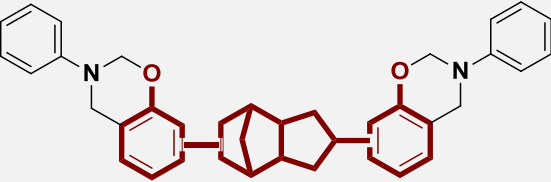
III.3.1. Commercialization of polybenzoxazine resins

Since World War II, only a few polymers reached the commercial stage. The unique characteristics of PBZ presented above (like low dielectric constant, good adhesive properties, high flame and chemical resistance) make them highly attractive for various applications including electronic packaging or aerospace. Subsequently, some companies started to commercialize the resins and their composites. Indeed, polybenzoxazines successfully provide composite materials with outstanding characteristics both in particulate-filled^{54–56}, and fiber-reinforced polybenzoxazine composites^{57–60}. Many studies reported their applications in different fields such as conductive polymeric systems^{61,62}, polymer electrolyte membrane^{63,64},

coatings^{65,66}, electronic packaging⁶⁷, aerospace composites⁶⁸, and wear-resistant composites⁶⁹. Today, different di-functional PBZs are commercialized by Huntsman Advanced Materials, Gurit, Henkel Corporation, and Shikoki Chemical Corporation.

Five main types of benzoxazines are commercialized, based on bisphenol A, bisphenol F, thiobiphenol, phenolphthalein, and dicyclopentadiene, listed in **Table 4**. These di-functional monomers are essentially class A benzoxazines (BZ) (see next section), synthesized with aniline as primary amine.

Table 4. Main commercialized benzoxazine monomers.

Benzoxazine monomer structure	Diphenol starting reagent	Abbreviation	Reference
	Bisphenol A	BPA-a	70
	Bisphenol F	BF-a	71
	Thiobiphenol	TD-a	72
	Phenolphthalein	Boz-BP	73
	Dicyclopentadiene	DCP-a	74

Bisphenol A is the most explored and used due to its various properties and ease of synthesis. Bisphenol A, bisphenol F, and thiobiphenol-based benzoxazines can be synthesized in a solventless media⁷⁵. From an industrially point of view, a solventless synthesis is highly

convenient, cost competitive, and environmentally friendly. Bisphenol A-based resins possess a low melt viscosity before cure, which is a useful property as it can easily wet the filler in processing composites⁵⁹. This low melt viscosity helps the mixing with another resin, which makes it a good candidate for copolymers or alloys^{58,76,77}. Thermal properties are important for industrial applications. For instance, in addition to thermal stability, the char yield may be important. The higher the char yield, the greater the fire-resistance behavior of the resin. Thus, among the commercialized BZ listed previously, thiobiphenol-based BZ presents outstanding properties with its high thermal stability⁷². The derivative of the thermal degradation profile (measured by TGA) presents a sharp peak around 300 °C followed by a broad shoulder around 350 °C with a significantly lower degradation rate with respect to bisphenol A-based resins. Moreover, thiobiphenol-based resins present the higher char yield of 57 % (**Table 5**), leading to a better fire-resistant material. Phenolphthalein and dicyclopentadiene-based BZ are synthesized in solvent media^{73,74}. Phenolphthalein-based resins show excellent thermal and thermo-mechanical properties with a high char yield of 51 %, and a high glass transition temperature (T_g) of 225 °C. Phenolphthalein is a phenolic derivative but also a color indicator depending on the pH. Cao *et al.*⁷⁸ found that the phenolphthalein-based BZ resins keep its color indicating property at a slightly higher pH than phenolphthalein (pH ~ 10 for the resin against pH ~ 8.2 for phenolphthalein). Dicyclopentadiene offers low costs and high reactivity, but its main interest is its good moisture resistance and high reduction of the dielectric constant. These properties are due to the high hydrophobicity induced by linking each phenolic part with a non-polar bridging group, leading to a hydrophobic cycloaliphatic structure. Shieh *et al.*⁷⁴ also studied the moisture absorption of the corresponding cured resin. Among the others, dicyclopentadiene-based resin presents the lowest moisture absorption which is an outstanding characteristic for commercial applications. The moisture uptakes can act as a plasticizer, reducing the mechanical and thermal properties of the cured resin. Moreover, the dielectric constant appeared to be much lower than that of bisphenol A-based resin or traditional phenolic resin, due to a greater free volume and hydrophobicity. Such characteristics perfectly fit for applications as integrated circuit packaging material, as the absorbed moisture may ionize ionic impurities and corrode electric circuit.

Table 5. Thermal characteristics of commercialized benzoxazine resins.

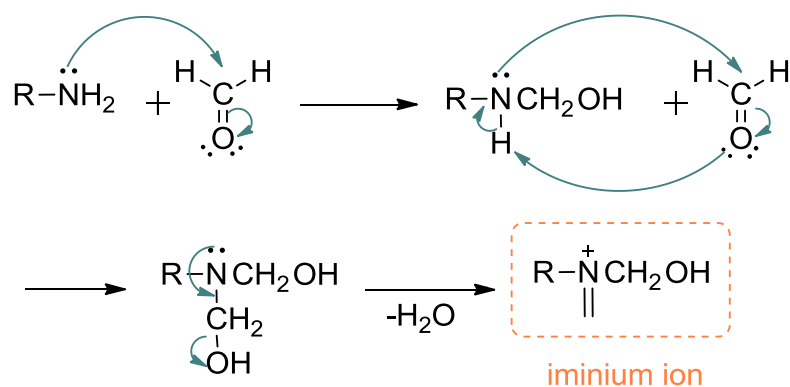
BZ system	T_g (°C) ^[a]	$T_{5\%}$ (°C) ^[b]	Char yield (%)	Ref.
BPA-a	173	325	29	70
BF-a	173	306	46	71
TD-a	216	342	57	72,79
Boz-BP	225	305	51	73
DCP-a	183	391	30.5	74,80

^[a] Glass transition temperature; ^[b] Temperature at 5 % of mass loss.

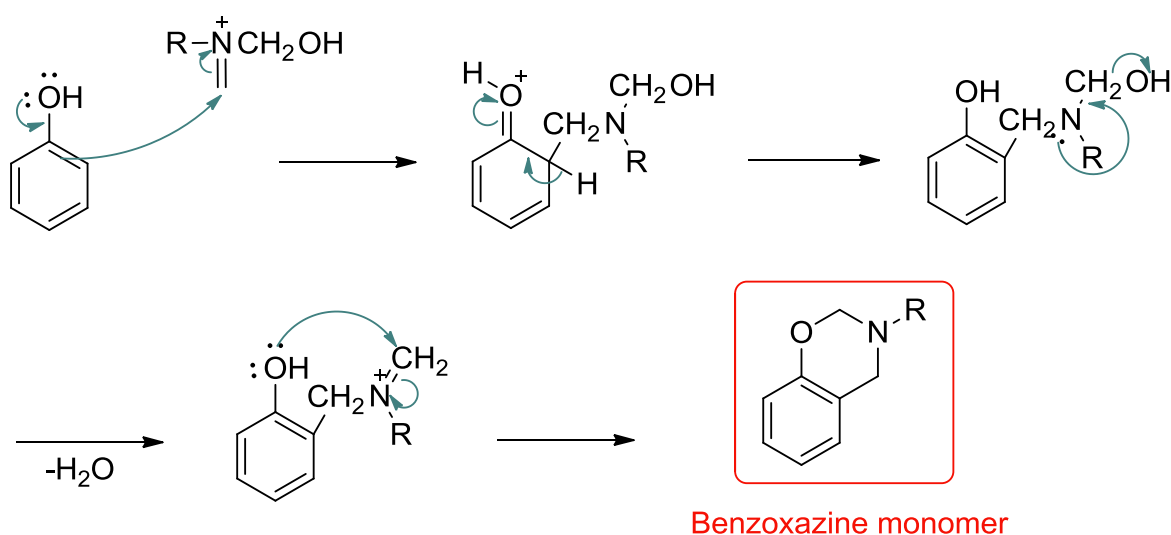
III.3.2. Synthesis of the monomer

Different methods were used to synthesize benzoxazine (BZ) monomers (3,4-dihydro-2H-1,3-benzoxazine). Typical methods that were reported consist in dehydration of *N*-(2-hydroxybenzyl)-3-aminopropanoic acid in the presence of sulfuric acid⁸¹, condensation between aldehyde and *o*-hydroxy benzylamine⁸², reaction of primary amines with 1-(bromoethyl)-2-(chloromethoxy) benzene⁸³, and Mannich condensation of phenol and a primary amine with formaldehyde^{84,85}. Among these different methods, the Mannich condensation was the first to be reported and is still considered as the best pathway for BZ monomer synthesis. This method was popularized by Ishida *et al.* and widely used for the synthesis of various monomers^{49,70,86}. Three precursors are required for the synthesis of BZ monomers: a phenolic derivative which is an active hydrogen containing compound, a primary amine, and formaldehyde. The synthesis described in **Scheme 4** occurs in two steps. In the first step, a Mannich-like reaction leads to the formation of an iminium ion. The second step is an electrophilic aromatic substitution followed by a ring-closure, leading to the final BZ monomer.

Step 1: Mannich reaction



Step 2: Electrophilic aromatic substitution



Scheme 4. Classical approach for the synthesis of mono-functional BZ.

Benzoxazines can be synthesized either as mono-functional or di-functional. Di-BZ can be divided into two main groups depending on whether a di-phenol (class A) or a diamine (class B) is used as the bridging group, increasing the molecular design flexibility. The different types of monomers are pictured in **Figure 2**.

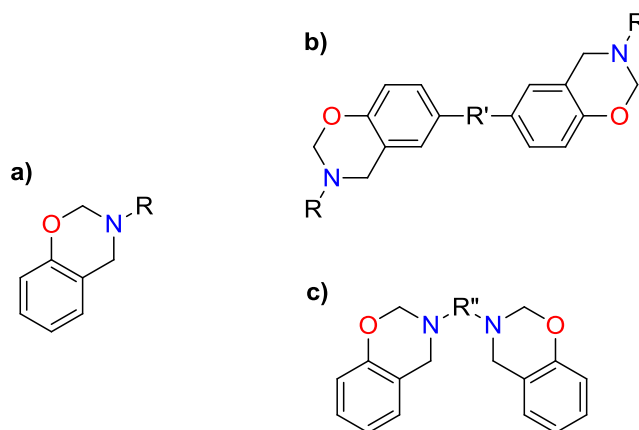


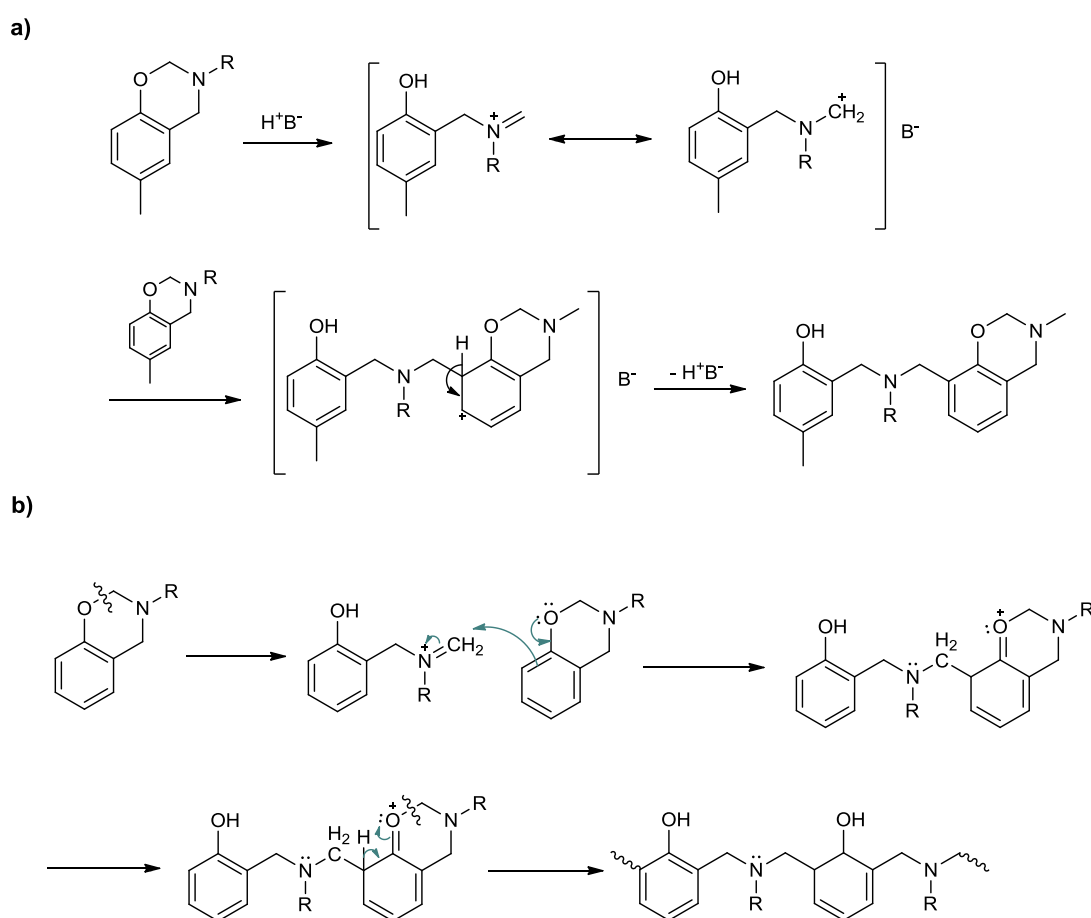
Figure 2. Chemical structures of **a)** mono-BZ, **b)** class A di-BZ, and **c)** class B di-BZ.

The synthesis can be performed with or without solvent. In a solventless method, the mixture of these products is heated to about 100 °C to produce BZ monomer but also ring-opened oligomers. The oligomers' concentration is particularly increased when the reaction is performed in the molten state using aliphatic diamine. The use of a solvent minimizes the formation of oligomers⁸⁷. Chloroform is usually preferred as its temperature of reflux is relatively low, which also limits the formation of oligomers. After the synthesis, BZ monomer is purified by removing the ring-opened structures using soft base washes. However, the purification step may not always be performed, depending on the following study or application, as the ring-opened oligomers may present an advantage. Indeed, the phenolic function of these ring-opened structures can catalyze the ring-opening and further polymerization to occur at lower temperatures. Cross-linking is obtained for di-functional BZ monomers^{70,88}, while mono-functional monomers lead to linear polymers⁸⁹.

III.3.3. Ring-opening polymerization and cure mechanism

The polymerization reaction of BZ is not well defined and different mechanisms have been proposed in the literature. McDonagh and Smith proposed in 1968 a mechanism describing a ring-opening through the formation of iminium ion along the chain. The mechanism presented in **Scheme 5** proposes a proton migration from the oxygen to nitrogen followed by tautomerism⁹⁰. In 1985, Riess *et al.* suggested a mechanism in which polymerization is triggered by condensation of amines with iminium ion⁸⁹. Finally, later in 1999, Dunkers and Ishida proposed a mechanism where the first step in the ring-opening of BZ is the protonation of the oxygen atom to form an iminium ion and in the second step, the polymerization occurs by a reaction of electrophilic aromatic substitution⁹¹. This mechanism proposed by Dunkers and Ishida, presented in **Scheme 5a)**, is more plausible considering the basicity of the

heteroatoms of the oxazine ring that may be in favor of a cationic mechanism for the ring opening polymerization of BZ monomers. However, the most common method for the curing of BZ monomer into cross-linked structure is thermal polymerization, without catalyst. The mechanism can be imagined as follow: breaking of the $-O-CH_2$ bond, tautomerism, and electrophilic aromatic substitution⁹². As the polymerization produces more phenolic groups, its acidity enhances the polymerization rate and creates an autocatalytic process. Thus, the reaction of polymerization of benzoxazines is essentially regioselective. The thermal curing generates a structure *via* the attack of iminium ions in *ortho* position of the phenolic moiety. The proposed polymerization mechanism is described in **Scheme 5b**).



Scheme 5. a) Proposed mechanism for the initiation of curing of benzoxazines⁹¹; b) Polymerization mechanism *via ortho* attack of iminium cation upon thermal activation.

III.3.4. Di-functional benzoxazine monomers

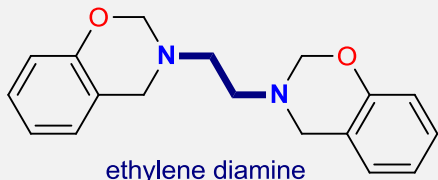

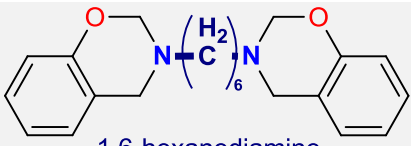
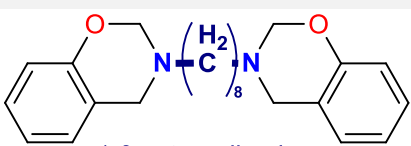
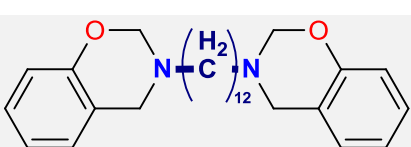
As previously mentioned, di-BZ are divided into two classes depending on the bridging group. Class A di-BZ are prepared from a di-phenol while class B are prepared from a diamine. Class B monomers bring more interest due to their large variety of phenolic derivatives and diamine reagents available, leading to a more interesting versatile synthesis. The general properties are

similar for class A and class B di-BZ. The rigidity or the electronic state of the bridging group presents a similar impact. However, for class B di-BZ, the nature of the diamine bridging group has a strong influence on the synthesis conditions and the thermal properties of both monomer and its corresponding polymer^{93–98}. Moreover, the nature of the substituents of the phenolic has also an important role on the monomer functionality such as the thermal activation of the ring-opening or the cross-link density of the polymerized resin^{99–101}.

III.3.4.1. Synthesis and properties of diamine bridging groups

Each reagent has an influence on the synthesis conditions and properties of cross-linked materials. Regarding the diamine bridging group, it can present an electron donating or withdrawing effect¹⁰². Electron donating groups such as alkyl chains can boost the formation of the oxazine ring, while electron withdrawing groups such as –CO or –SO₂ may reduce the ability to close the ring. This is explained by the ability of these groups to stabilize the mesomeric form of the phenolic groups. The basicity of the primary amine impacts its reactivity and thus the BZ synthesis⁸⁷. To promote the oxazine ring closure, the basicity of the primary amine should be increased. Thus, diamine bridging groups with electron donating effect are more suitable. Among electron donating groups, aliphatic diamines are often used. The presence of an alkyl chain may bring flexibility, which may impact the conditions of synthesis. The effect of the diamine aliphatic chain length on the reaction time and thermal properties was investigated by Allen *et al.*¹⁰³. As the aliphatic chain length increases, from short and relatively rigid to long and relatively flexible, the reaction time increases as described in **Table 6**.

Table 6. Main properties for linear aliphatic diamino-based series of BZ and their corresponding PBZ¹⁰³.

Monomer	Reaction time (h)	T_m (°C) ^[a]	T_g (°C) ^[b]	G'_{RT} (GPa) ^[c]	$T_{1\%}$ (°C) ^[d]
 ethylene diamine	1.5	112	184	2.08	254
 1,4-diaminobutane	4	94	160	1.53	257
 1,6-hexanediamine	8	83	169	1.32	266
 1,6-octanediamine	10	73	151	1.11	271
 1,6-dodecanediamine	12	49	118	0.87	272

^[a] Melting temperature; ^[b] Glass transition temperature; ^[c] Storage modulus at room temperature; ^[d] Temperature at 1 % of mass loss.

The diamine chain length has an important influence on the reaction time of the monomer synthesis. As mentioned in the previous table, short chain length allows a faster and easier monomer synthesis. Furthermore, the length of the diamine chain can modify the thermal properties. Indeed, the melting temperature of the monomer decreases as the chain length increases, from 112 °C for a C₂ chain to 49 °C for a C₁₂ chain. When the melting temperature decreases, the temperature range between melting and polymerization increases, leading to a larger processing window. Brittleness is a strong drawback of PBZ resins. By introducing a flexible chain, the final properties of the cross-linked polymer can be modulated. The storage modulus at room temperature (glassy state) is strongly impacted by the diamine chain length

decreasing from 2.08 GPa to 0.87 GPa, which corresponds to a decrease in the stiffness of the material. As the chain length and the flexibility increase, the glass transition temperature is itself modified and is decreased of 66 °C between a C₂ and C₁₂ chain length. Besides thermo-mechanical properties, the onset of thermal degradation is also impacted. Analyses were performed in nitrogen atmosphere where thermal stability is increased with the diamine chain length until 8-carbons length and beyond, the onset of degradation is not changed.

With the modifications of the properties of cross-linked polymers, there is a need to find a suitable compromise for the design of high performance thermosets with moderate processing conditions. Thus, the monomers synthesized in this thesis are essentially prepared from ethylenediamine (EDA).

III.3.5. Benzoxazine monomers from renewable phenolic derivatives

With the growing interest to produce eco-friendly and high performance materials derived from renewable resources, the use of naturally occurring phenolic derivatives for the synthesis of BZ monomers is considered as a viable alternative to petroleum-based phenolic analogues. During the last years, a broad screening of various mono- or di-functional BZ monomers from bio-based phenolic compounds and their resulting materials was achieved (**Figure 3**). Moreover, in addition to the bio-based phenols, some monomers are prepared using bio-based amines which can be obtained through a sustainable heterogeneous catalyst¹⁰⁴. This attests the clear trend to promote and valorize renewable resources and bio-based reagents for the development of bio-based thermosets.

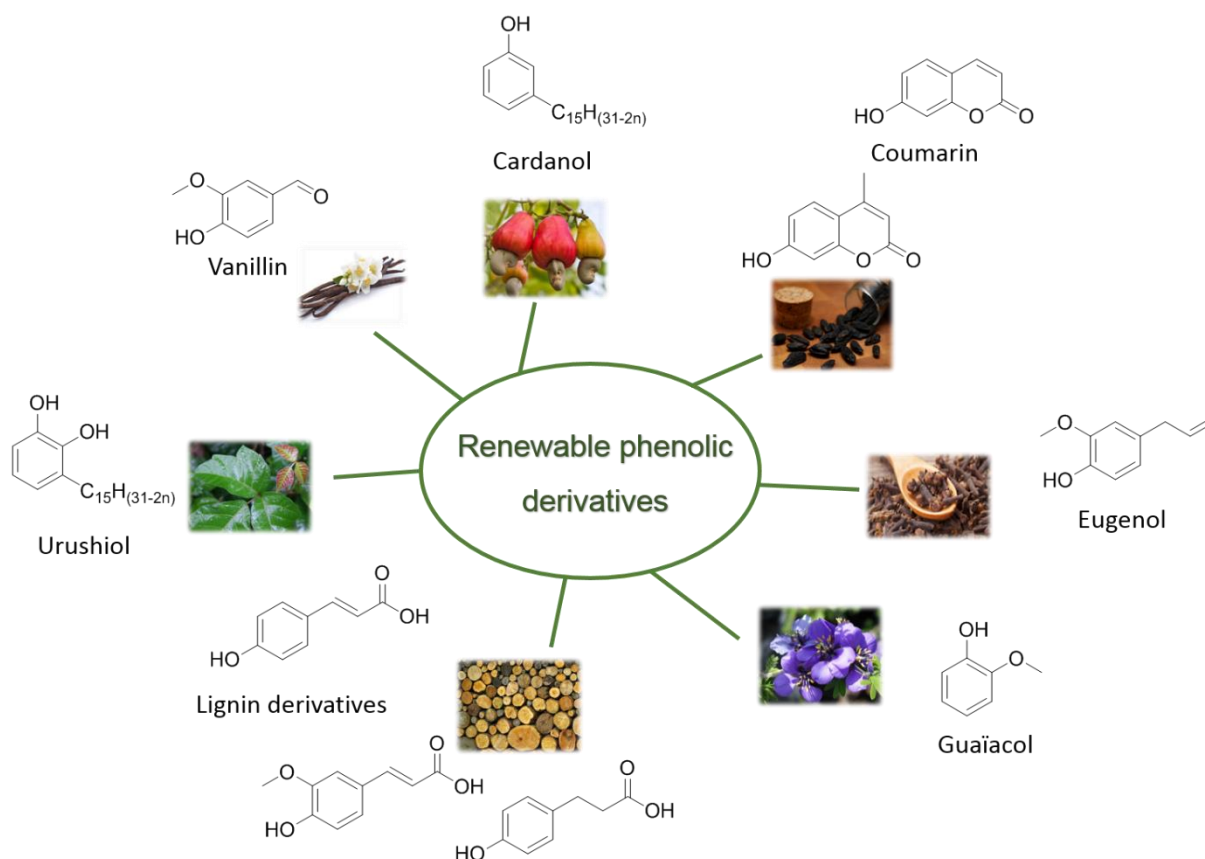


Figure 3. Examples of bio-based phenolic derivatives used for the synthesis of bio-based BZ monomers.

Among these naturally occurring phenolic derivatives, eugenol, guaiacol, urushiol, and ferulic acid from lignin do not present any free *ortho* position after monomer synthesis (**Figure 4**). Yet, *ortho* and *para* positions are the most reactive for the ring-opening polymerization (ROP). When these positions are blocked, the polymerization occurs on the lowest reactive site in *meta* position, hindering the formation of a cross-linked network.

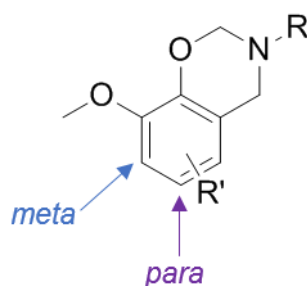


Figure 4. Free position for ring opening polymerization of *ortho* substituted BZ monomers.

Vanillin is historically produced through extraction of vanilla pod but industrially produced through lignin processing^{105,106}. Its use as a phenolic precursor for the synthesis of BZ monomer has recently been studied^{107–109}. Vanillin presents also a methoxy group in *ortho* position but

has the particularity to possess a formyl group in *para* position. With adequate synthesis conditions, the aldehyde function remains unaffected after the monomer synthesis. This function is considered as an additional reactive site on the monomer, as it participates to the ROP to increase the cross-link density by catalyzing the ROP, forming *inter*-molecular H-bonding, or creating additional cross-linking after decarboxylation^{107,110}.

With the use of bio-based phenolic derivatives for the synthesis of di-functional BZ monomers, it is often observed a high melting temperature, reducing the processing window. Particularly in the case of phenolic derivatives (coumaric acid, ferulic acid, or phloretic acid), the acid function presents a catalyst effect, reducing the polymerization temperature¹¹¹. Moreover, PBZ from lignin derivatives show relatively low thermal stability, though the polymerization proceeds with partial decomposition which is an inconvenient for the preparation of suitable materials.

When eugenol is used to synthesize fully bio-based mono-BZ with furfurylamine or stearylamine, it leads to monomers with lower melting temperature¹¹², while eugenol-based di-functional BZ display melting temperature over 90 °C hindering the elaboration of corresponding PBZ material¹¹³.

Coumarin is considered as a competitive bio-based reagent for the synthesis of high performance PBZ, comparable to traditional petroleum-based thermosets. Indeed, coumarin-based PBZ present high glass transition temperature over 180 °C and high thermal stability over 300 °C^{114,115}. However, as for other di-functional BZ from natural phenolic derivatives, coumarin-based BZ display high melting temperatures (around 150 °C) reducing the processing window.

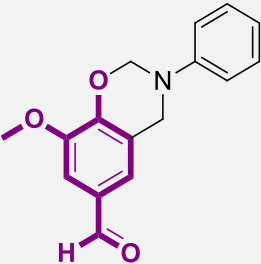
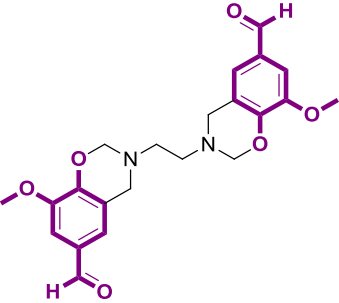
Urushiol is extracted from lacquer trees but is however a toxic compound. Urushiol is a catechol derivative with a C₁₅ aliphatic chain in *meta* position. This alkyl side chain presents varying unsaturations degrees from saturated to tri-unsaturated. Only one *ortho* position is available for the synthesis of the benzoxazine moiety. The polymerization should then occur *via* the *meta* and *para* positions. Using aniline for the synthesis of a mono-BZ monomer, its melting temperature is highly decreased as the corresponding monomer is liquid at ambient temperature¹¹⁶. Urushiol is a promising bio-based phenolic derivative as its corresponding PBZ materials display high glass transition temperature (around 150 °C) and high thermal stability reaching 350 °C.

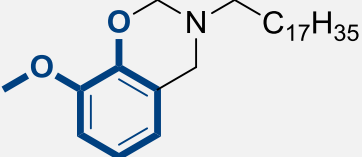
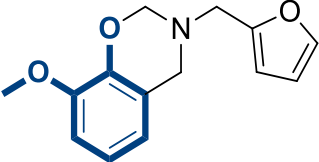
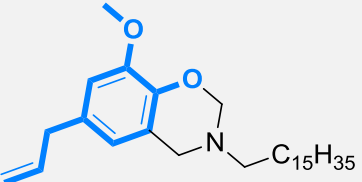
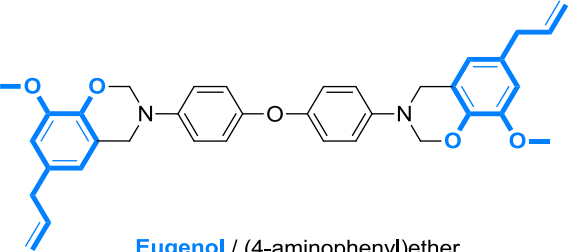
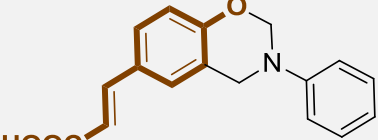
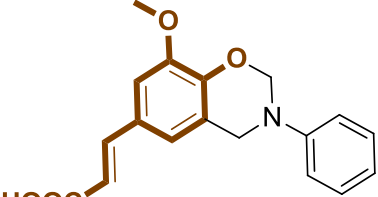
Finally, cardanol, extracted from the cashew nutshell liquid, present a growing interest for the synthesis of BZ monomers. The chemical structure of cardanol shows a similar reactivity to

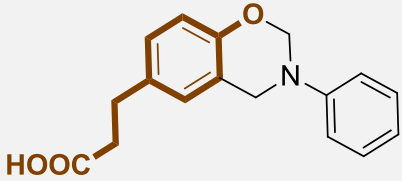
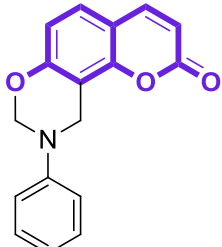
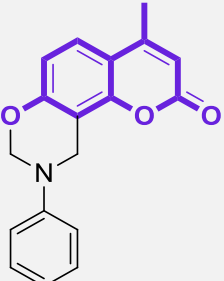
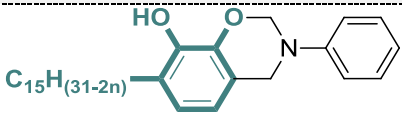
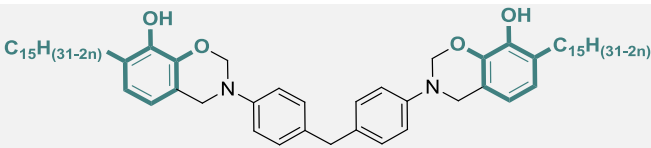
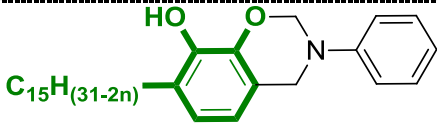
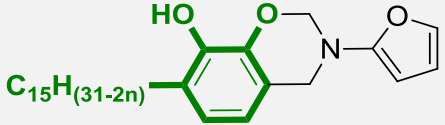
phenol through the presence of the hydroxyl group. Similarly to urushiol, cardanol displays an aliphatic chain of 15 carbons in *meta* position. This long alkyl side chain confers hydrophobicity and flexibility to the usually brittle PBZ polymers, through internal plasticization. In this case, both *ortho* and *para* positions are available for the ROP. In most cases, BZ monomers from cardanol present a melting temperature close to, or below ambient temperature as the C₁₅ side chain may hinder proper crystallization. Thus, the use of cardanol offers a wide processing window. A major drawback in the use of cardanol is that the alkyl side chain provides low cross-link density making difficult DMA analyses. A solution was proposed by Ambrozic *et al.*¹¹⁷, which consists to increase the functionality of the BZ monomer through the reaction between cardanol and furfurylamine, leading to a material with a glass transition temperature around 100 °C. Indeed, the furan ring is highly reactive and induces an increase of the cross-link density¹¹⁸.

Examples of different monomers obtained from naturally occurring phenolic derivatives and their respective thermal properties are displayed in **Table 7**.

Table 7. Examples of BZ monomers from bio-based phenolic derivatives and the thermal properties of monomers and respective PBZ materials.

BZ monomer		T_m (°C) ^[a]	T_p (°C) ^[b]	T_g (°C) ^[c]	$T_{5\%}$ (°C) ^[d]	Ref.
Vanillin	 <p>Vanillin / Aniline</p>	83	231	-	347	108
	 <p>Vanillin / Ethylenediamine</p>	205	213	-	283	119

Guaiacol	 <p>Guaiacol / Stearylamine</p>	-	-	82	329	120
	 <p>Guaiacol / Furfurylamine</p>	-	240	148	352	120
Eugenol	 <p>Eugenol / Stearylamine</p>	49	218	101	313	112
	 <p>Eugenol / (4-aminophenyl)ether</p>	140	225	-	240	113
Lignin derivatives	 <p>Coumaric acid / Aniline</p>	117	137	119	220	111
	 <p>Ferulic acid / Aniline</p>	121	130	120	200	111

		122	212	130	293	111
	Phloretic acid / Aniline					
Coumarin		147	220	183	327	114
	Umbelliferone / Aniline					
		153	232	189	312	121
	4-methylumbelliferone / Aniline					
Urushiol		-	211	140	325	116
	Urushiol / Aniline					
		110	212	135	350	122
	Urushiol / N,N-diaminodiphenylmethane					
Cardanol		-	271	58	-	117
	Cardanol / Aniline					
		-	265	99	-	117
	Cardanol / Furfurylamine					

The use of bio-based phenolic derivatives for the synthesis of BZ monomers presents numerous advantages such as a lower carbon footprint, and the introduction of some additional functional groups within the monomer. Among them, cardanol presents the advantage to highly decrease the melting temperature, resulting in a wide processing window. However, the cross-link density of cardanol-based PBZ need to be improved.

As previously described, the nature of the diamine bridging group plays an important role on the properties of the polymers and strongly affects the bio-based monomer. The use of short aliphatic diamines such as EDA is a good compromise to promote adequate processing window, while resulting in high cross-linked polymers with good thermo-mechanical properties.

IV. References

- (1) Whittington, L. R. *Whittington's Dictionary of Plastics*; Technomic Pub. Co., 1968.
- (2) Staudinger, H.; Fritschi, J. *Helv. Chim. Acta* **1922**, *5*, 785.
- (3) Pascault, J.-P.; Sautereau, H.; Verdu, J.; Williams, R. J. *Thermosetting Polymers*; Marcel Dekker, **2002**.
- (4) Pickering, S. J. Recycling Technologies for Thermoset Composite Materials—current Status. *Compos. Part A Appl. Sci. Manuf.* **2006**, *37* (8), 1206–1215.
- (5) La Rosa, A. D.; Blanco, I.; Banatao, D. R.; Pastine, S. J.; Björklund, A.; Cicala, G. Innovative Chemical Process for Recycling Thermosets Cured with Recyclamines® by Converting Bio-Epoxy Composites in Reusable Thermoplastic—An LCA Study. *Materials*. **2018**, *11*, 353.
- (6) Flory, P. J. *Principles of Polymer Chemistry*; Cornell University Press, **1953**.
- (7) Dusek, K.; MacKnight, W. J. Cross-Linking and Structure of Polymer Networks. In *Cross-linked Polymers*; ACS Symposium Series, **1988**; 2–27.
- (8) Gillham, J. K. Formation and Properties of Thermosetting and High Tg Polymeric Materials. *Polym. Eng. Sci.* **1986**, *26* (20), 1429–1433.
- (9) Goodman, S. H. *Handbook of Thermoset Plastics*; **1998**.
- (10) Vyazovkin, S.; Sbirrazzuoli, N. Mechanism and Kinetics of Epoxy–Amine Cure Studied by Differential Scanning Calorimetry. *Macromolecules* **1996**, *29* (6), 1867–1873.
- (11) Pascault, J.-P.; Williams, R. J. J. *Epoxy Polymers : New Materials and Innovations*; Wiley-VCH, **2010**.
- (12) Goodyear, C. Improvement in India-Rubber Fabrics. US26359A, **1859**.
- (13) Baekeland, L. H. Method of Making Insoluble Products of Phenol and Formaldehyde. US942699, **1909**.
- (14) Knop, A.; Pilato, L. A. *Phenolic Resins : Chemistry, Applications and Performance Future Directions*; Springer Berlin Heidelberg, 1985.
- (15) Baekeland, L. H. The Synthesis, Constitution, and Uses of Bakelite. *J. Ind. Eng. Chem.*

- 1909**, *I* (3), 149–161.
- (16) Baekeland, L. H. The Invention of Celluloid. *J. Ind. Eng. Chem.* **1914**, *6* (2), 90–91.
- (17) Odian, G. *Principles of Polymerization*; John Wiley & Sons, **2004**.
- (18) Hesse, W.; Lang, J. Phenolic Resins. In *Ullmann's Encyclopedia of Industrial Chemistry*; Wiley-VCH Verlag GmbH & Co. KGaA: Weinheim, Germany, **2011**.
- (19) Chanda, M.; Roy, S. K. *Plastics Technology Handbook*; CRC press, **2006**.
- (20) Plastic News. *March 31*. **1997**.
- (21) Ibeh, C. C.; Graham, G. Simulation Techniques for In-Lab Cost-Effective Optimization of Thermosetting Polymeric Materials Processes. American Society for Engineering Education, Midwest Section, 32nd Annual Conference Proceedings; **1997**.
- (22) Global Phenolic Resins Market - Industry Analysis, Size, Growth, Trends, Segment and Forecast, 2014-2020 <https://www.marketresearchstore.com/report/phenolic-resins-market-for-z37563> (accessed Oct 4, 2018).
- (23) Nair, C. P. R. Advances in Addition-Cure Phenolic Resins. *Prog. Polym. Sci.* **2004**, *29* (5), 401–498.
- (24) Wei, C.; Zeng, M.; Xiong, X.; Liu, H.; Luo, K.; Liu, T. Friction Properties of Sisal Fiber/Nano-Silica Reinforced Phenol Formaldehyde Composites. *Polym. Compos.* **2015**, *36* (3), 433–438.
- (25) Wei, J.; Wei, C.; Su, L.; Fu, J.; Lv, J. Synergistic Reinforcement of Phenol-Formaldehyde Resin Composites by Poly(Hexanedithiol)/Graphene Oxide. *J. Mater. Sci. Chem. Eng.* **2015**, *3* (8), 56–70.
- (26) Kumar, M.; Sanjay, A.; Sinha, K. Optimization of Wheat Straw Fibres/Phenol Formaldehyde Composites. *Appl. Polym. Compos.* **2014**, *2* (1), 37–44.
- (27) Neelamana, I. K.; Thomas, S.; Parameswaranpillai, J. Characteristics of Banana Fibers and Banana Fiber Reinforced Phenol Formaldehyde Composites-Macroscale to Nanoscale. *J. Appl. Polym. Sci.* **2013**, *130* (2), 1239–1246.
- (28) Singh, G. P.; Mangal, R.; Bhojak, N.; Dixit, M.; Saxena, N. S.; Pratap, A.; Saxena, N. S. Thermal Properties of Capparis Decidua (Ker) Fiber Reinforced Phenol Formaldehyde Composites. In *AIP Conference Proceedings*; American Institute of

- Physics, **2010**; Vol. 1249, pp 55–58.
- (29) Padmanabhan, C.; Nair, R.; Bindu, R. K. L.; Ninan, K. N. A Process for Preparing Addition Curable Phenolic Resin. IN 1999MA00449 A 20060811, **1970**.
- (30) Nair, C. P. R.; Bindu, R. L.; Ninan, K. N. Recent Advances in Phenolic Resins. *Met. Mater. Process.* **1997**, 9 (2), 179–200.
- (31) Nair, C. P. Non-Conventional Phenolic Resins—An Overview on Recent Advances. *J of Sci. Ind. Res.* **2002**, 61(1), 17-33.
- (32) Castan, P. Process of Preparing Synthetic Resins. US2324483, **1943**.
- (33) Henry, L.; Neville, K. Handbook of Epoxy Resins. *Mc Crow-Hill Book, NY-San Fr.* **1982**.
- (34) Stevens, C. L.; Tazuma, J. Epoxyethers. V. The Reaction of Perbenzoic Acid with Vinyl Ethers. *J. Am. Chem. Soc.* **1954**, 76 (3), 715–717.
- (35) Royals, E. E.; Harrell Jr, L. L. Oxygenated Derivatives of D- α -Pinene and d-Limonene. Preparation and Use of Monoperphthalic Acid1. *J. Am. Chem. Soc.* **1955**, 77 (12), 3405–3408.
- (36) Auvergne, R.; Caillol, S.; David, G.; Boutevin, B.; Pascault, J.-P. Biobased Thermosetting Epoxy: Present and Future. *Chem. Rev.* **2013**, 114 (2), 1082–1115.
- (37) Shechter, L.; Wynstra, J.; Kurkijy, R. P. Glycidyl Ether Reactions with Amines. *Ind. Eng. Chem.* **1956**, 48 (1), 94–97.
- (38) Gough, L. J.; Smith, I. T. A Gel Point Method for the Estimation of Overall Apparent Activation Energies of Polymerization. *J. Appl. Polym. Sci.* **1960**, 3 (9), 362–364.
- (39) Smith, I. T. The Mechanism of the Crosslinking of Epoxide Resins by Amines. *Polymer* **1961**, 2, 95–108.
- (40) Matejka, L.; Chabanne, P.; Tighzert, L.; Pascault, J. P. Cationic Polymerization of Diglycidyl Ether of Bisphenol A. *J. Polym. Sci. Part A Polym. Chem.* **1994**, 32 (8), 1447–1458.
- (41) Matějka, L.; Lövy, J.; Pokorný, S.; Bouchal, K.; Dušek, K. Curing Epoxy Resins with Anhydrides. Model Reactions and Reaction Mechanism. *J. Polym. Sci. Polym. Chem. Ed.* **1983**, 21 (10), 2873–2885.

- (42) Leukel, J.; Burchard, W.; Krüger, R.-P.; Much, H.; Schulz, G. Mechanism of the Anionic Copolymerization of Anhydride-Cured Epoxies – Analyzed by Matrix-Assisted Laser Desorption Ionization Time-of-Flight Mass Spectrometry (MALDI-TOF-MS). *Macromol. Rapid Commun.* **1996**, *17* (5), 359–366.
- (43) Su, Y. K. *Comprehensive Semiconductor Science and Technology*; Bhattacharya, P., Fornari, R., Kamimura, H., Eds.; Elsevier Science, **2011**.
- (44) Patrick, R. L. *Treatise on Adhesion and Adhesives. Volume 3*; Marcel Dekker: New York, **1973**.
- (45) Goosey, M. T. *Plastics for Electronics*; Goosey, M. T., Ed.; Elsevier: London, **1985**.
- (46) May, C. A. Resins for Aerospace; ACS Symposium Series, Vol. 132, **1985**; 557–580.
- (47) Ellis, P. Floor covering - Smooth-surfaced floor coverings | Britannica.com <https://www.britannica.com/technology/floor-covering/Smooth-surfaced-floor-coverings#ref66825> (accessed Jul 15, 2018).
- (48) Ishida, H. Versatile Phenolic Stands up to the Heat. *Mod. Plast. Int.* **1998**, *75* (6), 121–124.
- (49) Ishida, H.; Rodriguez, Y. Curing Kinetics of a New Benzoxazine-Based Phenolic Resin by Differential Scanning Calorimetry. *Polymer* **1995**, *36* (16), 3151–3158.
- (50) Ishida, H.; Allen, D. J. Gelation Behavior of Near-Zero Shrinkage Polybenzoxazines. *J. Appl. Polym. Sci.* **2001**, *79* (3), 406–417.
- (51) Santhosh Kumar K. S.; Nair, C. P. R. *Polybenzoxazines : Chemistry and Properties*; ISmithers, **2010**.
- (52) Santhosh Kumar K. S.; Nair, C. P. R. Bisphenol A Based Polybenzoxazine and Its Tailored Systems. In *Bisphenol A and Phthalates: Uses, Health Effects and Environmental Risks*; Vaughn, B. C., Ed.; Nova Science Publishers, **2010**; 217–174.
- (53) Ghosh, N. N.; Kiskan, B.; Yagci, Y. Polybenzoxazines—New High Performance Thermosetting Resins: Synthesis and Properties. *Prog. Polym. Sci.* **2007**, *32* (11), 1344–1391.
- (54) Ishida, H.; Rimdusit, S. Very High Thermal Conductivity Obtained by Boron Nitride-Filled Polybenzoxazine. *Thermochim. Acta* **1998**, *320* (1–2), 177–186.

- (55) Agag, T.; Takeichi, T. Synthesis and Characterization of Benzoxazine Resin-SiO₂ Hybrids by Sol-Gel Process: The Role of Benzoxazine-Functional Silane Coupling Agent. *Polymer* **2011**, *52* (13), 2757–2763.
- (56) Ganfoud, R.; Puchot, L.; Fouquet, T.; Verge, P. H-Bonding Supramolecular Interactions Driving the Dispersion of Kaolin into Benzoxazine: A Tool for the Reinforcement of Polybenzoxazines Thermal and Thermo-Mechanical Properties. *Compos. Sci. Technol.* **2015**, *110*, 1–7.
- (57) Dayo, A. Q.; Gao, B.; Wang, J.; Liu, W.; Derradji, M.; Shah, A. H.; Babar, A. A. Natural Hemp Fiber Reinforced Polybenzoxazine Composites: Curing Behavior, Mechanical and Thermal Properties. *Compos. Sci. Technol.* **2017**, *144*, 114–124.
- (58) Rimdusit, S.; Pathomsap, S.; Kasemsiri, P.; Jubsilp, C.; Tiptipakorn, S. KevlarTM Fiber-Reinforced Polybenzoxazine Alloys for Ballistic Impact Applications. *Eng. J.* **2011**, *15*, 23–40.
- (59) Rimdusit, S.; Kampangsaeree, N.; Tanthapanichakoon, W.; Takeichi, T.; Suppakarn, N. Development of Wood-Substituted Composites from Highly Filled Polybenzoxazine–phenolic Novolac Alloys. *Polym. Eng. Sci.* **2007**, *47* (2), 140–149.
- (60) Dansiri, N.; Yanumet, N.; Ellis, J. W.; Ishida, H. Resin Transfer Molding of Natural Fiber Reinforced Polybenzoxazine Composites. *Polym. Compos.* **2002**, *23* (3), 352–360.
- (61) Kiskan, B.; Yagci, Y.; Sahmetlioglu, E.; Toppare, L. Preparation of Conductive Polybenzoxazines by Oxidative Polymerization. *J. Polym. Sci. Part A Polym. Chem.* **2007**, *45* (6), 999–1006.
- (62) Wang, Y.-H.; Chang, C.-M.; Liu, Y.-L. Benzoxazine-Functionalized Multi-Walled Carbon Nanotubes for Preparation of Electrically-Conductive Polybenzoxazines. *Polymer* **2012**, *53* (1), 106–112.
- (63) Kim, S.-K.; Kim, K.-H.; Park, J. O.; Kim, K.; Ko, T.; Choi, S.-W.; Pak, C.; Chang, H.; Lee, J.-C. Highly Durable Polymer Electrolyte Membranes at Elevated Temperature: Cross-Linked Copolymer Structure Consisting of Poly(Benzoxazine) and Poly(Benzimidazole). *J. Power Sources* **2013**, *226*, 346–353.
- (64) Ye, Y.-S.; Yen, Y.-C.; Cheng, C.-C.; Chen, W.-Y.; Tsai, L.-T.; Chang, F.-C.

- Sulfonated Poly(Ether Ether Ketone) Membranes Crosslinked with Sulfonic Acid Containing Benzoxazine Monomer as Proton Exchange Membranes. *Polymer* **2009**, *50* (14), 3196–3203.
- (65) Kreilin, S.; Schonfeld, R.; Taden, A.; Kux, M.; Küster, H.; Lehmann, S. L. Benzoxazine-Based Compositions Containing Isocyanate-Based Tougheners. US20110172356A1, March 18, **2011**.
- (66) Taşdelen-Yücedağ, Ç.; Erciyes, A. T. Preparation of Oil-Modified Polycaprolactone and Its Further Modification with Benzoxazine for Coating Purposes. *Prog. Org. Coatings* **2013**, *76* (1), 137–146.
- (67) Rimdusit, S.; Ishida, H. Development of New Class of Electronic Packaging Materials Based on Ternary Systems of Benzoxazine, Epoxy, and Phenolic Resins. *Polymer* **2000**, *41* (22), 7941–7949.
- (68) Li, W. H.; Lehmann, S.; Mckillen, J.; Wong, A.; Wong, R.; Leach, D. *Benzoxazine Matrix Resins for Structural Composite Applications*; **2010**.
- (69) Wu, Y.; Zeng, M.; Xu, Q.; Hou, S.; Jin, H.; Fan, L. Effects of Glass-to-Rubber Transition of Thermosetting Resin Matrix on the Friction and Wear Properties of Friction Materials. *Tribol. Int.* **2012**, *54*, 51–57.
- (70) Ning, X.; Ishida, H. Phenolic Materials via Ring-Opening Polymerization: Synthesis and Characterization of Bisphenol-A Based Benzoxazines and Their Polymers. *J. Polym. Sci. Part A Polym. Chem.* **1994**, *32* (6), 1121–1129.
- (71) Kim, H. J.; Brunovska, Z.; Ishida, H. Dynamic Mechanical Analysis on Highly Thermally Stable Polybenzoxazines with an Acetylene Functional Group. *J. Appl. Polym. Sci.* **1999**, *73* (6), 857–862.
- (72) Low, H. Y.; Ishida, H. Structural Effects of Phenols on the Thermal and Thermo-Oxidative Degradation of Polybenzoxazines. *Polymer* **1999**, *40* (15), 4365–4376.
- (73) Yang, P.; Gu, Y. Synthesis and Curing Behavior of a Benzoxazine Based on Phenolphthalein and Its High Performance Polymer. *J. Polym. Res.* **2011**, *18* (6), 1725–1733.
- (74) Shieh, J.-Y.; Lin, C.-Y.; Huang, C.-L.; Wang, C.-S. Synthesis and Characterization of Novel Dihydrobenzoxazine Resins. *J. Appl. Polym. Sci.* **2006**, *101* (1), 342–347.

- (75) Ishida, H. Process for Preparation of Benzoxazine Compounds in Solventless Systems. U.S. Patent: 5543516, **1996**.
- (76) Rimdusit, S.; Liengvachiranon, C.; Tiptipakorn, S.; Jubsilp, C. Thermomechanical Characteristics of Benzoxazine-Urethane Copolymers and Their Carbon Fiber-Reinforced Composites. *J. Appl. Polym. Sci.* **2009**, *113* (6), 3823–3830.
- (77) Rimdusit, S.; Bangsen, W.; Kasemsiri, P. Chemorheology and Thermomechanical Characteristics of Benzoxazine-Urethane Copolymers. *J. Appl. Polym. Sci.* **2011**, *121* (6), 3669–3678.
- (78) Cao, H.-W.; Xu, R.-W.; Liu, H.; Yu, D.-S. Mannich Reaction of Phenolphthalein and Synthesis of a Novel Polybenzoxazine. *Des. Monomers Polym.* **2006**, *9* (4), 369–382.
- (79) Baranek, A. D.; Kendrick, L. L.; Tretbar, C. A.; Patton, D. L. Solvent-Free Copolymerization of Rigid and Flexible Bis-1,3-Benzoxazines: Facile Tunability of Polybenzoxazine Network Properties. *Polymer* **2013**, *54* (21), 5553–5559.
- (80) Hwang, H.-J.; Lin, C.-Y.; Wang, C.-S. Flame Retardancy and Dielectric Properties of Dicyclopentadiene-Based Benzoxazine Cured with a Phosphorus-Containing Phenolic Resin. *J. Appl. Polym. Sci.* **2008**, *110* (4), 2413–2423.
- (81) Aversa, M. C.; Giannetto, P.; Caristi, C.; Ferlazzo, A. Behaviour of an N-(*o*-Hydroxybenzyl)- β -Amino-Acid in the Presence of Dehydrating Agents. Synthesis of a 3,4-Dihydro-2H-1,3-Benzoxazine. *J. Chem. Soc., Chem. Commun.* **1982**, *0* (8), 469–470.
- (82) Palmieri, G. Synthesis of Enantiopure-*o*-Hydroxybenzylamines by Stereoselective Reduction of 2-Imidoylphenols: Application in the Catalytic Enantioselective Addition of Diethylzinc to Aldehydes. *European J. Org. Chem.* **1999**, *1999* (4), 805–811.
- (83) Colin, J. L.; Loubinoux, B. Nouvelle Voie d'accès Aux Dihydro-3,4-2H-Benzoxazines-1,3. *Tetrahedron Lett.* **1982**, *23* (41), 4245–4246.
- (84) Holly, F. W.; Cope, A. C. Condensation Products of Aldehydes and Ketones with *o*-Aminobenzyl Alcohol and *o*-Hydroxybenzylamine. *J. Am. Chem. Soc.* **1944**, *66* (11), 1875–1879.
- (85) Burke, W. J. 3,4-Dihydro-1,3,2H-Benzoxazines. Reaction of *p*-Substituted Phenols with N,N-Dimethylolamines. *J. Am. Chem. Soc.* **1949**, *71* (2), 609–612.

- (86) Ishida, H.; Allen, D. J. Physical and Mechanical Characterization of Near-Zero Shrinkage Polybenzoxazines. *J. Polym. Sci. Part B Polym. Phys.* **1996**, *34* (6), 1019–1030.
- (87) Allen, D. J.; Hishida, H. Polymerization of Linear Aliphatic Diamine-Based Benzoxazine Resins under Inert and Oxidative Environments. *Polymer* **2007**, *48* (23), 6763–6772.
- (88) Ning, X.; Ishida, H. Phenolic Materials via Ring-opening Polymerization of Benzoxazines: Effect of Molecular Structure on Mechanical and Dynamic Mechanical Properties. *J. Polym. Sci. Part B Polym. Phys.* **1994**, *32* (5), 921–927.
- (89) Riess, G.; Schwob, J. M.; Guth, G.; Roche, M.; Laude, B. Ring Opening Polymerization of Benzoxazines - a New Route to Phenolic Resins. *Polym. Sci. Technol.* **1985**, *31*, 27–49.
- (90) McDonagh, A. F.; Smith, H. E. Ring-Chain Tautomerism of Derivatives of o-Hydroxybenzylamine with Aldehydes and Ketones. The Nuclear Magnetic Resonance Spectra of Immonium Ions. *J. Org. Chem.* **1968**, *33* (1), 8–12.
- (91) Dunkers, J.; Ishida, H. Reaction of Benzoxazine-Based Phenolic Resins with Strong and Weak Carboxylic Acids and Phenols as Catalysts. *J. Polym. Sci. Part A Polym. Chem.* **1999**, *37* (13), 1913–1921.
- (92) Chutayothin, P.; Ishida, H. Cationic Ring-Opening Polymerization of 1,3-Benzoxazines: Mechanistic Study Using Model Compounds. *Macromolecules* **2010**, *43* (10), 4562–4572.
- (93) Liu, Y.; Hao, Z.; Lv, S.; Huang, J.; Liao, C.; Run, M. Structural Effects of Diamines on Synthesis, Polymerization, and Properties of Benzoxazines Based on o-Allylphenol. *Polymer* **2015**, *57*, 29–38.
- (94) Lin, C. H.; Chang, S. L.; Hsieh, C. W.; Lee, H. H. Aromatic Diamine-Based Benzoxazines and Their High Performance Thermosets. *Polymer* **2008**, *49* (5), 1220–1229.
- (95) He, X.; Wang, J.; Wang, Y.; Liu, C.; Liu, W.; Yang, L. Synthesis, Thermal Properties and Curing Kinetics of Fluorene Diamine-Based Benzoxazine Containing Ester Groups. *Eur. Polym. J.* **2013**, *49* (9), 2759–2768.

- (96) Allen, D. J.; Ishida, H. Physical and Mechanical Properties of Flexible Polybenzoxazine Resins: Effect of Aliphatic Diamine Chain Length. *J. Appl. Polym. Sci.* **2006**, *101* (5), 2798–2809.
- (97) Agag, T.; Lin, J.; Ishida, H. A New Synthetic Approach for Difficult Benzoxazines: Preparation and Polymerization of 4,4'-Diaminodiphenyl Sulfone-Based Benzoxazine Monomer. *Polymer* **2009**, *50* (25), 5940–5944.
- (98) Liu, Y.; Liao, C.; Hao, Z.; Luo, X.; Jing, S.; Run, M. The Polymerization Behavior and Thermal Properties of Benzoxazine Based on O-Allylphenol and 4,4'-Diaminodiphenyl Methane. *React. Funct. Polym.* **2014**, *75*, 9–15.
- (99) Allen, D. J.; Ishida, H. Effect of Phenol Substitution on the Network Structure and Properties of Linear Aliphatic Diamine-Based Benzoxazines. *Polymer* **2009**, *50* (2), 613–626.
- (100) Deng, Y.; Zhang, Q.; Zhou, Q.; Zhang, C.; Zhu, R.; Gu, Y. Influence of Substituent on Equilibrium of Benzoxazine Synthesis from Mannich Base and Formaldehyde. *Phys. Chem. Chem. Phys.* **2014**, *16* (34), 18341–18348.
- (101) Ohashi, S.; Iguchi, D.; Heyl, T. R.; Froimowicz, P.; Ishida, H. Quantitative Studies on the *p*-Substituent Effect of the Phenolic Component on the Polymerization of Benzoxazines. *Polym. Chem.* **2018**, *9*(31), 4194-4204.
- (102) Wang, X.; Chen, F.; Gu, Y. Influence of Electronic Effects from Bridging Groups on Synthetic Reaction and Thermally Activated Polymerization of Bisphenol-Based Benzoxazines. *J. Polym. Sci. Part A Polym. Chem.* **2011**, *49* (6), 1443–1452.
- (103) Allen, D. J.; Ishida, H. Physical and Mechanical Properties of Flexible Polybenzoxazine Resins: Effect of Aliphatic Diamine Chain Length. *J. Appl. Polym. Sci.* **2006**, *101* (5), 2798–2809.
- (104) Pelckmans, M.; Renders, T.; Van de Vyver, S.; Sels, B. F. Bio-Based Amines through Sustainable Heterogeneous Catalysis. *Green Chem.* **2017**, *19* (22), 5303–5331.
- (105) Brazinha, C.; Barbosa, D. S.; Crespo, J. G. Sustainable Recovery of Pure Natural Vanillin from Fermentation Media in a Single Pervaporation Step. *Green Chem.* **2011**, *13* (8), 2197.
- (106) Fache, M.; Boutevin, B.; Caillol, S. Vanillin Production from Lignin and Its Use as a

- Renewable Chemical. *ACS Sustain. Chem. Eng.* **2016**, *4* (1), 35–46.
- (107) Sini, N. K.; Bijwe, J.; Varma, I. K. Renewable Benzoxazine Monomer from Vanillin: Synthesis, Characterization, and Studies on Curing Behavior. *J. Polym. Sci. Part A Polym. Chem.* **2014**, *52* (1), 7–11.
- (108) Van, A.; Chiou, K.; Ishida, H. Use of Renewable Resource Vanillin for the Preparation of Benzoxazine Resin and Reactive Monomeric Surfactant Containing Oxazine Ring. *Polymer* **2014**, *55* (6), 1443–1451.
- (109) Puchot, L.; Verge, P.; Fouquet, T.; Vancaeyzeele, C.; Vidal, F.; Habibi, Y. Breaking the Symmetry of Dibenzoxazines: A Paradigm to Tailor the Design of Bio-Based Thermosets. *Green Chem.* **2016**, *18* (11), 3346–3353.
- (110) Ran, Q.-C.; Gu, Y. Concerted Reactions of Aldehyde Groups during Polymerization of an Aldehyde-Functional Benzoxazine. *J. Polym. Sci. Part A Polym. Chem.* **2011**, *49* (7), 1671–1677.
- (111) Comí, M.; Lligadas, G.; Ronda, J. C.; Galià, M.; Cádiz, V. Renewable Benzoxazine Monomers from “Lignin-like” Naturally Occurring Phenolic Derivatives. *J. Polym. Sci. Part A Polym. Chem.* **2013**, *51* (22), 4894–4903.
- (112) Thirukumaran, P.; Shakila Parveen, A.; Sarojadevi, M. Synthesis and Copolymerization of Fully Biobased Benzoxazines from Renewable Resources. *ACS Sustain. Chem. Eng.* **2014**, *2* (12), 2790–2801.
- (113) Thirukumaran, P.; Shakila, A.; Muthusamy, S. Synthesis and Characterization of Novel Bio-Based Benzoxazines from Eugenol. *RSC Adv.* **2014**, *4* (16), 7959.
- (114) Arza, C. R.; Froimowicz, P.; Ishida, H. Smart Chemical Design Incorporating Umbelliferone as Natural Renewable Resource toward the Preparation of Thermally Stable Thermosets Materials Based on Benzoxazine Chemistry. *RSC Adv.* **2015**, *5* (118), 97855–97861.
- (115) Froimowicz, P.; R. Arza, C.; Han, L.; Ishida, H. Smart, Sustainable, and Ecofriendly Chemical Design of Fully Bio-Based Thermally Stable Thermosets Based on Benzoxazine Chemistry. *ChemSusChem* **2016**, *9* (15), 1921–1928.
- (116) Xu, H.; Lu, Z.; Zhang, G. Synthesis and Properties of Thermosetting Resin Based on Urushiol. *RSC Adv.* **2012**, *2* (7), 2768.

- (117) Ambrožič, R.; Šebenik, U.; Krajnc, M. Synthesis, Curing Kinetics, Thermal and Mechanical Behavior of Novel Cardanol-Based Benzoxazines. *Polymer* **2015**, *76*, 203–212.
- (118) Liu, Y.-L.; Chou, C.-I. High Performance Benzoxazine Monomers and Polymers Containing Furan Groups. *J. Polym. Sci. Part A Polym. Chem.* **2005**, *43* (21), 5267–5282.
- (119) Sini, N. K.; Bijwe, J.; Varma, I. K. Thermal Behaviour of Bis-Benzoxazines Derived from Renewable Feed Stock “Vanillin.” *Polym. Degrad. Stab.* **2014**, *109*, 270–277.
- (120) Wang, C.; Sun, J.; Liu, X.; Sudo, A.; Endo, T. Synthesis and Copolymerization of Fully Bio-Based Benzoxazines from Guaiacol, Furfurylamine and Stearylamine. *Green Chem.* **2012**, *14* (10), 2799.
- (121) Froimowicz, P.; Rodriguez Arza, C.; Ohashi, S.; Ishida, H. Tailor-Made and Chemically Designed Synthesis of Coumarin-Containing Benzoxazines and Their Reactivity Study toward Their Thermosets. *J. Polym. Sci. Part A Polym. Chem.* **2016**, *54* (10), 1428–1435.
- (122) Xu, H.; Zhang, W.; Lu, Z.; Zhang, G. Hybrid Polybenzoxazine with Tunable Properties. *RSC Adv.* **2013**, *3* (11), 3677.

Chapter II

Cardanol-based benzoxazine resins:

Structure-to-properties relationship

I. Introduction	65
II. Materials and methods	69
II.1. Materials	69
II.2. Liquid state NMR characterization	69
II.3. Mass analysis	69
II.4. FT-IR characterization	69
II.5. Differential Scanning Calorimetry (DSC)	70
II.6. Rheological analysis	70
II.7. Dynamical Mechanical Analysis (DMA)	70
II.8. Thermogravimetric Analysis (TGA)	70
III. Results and Discussions	72
III.1. Monomers synthesis and structural characterization	72
III.1.1. Symmetric benzoxazines synthesis	72
III.1.1.1. ¹ H NMR characterization	73
III.1.1.2. Mass characterization	76
III.1.2. Asymmetric benzoxazines synthesis	79
III.1.2.1. ¹ H NMR characterization	79
III.1.2.2. Mass characterization	81
III.1.3. Purification process	82
III.1.4. FTIR characterization of benzoxazine monomers	83
III.2. Thermo-analytical follow-up of ring opening and cross-linking reactions	84
III.2.1. Characterization by DSC	84
III.2.2. DSC vs TGA correlation	89
III.2.3. Chemorheology of polymerization	90
III.3. After cure completion, characterization and final properties of the polybenzoxazine resins	92
III.3.1. Material elaboration	92
III.3.2. FTIR characterization of the polymers	93
III.3.3. Thermo-mechanical characterization by DMA	94
III.3.4. Thermal stability of the cured products	97
IV. Conclusions	100
V. References	101
VI. Supplementary Information	107

I. Introduction

Polybenzoxazine resins present outstanding properties which can be modulated by means of its molecular design flexibility. Moreover, new synthesis approaches like green strategy, click chemistry, main chain polymerization, etc. gain a lot of interest in research and industry. With this idea, a lot of work emerged using various renewable resources^{1–10} like eugenol¹¹, vanillin^{6,12}, urushiol^{13,14}, or coumarin¹⁵ as starting materials. Cardanol is another naturally occurring phenolic compound, extracted from the cashew nutshell liquid (CNSL), and frequently used as building block for the synthesis of benzoxazine (BZ) monomers. Cardanol is particularly interesting because it exhibits an alkyl side chain containing 15 methylene units being either saturated, mono-unsaturated, di-unsaturated or tri-unsaturated¹⁶. Calò *et al.*¹⁷ were the first who used cardanol to synthesize BZ monomer and now, a growing interest is clearly emerging attested by the surging number of works dedicated to cardanol-based benzoxazines^{1,18–30}.

The cashew tree, *Anacardium occidentale L.*, is native from Brazil and then spread in many countries around the world especially tropical regions such as India, Nigeria, Vietnam, Côte d'Ivoire, Tanzania, Philippines, Indonesia, and Guinea-Bissau. Global world contribution to the production of cashew is illustrated in **Figure 1**. The global production in 2015/2016 was close to 3.25 million tons. Brazil, although it is the native country of the tree, sees its production decreased due to adverse climatic conditions (104,650 tons in 2015/2016 against 107,713 tons in 2014/2015³¹).

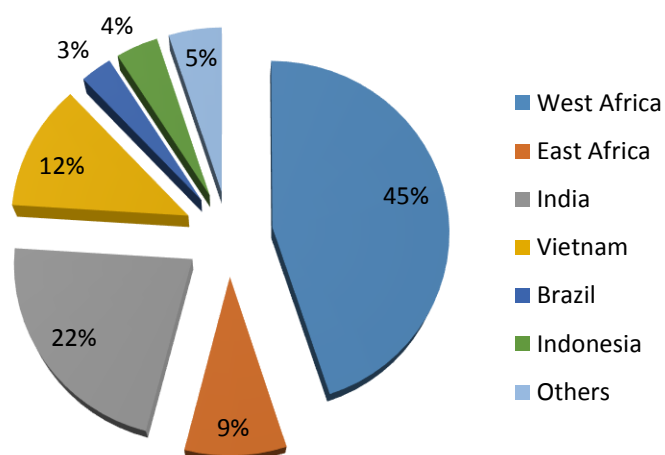


Figure 1. Contribution of different countries to the production of cashew nut in 2015/2016³¹.

The world interest lies in its edible fruits, wood properties, and scenic effects. The fruits present itself many interests. The colorful cashew apple (pseudo fruit) is edible and used for the production of sweet beverages and foods. The true fruit is the nut that grows at one end of the apple, covered by a hard shell. The cashew nut is the main commercial product of cashew plantation. The shell is filled with a dark and caustic oil called cashew nutshell liquid (CNSL). These products and by-products of the *Anacardium occidentale* L. are pictured in **Figure 2**.

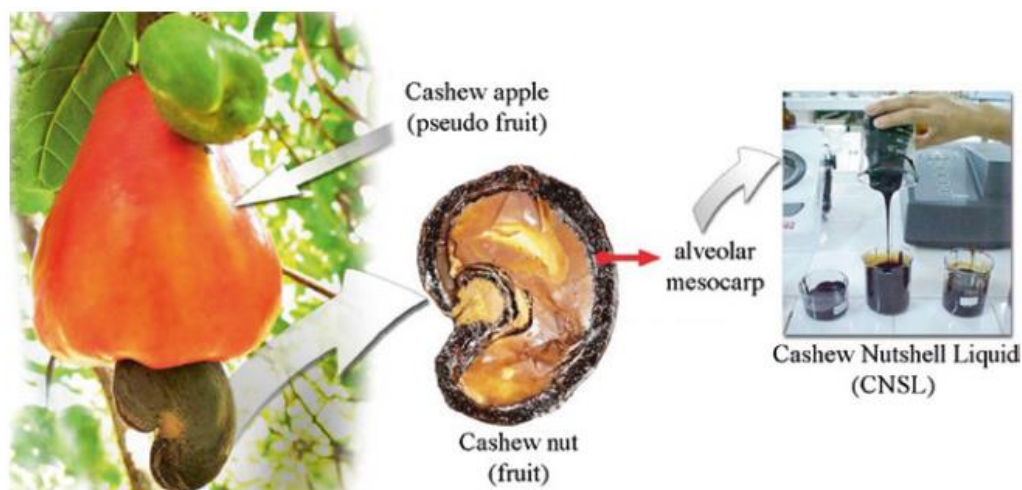


Figure 2. Cashew apple, nut, and shell filled with CNSL³².

The oil, CNSL, is mainly composed by phenolic derivatives. For this reason, this oil is highly attractive for scientific research, as it can be considered as a viable alternative to petroleum products^{33–35}. The CNSL is a brown dark oil with a peculiar odor. Different compounds are present in CNSL: anacardic acid, cardanol, cardol, and 2-methyl cardol³⁶ (**Figure 3**). Raw oil is essentially used as a pesticide and can be toxic to the human body as the major component of CNSL, anacardic acid, is closely related to urushiol, which causes hyperpigmented skin lesions³⁷.

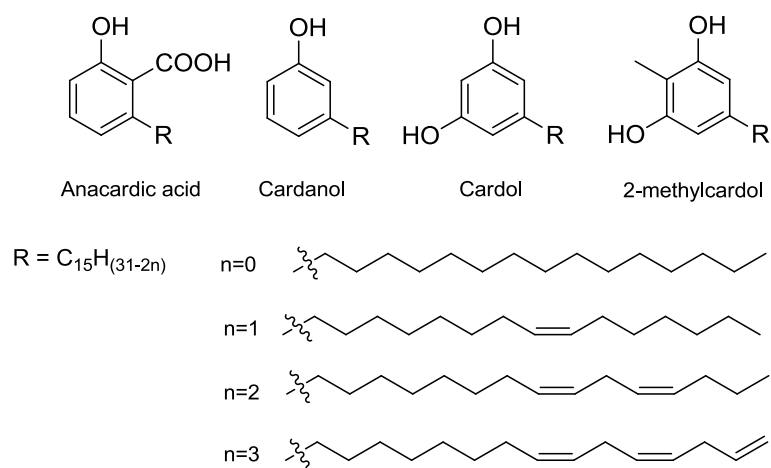
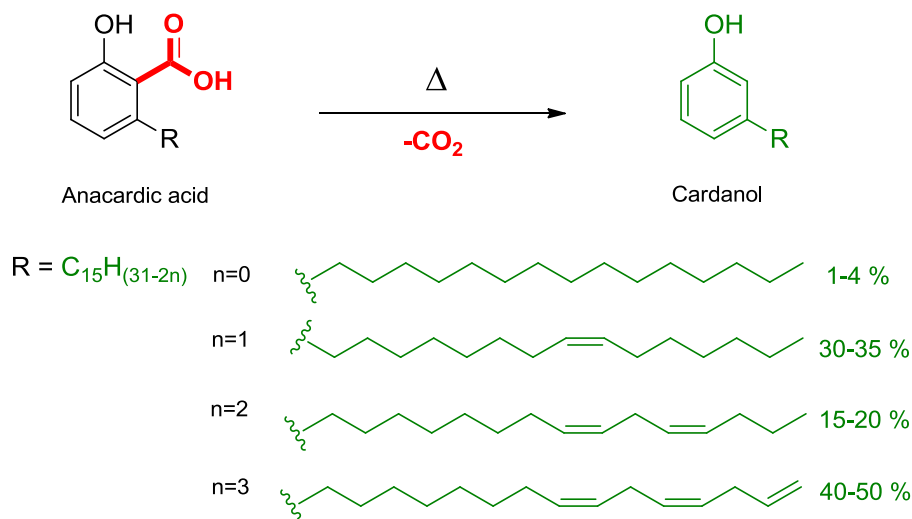


Figure 3. Chemical structure of CNSL components, n: number of unsaturations.

The characteristic of these compounds is the alkyl side chain of 15 carbon (C_{15}) atoms in *meta* position which can be either saturated, mono-unsaturated, di-unsaturated, or tri-unsaturated. All unsaturations are in *Z* configuration. During the extraction, which requires a heating to 180-190 °C, the anacardic acid undergoes a decarboxylation and converts into cardanol, as presented in **Scheme 1**.



Scheme 1. Decarboxylation reaction of anacardic acid to cardanol.

The side chain of cardanol presents an average of 1.5 unsaturations with a major fraction of tri-unsaturated chain (40-50 %), followed by the mono-unsaturated chain (30-35 %), then the di-unsaturated (15-20 %), and a very few amounts of saturated compound (1-4 %). The different reactive sites in cardanol allow many chemical modifications³⁸⁻⁴¹.

Another feature of such compound is the flexibility brought by a C₁₅ alkyl side chain. As mentioned in the previous chapter, major drawbacks of PBZ resins are their brittleness and high polymerization temperature. Cardanol with its flexible alkyl side chain is here an excellent candidate for modification of benzoxazine monomers in order to attempt to reduce cure temperature and to improve the ductility of the final polymer.

II. Materials and methods

II.1. Materials

Ethylenediamine (EDA, 99%), phenol (99-100.5%), paraformaldehyde (95%) and all the solvents used for the syntheses were purchased from Sigma-Aldrich. Cardanol (Ultra Lite 2023) was kindly supplied by Cardolite (Zhuhai, China). Chemicals were used as received without any purification.

II.2. Liquid state NMR characterization

NMR spectra were recorded in deuterated chloroform (CDCl_3) on a Bruker AVANCE III HD spectrometer operating at 400.17 MHz for ^1H . Experiments were recorded with a flip angle of 30° , and using sequences provided by Bruker. The spectrometer is equipped with the following probe: PA BBO 400S1 BBF-H-D-05 Z. The residual solvent signal at 7.26 ppm has been used as standard reference.

II.3. Mass analysis

Molecular characterization was also performed by high-resolution mass spectroscopy (HRMS), using a LTQ/Orbitrap Elite (Thermo Scientific) equipped with an atmospheric-pressure matrix-assisted laser desorption/ionization source (AP-MALDI PDF+, Masstech). This analytical setup allows for the investigation of MALDI-produced ions using accurate mass measurement (sub-ppm relative error) and structural confirmation by MSn. Samples were submitted to a solvent-free preparation. A matrix α -Cyano-4-hydroxycinnamic acid (CHCA) was used for the analyses and used as received from Sigma-Aldrich.

II.4. FT-IR characterization

FT-IR technique has been used in this thesis work for characterization of the products of syntheses (monomers) and their corresponding polymers to investigate the evolution of the structures before and after curing process. For this purpose, a Perkin Elmer Spectrum BX II Spectrophotometer was employed in Attenuated Total Reflectance (ATR) mode using a diamond crystal and Spectrum software. Each spectrum was recorded with 4 cm^{-1} resolution and 32 scans co-addition.

II.5. Differential Scanning Calorimetry (DSC)

DSC is a quantitative technique that measures the difference of heat flow between an empty pan used as reference, and another pan containing the sample. The heat flow is evaluated with a sensor composed of several thermocouples connected in series.

DSC measurements were performed on a Mettler-Toledo DSC 1 equipped with STAR[®] software. This apparatus has a very high sensitivity due to its heat flux ceramic sensor FRS5 (with 56 thermocouples Au-Au/Pd). Temperature and enthalpy calibrations were performed by using Indium ($T_m = 156.56$ °C) and Zinc ($T_m = 419.52$ °C) standards. Samples of about 10 mg were placed in 40 μ L aluminum crucibles

II.6. Rheological analysis

The chemorheological behavior of the three samples was followed using an Anton Paar Physica MCR 301 rheometer equipped with CTD 450 temperature control device with plate-plate geometry (diameter: 25 mm) and a gap of 0.5 mm. The measurements of storage (G') and loss (G'') moduli were recorded at a heating rate of 2 K.min⁻¹, from melting temperature of the monomer to 250 °C.

II.7. Dynamical Mechanical Analysis (DMA)

DMA was employed to characterize the mechanical and viscoelastic properties of a solid-like material as a function of frequency or temperature. In a similar way as presented in the above section for rheometry, the loss (E'' or G''), storage (E' or G') moduli and damping factor ($\tan \delta = E''/E'$) were determined. The T_α transition was assigned as the temperature of maximum of the $\tan \delta$. DMA experiments were conducted on a Mettler-Toledo DMA 1 with STAR[®] software. The samples of a dimension of 15 mm long, 5mm width, and 1 mm thick are submitted to a traction in non-isothermal mode (heating rate of 2 K.min⁻¹) from -100 to 300 °C, with a frequency of 1 Hz and an oscillation amplitude of 5 μ m (0.033 %) in auto-tension mode.

II.8. Thermogravimetric Analysis (TGA)

TGA is a thermo-analytical technique employed to determine the evolution of sample mass as a function of time and/or temperature. The mass variations allow to highlight the different physical and chemical transitions such as dehydration, loss of volatile compounds, degradation, etc.

Thermogravimetric measurements were performed on a TGA 851^e from Mettler-Toledo. The microbalance has a precision of $\pm 0.1 \mu\text{g}$. Samples of about 15 mg were placed into 70 μL alumina pans. Samples were heated at $4 \text{ K}\cdot\text{min}^{-1}$ from $25 \text{ }^\circ\text{C}$ to $700 \text{ }^\circ\text{C}$ under air atmosphere.

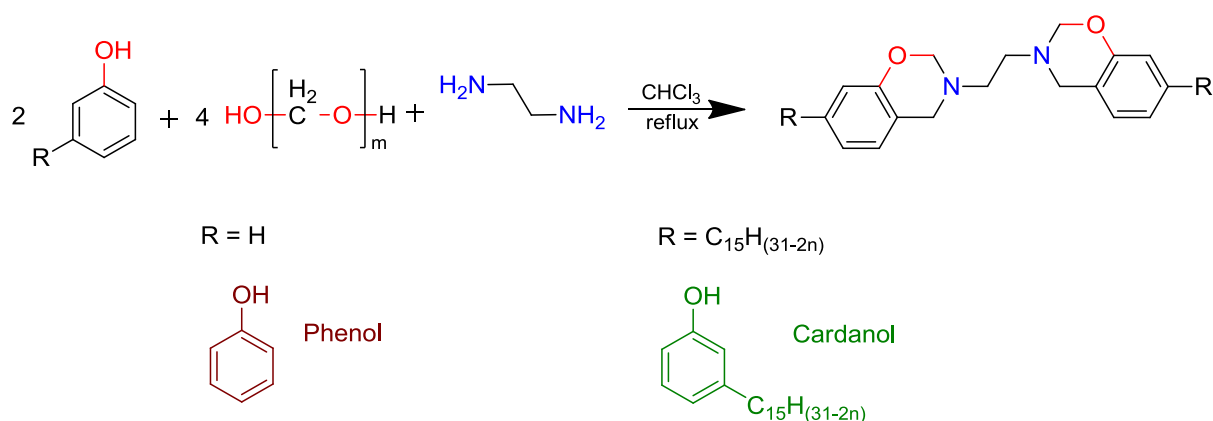
III. Results and Discussions

The work in this section focuses on how the long and flexible side chain of cardanol can modify the properties of polybenzoxazine polymers. Three monomers of di-functionalized BZ were synthesized using ethylenediamine as bridging group. The first monomer was synthesized using two phenols (di-phenol BZ), the second monomer was synthesized using one phenol and one cardanol to form an asymmetric monomer (card-phenol BZ), and for the third monomer two cardanols were used as phenol derivative (di-cardanol BZ). The substitution of phenol by cardanol aims to evaluate the effect of one and then two side chains on the polymerization, thermal stability and thermo-mechanical behavior, in comparison to a similar compound without alkyl side chain. Thus, di-phenol BZ was also the reference compound.

III.1. Monomers synthesis and structural characterization

III.1.1. Symmetric benzoxazines synthesis

Symmetric benzoxazine monomers from phenol (di-phenol) and from cardanol (di-cardanol) were synthesized following the same protocol, as described in **Scheme 2**. Phenol or cardanol, paraformaldehyde, and ethylenediamine (EDA) in a stoichiometric ratio 2:4:1, were reacting at reflux in chloroform, for 24 h for di-phenol BZ and 48 h for di-cardanol BZ.



Scheme 2. Synthesis of symmetric BZ monomers from phenol (R=H) or cardanol (R=C₁₅H_(31-2n)).

III.1.1.1. ^1H NMR characterization- Di-phenol BZ monomer

The proton NMR spectrum corresponding to the di-phenol monomer is depicted in **Figure 4**.

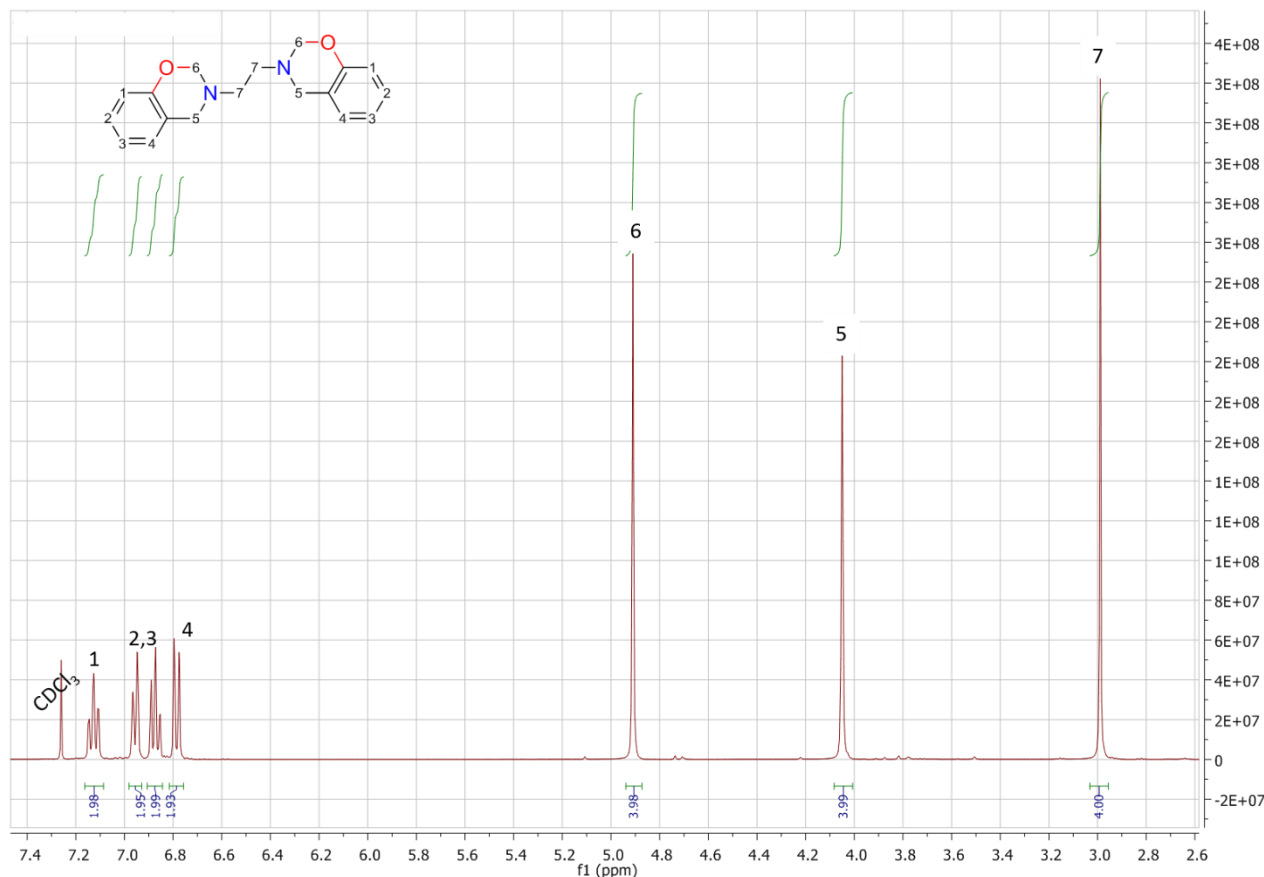


Figure 4. ^1H NMR spectrum of di-phenol BZ (solvent: CDCl_3).

The spectrum exhibits the characteristic peaks of a benzoxazine structure. The formation of the monomer was confirmed by the presence of the peak corresponding to the protons of the oxazine ring, *e.g.* $\text{O}-\text{CH}_2-\text{N}$ [6] and $\text{Ar}-\text{CH}_2-\text{N}$ [5]. The peaks corresponding to these groups were respectively observed at $\delta = 4.91$ ppm and $\delta = 4.05$ ppm. The structure of the symmetric di-benzoxazine from phenol and EDA was also confirmed by the signal integrations. The signal corresponding to the protons of EDA [7] at $\delta = 2.99$ ppm was taken as integration reference and set to 4 H. Thus, the integrations for $\text{O}-\text{CH}_2-\text{N}$ [6] and $\text{Ar}-\text{CH}_2-\text{N}$ [5] presented respectively an integration of $I_{\text{exp}} = 3.98$ H and $I_{\text{exp}} = 3.99$ H (with an expected integration of $I_{\text{th}} = 4.00$ H for each peak). The signals of the aromatic protons [1,2,3,4] at $\delta = 6.79 - 7.13$ ppm could successfully be integrated separately, and respective values of $I_{\text{exp}} = 1.98$ H, $I_{\text{exp}} = 1.95$ H, $I_{\text{exp}} = 1.99$ H, $I_{\text{exp}} = 1.93$ H were obtained, with respective expected integration of $I_{\text{th}} = 2$ H for

each signal. All values are summarized in **Table 1**. The expected chemical structure of the di-phenol BZ monomer was successfully confirmed by the ^1H NMR analysis.

Table 1. ^1H NMR data of di-phenol benzoxazine monomer.

Chemical shift (ppm)	Assignment	I _{experimental}	I _{theoretical}
2.99	N-(CH ₂) ₂ -N [7]	Ref. 4.00 H	4.00 H
4.05	Ar-CH ₂ -N [5]	3.99 H	4.00 H
4.91	O-CH ₂ -N [6]	3.98 H	4.00 H
6.79 / 6.87 / 6.95 / 7.13	H-Ar [1,2,3,4]	1.93 / 1.99 / 1.95 / 1.98 H	2.00 / 2.00 / 2.00 / 2.00 H

- *Di-cardanol BZ monomer*

The ^1H NMR spectra of di-cardanol BZ monomer depicted in **Figure 5**.

Precise integration of the NMR signals relative to cardanol compounds depends on the composition of cardanol and related proportion of different isomers. These integrations are usually calculated based on the abundance of the unsaturations described in the literature⁴²⁻⁴⁴. The abundance can slightly vary depending on the origin and the extraction process of cardanol from CNSL. The unsaturations abundance of the used cardanol is considered as: tri-unsaturated (n=3) ~ 41 %, di-unsaturated (n=2) ~ 23 %, mono-unsaturated (n=1) ~ 34 %, and saturated (n=0) ~ 3 %^{43,44}. Moreover, it is noteworthy that the relaxation times are different between aromatic and aliphatic hydrogen atoms, which may complicate the accurate quantification of all protons. To this point, the peaks related to the hydrogen atoms of the aliphatic chain were integrated regarding the aliphatic hydrogen in α position of the cardanol aromatic ring, which was taken as reference. This signal presents a triplet and should integrate for 2 H. For the integration of the signals corresponding to the aromatic and oxazine rings, the reference peak was the one of EDA.

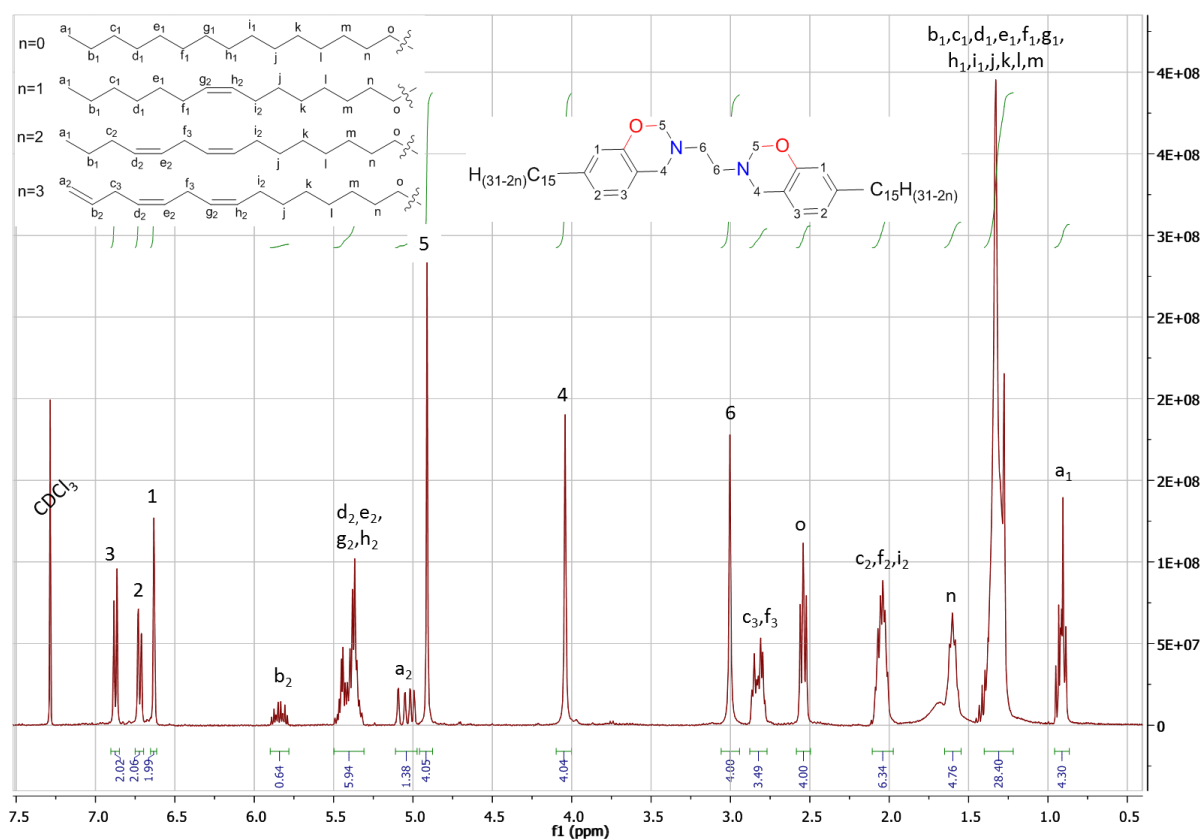


Figure 5. ^1H NMR spectrum of di-cardanol BZ monomer (solvent: CDCl_3).

The chemical structure of di-functional cardanol was confirmed by the corresponding ^1H NMR spectrum and the integration values confirm the presence of two cardanol moieties. Each peak corresponding to aromatic protons [1,2,3] at $\delta = 6.63 - 6.87$ ppm integrates for 2 H. The structure was also confirmed by the integration of the peaks from cardanol: the olefinic CH_2 protons [$b_2, d_2, e_2, g_2, h_2, a_2$] at $\delta = 4.99 - 5.89$ ppm, the protons in α of the alkyl chain unsaturations [c_2, f_2, i_2] at $\delta = 2.01 - 2.08$ ppm, as well as the CH_2 protons in α of the aromatic ring [o] at $\delta = 2.52 - 2.56$ ppm, the CH_2 from the alkyl chain [$b_1, c_1, d_1, e_1, f_1, g_1, h_1, i_1, j, k, l, m, n$] at $\delta = 1.27 - 1.61$ ppm and the CH_3 in the end of the alkyl chain [a_1] at $\delta = 0.88 - 0.96$ ppm. The CH_2 of the alkyl chain in between two unsaturations [c_3, f_3] were detected at $\delta = 2.79 - 2.85$ ppm. Experimental integrations are observed to be close to the expected theoretical integrations presented in **Table 2**.

The characteristic peaks of benzoxazine structure confirmed also the well formation of the BZ monomer. The peaks corresponding to oxazine ring were observed at $\delta = 4.04$ and 4.91 ppm respectively correlated to $\text{Ar}-\text{CH}_2-\text{N}$ [4] and $\text{O}-\text{CH}_2-\text{N}$ [5], and both peaks integrate for approximately 4.00 H confirming the successful ring closure and the absence of ring-opened structures.

Table 2. ¹H NMR data of di-cardanol benzoxazine monomer.

Chemical shift (ppm)	Assignment	I _{experimental}	I _{theoretical}
0.88 – 0.95	-CH ₃ [a ₁]	4.30 H	3.54 H
1.27 – 1.41	-CH ₂ [b ₁ ,c ₁ ,d ₁ ,e ₁ ,f ₁ ,g ₁ ,h ₁ ,i ₁ ,j ₁ ,k ₁ ,l ₁ ,m]	28.40 H	27.12 H
1.58 – 1.61	-CH ₂ in β from Ar [n]	4.76 H	4.00 H
2.01 – 2.08	-CH ₂ *=CH [c ₂ ,f ₂ ,i ₂]	6.34 H	6.20 H
2.52 – 2.56	-CH ₂ -Ar [o]	Ref. 4.00 H	4.00 H
2.79 – 2.85	-CH ₂ *=(CH) ₂ [c ₃ ,f ₃]	3.49 H	4.20 H
3.00	N-(CH ₂) ₂ -N [6]	Ref. 4.00 H	4.00 H
4.04	Ar-CH ₂ -N [4]	4.04 H	4.00 H
4.91	O-CH ₂ -N [5]	4.05 H	4.00 H
4.99 – 5.09	CH= [a ₂]	1.38 H	1.64 H
5.35 – 5.47	-CH= [d ₂ ,e ₂ ,g ₂ ,h ₂]	5.94 H	6.48 H
5.77 – 5.89	-CH= [b ₂]	0.64 H	0.82 H
6.63 / 6.73 / 6.87	H-Ar [1,2,3]	1.99 / 2.06 / 2.02 H	2.00 / 2.00 / 2.00 H

III.1.1.2. Mass characterization

The chemical structure of the monomers was confirmed by High-Resolution Mass Spectrometry (HRMS) characterization.

- *Di-phenol BZ monomer*

The corresponding spectrum for the structural characterization of di-phenol BZ monomer by HRMS is depicted in **Figure 6**.

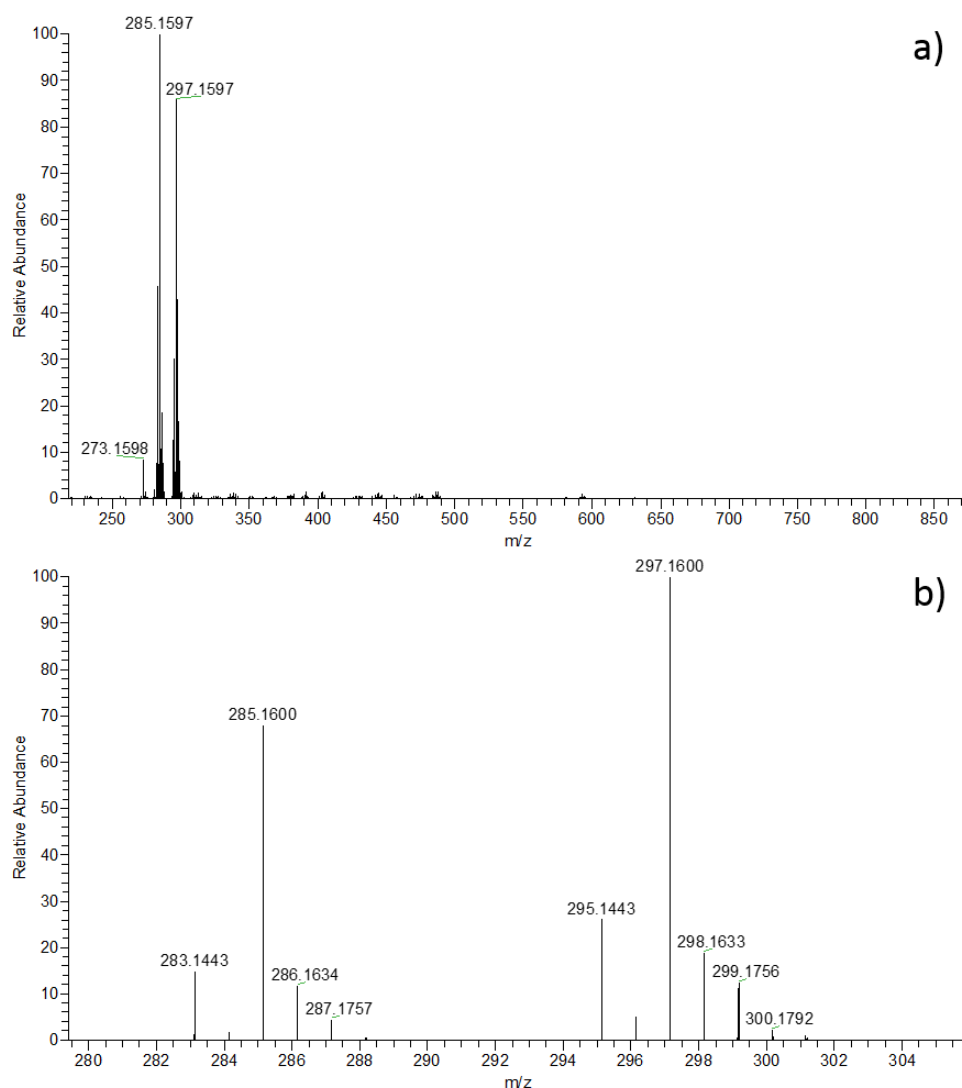


Figure 6. HRMS spectra of di-phenol BZ monomer. **a)** Full scan analysis – **b)** Zoom on the experimental product.

The protonated compound $[M+H]^+$ was observed at m/z 297. Other ions were also observed at m/z 285 and m/z 283 were assigned as $[M+H+H_2O-CH_2O]^+$ and $[M-H+H_2O-CH_2O]^+$ respectively. These ions resulted from a reaction during the analysis timeframe, as expected from mass spectrometry analyses of BZ monomers^{45,46}. It appeared that BZ monomers strongly react during the mass analysis through ion/molecules reactions in presence of water with the consequent release of formaldehyde from the protonated compound. Despite a solvent-less sample preparation, air humidity cannot be avoided and accounts for this ion/molecule reaction. The mass of the protonated di-phenol BZ monomer is similar to the expected mass of m/z 297.160, confirming the chemical structure verified by previous 1H NMR analysis.

- Di-cardanol BZ monomer

The expected typical peaks of di-cardanol monomer were present in the corresponding HRMS spectrum depicted in **Figure 7**. On the zoom of the spectrum region **Figure 7a)**, the expected protonated compound $[M+H]^+$ appeared at m/z 709. As for the previous monomer, products resulting from a reaction during the analysis appeared at m/z 697 and at m/z 695, respectively assigned as $[M+H+H_2O-CH_2O]^+$ and $[M-H+H_2O-CH_2O]^+$ ions of di-cardanol BZ monomer. The experimental mass observed at m/z 709.5673 is very close to the expected theoretical mass of m/z 709.5667, confirming the chemical structure of the synthesized di-cardanol BZ monomer.

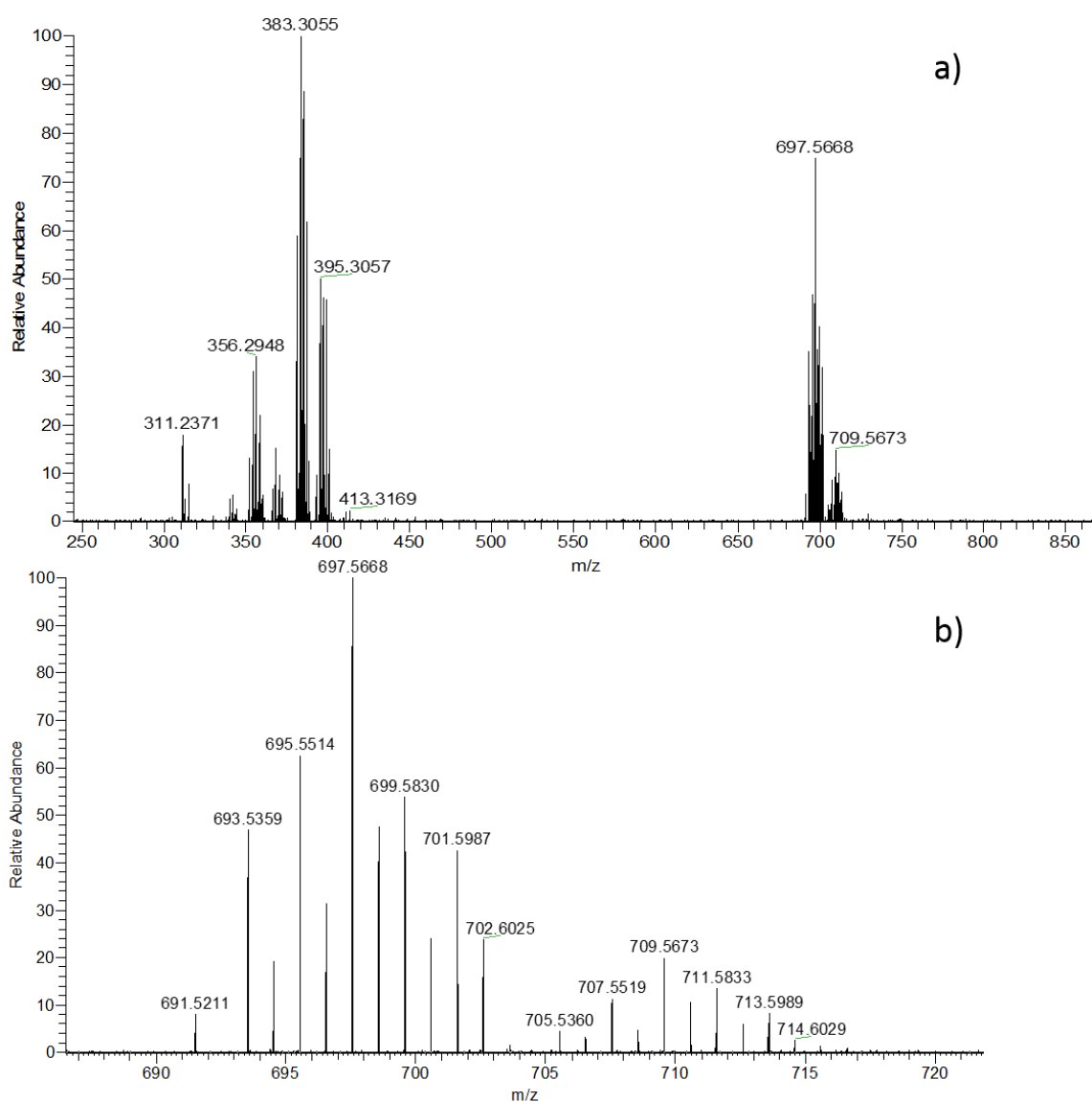


Figure 7. HRMS spectra fo di-cardanol BZ monomer. **a)** Full scan analysis – **b)** Zoom on the experimental product.

However, some unexpected additional peaks were observed on the full scan analysis on **Figure 7a**), appearing around m/z 380 – 400. These peaks were already observed in a previous study where further MS/MS analyses have been performed⁴⁷. Thus, the peaks observed in this region were not due to impurities but assigned to fragmentation during the analysis timeframe. Thus, as MS/MS confirmed that these peaks are fragments of the original di-cardanol BZ monomer, it can be concluded that the synthesized di-cardanol monomer was obtained with a good purity.

III.1.2. Asymmetric benzoxazines synthesis

The asymmetric monomer can be synthesized with an appropriate adjustment of the reagents stoichiometry⁴⁴. In the first step, cardanol, EDA, and paraformaldehyde were reacted in reflux of CHCl_3 , in stoichiometry 1:1:2, to obtain a mono-BZ with cardanol and pendent primary amine. In the second step, phenol and paraformaldehyde are added to the crude product in stoichiometric ratio 1:2 and the reaction was completed at reflux of CHCl_3 (**Figure 8**). Each step lasted for 24 h.

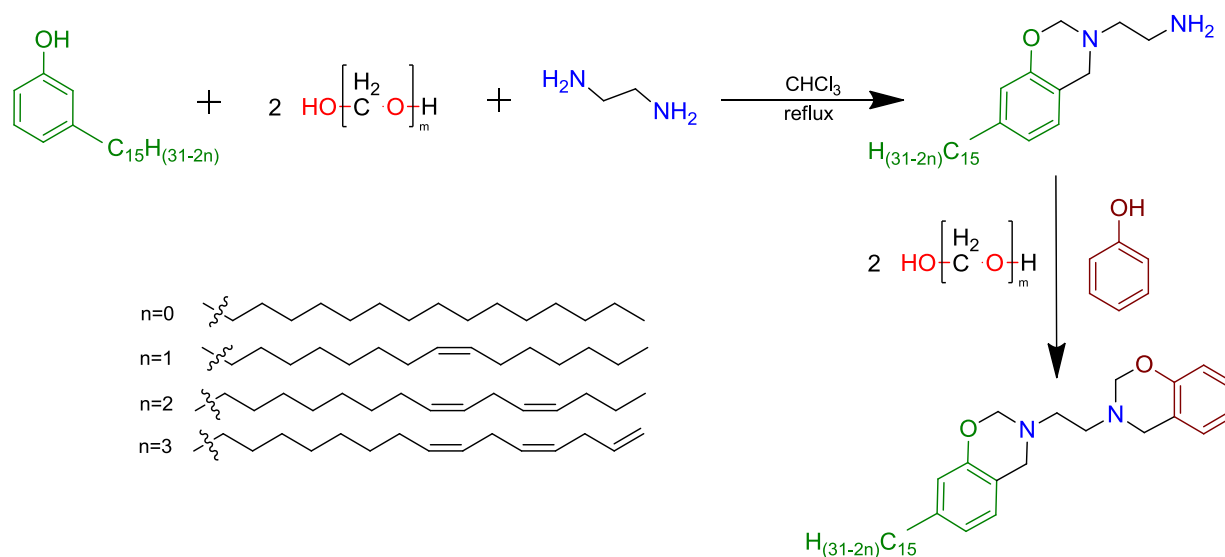


Figure 8. Synthesis of the asymmetric card-phenol BZ monomer from phenol and cardanol.

III.1.2.1. ¹H NMR characterization

The ¹H NMR spectrum of the asymmetric card-phenol depicted in **Figure 9** confirms the successful synthesis of the desired product. As for the previous cardanol-based compound, two peaks were taken as reference to integrate more precisely aromatic and aliphatic hydrogen atoms, as they do not present the same relaxation time. To this purpose, the signal corresponding

to the protons of EDA was taken as reference for the integration of the signal corresponding to the benzoxazine structure. This signal should integrate for 4 H. The peaks related to the cardanol side chain were integrated using the aliphatic hydrogen in α position of the cardanol aromatic ring as reference, which presents a well-defined triplet and should integrate for 2 H.

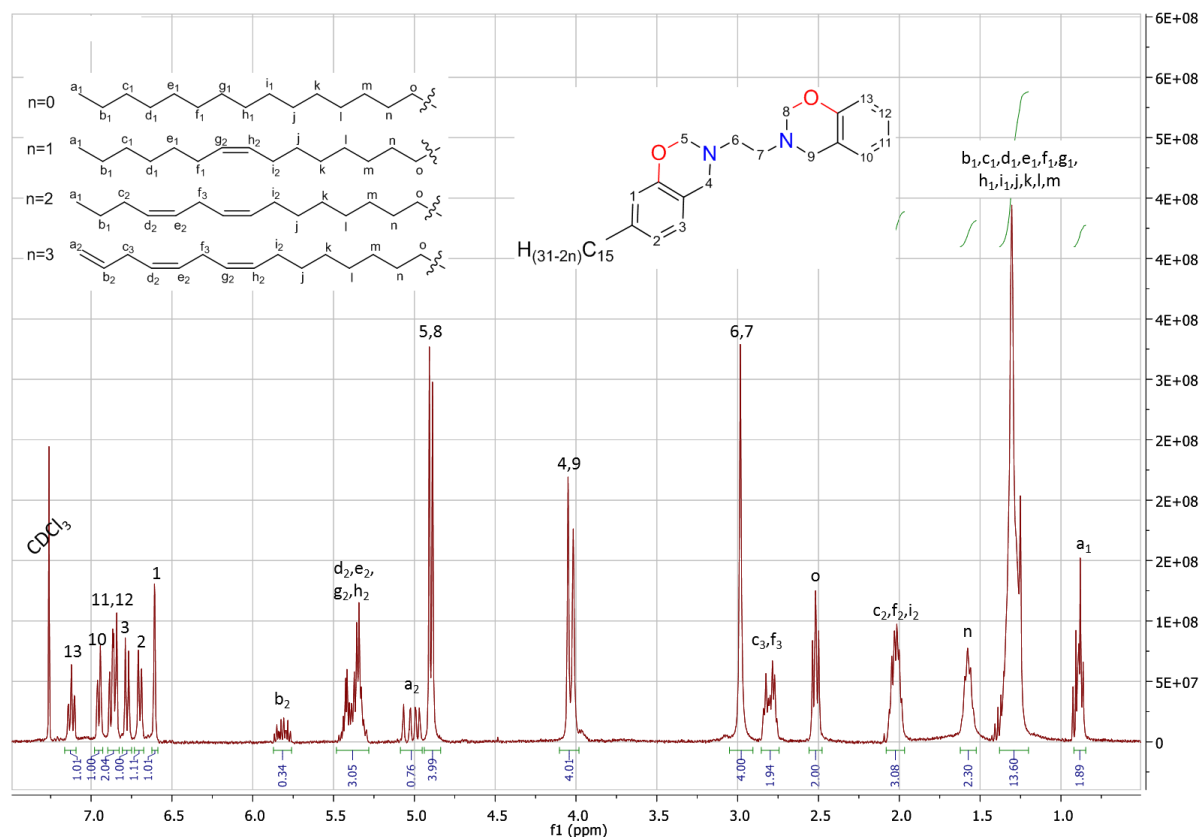


Figure 9. ^1H NMR spectrum of card-phenol BZ monomer (solvent: CDCl_3).

As previously described, all the characteristic peaks of cardanol were observed, from the aromatic protons to each aliphatic proton. The integration of the signals was divided by two compared to the previous di-cardanol monomer, indicating the presence of only one cardanol moiety. The experimental integrations were close to the expected integrations in the case of an asymmetric monomer (**Table 3**). The signals of the phenolic aromatic protons [10,11,12,13] integrated for approximately 4 H in total indicating the presence of one phenol moiety. The protons [1,2,3] integrated for approximately 1 H each, and successfully attributed to the aromatic ring of the cardanol moiety. Moreover, the asymmetry of this monomer was confirmed by the characteristic peaks of the oxazine rings, $\text{Ar}-\text{CH}_2-\text{N}$ [4,9] and $\text{O}-\text{CH}_2-\text{N}$ [5,8] which both integrate for approximately 4 H. But more specifically, these peaks appeared as singlet in the case of symmetric compounds. In this case of an asymmetric monomer, both peaks presented a doublet, as they did not present the same environment, whether the corresponding

oxazine ring is attached to phenol or cardanol. Thus, asymmetric structure of card-phenol BZ monomer was perfectly confirmed by ^1H NMR.

Table 3. ^1H NMR data of asymmetric card-phenol BZ monomer.

Chemical shift (ppm)	Assignment	I _{experimental}	I _{theoretical}
0.86 – 0.92	-CH ₃ [a ₁]	1.89 H	1.77 H
1.25 – 1.37	-CH ₂ [b ₁ ,c ₁ ,d ₁ ,e ₁ ,f ₁ ,g ₁ , h ₁ ,i ₁ ,j ₁ ,k ₁ ,l ₁ ,m ₁]	13.60 H	13.56 H
1.56 – 1.59	-CH ₂ in β from Ar [n]	2.30 H	2.00 H
1.98 – 2.06	-CH ₂ *=CH [c ₂ ,f ₂ ,i ₂]	3.08 H	3.10 H
2.49 – 2.53	-CH ₂ -Ar [o]	Ref. 2.00 H	2.00 H
2.77 – 2.84	-CH ₂ * (=CH) ₂ [c ₃ ,f ₃]	1.94 H	2.10 H
2.98	N-(CH ₂) ₂ -N [6,7]	Ref. 4.00 H	4.00 H
4.01 – 4.04	Ar-CH ₂ -N [4,9]	4.01 H	4.00 H
4.88 – 4.90	O-CH ₂ -N [5,8]	3.99 H	4.00 H
4.97 – 5.06	CH= [a ₂]	0.76 H	0.82 H
5.29 – 5.45	-CH= [d ₂ ,e ₂ ,g ₂ ,h ₂]	3.05 H	3.24 H
5.76 – 5.87	-CH= [b ₂]	0.34 H	0.41 H
6.60 / 6.69 / 6.77	H-Ar [1,2,3]	1.01 / 1.11 / 1.00 H	1.00 / 1.00 / 1.00 H
6.86 / 6.94 / 7.12	H-Ar [10,11,12,13]	1.00 / 2.04 / 1.01 H	1.00 / 2.00 / 1.00 H

III.1.2.2. Mass characterization

The card-phenol asymmetric BZ monomer was characterized by HRMS (**Figure 10**). The expected compound was successfully detected with the protonated specie observed at m/z 501, as well as the expected ions $[\text{M}+\text{H}+\text{H}_2\text{O}-\text{CH}_2\text{O}]^+$ at m/z 489 and $[\text{M}-\text{H}+\text{H}_2\text{O}-\text{CH}_2\text{O}]^+$ at m/z 487. The exact mass for card-phenol monomer was found to be similar to the theoretical expected mass of m/z 501.3476.

However, despite a meticulous purification and a relatively good ^1H NMR spectrum with appropriate integrations which may indicate a pure product, traces of di-phenol BZ and di-cardanol BZ monomers were observed on the global scan analysis, resulting from the synthesis.

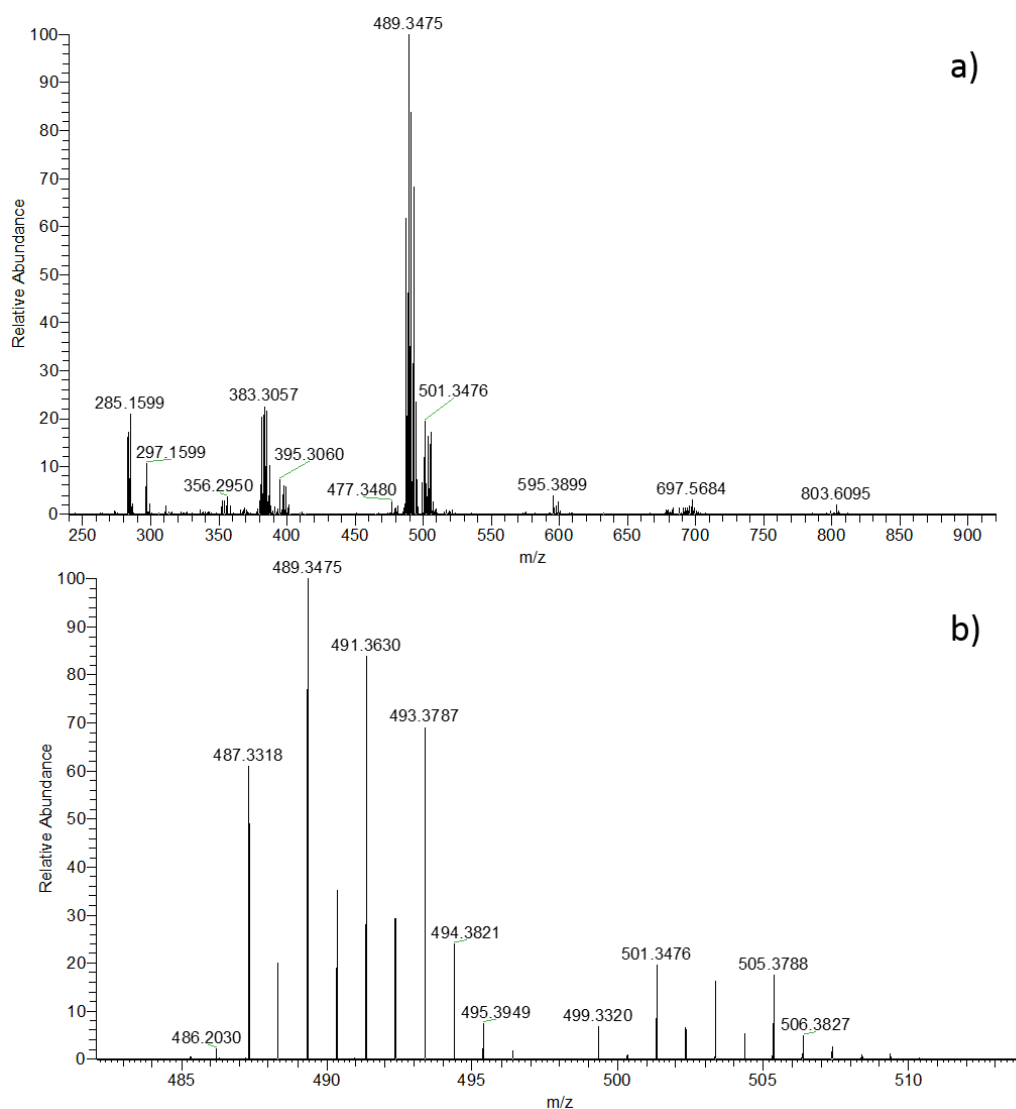


Figure 10. HRMS spectra of card-phenol BZ monomer. **a)** Full scan analysis – **b)** Zoom on the experimental product.

III.1.3. Purification process

Traditional extractions with basic solution were performed on the raw products to remove any traces of non-reacted reagent. For cardanol-based monomers, an additional purification by column chromatography was performed. Indeed, in the case of di-cardanol, the kinetics of synthesis is relatively low, thus, in a minor part, mono-benzoxazine was also obtained. In the case of card-phenol BZ synthesis, even though the stoichiometry was controlled, some minor products were also obtained such as di-phenol BZ and di-cardanol BZ. For this reason, the purification of these monomers required column chromatography, using Heptane / Ethyl Acetate in a 7/3 ratio as eluent. However, to avoid any undesirable gradient, the silica was first conditioned using the apolar solvent. The crude product was solubilized in the minimum of the apolar solvent and added above the silica. Then, the mixture of eluent was poured for separation.

After obtention of the pure product, an extra-recrystallization step was performed in cold ether to remove all traces of grease which may be present in the solvents, but also to remove oily oligomeric compounds that may present the same retention time as the desired product. However, relatively low yields were obtained for cardanol-based monomer (60 % for di-cardanol BZ and 50 % for card-phenol BZ), as in this case, the separation through column chromatography was followed by thin layer chromatography (TLC), which is not very precise. Thus, several fractions were not collected to avoid fractions containing a mixture of by-products. However, it seemed according to HRMS that some fractions containing mixtures could not be avoided. Finally, relatively pure cardanol-based monomers were obtained as a white wax while a white powder was obtained for the di-phenol BZ monomer with a yield of 85 %.

III.1.4. FTIR characterization of benzoxazine monomers

The FT-IR spectra of di-phenol, card-phenol, and di-cardanol BZ monomers are shown in **Figure 11a** and **11b**. **Figure 11a** shows a strong C-H band ($2850\text{-}2920\text{ cm}^{-1}$), as the aliphatic carbon content increased. The ring closure was confirmed by the absence of -OH band over 3000 cm^{-1} . The characteristic band of oxazine ring for the O-CH₂-N stretching appeared at 912 cm^{-1} (**Figure 11b**).

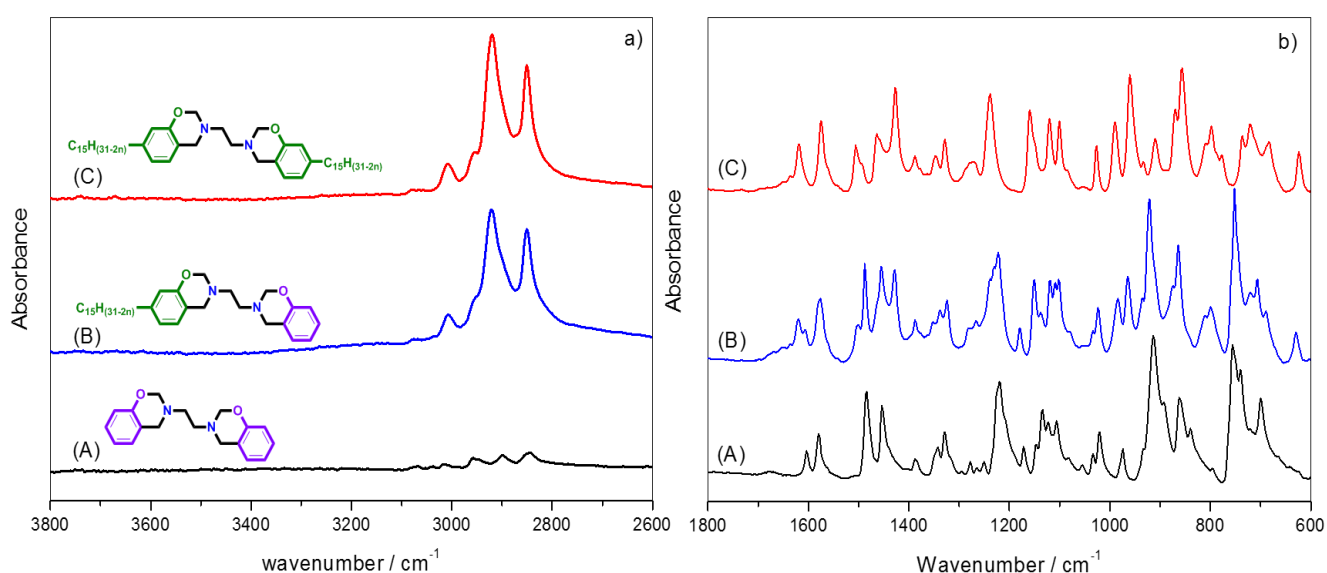


Figure 11. FT-IR spectra of di-phenol (A), card-phenol (B), and di-cardanol (C) BZ monomers: **a)** from 3800 to 2600 cm^{-1} – **b)** from 1800 to 600 cm^{-1} .

This band was shifted when cardanol was used as phenol source, to 925 cm^{-1} for card-phenol and to 960 cm^{-1} for di-cardanol BZ. Another major difference was observed for the bands characterizing the aromatic rings. For di-phenol BZ, all benzene rings are *ortho* di-substituted. This was confirmed with the band at 752 cm^{-1} for C-H out of plane deformation. For card-phenol the band at 752 cm^{-1} was still present while another band at 798 cm^{-1} appeared, characterizing a tri-substituted benzene. These bands confirmed the asymmetric structure of this monomer. Di-cardanol BZ did not show any signal at 752 cm^{-1} but only a more intense band at 798 cm^{-1} for the tri-substituted benzene rings of cardanol. The structures of the monomers were also confirmed by the presence of aromatic C=C at $1604\text{-}1430\text{ cm}^{-1}$, the asymmetric and symmetric stretching of aromatic ether Ar-O-C at 1222 and 1022 cm^{-1} respectively, and tertiary amine at $1100\text{-}1160\text{ cm}^{-1}$. For both cardanol-based BZ, a small band at 1620 cm^{-1} appeared with a shoulder, characteristic of conjugated C=C of aliphatic alkenes.

III.2. Thermo-analytical follow-up of ring opening and cross-linking reactions

III.2.1. Characterization by DSC

The thermal behavior of di-phenol, card-phenol, and di-cardanol BZ monomers were investigated by DSC (**Figure 12**). Analyses were performed at $4\text{ K}\cdot\text{min}^{-1}$ under air atmosphere.

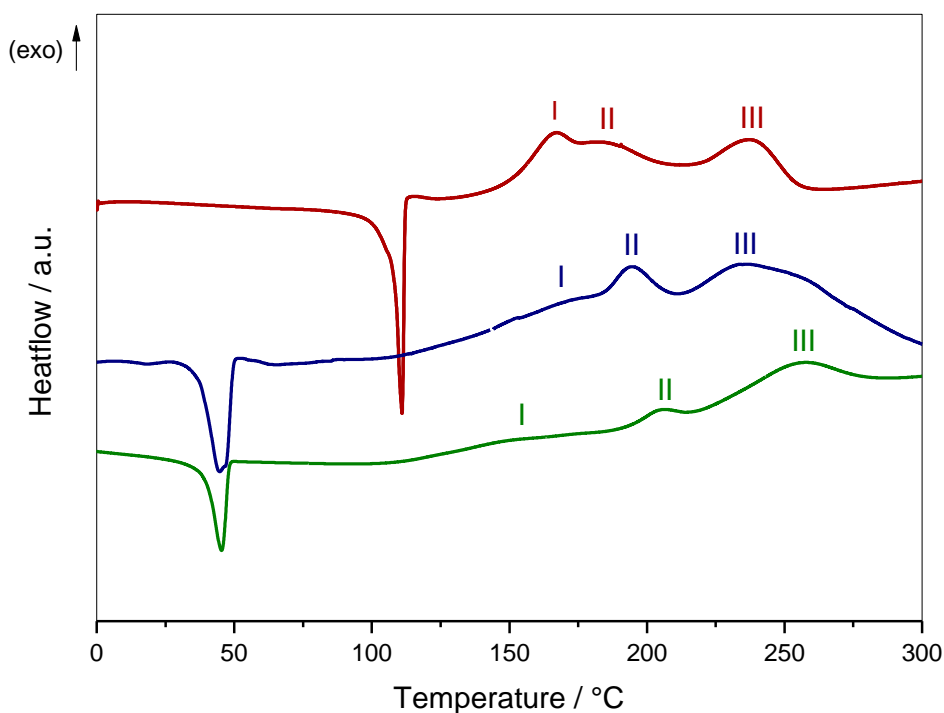


Figure 12. DSC thermograms (air, 4 K.min⁻¹) of di-phenol (red), card-phenol (blue), and di-cardanol (green).

For each DSC curve, the endothermic thermal event occurring at low temperatures was attributed to monomers melting, while the exothermic peak ranging between 120 and 280 °C was associated to the heat released during BZ polymerization. It is worthy to note that the highest melting temperature was obtained for di-phenol BZ at 110 °C (red) while the melting temperatures for card-phenol (blue) and di-cardanol (green) BZs were both reached at around 45 °C. This is in agreement with previous studies where cardanol-based systems showed lower melting temperatures²⁸. It suggests that cardanol-based crystal structures were less thermally stable, *i.e.* melt at lower temperatures, due to the lower efficiency of chain packing in the presence of the aliphatic side-chain. The modification of the H-bond network due to the cardanol might also have an influence on the physical properties of crystals and thus on melting temperature. Three main exothermic peaks (noted I, II and III in **Figure 12**) were observed. These peaks were observed at slow heating rates. Indeed, **Figure 13** shows the convolution of the peaks when increasing the heating rate for di-phenol BZ.

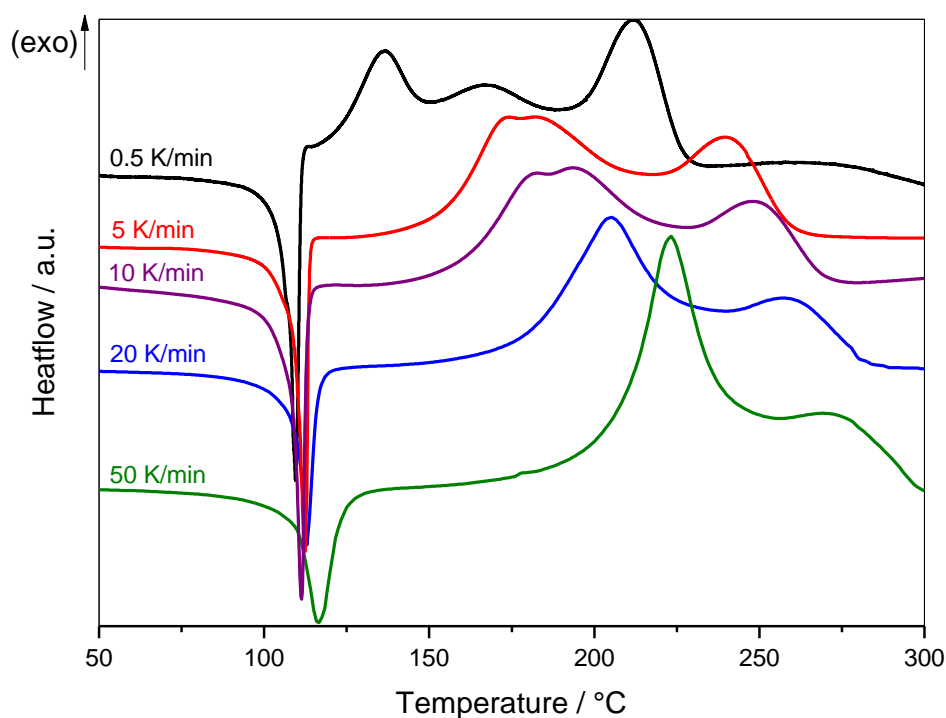


Figure 13. DSC thermograms of di-phenol BZ at 0.5, 5, 10, 20, and 50 K.min⁻¹.

The polymerization is known to start with an irreversible ring-opening and is followed by the formation of the methylene bridge between the nitrogen and the phenolic derivative cycle⁴⁸, and is supposed to continue with an aromatic electrophilic substitution and the formation of H-bonds to complete the cross-link. The kinetic study discussed in the next chapter tried to determine the temperature range attributed to each step. It was suggested that these reactions may correspond respectively to peak I, peak II, and peak III. For di-phenol BZ, the overall enthalpy considered the whole exotherm, while for cardanol-based benzoxazines the enthalpy of polymerization was assigned only to peak I and peak II. Explications are developed in the next section. For sake of comparison, the enthalpy of polymerization of di-phenol BZ monomer was also integrated without considering peak III. Obtained values are summarized in **Table 4**. The heat of polymerization highly decreased when cardanol was used as phenol source: from around 136 kJ.mol⁻¹ for the di-phenol BZ (peaks I, II, III) to around 33 kJ.mol⁻¹ for card-phenol BZ and 25 kJ.mol⁻¹ for di-cardanol BZ (peaks I and II). As the enthalpies were evaluated per mol, it can be considered that lower reaction heat is not due to a dilution effect but to a reduction of both the cross-link density and the amount of branching. This is directly linked to the presence of the flexible alkyl chain that hinders the ability to branch through ring-opening.

Thus, when di-cardanol polymerizes, it results into lower polymerization reaction heat compared to card-phenol which has itself a lower overall enthalpy compared to di-phenol.

Table 4. Enthalpy of polymerization for each BZ monomer obtained by integration of the exotherm with and without peak III.

Peaks integrated	ΔH (kJ.mol ⁻¹) Di-phenol BZ	ΔH (kJ.mol ⁻¹) Card-phenol BZ	ΔH (kJ.mol ⁻¹) Di-cardanol BZ
I / II / III	136.1 ± 5.4	-	-
I / II	41.4 ± 1.7	32.5 ± 1.3	24.9 ± 0.9

It is worthy to note a decrease in the onset temperature of polymerization when cardanol was introduced, from 135 °C for di-phenol BZ to 110 °C for cardanol-based monomers. An explanation could be the triggering of the ROP by the presence of residual and free cardanol species as shown in a recent publication⁴⁹. However, the BZ/cardanol ratio in the abovementioned study is very high (>>1) while in the present case, no trace of cardanol was detected. Another explanation may be related to some reactions of oligomerization between the unsaturations of cardanol moieties that can occur under high temperatures³². A complementary synthesis was performed for a better understanding. Therefore, pentadecylphenol (ptdp) was used as source of phenol for the synthesis of a di-functionalized BZ monomer with ethylenediamine as bridging group, so-called di-ptdp BZ (synthesis and characterization presented in supporting information at the end of the chapter). This di-ptdp BZ is a homologous to di-cardanol BZ monomer, without any unsaturation. Thermal characterization of di-ptdp BZ monomer with DSC and TGA is depicted in **Figure 14**. Analyses were performed at 4 K.min⁻¹ under air atmosphere. DSC thermogram presented an exothermic phenomenon with an onset temperature at 180 °C. Thus, as the exothermic thermal event started at much higher temperature, it can be confirmed that the presence of unsaturations on the cardanol aliphatic side chain may provoke some oligomerization reactions. However, for di-ptdp BZ, despite the wide processing window, polymerization and thermal degradation occurred simultaneously, thus, no further analyses on the impact of the unsaturations on the final properties of the polymer could be performed.

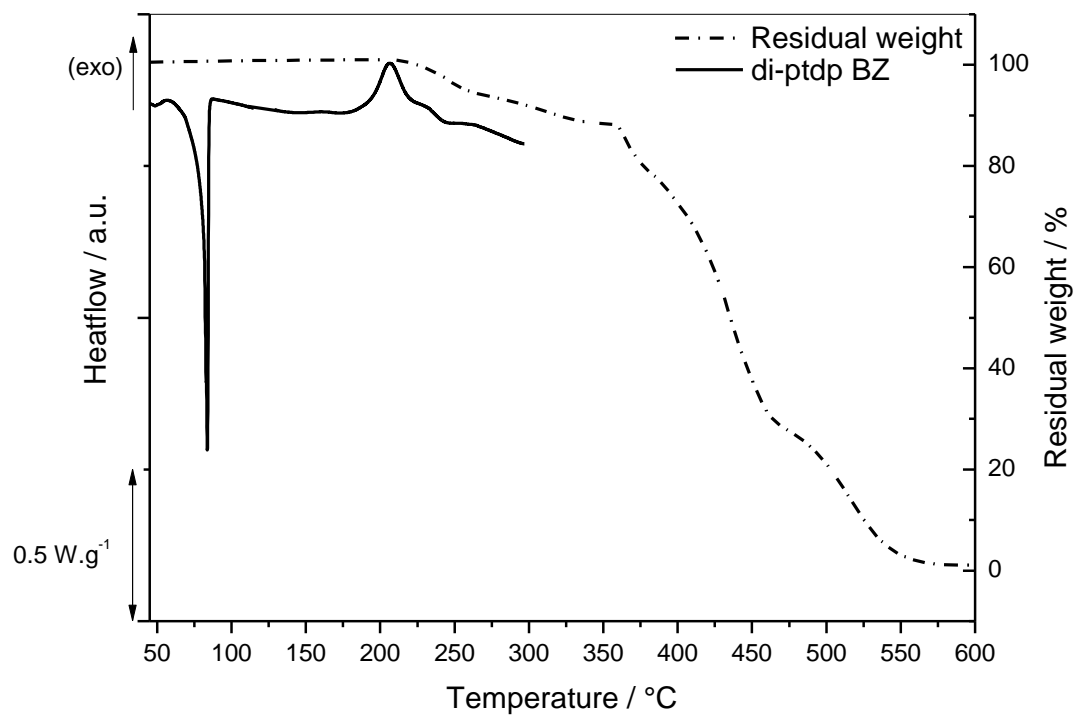


Figure 14. Thermal characterization of di-ptdp BZ monomers. Right axis: DSC (full line) and left axis: TGA (dotted line) characterization of di-BZ monomer from pentadecylphenol at 4 K.min⁻¹ under air atmosphere.

III.2.2. DSC vs TGA correlation

To analyze DSC thermograms in the best possible manner, it is important to determine if an eventual mass loss occurs during DSC scanning. For each monomer, DSC thermogram was compared with TGA thermogram at the same heating rate (4 K.min⁻¹, air atmosphere). Results are depicted in **Figure 15**.

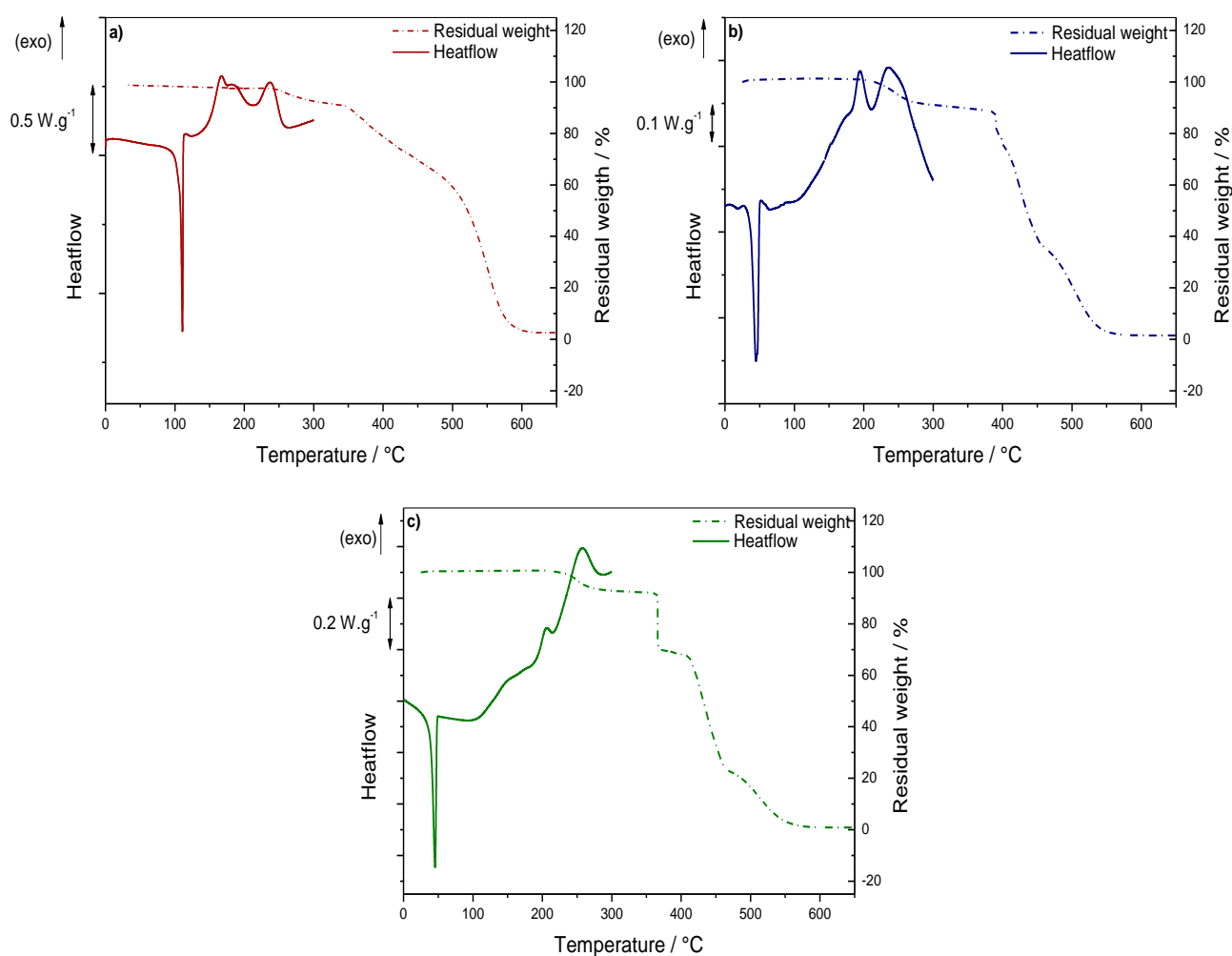


Figure 15. DSC and TGA thermograms (air atmosphere, 4 K.min⁻¹) of **a)** di-phenol BZ, **b)** card-phenol BZ, and **c)** di-cardanol BZ monomers.

For di-phenol BZ monomer, the overall enthalpy of polymerization was assigned to the whole exotherm of the three peaks; however, the TGA curve of the di-phenol BZ at the same heating rate shows a slight weight loss of 2.7 % between 240 °C and 270 °C, which could indicate that at high temperatures (peak III) there is a convolution between final branching and beginning of decomposition of the monomer. This low amount of decomposition was neglected for the consideration of the enthalpy of polymerization. Nevertheless, the same approximation could

not be applied to the two cardanol-based monomers. Indeed, the temperature at which started the peak III for card-phenol and di-cardanol matched with the onset temperature of degradation, respectively at 210 and 220 °C. Thus, peak III could not be included in the enthalpy of polymerization. Moreover, it is noteworthy that DSC thermograms for card-phenol and di-cardanol did not finish on the baseline, which may be due to the loss of a product. Unfortunately, it was not possible to identify this lost compound.

III.2.3. Chemorheology of polymerization

Non-isothermal rheology analyses were performed with plate-plate geometry (diameter 25 mm, gap 0.5 mm) and recorded at an imposed 0.1 % deformation at a frequency of 1 Hz and a heating rate of 2 K.min⁻¹. Rheograms with the evolution of both storage (G') and loss (G'') moduli as a function of temperature of the three synthesized BZ monomers are depicted in **Figure 16**.

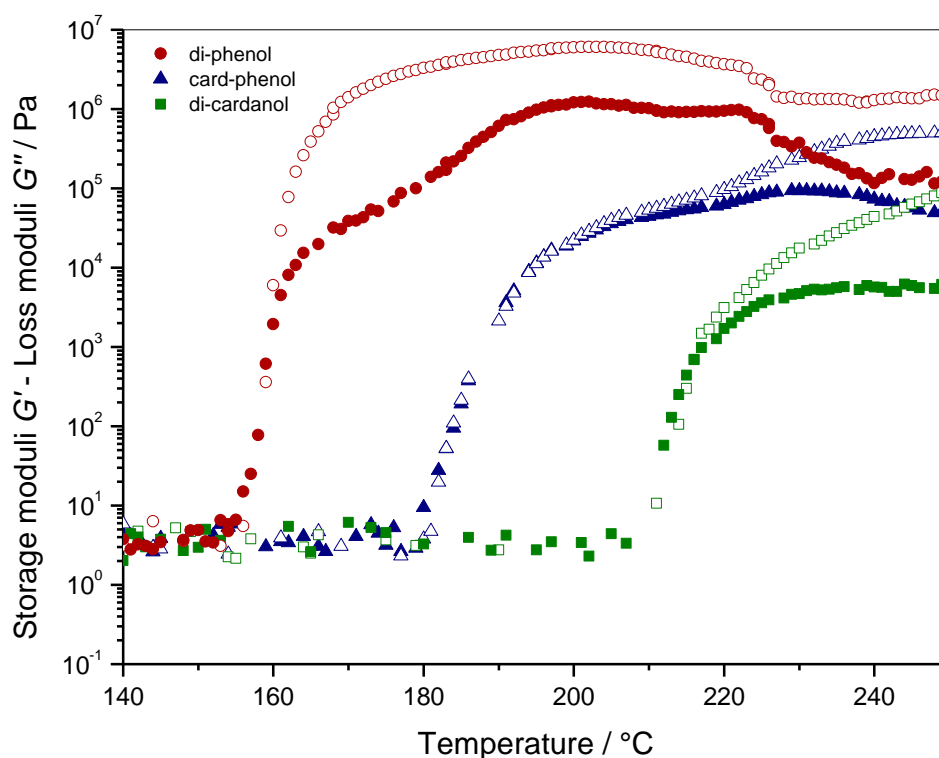


Figure 16. Evolution of storage moduli (G' , empty markers) and loss moduli (G'' , filled markers) for di-phenol (circles), card-phenol (triangles), and di-cardanol (squares) at 2 °C.min⁻¹.

For di-phenol BZ the crossover of G' and G'' (*i.e.* gel point) was observed at a temperature of 159 °C. Below this temperature, the loss modulus appeared higher than the storage modulus, corresponding to the viscous nature of the system. Above this temperature, the storage

component prevails, and the system rather showed the behavior of an elastic solid⁵⁰. The evolution of G' and G'' for card-phenol BZ shows that its gelation occurred at a higher temperature of 197 °C, and for di-cardanol BZ, the system became an elastic solid at a temperature as high as 215 °C. These results are summarized in **Table 5**.

Table 5. Rheological data at the gel point and at the glassy plateau.

Sample	$T_{gel}^{[a]}$ (°C)	$T_v^{[b]}$ (°C)	$G'_v^{[c]}$ (Pa)	$\eta^{*}_v^{[d]}$ (10^3 Pa.s)
Di-phenol	159	200	$6.08 \cdot 10^6$	986
Card-phenol	197	245	$4.97 \cdot 10^5$	79.7
Di-cardanol	215	250	$9.08 \cdot 10^4$	14.5

^[a] Temperature at gelation; ^[b] Temperature at vitrification; ^[c] Storage modulus at vitrification temperature; ^[d] Complex viscosity at vitrification temperature.

In the later stage of curing, each system reached the glassy state which is observed on the rheograms as a glassy plateau (**Figure 16**). At this stage of curing, the polymerization is mainly controlled by diffusion^{51,52}. Di-phenol BZ reached the glassy plateau at lower temperatures, while di-cardanol BZ reached the glassy state at a much higher temperature. The most important difference in G' values was observed between di-phenol and card-phenol, which has an intermediate chemical structure. The final storage modulus obtained at this stage decreased by an order of magnitude, from $6 \cdot 10^6$ Pa for di-phenol BZ, to $5 \cdot 10^5$ Pa for card-phenol, and to $9 \cdot 10^4$ Pa for di-cardanol (**Table 5**). This result is in agreement with the higher value of viscosity at the glassy plateau obtained for di-phenol monomer (**Table 5**). Addition of cardanol shifted gelation and vitrification to higher temperatures. In contrast with epoxy-amine systems^{51,52}, chemical reactions are not hindered neither at gelation nor at vitrification, which explains that glass transition temperature (T_g) can be much higher than curing temperatures for polyBZ⁵³, while this is not possible for epoxy. This is a considerable advantage of these systems. A decrease of the moduli for di-phenol BZ was observed from 225 °C, which may be due to a devitrification of the system. Also, **Figure 17** shows the evolution of complex viscosity as a function of temperature. It was again observed that the behavior depends on the BZ chemical structure. As a matter of fact, the first increase of viscosity coincided to di-phenol BZ. This component possesses the higher aromatic ring content. This explained the sharp increase of η^* starting at 155 °C. In contrast, di-cardanol BZ had a more progressive increase of its complex viscosity, until $14.5 \cdot 10^3$ Pa.s at 250 °C. This behavior can be explained because of the

plasticizing effect of the long alkyl side chain of cardanol which resulted in a lower cross-link density. Card-phenol BZ showed an intermediate behavior that matched its intermediate chemical structure. Its aromatic ring content was responsible for a sharp increase of η^* but less significant than for di-phenol, and this increase was here buffered by the presence of the side chain of cardanol. It was also observed that as the monomer gained in cardanol content, the onset of the complex viscosity was shifted to 30 °C to higher temperatures.

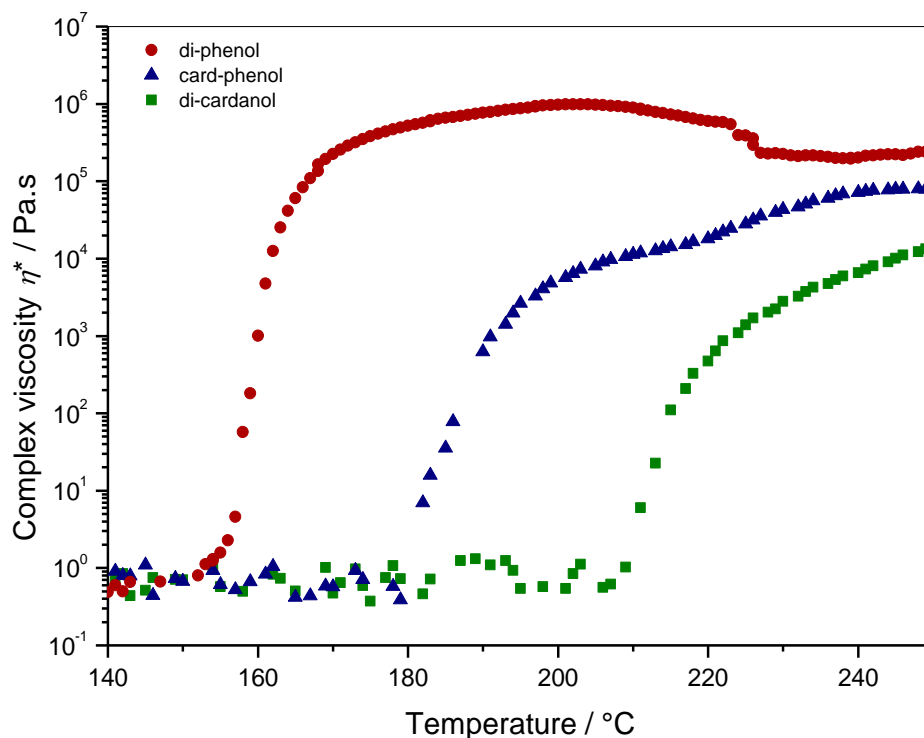


Figure 17. Evolution of complex viscosity (η^*) with temperature for di-phenol (circles), card-phenol (triangles), and di-cardanol (squares) at 2 °C.min⁻¹

III.3. After cure completion, characterization and final properties of the polybenzoxazine resins

III.3.1. Material elaboration

Monomers were polymerized into a silicon mold. The samples were heated to their melting temperature and were degassed under vacuum for 30 minutes to avoid the formation of bubbles and ensure good polymerization. Then, each system was cured into the oven. Di-phenol BZ monomer was then cured during 1 h at 150 °C, 1 h at 170 °C, followed by a post curing at 180 °C during 1 h. Di-cardanol was cured during 2 h at 190 °C followed by a post curing at 210 °C for 2 h. Card-phenol BZ was cured during 2 h 30 at 200 °C and a post curing was

performed at 210 °C during 30 min. Both cardanol-based BZ monomers followed a further post-curing step at 250 °C for 2 h. In each case, the cure completion was experimentally verified by means of DSC experiments which did not highlight any residual enthalpy.

III.3.2. FTIR characterization of the polymers

The FT-IR spectra of the corresponding polybenzoxazines are displayed in **Figure 18**.

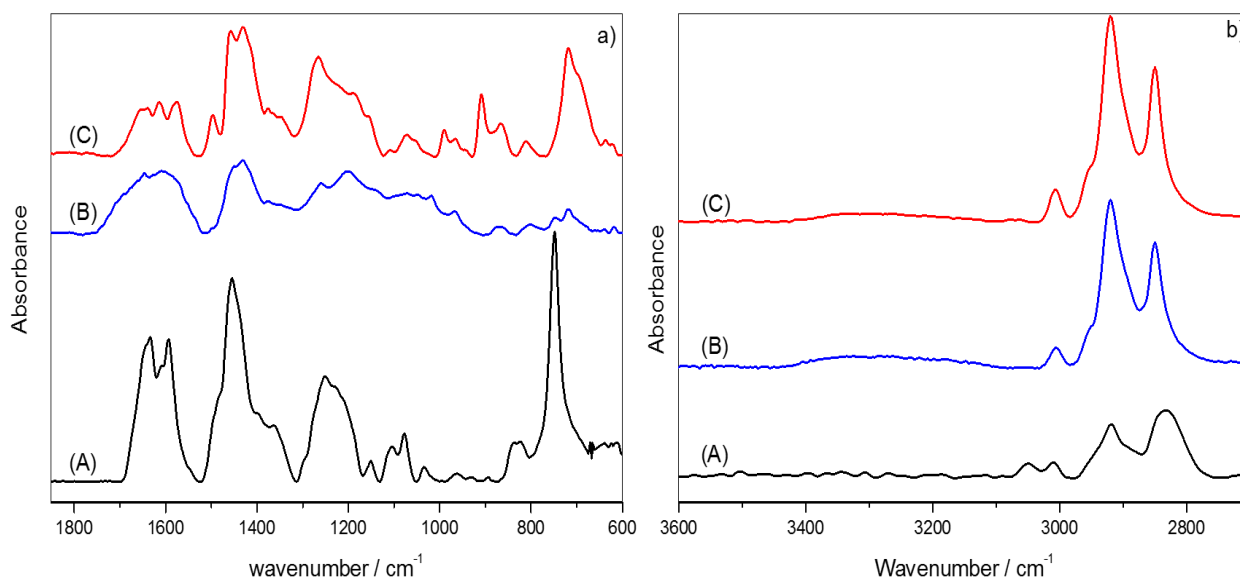


Figure 18. FT-IR spectra of poly(di-phenol) (A), poly(card-phenol) (B), and poly(di-cardanol) (C): **a)** from 1800 to 600 cm^{-1} , **b)** from 3600 to 2700 cm^{-1} .

The disappearance of the band characterizing the oxazine rings, at respectively 912, 925, and 960 cm^{-1} for di-phenol, card-phenol, and di-cardanol BZs was the main modification compared to the spectra of monomers and confirmed the ring opening polymerization. The symmetric stretching of aromatic ether at 1022 cm^{-1} decreased as the rings open, in favor of a shoulder emerging around 1370 cm^{-1} for phenolic alcohol. **Figure 18b)** shows a focus on the area of CH and –OH stretching. After ring-opening polymerization, a phenol moiety is produced; however, poly(di-phenol) did not show any signal for –OH stretching because the phenolic –OH was strongly involved in *inter* and *intra*-H-bonding⁵⁴ as depicted in **Chart1a**). Indeed, these several geometrical possibilities (*inter* and *intra*) for H-bond in poly(di-phenol) lead to a large possibility of vibration frequencies which consequently broaden the –OH peak so that it cannot be highlighted. On the other hand, a weak, broad but detectable –OH band appeared between 3092-3430 cm^{-1} for poly(card-phenol) and poly(di-cardanol). Thus, it might indicate that the phenolic –OH possesses less geometrical possibilities for H-bonding. Indeed, the alkyl side

chain of cardanol might force the –OH group to adopt the *intra*-H-bond conformation as presented in **Chart 1b**). The hydroxyl functions produced through ring-opening polymerization for cardanol-based BZ were not as strongly involved in *inter*-H-bonds as for poly(di-phenol). The width of –OH band signal observed for poly(card-phenol) and poly(di-cardanol) were almost identical which would indicate that one cardanol moieties is enough to reduce the possibilities of *inter*-H-bonding and thus modify the H-bonds network.

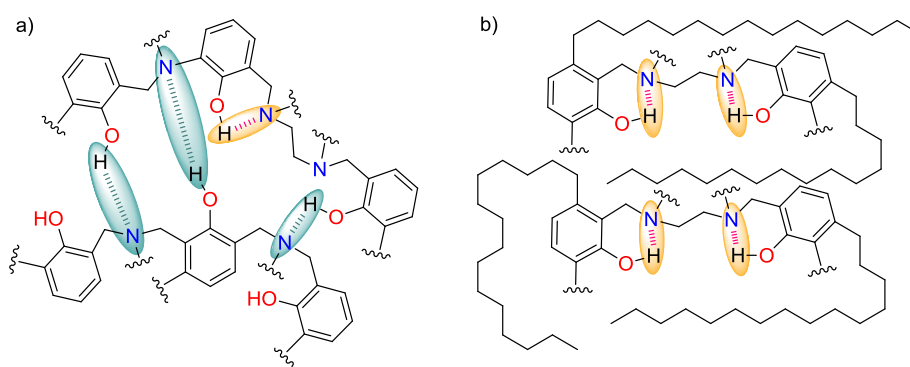


Chart 1. Favorable H bonding in the cross-linked structure a) with phenol and b) with cardanol.

III.3.3. Thermo-mechanical characterization by DMA

Dynamic mechanical analyses were performed on the three polyBZ materials after cross-linking with the objective to draw the structure-to-properties relationships. The evolutions of the storage modulus (E') and the damping factor ($\tan \delta$) as function of temperature are shown in **Figure 19**.

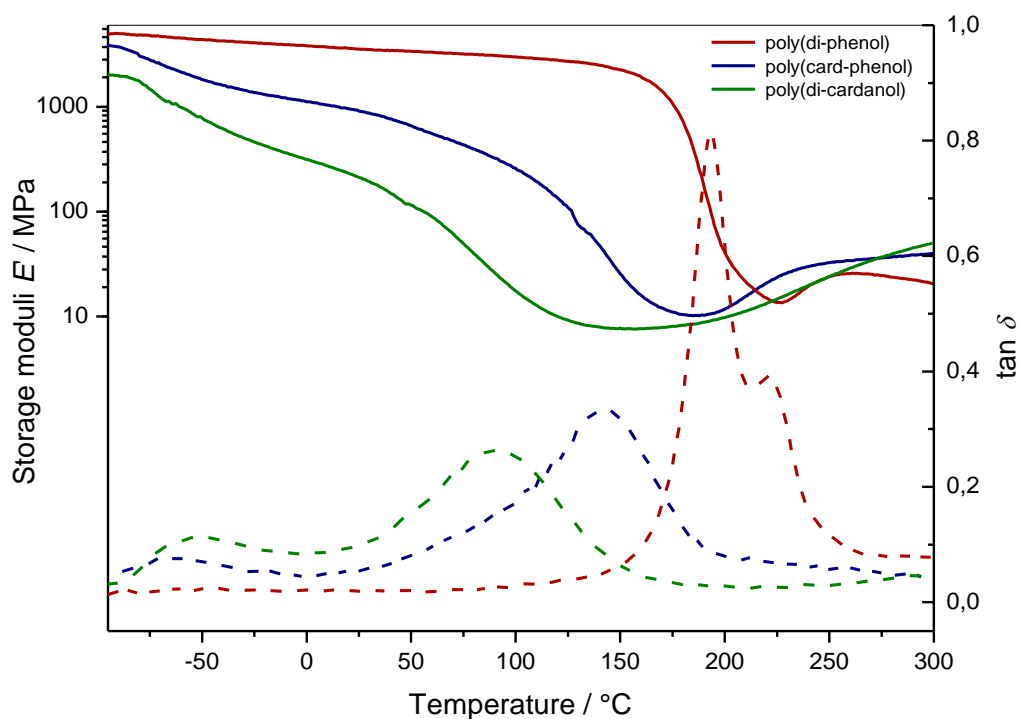


Figure 19. DMA thermograms of poly(di-phenol) (red), poly(card-phenol) (blue), and poly(di-cardanol) (green) – Left axis: Evolution of storage moduli E (solid lines) - Right axis: Evolution of $\tan \delta$ (dash lines).

The main analytical data are summarized in **Table 6**. The polymerized di-phenol, card-phenol, and di-cardanol are so-called poly(di-phenol), poly(card-phenol), and poly(di-cardanol). The storage modulus represents the capacity of the material to restore the energy in the form of an elastic deformation when it is subjected to a mechanical strain. The higher is the storage modulus, the higher is the stiffness of the material. The peak in the $\tan \delta$ curves (**Figure 19**) is associated with the decrease of the storage modulus and corresponds to mechanical relaxations. The relaxations in amorphous materials are associated with different motional processes involving different dynamics: γ and β -relaxations associated to local motions, are secondary relaxations occurring at low temperature, while α -relaxation, which is associated to cooperative motions of main chains, occurs at higher temperatures. This α -relaxation causes very large changes in the mechanical properties of the material and is frequently assimilated, as a first approximation, to the glass transition. As shown in **Figure 19**, the $\tan \delta$ curve of poly(di-phenol) shows a thin and sharp peak at 190 °C which was unambiguously attributed to the α -relaxation. The shape of the peak suggests a good homogeneity within the network together with a high cross-linking density. When cardanol units were inserted, the relaxation processes change

drastically. The intensity of the $\tan \delta$ curves for poly(card-phenol) and poly(di-cardanol) were observed much lower in comparison with poly(di-phenol). Poly(card-phenol) showed an α -relaxation (*i.e.* $T_{\alpha} = 140$ °C) shifted to lower temperatures compared to poly(di-phenol) and that significantly broadened. This pointed out the heterogeneity in the cross-links associated with a softening induced by the aliphatic chains. It was also associated with lower values of the E' modulus in the glassy state. When two cardanols are used (poly(di-cardanol)), the α -relaxation was shifted to much lower temperatures (*i.e.* $T_{\alpha} = 65$ °C). It characterized a polymer network with a much lower degree of cross-link, as reflected in the low E' and T_{α} values. Another transition was observed at low temperatures in the $\tan \delta$ curves, around -60 and -70 °C for poly(card-phenol) and poly(di-cardanol) respectively. Similar DMA profiles with low transitions have been described in the literature⁵⁵ and have been associated to very local motions of the main chain cycles, namely β -relaxation. The authors have also estimated that the amplitude of $\tan \delta$ peak for β -relaxation was decreased when the curing was improved. In the present case, it can be assumed that the cardanol was responsible of the apparition of the β -relaxation as this peak was not observed in poly(di-phenol) DMA profile. Poly(di-phenol) showed the highest cross-linking density because it was not hindered by the presence of an alkyl side chains, which explained that poly(di-phenol) did not show a β -relaxation. Interestingly, the intensity of the β -relaxation has increased for poly(di-cardanol) compared to poly(card-phenol), which also confirmed that the higher the amount of aliphatic chain, the lower the cross-link density. Poly(di-phenol) appeared stiffer compared to poly(card-phenol) and poly(di-cardanol), this last one being the most flexible. This flexibility was brought by the long aliphatic side chain of cardanol, responsible of a plasticizing effect. This alkyl side chain also brought steric hindrance which explained a lower cross-link density and so a lower T_{α} , and a more intense β -relaxation. This cardanol moiety could also be responsible for the heterogeneity of the structure. As poly(card-phenol) possesses an intermediate structure between poly(di-phenol) and poly(di-cardanol), it showed an intermediate thermo-mechanical response.

Table 6. T_{α} , T_{β} and E values for all polyBZ systems.

Sample	T_{β} (°C)	T_{α} (°C)	$E^{[a]}$ (MPa)
Poly(di-phenol)	-	190	3,550
Poly(card-phenol)	-65	140	915
Poly(di-cardanol)	-55	65	195

^[a] Storage modulus at ambient temperature.

III.3.4. Thermal stability of the cured products

The thermal stability of the cured polybenzoxazines were investigated by TGA at 4 K.min⁻¹ under air atmosphere. **Figure 20** shows the TG curves for the three systems and the corresponding derivative thermogravimetric curves (DTG).

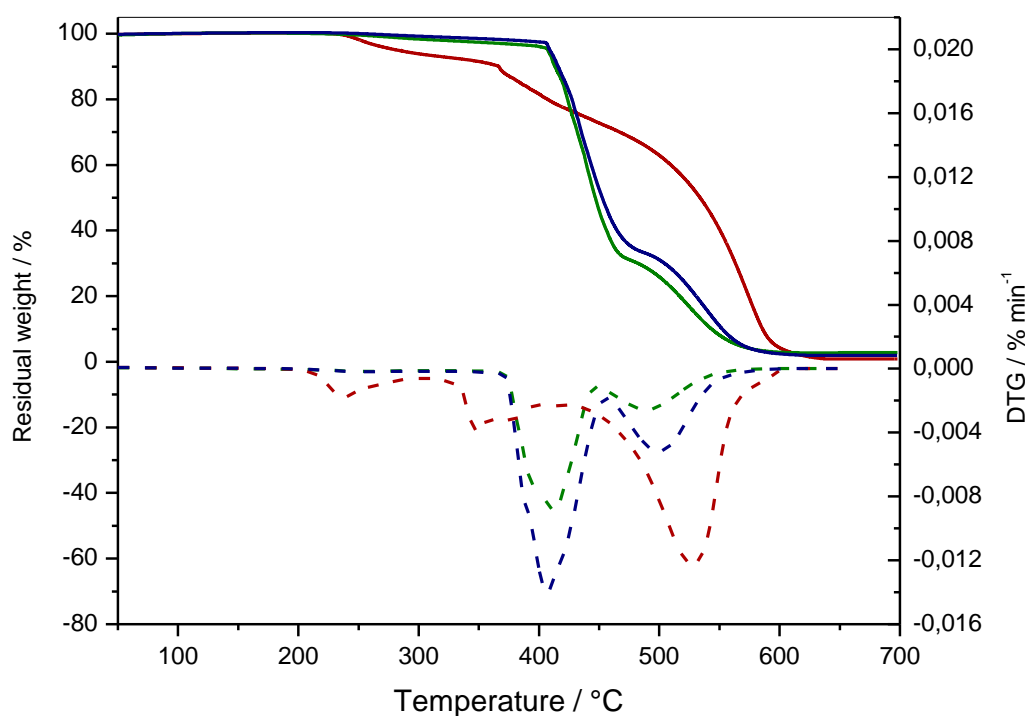


Figure 20. TGA thermograms under air atmosphere of poly(di-phenol) (red), poly(card-phenol) (blue), and poly(di-cardanol) (green) - Left axis: TG (solid lines) – Right axis: DTG (dash lines).

Poly(di-phenol) exhibited three main stages of mass loss. The degradation pathway of poly(di-phenol) was consistent with the study of Low *et al.* on the thermal degradation of various polybenzoxazine systems⁵⁶. The initial mass loss below 300 °C could be correlated to

the thermal cleavage of Mannich base. The temperature at 10 % of mass loss ($T_{10\%}$) of poly(card-phenol) and poly(di-cardanol) were respectively of 415 and 414 °C (**Table 7**). These $T_{10\%}$ values were shifted of about 50 °C to higher temperatures compared to poly(di-phenol) ($T_{10\%} = 366$ °C). Thus, introducing the cardanol chain led to a high increase in the thermal stability. In addition, the first mass loss which started at around 240 °C was extremely limited in the cardanol-based polymers (~1 % of mass loss), while it was not negligible for poly(di-phenol). If this step is neglected for cardanol-based polyBZ, it can be concluded that the first significant degradation step occurs at around 400 °C, instead of a first degradation step at around 240 °C for poly(di-phenol), *i.e.* about 150-160 °C higher. It would indicate that the first aliphatic amine formations through the Mannich base cleavage were shifted to much higher temperatures. Low *et al.*⁵⁶ have postulated that *inter* and *intra* hydrogen bonds played a major role in the Mannich base cleavage. The *intra* hydrogen bonding between the phenolic -OH group and the nitrogen of the Mannich base resulted in an energetically stable six membered ring. On the other hand, the authors have postulated that *inter* H-bonds were involved in the degradation at lower temperatures since in that case the structure was not stabilized which facilitated the C-N cleavage. Herein, the presence of the long alkyl chain from the cardanol backbone seemed likely to prevent the formation of *inter* H-bonds between the phenolic compounds. Then, as depicted in the abovementioned **Chart 1b**), *intra* H-bonds were preferentially formed in cardanol-based polyBZ. Accordingly, such stabilized six membered ring structure prevented the cleavage of the Mannich base compared to the poly(di-phenol) system where *inter* H-bonds were more possible. The small amount of mass loss below 240 °C observed on TG curves of poly(card-phenol) and poly(di-cardanol) (~1 % of mass loss) could be correlated to the decomposition of the unsaturated alkyl side chains of cardanol⁵⁷. Maximum rate of mass loss was obtained at 465 °C for poly(di-phenol), while the maximum of mass loss occurred at 400 °C for poly(di-cardanol) and poly(card-phenol). As shown in **Figure 20**, the decomposition was faster for the cardanol-based polyBZ than for poly(di-phenol) for which it occurred more progressively. This might indicate that different decomposition mechanism occurred between poly(di-phenol) and the cardanol moieties. All polyBZ had their decomposition finished after 600 °C.

These improvements of thermal stability when cardanol was used were assumed to be due to the alkyl side chains which protect the Mannich bridge. The aliphatic chains caused an increase of flexibility and a steric hindrance which delayed the decomposition of the Schiff base; however, it should be mentioned that no major differences were observed between the degradation pathway of poly(card-phenol) and poly(di-cardanol). It would suggest that one

single aliphatic side chain from one cardanol moieties would be sufficient to thermally stabilize the cross-linked structure through H-bonds reorganization. It is interesting to highlight how one amount of cardanol could increase the flexibility of the corresponding polymer but also brought such important thermal stability. Indeed, the $T_{10\%}$ obtained for cardanol-based polyBZ in this study was relatively close to the highest value obtained for coumarin-based polyBZ recently studied by Froimowicz *et al.*¹⁵ This strengthened the idea that natural renewable resources can lead to high performance thermosets.

Table 7. Thermogravimetric data for poly(di-phenol), poly(card-phenol), and poly(di-cardanol).

Sample	$T_{5\%}$ ^[a]	$T_{10\%}$ ^[b]	T_{\max} ^[c]
Poly(di-phenol)	282	366	465
Poly(card-phenol)	408	415	400
Poly(di-cardanol)	407	414	400

^[a] Temperature of 5 % of mass loss; ^[b] Temperature of 10 % of mass loss; ^[c] Temperature of maximum of degradation.

IV. Conclusions

Three systems of benzoxazine monomers were synthesized in order to study the influence of the introduction of a C₁₅ aliphatic side chain on thermal and mechanical properties. Rheological analyses showed that the presence of the alkyl side chain delayed gelation and vitrification, and it was observed that the polymerization was not stopped by these processes. We assumed that the high degree of H-bonding during the formation of the polymer from the di-phenol BZ was responsible for the early vitrification. On the contrary, the hindering role of cardanol delayed the vitrification process by limiting the H-bonding extent during the polymerization process. A rearrangement of the H-bonds network was confirmed by FT-IR measurements. DMA results indicated a high cross-link density for the polymerized di-phenol which was, in this study, the material with the highest glass transition temperature (T_g) and with a very low polydispersity as shown through the sharp peak obtained for the damping factor curve ($\tan \delta$). The cross-linked polymer with two cardanols (poly(di-cardanol)) showed a higher polydispersity and a more significant β -transition which indicated a lower cross-link density of the network. The cross-linked polymer with one cardanol unit (poly(card-phenol)) exhibited intermediate thermo-mechanical properties, in adequation with its intermediate chemical structure. Thermogravimetric analyses indicated that the presence of cardanol greatly improved the thermal stability of the polymers by delaying the decomposition of about 150 °C, assumed to be correlated to the lower *inter* H-bonding when cardanol was used.

V. References

- (1) Lligadas, G.; Tüzün, A.; Ronda, J. C.; Galià, M.; Cádiz, V. Polybenzoxazines: New Players in the Bio-Based Polymer Arena. *Polym. Chem.* **2014**, *5* (23), 6636–6644.
- (2) Rao, B. S.; Palanisamy, A. Synthesis of Bio Based Low Temperature Curable Liquid Epoxy, Benzoxazine Monomer System from Cardanol: Thermal and Viscoelastic Properties. *Eur. Polym. J.* **2013**, *49* (8), 2365–2376.
- (3) Liu, Y.-L.; Chou, C.-I. High Performance Benzoxazine Monomers and Polymers Containing Furan Groups. *J. Polym. Sci. Part A Polym. Chem.* **2005**, *43* (21), 5267–5282.
- (4) Wang, C.; Sun, J.; Liu, X.; Sudo, A.; Endo, T. Synthesis and Copolymerization of Fully Bio-Based Benzoxazines from Guaiacol, Furfurylamine and Stearylamine. *Green Chem.* **2012**, *14* (10), 2799.
- (5) Wang, C.; Zhao, C.; Sun, J.; Huang, S.; Liu, X.; Endo, T. Synthesis and Thermal Properties of a Bio-Based Polybenzoxazine with Curing Promoter. *J. Polym. Sci. Part A Polym. Chem.* **2013**, *51* (9), 2016–2023.
- (6) Van, A.; Chiou, K.; Ishida, H. Use of Renewable Resource Vanillin for the Preparation of Benzoxazine Resin and Reactive Monomeric Surfactant Containing Oxazine Ring. *Polymer (Guildf)*. **2014**, *55* (6), 1443–1451.
- (7) Dumas, L.; Bonnaud, L.; Olivier, M.; Poorteman, M.; Dubois, P. Arbutin-Based Benzoxazine: En Route to an Intrinsic Water Soluble Biobased Resin. *Green Chem.* **2016**, *18* (18), 4954–4960.
- (8) Dumas, L.; Bonnaud, L.; Olivier, M.; Poorteman, M.; Dubois, P. Bio-Based High Performance Thermosets: Stabilization and Reinforcement of Eugenol-Based Benzoxazine Networks with BMI and CNT. *Eur. Polym. J.* **2015**, *67*, 494–502.
- (9) Dumas, L.; Bonnaud, L.; Olivier, M.; Poorteman, M.; Dubois, P. High Performance Bio-Based Benzoxazine Networks from Resorcinol and Hydroquinone. *Eur. Polym. J.* **2016**, *75*, 486–494.
- (10) Trejo-Machin, A.; Verge, P.; Puchot, L.; Quintana, R. Phloretic Acid as an Alternative to the Phenolation of Aliphatic Hydroxyls for the Elaboration of Polybenzoxazine. *Green Chem.* **2017**, *19* (21), 5065–5073.

- (11) Thirukumar, P.; Shakila, A.; Muthusamy, S. Synthesis and Characterization of Novel Bio-Based Benzoxazines from Eugenol. *RSC Adv.* **2014**, *4* (16), 7959.
- (12) Fache, M.; Darroman, E.; Besse, V.; Auvergne, R.; Caillol, S.; Boutevin, B. Vanillin, a Promising Biobased Building-Block for Monomer Synthesis. *Green Chem.* **2014**, *16* (4), 1987–1998.
- (13) Xu, H.; Lu, Z.; Zhang, G. Synthesis and Properties of Thermosetting Resin Based on Urushiol. *RSC Adv.* **2012**, *2* (7), 2768.
- (14) Xu, H.; Zhang, W.; Lu, Z.; Zhang, G. Hybrid Polybenzoxazine with Tunable Properties. *RSC Adv.* **2013**, *3* (11), 3677.
- (15) Froimowicz, P.; R. Arza, C.; Han, L.; Ishida, H. Smart, Sustainable, and Ecofriendly Chemical Design of Fully Bio-Based Thermally Stable Thermosets Based on Benzoxazine Chemistry. *ChemSusChem* **2016**, *9* (15), 1921–1928.
- (16) Gedam, P. H.; Sampathkumar, P. S. Cashew Nut Shell Liquid: Extraction, Chemistry and Applications. *Prog. Org. Coatings* **1986**, *14* (2), 115–157.
- (17) Calò, E.; Maffezzoli, A.; Mele, G.; Martina, F.; Mazzetto, S. E.; Tarzia, A.; Stifani, C. Synthesis of a Novel Cardanol-Based Benzoxazine Monomer and Environmentally Sustainable Production of Polymers and Bio-Composites. *Green Chem.* **2007**, *9* (7), 754.
- (18) Ghosh, N. N.; Kiskan, B.; Yagci, Y. Polybenzoxazines—New High Performance Thermosetting Resins: Synthesis and Properties. *Prog. Polym. Sci.* **2007**, *32* (11), 1344–1391.
- (19) Sharma, P.; Lochab, B.; Kumar, D.; Roy, P. K. Interfacial Encapsulation of Bio-Based Benzoxazines in Epoxy Shells for Temperature Triggered Healing. *J. Appl. Polym. Sci.* **2015**, *132* (47), n/a-n/a.
- (20) Li, X.; Luo, X.; Gu, Y. A Novel Benzoxazine/Cyanate Ester Blend with Sea-Island Phase Structures. *Phys. Chem. Chem. Phys.* **2015**, *17* (29), 19255–19260.
- (21) Sethuraman, K.; Alagar, M. Thermo-Mechanical and Dielectric Properties of Graphene Reinforced Caprolactam Cardanol Based Benzoxazine–epoxy Nanocomposites. *RSC Adv.* **2015**, *5* (13), 9607–9617.

- (22) Quirino, R. L.; Garrison, T. F.; Kessler, M. R. Matrices from Vegetable Oils, Cashew Nut Shell Liquid, and Other Relevant Systems for Biocomposite Applications. *Green Chem.* **2014**, *16* (4), 1700–1715.
- (23) Selvaraj, V.; Jayanthi, K. P.; Lakshmikandhan, T.; Alagar, M. Development of a Polybenzoxazine/TSBA-15 Composite from the Renewable Resource Cardanol for Low-k Applications. *RSC Adv.* **2015**, *5* (60), 48898–48907.
- (24) Shukla, S.; Lochab, B. Role of Higher Aromatic Content in Modulating Properties of Cardanol Based Benzoxazines. *Polymer* **2016**, *99*, 684–694.
- (25) Li, S.; Zou, T.; Feng, L.; Liu, X.; Tao, M. Preparation and Properties of Cardanol-Based Polybenzoxazine/SiO₂ Hybrids by Sol-Gel Technique. *J. Appl. Polym. Sci.* **2013**, *128* (6), 4164–4171.
- (26) Lochab, B.; Varma, I. K.; Bijwe, J. Cardanol-Based Bisbenzoxazines. *J. Therm. Anal. Calorim.* **2012**, *107* (2), 661–668.
- (27) Oie, H.; Sudo, A.; Endo, T. Synthesis of Networked Polymers by Crosslinking Reactions of Polybenzoxazine Bearing Allyl Group in the Side Chain. *J. Polym. Sci. Part A Polym. Chem.* **2013**, *51* (9), 2035–2039.
- (28) Zhang, C.; Zhang, Y.; Zhou, Q.; Ling, H.; Gu, Y. Processability and Mechanical Properties of Bisbenzoxazine Modified by the Cardanol-Based Aromatic Diamine Benzoxazine. *J. Polym. Eng.* **2014**, *34* (6), 561–568.
- (29) Ambrožič, R.; Šebenik, U.; Krajnc, M. Synthesis, Curing Kinetics, Thermal and Mechanical Behavior of Novel Cardanol-Based Benzoxazines. *Polymer* **2015**, *76*, 203–212.
- (30) Kiratitanavit, W.; Ravichandran, S.; Xia, Z.; Kumar, J.; Nagarajan, R. Thermally Stable Polymers of Cardanol as Char-Forming Additives for Polypropylene. *J. Renew. Mater.* **2013**, *1* (4), 289–301.
- (31) CashewInfo.com http://www.cashewinfo.com/geographical_distribution.html.
- (32) Lomonaco, D.; Mele, G.; Mazzetto, S. E. Cashew Nutshell Liquid (CNSL): From an Agro-Industrial Waste to a Sustainable Alternative to Petrochemical Resources. In *Cashew Nut Shell Liquid*; Springer International Publishing: Cham, **2017**; 19–38.

- (33) Guo, Y.-C.; Mele, G.; Martina, F.; Margapoti, E.; Vasapollo, G.; Xiao, W.-J. An Efficient Route to Biscardanol Derivatives and Cardanol-Based Porphyrins via Olefin Metathesis. *J. Organomet. Chem.* **2006**, *691* (24–25), 5383–5390.
- (34) Hoang, A. S.; Tran, T. H.; Nguyen, H. N.; Vu, H. S.; Vo, T. P.; Phan, C.; Nguyen, T. V. Synthesis of Oxime from a Renewable Resource for Metal Extraction. *Korean J. Chem. Eng.* **2015**, *32* (8), 1598–1605.
- (35) Horváth, I. T.; Anastas, P. T. Innovations and Green Chemistry. *Chem. Rev.* **2007**, *107* (6), 2169–2173.
- (36) Lopes, A. A. S.; Carneiro, E. A.; Rios, M. A. S.; Hiluy Filho, J. J.; Carioca, J. O. B.; Barros, G. G.; Mazzetto, S. E. Study of Antioxidant Property of a Thiosphorated Compound Derived from Cashew Nut Shell Liquid in Hydrogenated Naphthenics Oils. *Brazilian J. Chem. Eng.* **2008**, *25* (1), 119–127.
- (37) Balasubramanian, B.; Sherfudeen, K. M.; Kaliannan, S. K.; Murugesan, K. Cashew Nut Shell Liquid Poisoning. *Indian J. Crit. Care Med.* **2016**, *20* (1), 57–58.
- (38) Greco, A.; Brunetti, D.; Renna, G.; Mele, G.; Maffezzoli, A. Plasticizer for Poly(Vinyl Chloride) from Cardanol as a Renewable Resource Material. *Polym. Degrad. Stab.* **2010**, *95* (11), 2169–2174.
- (39) Thibeault, D.; Rouillard, F.; Carrier, S.; Vuillaume, P. Preparation of Methacrylated Cardanol Glycidyl Ether Derivatives as Monomers for Polymer Compositions. *Oilseeds fats Crop. Lipids* **2016**, *23* (5).
- (40) Kanehashi, S.; Yokoyama, K.; Masuda, R.; Kidesaki, T.; Nagai, K.; Miyakoshi, T. Preparation and Characterization of Cardanol-Based Epoxy Resin for Coating at Room Temperature Curing. *J. Appl. Polym. Sci.* **2013**, *130* (4), 2468–2478.
- (41) Van Schalkwyk, J. D.; Marais, J. L. C.; Neuse, E. W. Epoxidation of Cardanol with Peroxycarboximidic Acids. *Indian J. Chem. Sect. B, Org. Incl. Med. Chem.* **1976**, *14B* (12), 955–960.
- (42) Tyman, J. H. P. Long-Chain Phenols : IV. Quantitative Determination of the Olefinic Composition of the Component Phenols in Cashew Nut-Shell Liquid. *J. Chromatogr. A* **1975**, *111* (2), 277–284.
- (43) Suresh, K. I.; Kishanprasad, V. S. Synthesis, Structure, and Properties of Novel Polyols

- from Cardanol and Developed Polyurethanes. *Ind. Eng. Chem. Res.* **2005**, *44*(13), 4504–4512.
- (44) Puchot, L.; Verge, P.; Fouquet, T.; Vancaeyzeele, C.; Vidal, F.; Habibi, Y. Breaking the Symmetry of Dibenzoxazines: A Paradigm to Tailor the Design of Bio-Based Thermosets. *Green Chem.* **2016**, *18* (11), 3346–3353.
- (45) Guo, Z.-Q.; Fang, D.-M.; Wang, J.-H.; Zhang, G.-L.; Wu, Z.-J. $[M-H]^+$ Ions in 3-Alkyl Substituted Indoles Detected by Electrospray Mass Spectrometry. *Int. J. Mass Spectrom.* **2014**, *361*, 54–58.
- (46) Sioud, S.; Kharbatia, N.; Amad, M. H.; Zhu, Z.; Cabanetos, C.; Lesimple, A.; Beaujuge, P. The Formation of $[M-H]^+$ Ions in *N*-Alkyl-Substituted Thieno[3,4-*c*]Pyrrole-4,6-Dione Derivatives during Atmospheric Pressure Photoionization Mass Spectrometry. *Rapid Commun. Mass Spectrom.* **2014**, *28* (22), 2389–2397.
- (47) Puchot, L. Cardanol : A Bio-Based Building Block for New Sustainable and Functional Materials, Cergy-Pontoise, 2016.
- (48) Ishida, H.; Rodriguez, Y. Curing Kinetics of a New Benzoxazine-Based Phenolic Resin by Differential Scanning Calorimetry. *Polymer* **1995**, *36* (16), 3151–3158.
- (49) Ma, H.-X.; Xu, Z.-B.; Qiu, J.-J.; Liu, C.-M. Synthesis of Artificial Urushi via Ring-Opening Reaction of Benzoxazine with Renewable Cardanol. *Polymer* **2017**, *132*, 41–50.
- (50) Ishida, H.; Allen, D. J. Gelation Behavior of Near-Zero Shrinkage Polybenzoxazines. *J. Appl. Polym. Sci.* **2001**, *79* (3), 406–417.
- (51) Sbirrazzuoli, N.; Vyazovkin, S.; Mititelu, A.; Sladic, C.; Vincent, L. A Study of Epoxy-Amine Cure Kinetics by Combining Isoconversional Analysis with Temperature Modulated DSC and Dynamic Rheometry. *Macromol. Chem. Phys.* **2003**, *204* (15), 1815–1821.
- (52) Vyazovkin, S.; Sbirrazzuoli, N. Mechanism and Kinetics of Epoxy–Amine Cure Studied by Differential Scanning Calorimetry. *Macromolecules* **1996**.
- (53) Ishida, H.; Allen, D. J. Physical and Mechanical Characterization of Near-Zero Shrinkage Polybenzoxazines. *J. Polym. Sci. Part B Polym. Phys.* **1996**, *34* (6), 1019–1030.

- (54) Allen, D. J.; Hishida, H. Polymerization of Linear Aliphatic Diamine-Based Benzoxazine Resins under Inert and Oxidative Environments. *Polymer* **2007**, *48* (23), 6763–6772.
- (55) Ning, X.; Ishida, H. Phenolic Materials via Ring-Opening Polymerization: Synthesis and Characterization of Bisphenol-A Based Benzoxazines and Their Polymers. *J. Polym. Sci. Part A Polym. Chem.* **1994**, *32* (6), 1121–1129.
- (56) Low, H. Y.; Ishida, H. Mechanistic Study on the Thermal Decomposition of Polybenzoxazines: Effects of Aliphatic Amines. *J. Polym. Sci. Part B Polym. Phys.* **1998**, *36* (11), 1935–1946.
- (57) Yagci, Y.; Kiskan, B.; Ghosh, N. N. Recent Advancement on Polybenzoxazine-A Newly Developed High Performance Thermoset. *J. Polym. Sci. Part A Polym. Chem.* **2009**, *47* (21), 5565–5576.

VI. Supplementary Information

Synthesis and characterization of di-ptdp BZ monomer

Di-functional BZ monomer from pentadecylphenol (ptdp) was synthesized following the same protocol as symmetric di-phenol and di-cardanol monomers.

Pentadecylphenol (5g, 0.016 mol), paraformaldehyde (1.06g, 0.032 mol), and EDA (0.498g, 8.3 mmol) were reacted at reflux of chloroform and under magnetic stirring for 48 h. After complete reaction, the monomer was purified by NaOH treatment follow by column chromatography.

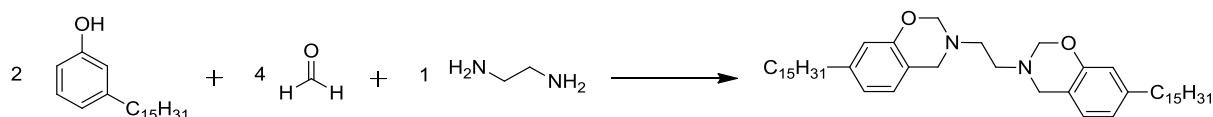


Figure S121. Synthesis reaction of di-ptdp BZ monomer.

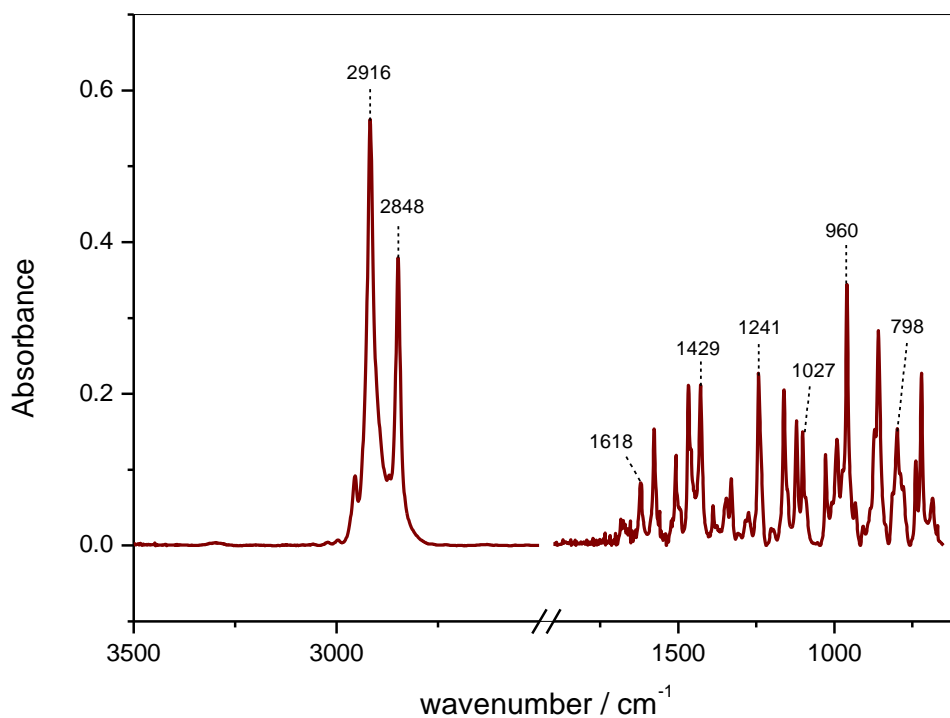
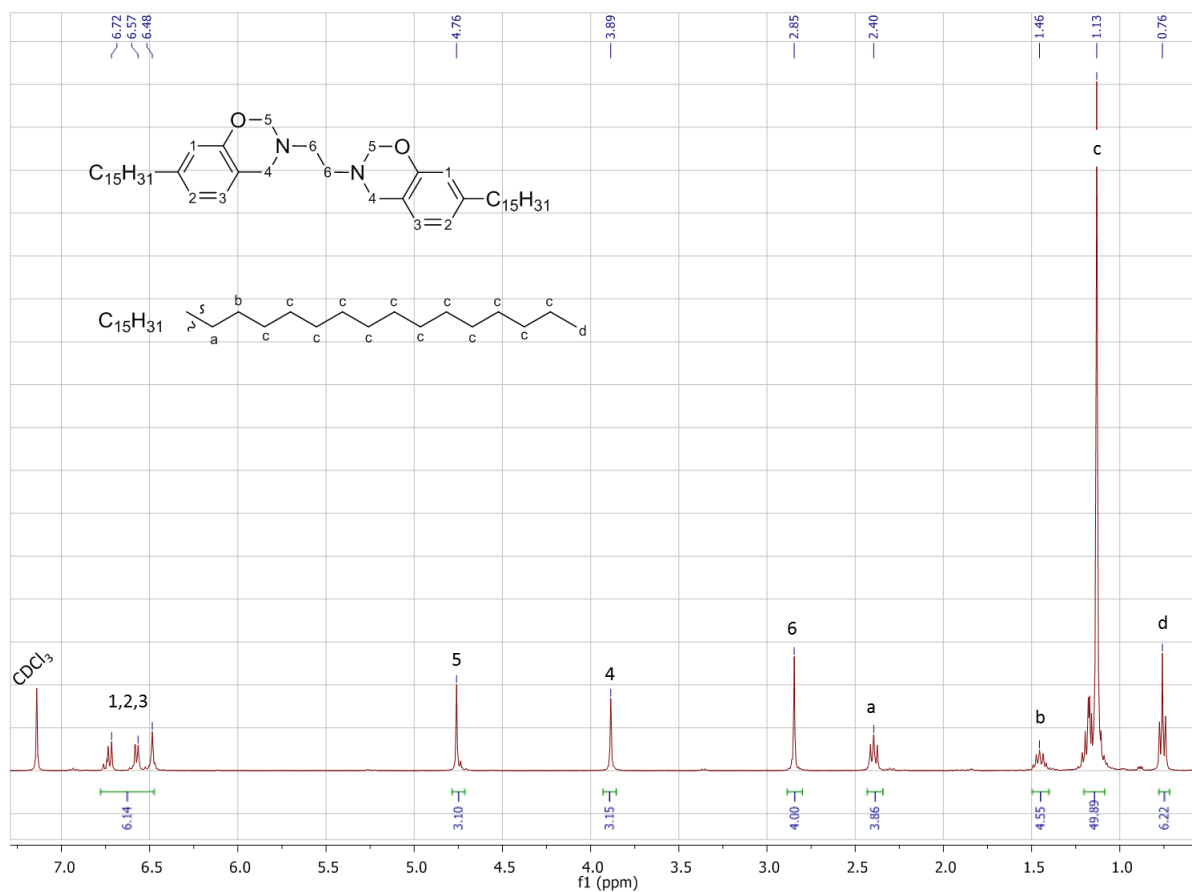


Figure S2. FTIR characterization of di-ptdp BZ monomer.



FigureS3. ¹H NMR characterization of di-ptdp BZ monomer.

Chapter III

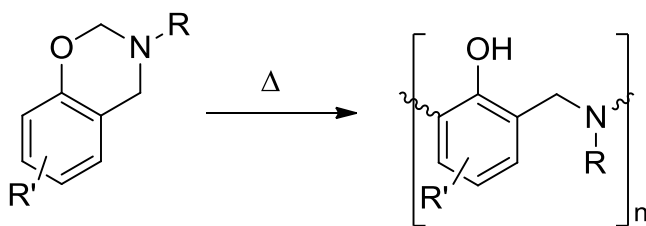
Physico-chemical aspect of phenol- based benzoxazine polymerization

I. Introduction	111
II. Thermo-kinetic Analysis	113
II.1. Extent of conversion and apparent activation energy	113
II.2. Isoconversional methods: Principle and Advanced kinetic methods	114
II.3. Advanced isoconversional analysis	115
III. Results and discussion	116
III.1. Non-isothermal kinetic analysis of di-phenol benzoxazine polymerization reaction	116
III.2. Apparent activation energy	117
III.3. Thermal and thermomechanical analyses and kinetic studies	120
III.4. Chemorheological analysis and kinetic study	121
III.5. Evolution of glass transition temperature (T_g) over curing	122
IV. Isothermal analysis	124
IV.1. DSC measurements	124
IV.2. Isoconversional analysis in isothermal mode of di-phenol BZ	125
V. Conclusion	127
VI. References	128

I. Introduction

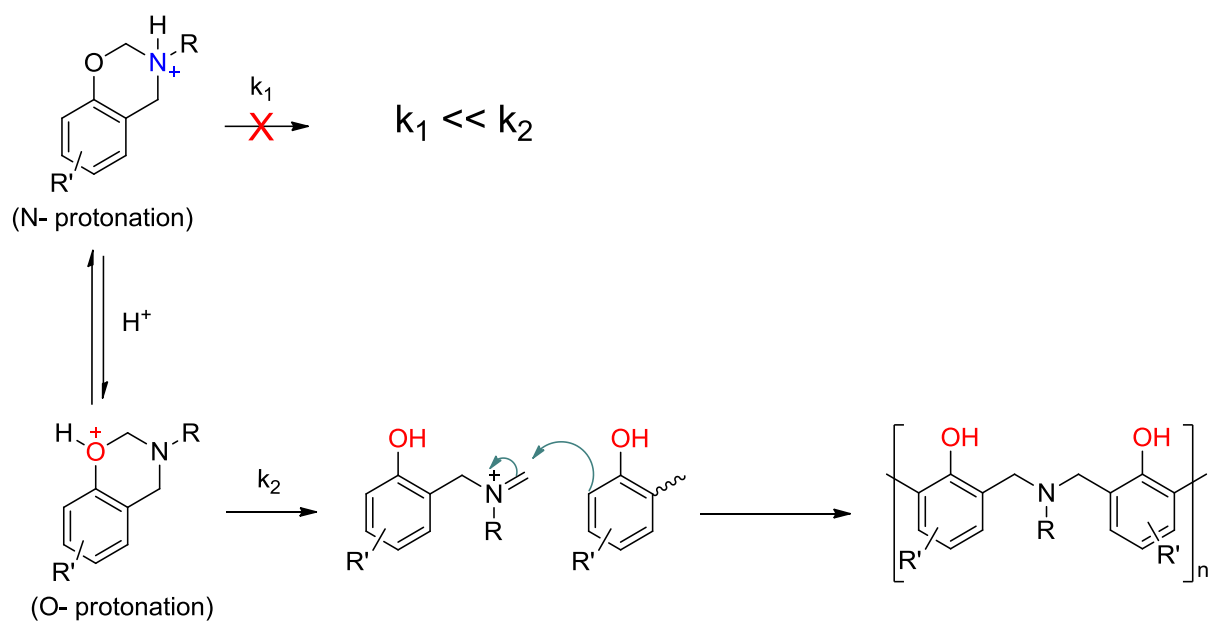
Usually, the nature of the polymerization reactions of a thermosetting polymer are very complex as many reactive processes may occur simultaneously. Thus, the understanding of polymerization kinetics allows a better knowledge of the process development and an improvement in the quality of the final products regarding the structures of the polymer networks^{1,2}. Among different techniques used to determine the kinetics of thermoset cure, differential scanning calorimetry is the most used to determine the kinetic parameters and the corresponding rate equation³⁻⁶.

Polymerization of benzoxazine resins is thermally induced ring-opening reaction to form a phenolic structure characterized by a Mannich base bridge ($-\text{CH}_2-\text{NR}-\text{CH}_2-$) instead of the methylene bridge of traditional phenolic resins^{7,8} (**Scheme 1**).



Scheme 1. Benzoxazine ring-opening polymerization (ROP) with the formation of Mannich base bridge

This ring-opening polymerization (ROP) leads to the formation of a reactive amine that can crosslink preferentially to the *ortho* positions⁹ of another phenolic compound. In a previous study, Chutayothin *et al.* tried to understand cationic ROP mechanism¹⁰. Authors confirmed the preferential attack on *ortho* position. Moreover, as presented in **Scheme 2**, initiation mechanism can occur either *via* protonation of nitrogen atom or oxygen atom; however, only the final product from oxygen atom protonation was observed, as the nitrogen protonation specie is much more stable than the oxygen protonation specie.



Scheme 2. Proposed mechanism of benzoxazine initiation polymerization mechanism¹⁰

The current chapter section is dedicated to the kinetic analysis of the polymerization mechanism and the study of the apparent activation energy and its evolution upon curing, for di-phenol BZ monomer.

II. Thermo-kinetic Analysis

The advanced isoconversional method proposed in this thesis work allows to calculate the apparent activation energy E_a , based on thermoanalytical data, for each extent of conversion α in a model “free” way.

II.1. Extent of conversion and apparent activation energy

When a physico-chemical transition or a chemical reaction occurs under the effect of temperature, the extent of conversion at time t_i , α_i , is defined as the ratio between the heat ΔH_i exchanged at time i and the total heat ΔH_{tot} released during the transition or reaction.

Equation 1

$$\alpha_i = \frac{\Delta H_i}{\Delta H_{\text{tot}}} = \frac{\int_{t_1}^{t_i} (dH/dt)_i dt}{\int_{t_1}^{t_2} (dH/dt)_i dt}$$

In this equation, α_i represents the extent of conversion at time i , $(dH/dt)_i$ represents the heat flow measured at time t_i , t_1 and t_2 are respectively associated to the first and second integration bounds of the thermal event. Thus, the heat flow rate is a function of time (dH/dt) and proportional to the total heat (ΔH_{tot}) exchanged and to the reaction rate $(d\alpha/dt)$:

Equation 2

$$\frac{dH}{dt} = \Delta H_{\text{tot}} \frac{d\alpha}{dt} = \Delta H_{\text{tot}} k(T) f(\alpha)$$

Where $k(T)$ is the rate constant, T the temperature, and $f(\alpha)$ the mathematical function associated to the reaction mechanism. The relation between the temperature and the rate constant is given by Arrhenius equation:

Equation 3

$$k(T) = A e^{-E/RT}$$

Thus, **Equation 2** can be re-written as follow¹¹:

Equation 4

$$\frac{d\alpha}{dt} = A e^{-E/RT} f(\alpha)$$

Where A is the pre-exponential factor, E the activation energy, and R the molar gas constant. For non-isothermal measurements, the dependency in time should be substituted by the temperature, considering the constant heating rate β imposed to the sample:

Equation 5

$$\frac{d\alpha}{dT} = \frac{A}{\beta} e^{-E/RT} f(\alpha)$$

Where $\beta = dT/dt$ is the heating rate.

II.2. Isoconversional methods: Principle and Advanced kinetic methods

Isoconversional methods are amongst the more reliable kinetic methods for the treatment of thermoanalytical data¹²⁻¹⁴. Several methods have been developed to calculate an apparent activation energy E_α . Several isoconversional methods are commonly used such as Friedman¹⁵, Ozawa¹⁶, and Flynn and Wall¹⁷. These methods which need experiments at several temperature program have the advantage to give a value of E_α without taking into account the mathematic function of reaction $f(\alpha)$ (*i.e.* with no assumption on the reaction mechanism involved during the reaction). Thus, the activation energy calculated does not depend on the choice of the kinetic model; moreover, each change in the activation energy can be associated to a change in the mechanism reaction, or a modification of the rate limiting step of the global reaction. For example, the calculated activation energy (E_α) is a global energy which can include several chemical reactions and/or physical transitions. Because of the complexity of the studied transitions, it is interesting to use these methods in this work because most of the reaction mechanisms are not well known.

The isoconversional principle postulates that for a given extent of conversion α , the reaction rate is only function of temperature¹⁸:

Equation 6

$$\frac{d \ln(d\alpha/dt)}{dT^{-1}} = -\frac{E_\alpha}{R}$$

By using the logarithmic function of **Equation 5**, the Friedman method allows to calculate E_α for any extent of conversion:

Equation 7

$$\ln\left(\frac{d\alpha}{dt}\right)_{\alpha,i} = \ln[A_\alpha f(\alpha)] - \frac{E_\alpha}{RT}$$

Where i is the index of the experiment performed for a heating or cooling rate β . For a constant extent of conversion α , the term $\ln[A_\alpha f(\alpha)]$ is constant, because E_α is determined for any α without offering a reaction mechanism hypothesis (*i.e.* $f(\alpha)$).

Despite the efficiency of isoconversional methods for the study of complex mechanisms, these methods present diverse issues such as sensibility to noise, or approximation for equation

solving¹⁹. To overcome these drawbacks, Sbirrazzuoli and Vyazovkin developed a new method based on numerical integration: advanced isoconversional methods^{11,12,20–23}.

II.3. Advanced isoconversional analysis

These methods are applicable for n experiments realized with either isothermal or non-isothermal program $T_i(t)$. For each α value, E_α is determined as the energy value which minimizes the following function:

Equation 8

$$\Phi(E_\alpha) = \sum_{i=1}^n \sum_{j \neq 1}^n \frac{J[E_\alpha, T_i(t_\alpha)]}{J[E_\alpha, T_j(t_\alpha)]}$$

with:

Equation 9

$$J[E_\alpha, T_i(t_\alpha)] \equiv \int_{t_{\alpha-\Delta\alpha}}^{t_\alpha} e^{\left[-\frac{E_\alpha}{RT_i(t)}\right]} dt$$

This method is applicable regardless of the temperature program $T_i(t)$ and uses a numerical integration in function of time. E_α is calculated for each value of α lying in between 0.02 to 0.98 with a step of 0.02. An accurate interpolation of the integrated α - T curves was performed to find the time $t_{\alpha,i}$ and temperature $T_{\alpha,i}$ that correspond to a given α for the i temperature program used^{19,20}. The value of J function described above is calculated by trapezoidal rule. For each value of α , the minimization of $\Phi(E_\alpha)$ is re-evaluated, thus the activation energy dependency is determined on all the conversion process^{11,24,25}.

The apparent activation energy calculated by this model “free” isoconversional method can characterize both chemical reactions and physical transitions such as curing, thermal degradation, vitrification, or glass transition for example. This powerful method is also particularly interesting to describe multi-step processes such as cross-linking polymerization or highlighting the preponderant physico-chemical process at a defined extent of conversion. The final objective is to be able to associate the apparent activation energy variation to a change on the rate limiting step during the polymerization. Because of the intrinsic complexity of the polymeric transformation from liquid to solid state which induces a high increase of viscosity, classical chromatography techniques are unfortunately most often not suitable to evaluate polymerization process^{18,26–28}.

Isoconversional methods can be applied to all type of data originated from thermal analyses such as DSC, TGA, DMA, or Rheometry. The use of these techniques is currently the most appropriate. Specialized software was developed to treat any kind of thermo-analytical data^{72-74,83}. The extent of conversion α can be calculated as a function of time t or temperature T , and the resulting apparent activation energy E_α as a function of α or T . In that last case, each value of E_α is associated to an average temperature value computed over the i temperatures that correspond to each α value used for the calculation. For the computations, 3 to 5 temperatures (isothermal mode) or heating/cooling rates (non-isothermal mode) are generally used¹³. Thus, to a given α corresponds an average temperature \bar{T}_α making possible the interpretation of the activation energy dependency with temperature $E_\alpha = f(\bar{T}_\alpha)$.

III. Results and discussion

III.1. Non-isothermal kinetic analysis of di-phenol benzoxazine polymerization reaction

Computations were performed with di-phenol BZ monomer, synthesized as described in the previous chapter. Different heating rates were used for computation: 0.5, 1, 2, 4, and 10 K.min⁻¹ under air atmosphere. As depicted in **Figure 1**, the exothermic phenomena and extent of conversion α were shifted to higher temperatures when increasing the heating rate. This reflects the temperature dependency of the reaction rate.

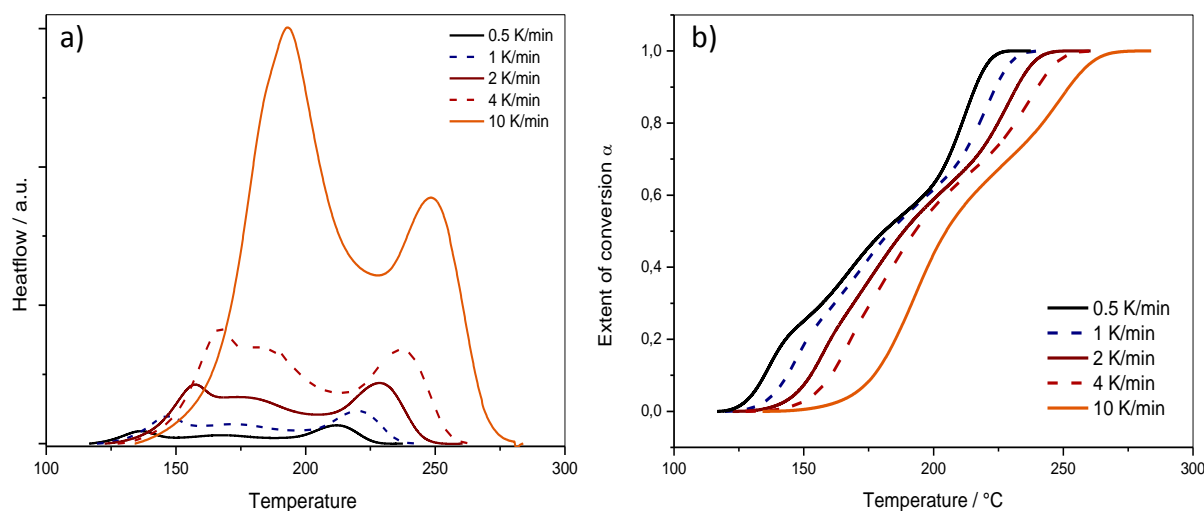


Figure 1. a) Exothermic phenomena from DSC thermograms of di-phenol BZ at 0.5, 1, 2, 4, and 10 K.min⁻¹; b) Related extent of conversion in function of temperature.

As the evolution of the extent of conversion in function of temperature was shifted to higher temperatures when increasing the heating rate, the curves should not cross as it may causes errors in computation results. As mentioned in the previous chapter, the overall enthalpy of polymerization for di-phenol BZ monomer considers the entire exotherm signal. **Figure 1a)** shows the exotherm signal at the different selected heating rates, according to the integration limits used for computations. It is noticed that the enthalpy was progressively increased with the heating rate, from 32.5 kJ.mol⁻¹ at 0.5 K.min⁻¹ to 43.5 kJ.mol⁻¹ at 10 K.min⁻¹ (**Table 1**).

Table 1. Evolution of overall enthalpy of polymerization with the heating rate.

Heating rate	0.5 K/min	1 K/min	2 K/min	4 K/min	10 K/min
Enthalpy (KJ.mol ⁻¹)	32.5	35.2	37.0	39.4	43.5

III.2. Apparent activation energy

Figure 2 relates the complexity of the reaction mechanism through the evolution of activation energy E_a . Computations were performed using three, four, or five heating rates comprised between 0.5 and 10 K.min⁻¹.

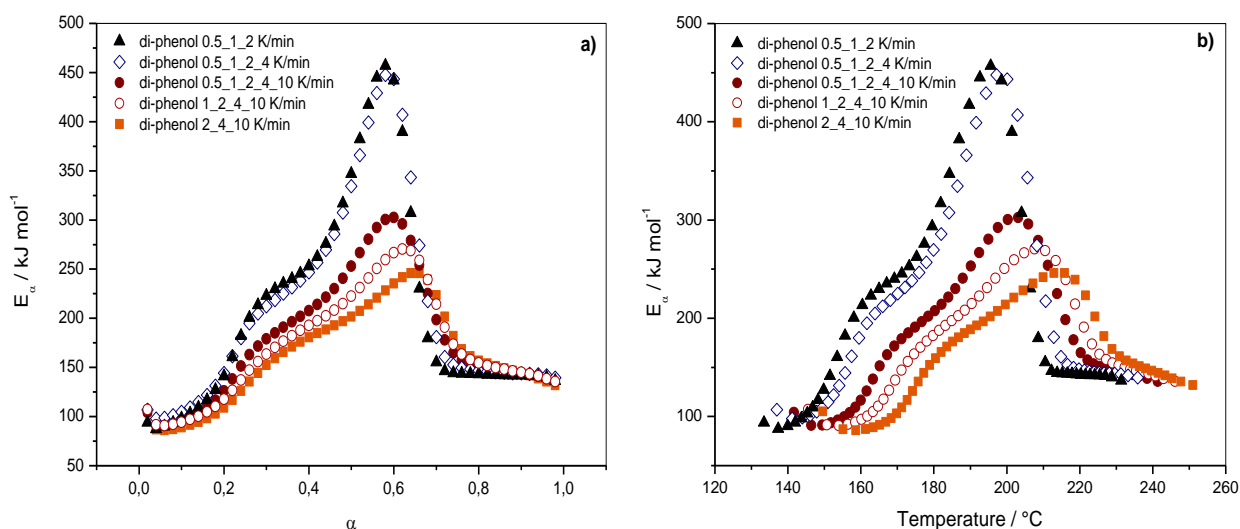


Figure 2. Apparent activation energy computed using different heating rates between 0.5 $\text{K}\cdot\text{min}^{-1}$ and 10 $\text{K}\cdot\text{min}^{-1}$ **a)** in function of extent of conversion α ; **b)** in function of temperature.

It is first noticed that E_α showed a similar trend for each computation, whether with slow heating rates, fast heating rates, or both. If each modification of the slope in the E_α -dependencies correspond to a reaction step, it can first be assumed that the mechanism of polymerization consists of 5 different steps. However, until an extent of conversion of 0.4, the shoulder inducing a slope modification might also be correlated to a modification in the reaction rate. Indeed, the first step of the reaction mechanism starting around 90 $\text{kJ}\cdot\text{mol}^{-1}$ could be an autocatalytic ring opening reaction which usually achieves a maximum rate in the range of $0.2 < \alpha < 0.4$. Such energy is in adequation with epoxy/amine systems, which also start with a ring-opening reaction³⁰. In this case, the maximum seemed to be obtained at around 30 % of conversion. Then, the second step occurred at $0.4 < \alpha < 0.6$ for computation using the lowest heating rates, and at $0.48 < \alpha < 0.66$ using the highest heating rates. This step might correspond to the electrophilic aromatic substitution reaction step. The next step between $0.6 < \alpha < 0.75$ for the lowest heating rates and $0.66 < \alpha < 0.78$ for the highest, might be correlated to the rearrangement step proposed in the improved mechanism suggested by Liu *et al.*³¹ During the final step, E_α appeared constant at approximately 140 $\text{kJ}\cdot\text{mol}^{-1}$. This high value might correspond to the termination of the chemical reactions in the solid state and/or to the beginning of the thermal degradation. This last point will be clarified in the following section in the light of TGA and DMA analyses.

Even though the E_{α} -dependencies presented a similar trend regardless of the selected heating rates, a drastic difference in the E_{α} values was observed. With a focus on the same trend in function of temperature (**Figure 2b**), the first autocatalytic step showed its maximum at $\alpha \sim 0.3$ for each computation, which could be correlated to different energies and different temperatures depending on the selected heating rates. Using the lowest heating rates (0.5, 1, 2 K.min⁻¹), the maximum of the autocatalytic step reached an activation energy of 223 kJ.mol⁻¹ at 162 °C. Then, by including higher heating rates, the maximum was progressively shifted to higher temperatures and lower values of activation energy, until 165 kJ.mol⁻¹ at 182 °C. The second maximum of the activation energy was obtained at 60 – 66 % of conversion. As for the previous maximum, the second peak was shifted to higher temperatures (from 195 to 215 °C) and lower energy values (from 456 to 246 kJ.mol⁻¹) when performing computation with faster heating rates. Data are summarized in **Table 2**. As mentioned in the previous chapter, polymerization reaction presented a temperature dependency and all reaction phenomena were shifted to higher temperatures when increasing the heating rate, explaining the temperature modification of the peak maxima. In addition, it was observed a clear diminution of the activation energies when considering higher heating rates for computation. At low heating rates, reactions may occur properly and can take more time to complete. Thus, at very low heating rate, some reaction step may require more energy to reach completion. On the opposite, with faster heating rate, reactions were accelerated, and as high temperatures were reached faster, lower activation energies were correlated with the steps modifications. It can also be postulated that at low heating rates some reactions with high activation energy have enough time to occur, while at higher heating rates the reactions with the lower activation energy occurred first. Due to the temperature increase, the system considered the next reactions with lower activation energies which occurred at higher temperatures. This would indicate that the pre-exponential factor should be higher in this case, which would correspond to higher steric constraints.

Table 2. Kinetic data of peak maxima in relation to the heating rates used for computation.

Heating rates (K/min)	0.5/1/2	0.5/1/2/4	0.5/1/2/4/10	1/2/4/10	2/4/10
$T_{\max 1}$ (°C)	162	163	173	175	182
$E_{\alpha \max 1}$ (kJ.mol ⁻¹)	223	205	185	170	165
$T_{\max 2}$ (°C)	195	197	203	207	215
$E_{\alpha \max 2}$ (kJ.mol ⁻¹)	456	447	302	270	246
$T_{\max i}$: Temperature at maximum; $E_{\alpha \max i}$: Activation energy at maximum.					

III.3. Thermal and thermomechanical analyses and kinetic studies

Considering the computation using 1, 2, 4, and 10 K.min⁻¹ for which the average rate is around 4 K.min⁻¹, a correlation can be made with DSC and TGA measurements, depicted in **Figure 3**.

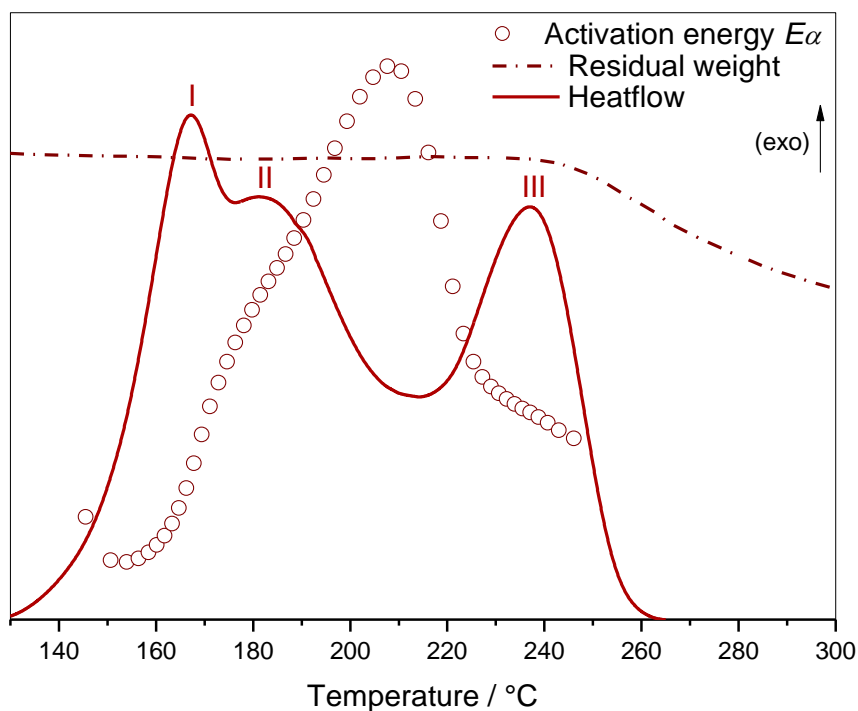


Figure 3. Evolution of activation energy E_α in function of temperature (empty circles) regarding DSC exotherm signal (full line) and TGA thermogram (dotted line) at 4 K.min⁻¹ under air atmosphere.

Finally, more appropriate conclusions could be established regarding the three peaks obtained on the DSC thermogram. Peak I and peak II are partially convoluted. Thus, peak I ($130 < T < 175$ °C) seemed to fit with the autocatalytic ring-opening step; while peak II, for which the beginning of the peak is mainly convoluted with peak I, presented a correlation with the end of the ring-opening, and with the second step of aromatic electrophilic substitution as there was a correlation between the maximum of E_α and the end of the peak, around 210 °C. Lastly, the increase of heat flow of peak III until its maximum at 235 °C corresponded to the diminution of the activation energy attributed to the rearrangement step.

Moreover, it is noteworthy that the onset of degradation occurred at the end of the reaction (last E_α value), and did not present an influence on the polymerization mechanism. Thus, the 2.7 % of decomposition included in peak III could successfully be neglected as they were not considered and did not impact the computations of E_α .

III.4. Chemorheological analysis and kinetic study

Chemorheological studies presented in the previous chapter permitted to identify the physical phenomena associated to the network formation, *i.e.* gelation and vitrification. Because these phenomena are associated to high viscosity change, which often leads to a shift from chemical control to diffusion control⁵, thermokinetic studies can be combined with rheometric data to obtain more information on the rate-limiting steps that control the overall reaction kinetic. **Figure 4** represents the associated results of non-isothermal rheological data at 2 K.min⁻¹ and kinetic computations using 0.5, 1, 2, and 4 K.min⁻¹ which present an average heating rate close to 2 K.min⁻¹.

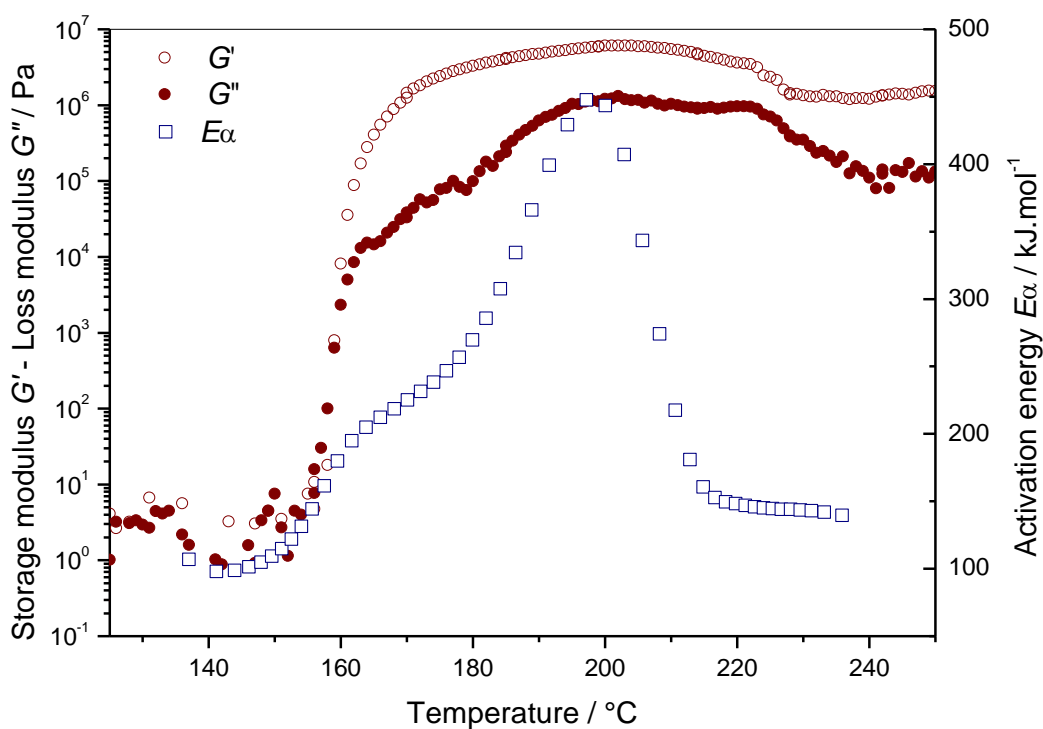


Figure 4. Right axis: Evolution of E_{α} computed with 0.5, 1, 2, 4 K.min⁻¹ with temperature (empty squares) – Left axis: Evolution of storage (empty circles) and loss (full circles) moduli with temperature at 2 K.min⁻¹.

Reactions started in the liquid state with an activation energy close to 100 kJ.mol⁻¹. Then, from 150 °C, both E_{α} and the moduli started to increase until E_{α} reached its first maximum for the ring-opening reaction when the gelation occurs. A good correlation was observed between these data, with a change in the slope of the E_{α} increase that corresponded to gelation (crossover between G' and G''). As gelation induced an increase of viscosity, the molecular mobility was

decreased inducing a lower reaction rate. Thus, in this case, the slope modification did not correspond to a step modification but to a modification in the reaction rate. Such slight slope modification in the E_α evolution in the gel state may be due to a transition from a chemical control to a diffusion control (motion of longer chains), which is in agreement with obtained results for epoxy-amine systems^{5,32}. From this stage, the system presented a viscous behavior as it followed the loss modulus profile. Thus, the maximum in E_α (around 450 kJ.mol⁻¹) reached at 197 °C was correlated with the vitrification plateau of the loss modulus. Finally, the drastic decrease of E_α from 450 kJ.mol⁻¹ to 150 kJ.mol⁻¹ was due to a sudden change in the rate limiting step that could be explained by the vitrification of the system which was shown to occur exactly at this temperature of 200°C.

III.5. Evolution of glass transition temperature (T_g) over curing

To confirm or infirm the hypothesis of the cross-link in the rubbery state, a follow-up of the glass transition temperature was performed. The variation of the glass transition temperature is indeed a good sign of the well evolution of the cross-link, as T_g is supposed to gradually increase with the cross-link. For this purpose, a first heating was performed to reach a given temperature, then, a second scan was completed by heating until 300 °C at 20 K.min⁻¹ to determine both T_g and residual enthalpy. The first heating was performed at 10 K.min⁻¹, until 180, 195, 225, and 280 °C. These temperatures were selected according to the DSC thermogram at the same heating rate. Peak I presented a maximum at 180 °C, matching with the temperature of the maximum of the catalytic step for the E_α -dependencies computed using the highest heating rates. The maximum of peak II at 10 K.min⁻¹ occurred at 195 °C, at the same temperature of the next change in the slope. Peak II and peak III seemed completely separated with a temperature at the minimum between those two peaks of 225 °C. Finally, the reaction was completed before 280 °C, thus, the evaluation of the T_g at this temperature should be a good indication of whether or not the final stage of curing corresponds to the completion of the cross-link in the solid state. **Table 3** summarizes the results obtained by DSC while the thermograms of the second scans at 20 K.min⁻¹ are depicted in **Figure 5**.

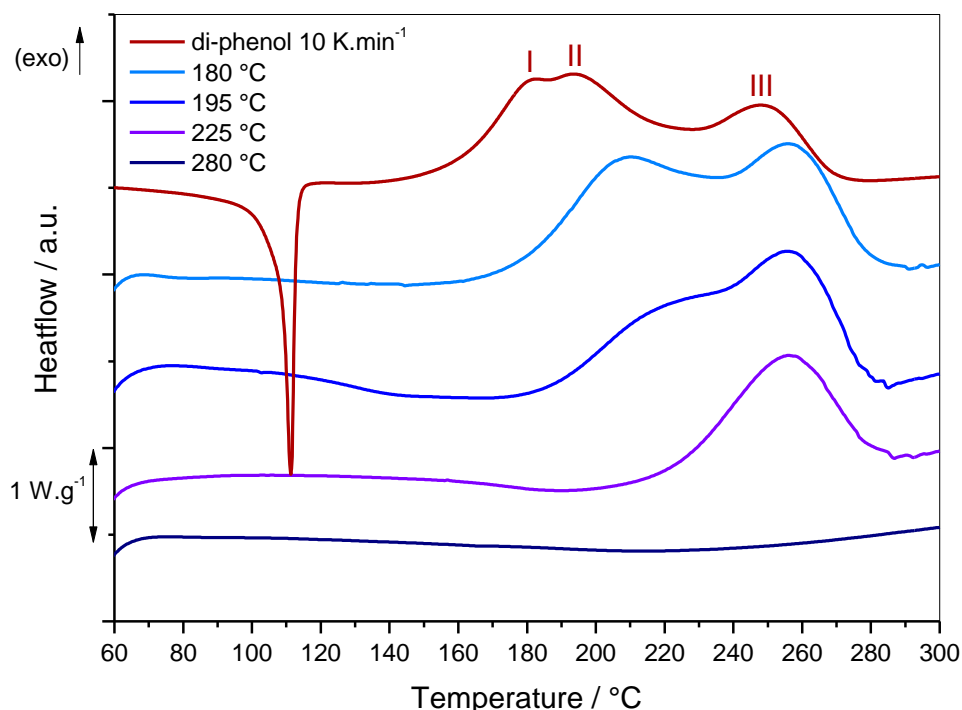


Figure 5. DSC thermograms of di-phenol BZ at 10 K.min⁻¹, and T_g follow-up at 20 K.min⁻¹ after a first heating until different temperatures.

As presented in **Figure 13** of **Chapter II**, peaks II and III were still deconvoluted at the heating rate of 20 K.min⁻¹. By heating the di-phenol BZ monomer until 225 °C, reactions of peak II were completed and peak III could be isolated. Residual enthalpies obtained after the first heating are progressively decreased as the final temperature was increased (**Table 3**). Thus, the last peak presenting a residual enthalpy of about 40 kJ.mol⁻¹ should consider the last step of the polymerization where the activation energy E_a was nearly constant, around 140 kJ.mol⁻¹.

After a first heating to the maximum of peak I, which coincided with the maximum of the autocatalytic step, the polymerization was still at its beginning as the corresponding T_g was relatively low (73 °C). When the temperature of change in the slope of E_a -dependencies was reached (maximum of peak II), the T_g was increased to 131 °C as the cross-link started to occur. The temperature of 225 °C, after peaks I and II and before peak III, was supposed to be correlated to the rearrangement step. Thus, the glass transition continued to increase and reached 158 °C. After completion of the reaction, no more residual enthalpy was observed, and a T_g of 165 °C was obtained. Therefore, the final stage of cross-linking effectively corresponded to the termination of the reaction in the solid state, as a higher glass transition temperature was

obtained. Indeed, after a more important molecular reorganization, a more important network can consequently be built, increasing the cross-link of the polymer.

Table 3. Evolution of T_g upon curing after a first heating at 10 K.min⁻¹ until different temperatures.

T (°C) [a]	T_g (°C) [b]	Δ_rH (kJ.mol ⁻¹) [c]
180	73	94.7
195	131	77.5
225	158	39.9
280	165	-

[a] Temperature reached at first heating at 10 K.min⁻¹; [b] Glass transition temperature and [c] Residual enthalpy both obtained by DSC with a 2nd heating at 20 K.min⁻¹.

IV. Isothermal analysis

IV.1. DSC measurements

Isoconversional analysis was also performed with isothermal measurements. Computations were performed using 4 temperatures maintained for 10 or 5 hours. A first measurement at relatively low temperature was performed at 110 °C for 10 h. The further measurements were performed at 120, 130, and 150 °C, for 5 h each. Resulting DSC thermograms are depicted in **Figure 6a**).

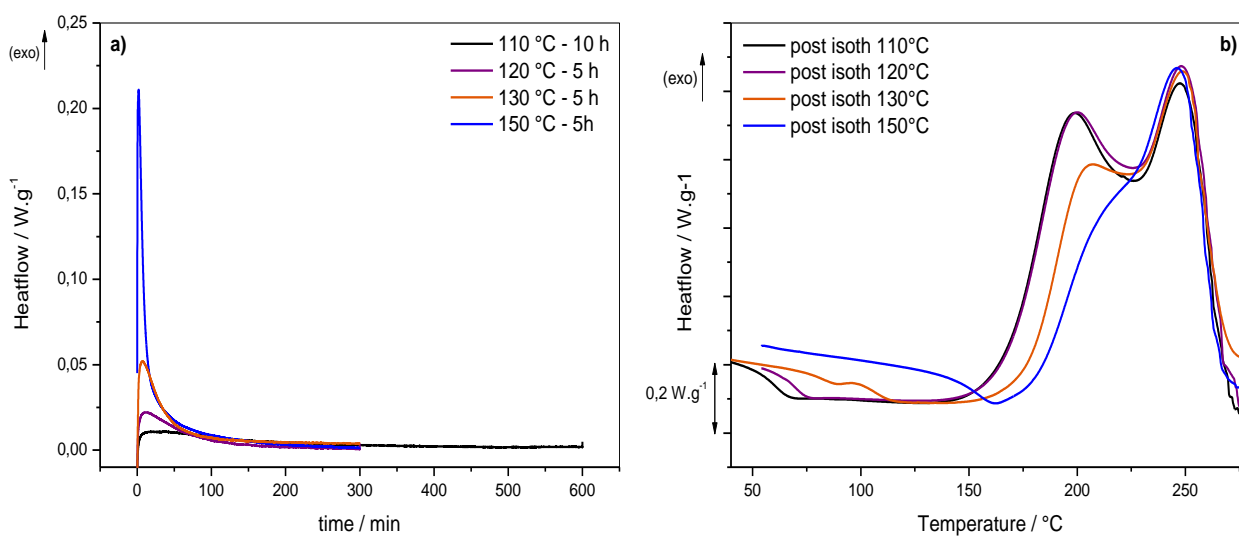


Figure 6. DSC thermograms **a**) in isothermal mode at 110, 120, 130, and 150 °C; and **b**) at 10 K.min⁻¹ after isothermal cure, for di-phenol BZ monomer under air atmosphere.

The isothermal thermograms presented a progressively increasing enthalpy from around 24 kJ.mol⁻¹ for the isotherm performed at 110 °C, to 26 kJ.mol⁻¹ for the isotherm at 120 °C, 33 kJ.mol⁻¹ for the isotherm at 130 °C, to finally reach 62 kJ.mol⁻¹ for the isotherm at 150 °C. Such result confirmed that some reactions take place only at high temperatures. Indeed, the lowest isotherm performed at 110 °C was maintained for 10 hours, thus, it was not a sufficient time to record all the polymerization process as the resulting enthalpy was only of 24 kJ.mol⁻¹ with a residual enthalpy of around 122 kJ.mol⁻¹ which was close to the overall enthalpy of polymerization for di-phenol BZ, as described in section III.2.1. DSC data are summarized in **Table 4**.

Each isothermal analysis was followed by a non-isothermal measurement depicted in **Figure 6b**), in order to determine the resulting T_g and the residual enthalpy. It is worthy to note that T_g was logically increased as the temperature of isotherm increased, while the residual enthalpy decreased. This is a good indication that the progression of the polymerization reaction requires an increasingly intake of energy. Thus, an isotherm curing at 150 °C for 5 hours still did not seem to be enough, as the resulting T_g is of about 154 °C, against a $T_{g\infty}$ of 190 °C obtained for a completely cured poly(di-phenol), as mentioned in the previous chapter. Thus, performing kinetic analysis using isothermal mode can be a favorable alternative to better separate the phenomena.

Table 4. DSC data obtained from isothermal analysis followed by non-isothermal measurement of di-phenol BZ monomer.

$T_{\text{isoth}} (\text{°C})$	110	120	130	150
$\Delta H_{\text{isoth}} (\text{kJ.mol}^{-1})$ ^[a]	23.9 ± 0.9	25.8 ± 1.0	33.0 ± 1.3	61.9 ± 2.5
$T_g (\text{°C})$ ^[b]	60.7	69.1	78.3	154.2
$\Delta H_{\text{residual}} (\text{kJ.mol}^{-1})$ ^[c]	123.8 ± 4.9	121.1 ± 4.9	89.1 ± 3.6	81.9 ± 3.3

^[a] Enthalpy of the isotherm. ^[b] Glass transition temperature after isothermal treatment.

^[c] Residual enthalpy after isothermal treatment.

IV.2. Isoconversional analysis in isothermal mode of di-phenol BZ

Previous section was dedicated to isoconversional analysis using non-isothermal DSC measurement for computation. Here isothermal measurements were considered. Indeed, previous computation evidenced a complex mechanism for the polymerization of di-phenol BZ. The literature describes a first autocatalytic step for the ring-opening polymerization (ROP)³³.

The first step appeared with an increase in the apparent activation energy which is not consistent with an autocatalytic step. Indeed, once a ring is opened, a phenolic function is generated which is able to catalyze further ring-opening reactions. Thus, an increasing activation energy should not be necessary. **Figure 7** presents the resulting computation from isothermal DSC measurements, in comparison with previous results obtained from non-isothermal measurements.

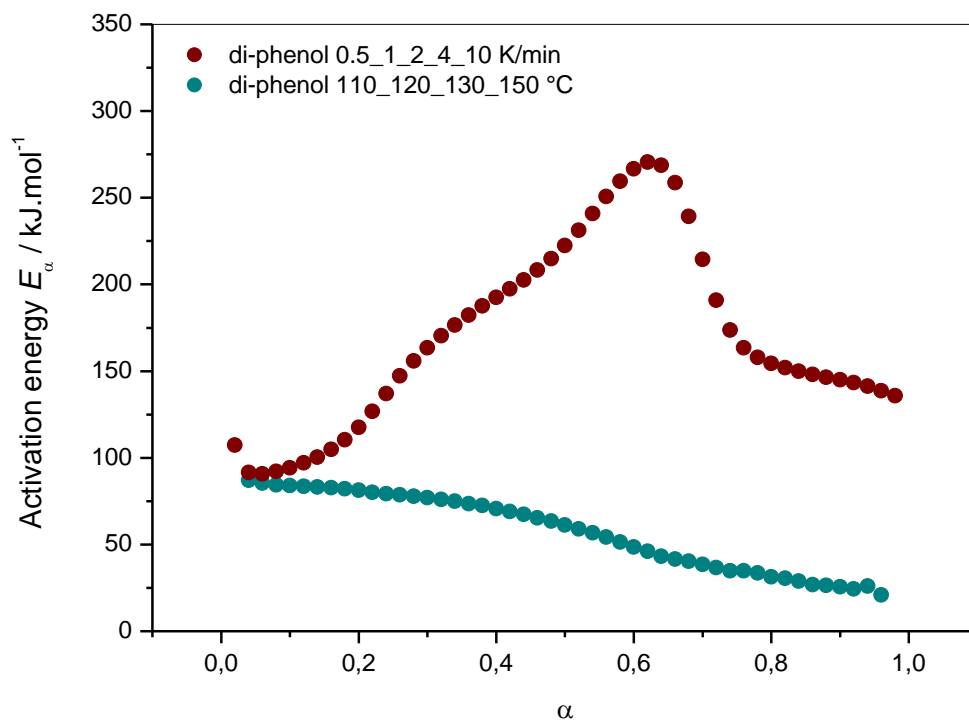


Figure 7. Evolution of apparent activation energy E_α in function of extent of conversion for non-isothermal (red dots) and isothermal computations (blue dots).

Taking apart the first point for non-isothermal computation as it includes a larger error, the chemical reaction for the ROP seemed to start at the same activation energy in both computations ($87 \text{ kJ}\cdot\text{mol}^{-1}$). Then, unlike non-isothermal computation, the activation energy from isothermal computation appeared to slightly decrease to reach a final E_α of about $25 \text{ kJ}\cdot\text{mol}^{-1}$. This result is more consistent with the behavior of an autocatalytic ring-opening reaction. However, this computation considered different temperatures including an isotherm at a relatively high temperature of $150 \text{ }^\circ\text{C}$. At such temperature, other reactions should take place to further cross-link, though the activation energy continued to decrease. Thus, this would indicate that the polymerization process does not take place in the same way whether the

monomer is cured in isothermal or non-isothermal mode, as it does not require the same amount of energy.

V. Conclusion

Kinetic follow-up by advanced isoconversional analysis allowed to determine the evolution of the apparent activation energy during the polymerization process of the di-phenol BZ monomer. Three main steps seemed to occur, correlated with the ring-opening reaction, followed by aromatic electrophilic substitution, and finally a rearrangement step. A final stage of cross-link in the solid state, occurred with a nearly constant energy of $140 \text{ kJ}\cdot\text{mol}^{-1}$. Kinetic analyses also reflected the temperature dependency of the reaction rate, as the polymerization reaction was shifted to higher temperatures with increasing the heating rate. Thus, chemical reactions did not proceed in the same way whether they are performed at fast or low heating rate. At low heating rate, some reactions may require more energy to reach completion, while at faster heating rate higher temperatures were reached faster and lower energies were required. Thus, when the lowest heating rates were used for computation, activation energy reached a maximum of about $450 \text{ kJ}\cdot\text{mol}^{-1}$ against $250 \text{ kJ}\cdot\text{mol}^{-1}$ using the highest heating rates. Despite the difference in E_a values, its overall evolution presented a similar tendency for the different heating rates.

Using isothermal measurements for computation allowed a better separation of the reactions, as the obtained activation energy evolution was decreasing, from 87 to $25 \text{ kJ}\cdot\text{mol}^{-1}$, which was consistent with an autocatalytic ring-opening reaction. However, the energy kept decreasing even considering higher temperature ($150 \text{ }^\circ\text{C}$), indicating that the polymerization did not progress similarly to non-isothermal curing, or at least would take more time.

Thus, these kinetic analyses show a complex reaction mechanism which depends on the time, temperature, and heating rate.

VI. References

- (1) Roșu, D.; Mititelu, A.; Cașcaval, C. N. Cure Kinetics of a Liquid-Crystalline Epoxy Resin Studied by Non-Isothermal Data. *Polym. Test.* **2004**, *23* (2), 209–215.
- (2) Roșu, D.; Cașcaval, C. .; Mustață, F.; Ciobanu, C. Cure Kinetics of Epoxy Resins Studied by Non-Isothermal DSC Data. *Thermochim. Acta* **2002**, *383* (1–2), 119–127.
- (3) Ishida, H.; Rodriguez, Y. Curing Kinetics of a New Benzoxazine-Based Phenolic Resin by Differential Scanning Calorimetry. *Polymer* **1995**, *36* (16), 3151–3158.
- (4) Sbirrazzuoli, N.; Vyazovkin, S.; Mititelu, A.; Sladic, C.; Vincent, L. A Study of Epoxy-Amine Cure Kinetics by Combining Isoconversional Analysis with Temperature Modulated DSC and Dynamic Rheometry. *Macromol. Chem. Phys.* **2003**, *204* (15), 1815–1821.
- (5) Vyazovkin, S.; Sbirrazzuoli, N. Mechanism and Kinetics of Epoxy–Amine Cure Studied by Differential Scanning Calorimetry. *Macromolecules* **1996**.
- (6) Sbirrazzuoli, N.; Vincent, L.; Mija, A.; Guigo, N. Integral, Differential and Advanced Isoconversional Methods: Complex Mechanisms and Isothermal Predicted Conversion–time Curves. *Chemom. Intell. Lab. Syst.* **2009**, *96*, 219–226.
- (7) Santhosh Kumar, K. S.; Reghunadhan Nair, C. P.; Ninan, K. N. Rheokinetic Investigations on the Thermal Polymerization of Benzoxazine Monomer. *Thermochim. Acta* **2006**, *441* (2), 150–155.
- (8) Ishida, H.; Sanders, D. P. Regioselectivity and Network Structure of Difunctional Alkyl-Substituted Aromatic Amine-Based Polybenzoxazines. *Macromolecules* **2000**, *33* (22) 8149-8157.
- (9) Allen, D. J.; Ishida, H. Effect of Phenol Substitution on the Network Structure and Properties of Linear Aliphatic Diamine-Based Benzoxazines. *Polymer* **2009**, *50* (2), 613–626.
- (10) Chutayothin, P.; Ishida, H. Cationic Ring-Opening Polymerization of 1,3-Benzoxazines: Mechanistic Study Using Model Compounds. *Macromolecules* **2010**, *43* (10), 4562–4572.
- (11) Sbirrazzuoli, N.; Vincent, L.; Vyazovkin, S. Comparison of Several Computational Procedures for Evaluating the Kinetics of Thermally Stimulated Condensed Phase Reactions. *Chemom. Intell. Lab. Syst.* **2000**, *54* (1), 53–60.
- (12) Vyazovkin, S.; Sbirrazzuoli, N. Isoconversional Kinetic Analysis of Thermally Stimulated Processes in Polymers. *Macromol. Rapid Commun.* **2006**, *27* (18), 1515–1532.
- (13) Vyazovkin, S.; Burnham, A. K.; Criado, J. M.; Pérez-Maqueda, L. A.; Popescu, C.; Sbirrazzuoli, N. ICTAC Kinetics Committee Recommendations for Performing Kinetic Computations on Thermal Analysis Data. *Thermochim. Acta* **2011**, *520* (1–2), 1–19.
- (14) Papageorgiou, G. Z.; Achilias, D. S.; Karayannidis, G. P. Estimation of Thermal Transitions in Poly(Ethylene Naphthalate): Experiments and Modeling Using Isoconversional Methods. *Polymer (Guildf)*. **2010**, *51* (12), 2565–2575.
- (15) Friedman, H. L. Kinetics of Thermal Degradation of Char-Forming Plastics from

- Thermogravimetry. Application to a Phenolic Plastic. *J. Polym. Sci. Part C Polym. Symp.* **1964**, 6 (1), 183–195.
- (16) Ozawa, T. Kinetic Analysis of Derivative Curves in Thermal Analysis. *J. Therm. Anal.* **1970**, 2 (3), 301–324.
- (17) Flynn, J. H.; Wall, L. A. A Quick, Direct Method for the Determination of Activation Energy from Thermogravimetric Data. *J. Polym. Sci. Part B Polym. Lett.* **1966**, 4 (5), 323–328.
- (18) Sbirrazzuoli, N.; Girault, Y.; Elégant, L. Simulations for Evaluation of Kinetic Methods in Differential Scanning Calorimetry. Part 3 — Peak Maximum Evolution Methods and Isoconversional Methods. *Thermochim. Acta* **1997**, 293 (1–2), 25–37.
- (19) Sbirrazzuoli, N. Is the Friedman Method Applicable to Transformations with Temperature Dependent Reaction Heat? *Macromol. Chem. Phys.* **2007**, 208 (14), 1592–1597.
- (20) Sbirrazzuoli, N. Determination of Pre-Exponential Factors and of the Mathematical Functions $f(\alpha)$ or $G(\alpha)$ That Describe the Reaction Mechanism in a Model-Free Way. *Thermochim. Acta* **2013**, 564, 59–69.
- (21) Vyazovkin, S. Evaluation of Activation Energy of Thermally Stimulated Solid-State Reactions under Arbitrary Variation of Temperature. *J. Comput. Chem.* **1997**, 18 (3), 393–402.
- (22) Vyazovkin, S.; Sbirrazzuoli, N. Isoconversional Method to Explore the Mechanism and Kinetics of Multi-Step Epoxy Cures. *Macromol. Rapid Commun.* **1999**, 20 (7), 387–389.
- (23) Vyazovkin, S. Advanced Isoconversional Method. *J. Therm. Anal.* **1997**, 49 (3), 1493–1499.
- (24) Sbirrazzuoli, N.; Vyazovkin, S. Learning about Epoxy Cure Mechanisms from Isoconversional Analysis of DSC Data. *Thermochim. Acta* **2002**, 388 (1–2), 289–298.
- (25) Sbirrazzuoli, N.; Mititelu-Mija, A.; Vincent, L.; Alzina, C. Isoconversional Kinetic Analysis of Stoichiometric and Off-Stoichiometric Epoxy-Amine Cures. *Thermochim. Acta* **2006**, 447 (2), 167–177.
- (26) Sbirrazzuoli, N.; Vyazovkin, S.; Mititelu, A.; Sladic, C.; Vincent, L. A Study of Epoxy-Amine Cure Kinetics by Combining Isoconversional Analysis with Temperature Modulated DSC and Dynamic Rheometry. *Macromol. Chem. Phys.* **2003**, 204 (15), 1815–1821.
- (27) Vyazovkin, S.; Sbirrazzuoli, N. Mechanism and Kinetics of Epoxy–Amine Cure Studied by Differential Scanning Calorimetry. *Macromolecules* **1996**, 29 (6), 1867–1873.
- (28) Vyazovkin, S.; Sbirrazzuoli, N. Effect of Viscosity on the Kinetics of Initial Cure Stages. *Macromol. Chem. Phys.* **2000**, 201 (2), 199–203.
- (29) Sbirrazzuoli, N.; Brunel, D.; Elegant, L. Different Kinetic Equations Analysis. *J. Therm. Anal.* **1992**, 38 (6), 1509–1524.
- (30) Vyazovkin, S.; Sbirrazzuoli, N. Effect of Viscosity on the Kinetics of Initial Cure Stages. *Macromol. Chem. Phys.* **2000**, 201 (2), 199–203.

- (31) Liu, C.; Shen, D.; Sebastià, R. M.; Marquet, J.; Schönfeld, R. Catalyst Effects on the Ring-Opening Polymerization of 1,3-Benzoxazine and on the Polymer Structure. *Polymer* **2013**, *54* (12), 2873–2878.
- (32) Sbirrazzuoli, N.; Mititelu-Mija, A.; Vincent, L.; Alzina, C. Isoconversional Kinetic Analysis of Stoichiometric and Off-Stoichiometric Epoxy-Amine Cures. *Thermochim. Acta* **2006**, *447* (2), 167–177.
- (33) Ishida, H.; Agag, T. *Handbook of Benzoxazine Resins*; Elsevier, **2011**.

Part II

Dialdehyde cellulose-based composites

Chapter IV

From lignocellulosic biomass to bio-based thermosets – State of the art

I. Vegetable biomass	137
I.1. The complex architecture of plant cell wall	137
I.2. Composition of plants	138
I.2.1. Cellulose	138
I.2.1.1. Molecular structure	139
I.2.1.2. Cellulose biosynthesis	140
I.2.2. Hemicellulose	140
I.2.3. Lignin	142
I.2.4. Other compounds	143
II. From in situ cellulose to cellulosic raw materials	143
II.1. The different sources of cellulose	143
II.2. Extraction of cellulose from biomass	144
II.2.1. Mechanical pulp	144
II.2.2. Chemical pulp	144
II.2.3. Chemi-(thermo)mechanical pulp	144
II.3. The different forms of isolated cellulose	144
II.3.1. Thermo-mechanical properties	146
II.4. Surface modification of cellulose	147
II.4.1. Substitution: cellulose esterification	148
II.4.2. Substitution: cellulose etherification	148
II.4.3. Cellulose oxidation	149
III. From lignocellulosic biomass to furanic building blocks and polymers	152
III.1. Furfuryl alcohol	155
III.1.1. Synthesis of furfuryl alcohol	155
III.1.2. Properties, reactivity, and applications	156
III.1.3. From furfuryl alcohol to poly(furfuryl alcohol): polymerization mechanism	157
IV. References	161

I. Vegetable biomass

From an etymological point of view, the term “biomass” comes from the Greek *bio* meaning life and *maza* meaning mass. Thus, it concerns all non-fossilized and biodegradable organic material coming from plants, animals, and micro-organisms. Biomass covers a set of organic materials that store the sunlight in the form of chemical energy. This chapter focuses on the lignocellulosic biomass composition to introduce the overall chain value of some biobased raw materials (cellulose, fufuryl alcohol), which will be studied in further sections.

I.1. The complex architecture of plant cell wall

The most complex hierarchical architecture is found in wood, as presented in **Figure 1**. Each plant is constituted by a high density of cells. Each cell, with an average size of 30 μm , is composed of three main regions: the middle lamella (ML), the primary wall (P), and the secondary wall (S). These layers, intimately linked together, are composed by three major macromolecular components: cellulose microfibrils, hemicellulose, and lignin. Pectins and proteins are additional components included in the cell composition. All these constituents are linked together and impose the peculiar mechanical properties of plant.

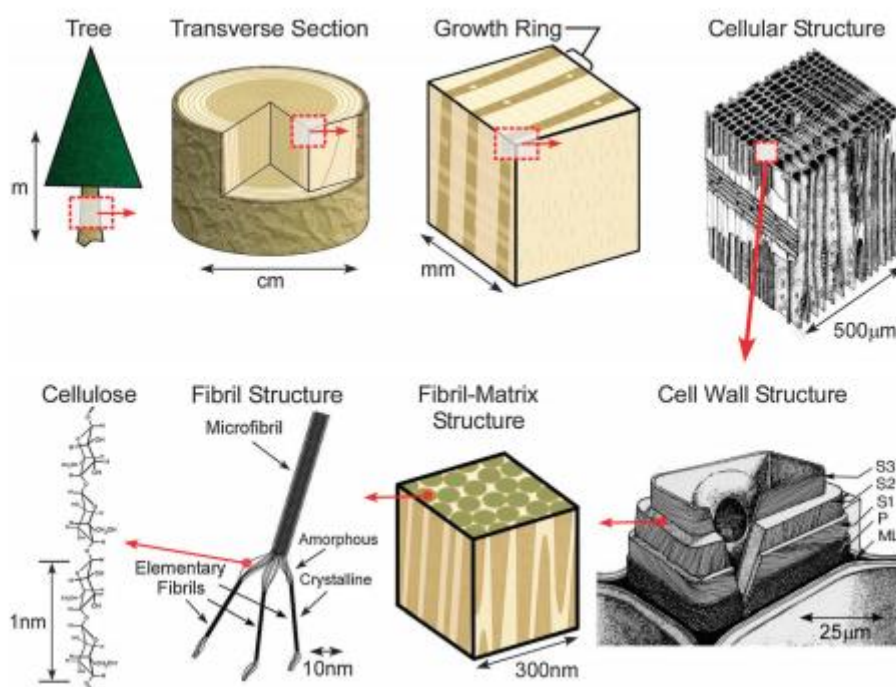


Figure 1. Multi scale structure of wood from the tree to the cellulose chain¹.

Cellulose forms long and linear chains merging together to form microfibrils. Lignin plays the role of matrix fixing the cellulose microfibrils. Hemicellulose, composed of branched polysaccharides, helps to compatibilized cellulose with lignin.

The main characteristic distinguishing the primary wall from the secondary wall is the different orientation of the microfibrils (helix or angles). Depending on the environmental conditions, the helix angle of microfibrils tends to adapt and leads to different mechanical properties². With a low orientation of the cellulose microfibrils, the elastic modulus is smaller and the elongation at break is higher, compared with a high microfibrils orientation. This characteristic structure gives high mechanical properties, inspiring the use of cellulose as reinforcement for natural rubber biocomposites for example³.

1.2. Composition of plants

As previously described, each plant is composed by three main macromolecules: cellulose, hemicellulose, and lignin. These biopolymers are considered as precursor of biomass. However, the proportion of these constituent may vary depending on the botanical origin, the geographic location, or the age of the plant⁴ (**Table 1**).

Table 1. Content of cellulose, hemicellulose, and lignin in different type of plant⁴.

Lignocellulosic materials	Cellulose (%)	Hemicellulose (%)	Lignin (%)
Hardwood stems	40 – 55	24 – 40	18 – 25
Softwood stems	45 – 50	25 – 35	25 – 35
Nut shells	25 – 30	25 – 30	30 – 40
Grasses	25 – 40	35 – 50	10 – 30
Paper	85 – 99	0	0 – 15
Wheat straws	30	50	15
Cotton seed hairs	80 – 95	5 – 20	0

1.2.1. Cellulose

In 1839, the French chemist Anselme Payen, after several acido-basic treatments of plants, isolate and identify the molecular formula of a solid and fibrous compound⁵. He found that this fibrous substance of all plant cells is constituted by a uniform carbohydrate composed of glucose residues which have for composition: 50 % of oxygen, 44 % of carbon, and 6 % of

hydrogen. Later in the same year, the French Science Academy named this compound “cellulose”, which literally means “sugar from cells”⁶.

The production of cellulose by photosynthesis is estimated to be about 10^{11} – 10^{12} tons per year⁷, and is considered as a raw material almost inexhaustible⁸. The major sources of cellulose are wood and cotton. But cellulose can also be derived from bast fibers (flax, hemp), grasses (bagasse, bamboo), fungi, bacteria, or marine animals (tunicate)⁹. Cellulose consists of a linear homopolymer composed of D-glucopyranose units, also named D-AnhydroGlucopyranose Unit (AGU), linked together by β -1,4 linkage, as presented in **Figure 2**. This macromolecule can reach a degree of polymerization (DP) of 9,000 to 10,000 units¹⁰, where the repeating unit is the disaccharide cellobiose.

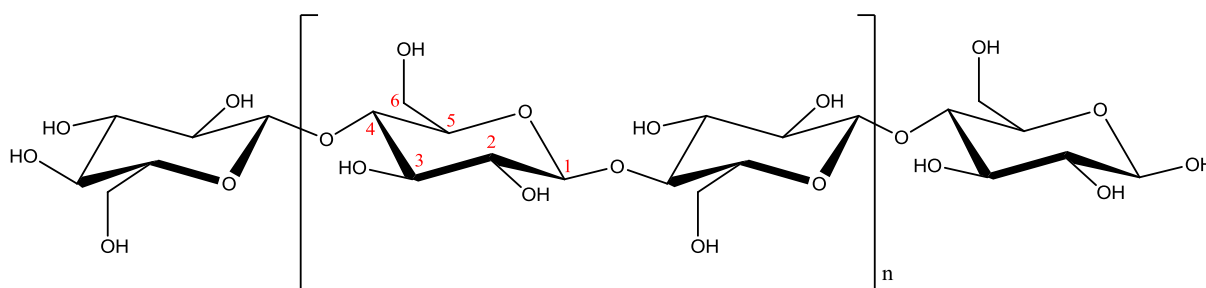


Figure 2. Chemical structure of cellulose.

1.2.1.1. Molecular structure

AGU are 6-membered rings and adopt the chair conformation where hydroxyl groups (and glycosidic linkage) are in equatorial position, while hydrogens are in axial position, leading to a maximal extension of the chain^{11,12}. The hydroxyl groups (presented in **Figure 2**) consist of two secondary hydroxyls in position 2 and 3, and one primary hydroxyl in position 6. These hydroxyl functions allow to form a complex *intra*- and *inter*-molecular hydrogen bonding network which tightly binds the glucose units (**Figure 3**)¹³. The hydrogen bonding network lead to a semi crystalline polymer by fixing several layers in parallel order. This allows to form the fibrillar structure of cellulose.

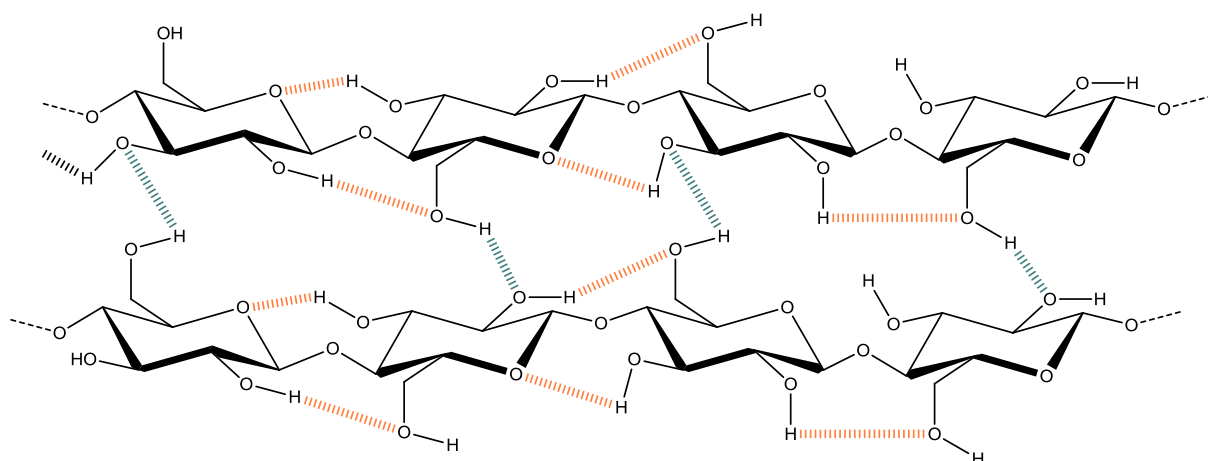


Figure 3. Cellulose structure with *inter-* (green) and *intra-* (orange) hydrogen bonds.

1.2.1.2. Cellulose biosynthesis

The biosynthesis of several chains of cellulose is simultaneous and allows the formation of secondary linkage network such as molecular hydrogen bonds between hydroxyl groups and van der Waals interactions between glucopyranose rings leading to the formation of glucan sheets, assembling cellulose polymers into a supramolecular structure^{14,15}. Because of the high density of these bonds, the formation of elementary fibrils is possible, and these fibrils can further aggregate into larger microfibrils, with a diameter of about 3-4 nm¹⁶ and a length of several hundred of nanometers⁸. These microfibrils are composed of an alternation of crystalline and amorphous regions. At a larger scale, the so-called macrofibrils, with a diameter of 10-25 nm¹⁷, are composed of microfibrils which are aligned and bounded together with a matrix of hemicellulose, lignin, and pectin. This complex architecture provides thermal and mechanical stability.

The cellulose fibrils are synthesized in the plasma membrane, by photosynthesis from two enzymes¹⁸: cellulose synthase, which allows the formation of β-1,4 linkage between glycoside groups; and chitinase-like proteins, which help the crystallization and allow the formation of the supramolecular structure. Spectroscopic studies show that native cellulose is mostly crystalline with two distinguishable polymorph forms, I_α and I_β, while the cellulose synthesized experimentally is mainly amorphous¹⁹.

1.2.2. Hemicellulose

The word hemicellulose was introduced for the first time in 1891 by E. Schulze to identify a polysaccharide which is water insoluble, but which can be extracted from plants by an alkali solvent²⁰. Compared to cellulose, the hemicellulose has a higher solubility and hydrolysis

sensitivity, because of its amorphous structure and its lower molecular weight (500 to 3,000 units¹⁰).

Hemicellulose is the second most abundant biopolymer on Earth after cellulose²¹. Unlike cellulose, hemicellulose has a more complex structure. The heteropolymers of hemicellulose are composed of different monosaccharides units, with both pentoses (xylose or arabinose), hexoses (mannose or galactose), acetylated sugars^{20,22}, and acidic hemicellulose contains a large number of acid sugars such as D-glucuronic acid and 4-*O*-methyl-D-glucuronic acid²³. The composition can vary depending on the treatment used to extract the sugars and can also vary with the source of biomass²², as presented in **Table 2**.

Table 2. Carbohydrate content of the main biomass types²².

Origin	Species	Carbohydrate content (% of dry mass)	C ₆ sugars*					C ₅ sugars*	
			Glu	Man	Gal	Rha	Fuc	Xyl	Ara
Hardwoods (average)	Mixed (stem)	67 – 75 %	43	0.4	0.9	0.5	0.1	16	1.3
Softwoods (average)	Mixed (stem)	67 – 75 %	44	4.9	7.8	0.4	0.3	8.9	5.9
Grasses	Sugarcane bagasse	/	32 – 34	0.5	1.6	/	/	20 – 23	2
Agricultural residues	Corn cobs	75	39	/	/	/	/	30	3.3
	Wheat straw	57	32	/	/	/	/	20	2.8
	Rice Husks	49	30	/	/	/	/	17	2

* Glu, Glucose; Man, Mannose; Gal, Galactose; Rha, Rhamnose; Fuc, Fucose; Xyl, Xylose; Ara, Arabinose

Hemicelluloses are synthesized by glycosyltransferase located in the Golgi membrane²⁴. These linear polymers are imbedded in the plant cell walls to form a complex network of bonds with cellulose and lignin, either by covalent or hydrogen bonds, or by ionic and hydrophobic interactions. These interactions allow the linking of cellulose fibers into microfibrils and the cross-link with lignin, providing the structural strength of the cell walls which is the most important role of hemicelluloses^{24,25}.

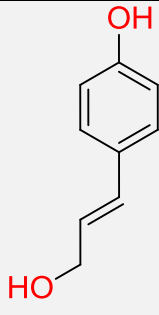
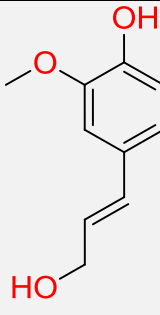
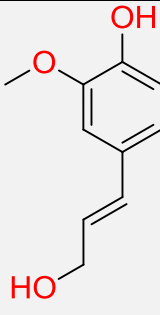
1.2.3. Lignin

In 1856, Franz Ferdinand Schulze reported the isolation of cellulose by an acidic treatment of wood performed by Payen. The solved part was then named for the first time: *lignin*, from the latin word ‘*lignum*’ which literally means wood²⁶.

This polymer has a complex three-dimensional amorphous structure, synthesized by oxidative coupling between three phenylpropane building blocks: *p*-coumaryl alcohol, coniferyl alcohol, and sinapyl alcohol. In the lignin polymer, the corresponding phenylpropanoid monomeric units are respectively identified as *p*-hydroxyphenyl, guaiacyl, and syringyl units²⁷. Lignin composition can differ between species or even between different tissues of an individual plant (**Table 3**). By its high aromatic content, lignin is responsible of mechanical structure and resistance of the woody biomass, as it behaves as the cellular glue providing compressive strength to the plant tissue and to the individual fibres, stiffness to the cell wall, as well as resistance against micro-organisms, molds, insects, pathogens, and oxidative stress, thus slowing its degradation^{10,25,28}. During the polymerization, the monomers are mainly interconnected by β -O-4 aryl ether bonds^{22,29}; other diverse types of bond are reported by Azadi *et al*³⁰.

Isolation of lignin from wood is possible by means of different treatments (kraft, organosolv,...), but the high heterogeneity of its structure makes difficult the separation without modifying the initial structure. This drawback leads to isolated lignin depending on the applied thermal and chemical treatment.

Table 3. Lignin content and chemical structures of the three primary phenolic units of lignocellulosic biomass³⁰.

	Lignin (%)	Phenylpropane units (%)		
Structure				
		Coumaryl	Coniferyl	Sinapyl
Hardwood	27 – 33	-	90 – 95	5 – 10
Softwood	18 – 25	-	50	50
Grasses	17 – 24	5	75	25

1.2.4. Other compounds

In addition to the main constituents previously mentioned, other organic compounds can be extracted from plants by polar or apolar solvents. It is possible to obtain fatty acid esters, terpenes, phenolic derivatives, or resin acid which is found in suberin, tannins, or oilseeds. In a minor part, plants may also contain some inorganic compounds such as potassium, silicon, or calcium.

II. From *in situ* cellulose to cellulosic raw materials

II.1. The different sources of cellulose

Three different sources of cellulose are known: cell walls of plants, animals, or bacteria³¹.

- Vegetable cellulose is mainly derived from wood, plants, and algae. The main industrial use of cellulose is the cellulose from wood, for pulp and paper industry. Cellulose from annual plants such as cotton, flax, sisal, etc. can be treated as wood cellulose and has already an important place, particularly in textile industry. Regarding algae, they can provide pure cellulose, which makes them an interesting alternative source of cellulose, already studied for some years³².
- Animals can also be a source of cellulose. Tunicate is a sea animal mollusk which exists in more than 2,300 species and produces pure cellulose. The production of pure monoclinic cellulose I_β allomorph does not require many treatments to extract the microfibrils from its mantle. The obtained cellulose is highly crystalline and presents a randomly entangled microfibrils following a helical organization¹.
- Bacterial cellulose is produced by biosynthesis of several aerobic and non-synthetic bacteria which are able to convert glucose and glycerol into cellulose within few days. They are mainly located in fruits, vegetables, vinegar, and alcoholic beverages. Bacterial cellulose has a high purity as it is free of hemicelluloses, lignin, and residues, in opposition to cell wall cellulose. This type of cellulose is characterized by its specific structure as it shows entangled and ultrafine fibers providing high mechanical strength. Other advantages are its biodegradability, biocompatibility, high capacity to hold water, and high crystallinity. Thus, bacterial cellulose can find various applications as artificial temporary skin, DNA separation, fuel cell membranes, composite reinforcement, etc³³.

II.2. Extraction of cellulose from biomass

The extraction of cellulose from plant involves the removal of all the non-cellulosic compounds either by mechanical or chemical treatment. Three different kinds of pulp can be obtained: mechanical pulp, chemical pulp, and chemi-(thermo)mechanical pulp. The so-called pulp is a mixture of lignocellulosic materials, which has its structure broken down by chemical and/or physical treatment³⁴.

II.2.1. Mechanical pulp

The mechanical process does not require chemicals, but only mechanical energy. To produce mechanical pulp, wood chips are processed using high temperature steam, and mechanical refining. It represents 20 – 25 % of the world production, and mainly used for newsprint and catalogue papers³⁴.

II.2.2. Chemical pulp

Chemical treatments lead to almost pure cellulose, using heat and acidic (sulfite process) or basic (soda process) solution. Such treatment results in high yield of individual fibres with high purity and low degradation, giving high mechanical properties. This results in a great interest for the derivatization in other cellulose morphologies. Such high quality of chemical pulp represents about 70 – 75 % of the world production³⁴.

II.2.3. Chemi-(thermo)mechanical pulp

It is a combination of a chemical treatment and a drastic mechanical treatment. First, as for chemical pulp, the wood chips are treated with a small amount of sodium sulfite or sodium hydroxide. Then, pressure with elevated temperature is applied to help the penetration of chemicals by softening lignin and hemicelluloses from the middle lamella and stimulate fibres separation. The elevated temperature helps to dissociate the different compounds although it is not primordial as the same process is possible using only pressure. Chemi-(thermo)mechanical pulp represents 5 – 10 % of the world production³⁴.

II.3. The different forms of isolated cellulose

Different morphologies of cellulose can be isolated depending on the treatment employed. Cellulose properties depend both on the source from which it has been extracted and on the morphological aspect. Three main technical cellulose forms are used: microcrystalline (MCC),

microfibrillar (MFC), and nanocrystalline (NCC) cellulose. The different morphologies are represented in **Chart 1**.

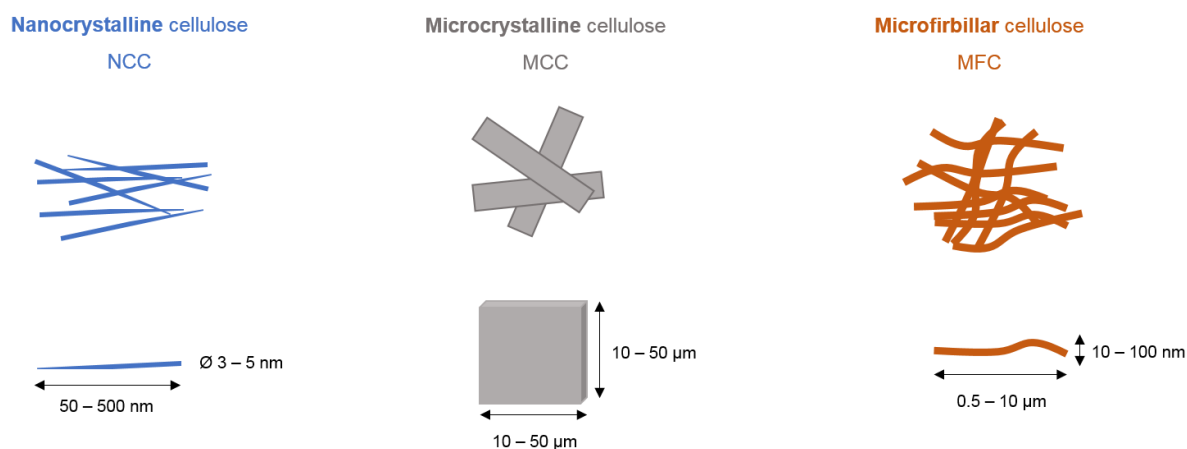


Chart 1. Different cellulose morphologies.

The nanocrystals and the microfibrils have nanoscale dimensions. These particles are obtained by hydrolysis action, which breaks the amorphous regions resulting in small cellulose crystals as represented in **Figure 4**. Nanocrystals are composed of elongated rod-like crystalline nanoparticles. Microfibrils, on the other hand, denominate a network of entangled flexible fibrils, consisting of an alternation of crystalline and amorphous domains.

In 1983, Herrick *et al.* and Turbak *et al.* were the first to isolate cellulose microfibrils from softwood, using a mechanical disintegration process^{35,36}. The process consists to pre-cut the fibers to reduce their length, then, several homogenization treatments are performed using high pressure and temperature, resulting in a diluted dispersion of MFC with a gel-like appearance, which shows an increase in viscosity³⁵⁻³⁷. An alternative method is to use a microfluidizer which also allows the defibrillation of cellulosic pulps. It is necessary to repeat the homogenization process several times in order to increase the degree of fibrillation³⁵⁻³⁸. During the refining process, the fibers are subjected to shearing and compression, leading to a partial delamination of the cell wall, called fibrillation. As the obtained cellulose fibrils consists of an alternance of crystalline and amorphous fractions, purified MFC presents a relatively low crystallinity of about 51 – 69 % and are kept as a suspension in water to preserve the fibers from agglomeration. Because of its properties like high strength, flexibility, and high specific area, MFC are attractive in different applications as nanocomposite reinforcement, paper coating³⁹, but also in a wide range of commercial use in food industry, cosmetics, paints, etc^{35,36}.

It is common to find the term “nanofbrils” in the literature. A recent review by Chinga-Carrasco⁴⁰ calls attention on the different appellations of cellulose fibers, nanofibrils

(NFC), and microfibrils (MFC), and whether MFC is considered a micro-structure. The author agrees that the microfibrils mentioned by Turbak *et al.* do not refer to micrometer-sized particles but to individualized microfibrils with a diameter less than 100 nm. Thus, if the nano-scale is accepted to refer to sizes between 1 and 100 nm, the term nanofibril refers to fibrils with a diameter below 100 nm. Based on this, microfibrils can be considered nanofibrils. The difference between both terms is that microfibrils are a well-defined biological structure found in plant cell walls, whereas the term nanofibrils is considered a technological term introduced to describe structures with diameter below 100 nm⁴⁰.

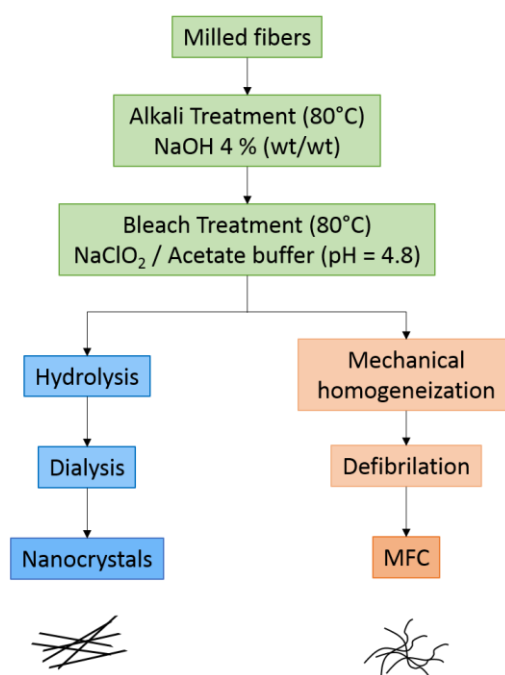


Figure 4. The main steps involved in the preparation of cellulose nanoparticles⁴¹.

II.3.1. Thermo-mechanical properties

Recently, the elastic modulus of single cellulosic microfibrils were recently evaluated using Atomic Force Microscopy (AFM)⁴². Authors proposed a modulus of 145.2 ± 31.3 GPa for microfibrils prepared by TEMPO-oxidation and a modulus of 150.7 ± 28.8 GPa for microfibrils obtained by acid hydrolysis. Such high moduli make it an attractive reinforcing material. Regarding cellulose crystals, its elastic modulus was estimated to 137 GPa⁴³ in the longitudinal direction. In 1995, Favier *et al.*⁴⁴ demonstrate that cellulose nanocrystals can be used in nanocomposites to improve the mechanical properties. Since then, many studies have been dedicated to nanocomposite materials incorporating cellulose nanocrystal^{45–53}. More recently, some studies focus on the use of cellulose nanofibrils and microfibrils as filler in composites^{54–62}.

Concerning its physical properties, the glass transition temperature (T_g) of dry cellulose is estimated to be around 220 °C^{63,64} and the melting temperature (T_m) is roughly estimated to be 450 °C⁶⁵; however, no direct measurements were reported because of the overlapping with thermal degradation. Szcześniak *et al.*⁶⁴ reported a first step of degradation starting at 220 °C. The cellulose is a stiff macromolecule, which organizes in highly crystalline domains. This structure of cellulose is responsible of these high transition temperatures. Because of these properties, the industrial transformation of neat cellulose as a thermoplastic is impossible. To overcome this problem, chemical modification of the cellulose is required but the high density of hydrogen bonds network makes difficult the penetration of reagent into the fibrils, which is why it is necessary to break these bonds.

II.4. Surface modification of cellulose

Each AGU contains three hydroxyl groups which facilitate the chemical modification. Three main ways of modification can be employed⁶⁶, etherification, esterification, and oxidation, with respective reactive sites described in **Figure 5**. The chemical and physical properties of the final product depend on the modification, the type of substituting group, the degree of substitution (average number of substituting groups per AGU), and the uniformity of products. The higher is the degree of substitution the lower is the material cohesion, because of the loss of the hydrogen bonds.

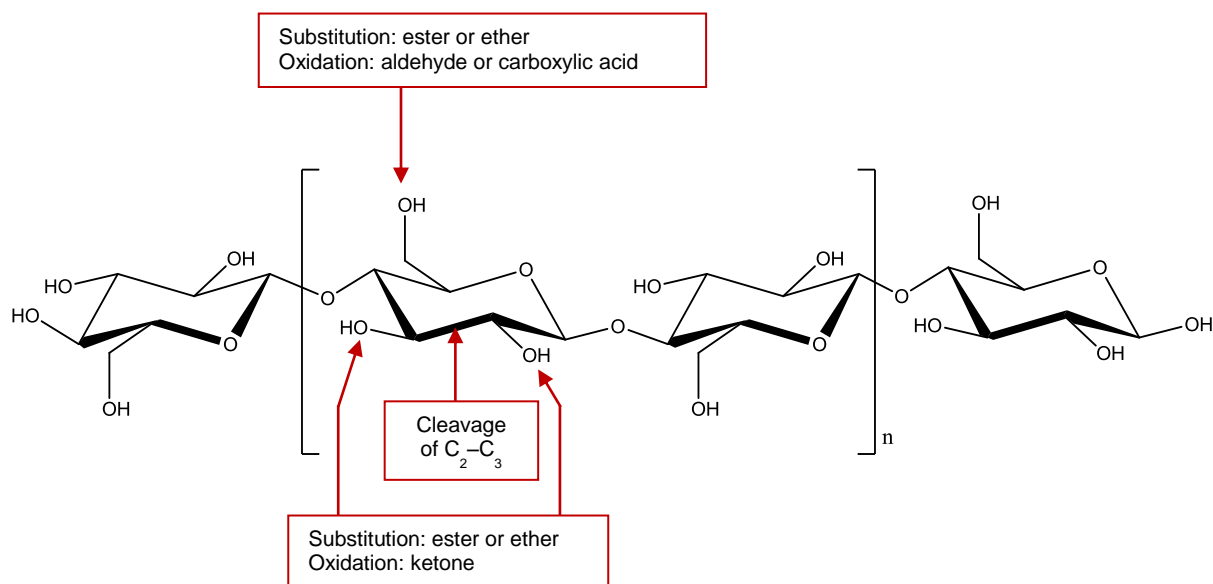
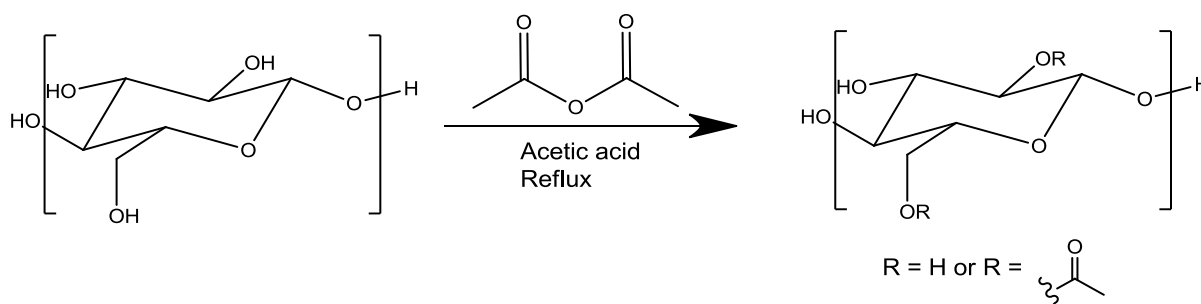


Figure 5. Most typical cellulose modifications depending on the target site.

II.4.1. Substitution: cellulose esterification

The review by Ganster and Fink describes cellulose ester derivatizations, its applications, and industrial process or interest⁶⁷. Esterified cellulose is widely used to form transparent and flexible films with good moisture and oxygen barrier properties. The partial or full esterification of the three hydroxyl groups results in cellulose acetate⁶⁸. It is currently one of the most cellulose-based polymer used in industry. As presented in **Scheme 1**, cellulose acetate results of the reaction in alkali conditions between raw cellulose and acetic anhydride, which converts the hydroxyl groups into acetyl groups. The degree of substitution can vary between 0 (raw cellulose) and 3 (cellulose triacetate). The usual degree of substitution for fibers and filters applications is around 2.45. In a standard industrial process, cellulose triacetate is first obtained in the form of a solution in acetic acid. Then, the degree of substitution can be controlled by addition of water to decrease the degree of substitution to a desired value, by hydrolysis⁶⁹.



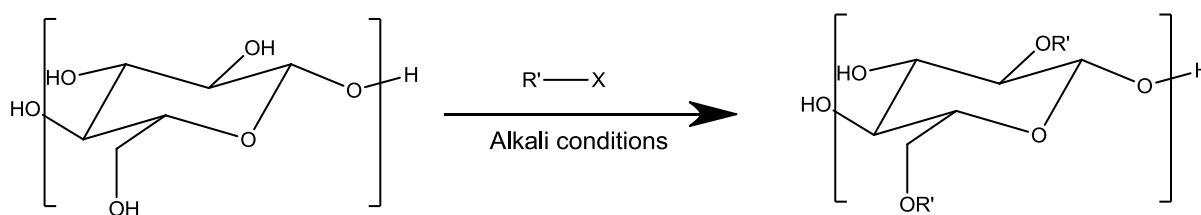
Scheme 1. Cellulose esterification – Synthesis of cellulose acetate.

Cellulose acetate is often used as a film base in photography replacing nitrate films as cellulose acetate is cheaper and less flammable. Cellulose acetate can also be used as a frame material for eyeglasses or as fibers in textile industry^{70,71}. Cellulose acetate butyrate and cellulose acetate propionate are associated derivatives often used in inks and coatings⁷².

II.4.2. Substitution: cellulose etherification

Etherification is usually performed in concentrated alkali media, resulting in cellulose alkoxides which can react with an alkylating agent⁷³. The heterogeneous nature of cellulose leads to variations in the availability and reactivity of the hydroxyl groups. The treatment in caustic alkaline solution creates a disorder in the hydrogen bonding network, making most of the hydroxyl groups available for modification, with C₂ and C₆ hydroxyl sites more reactive than the C₃ site⁷⁴. **Scheme 2** represents the general synthetic pathway for the obtention of cellulose ethers. In this category of cellulose derivative, the alkyl halide attacks the alkali-cellulose to obtain (R_{cell}-O-R') with R' an alkyl group. Methyl cellulose R_{cell}-O-CH₃ (obtained with

methyl halide), carboxymethyl cellulose $R_{\text{cell}}\text{-O-CH}_2\text{-COOH}$ (usually obtained with chloroacetic acid), and hydroxyethyl cellulose $R_{\text{cell}}\text{-O-CH}_2\text{-CH}_2\text{-OH}$ (obtained with epoxide) are often used as thickener agent for food, as viscosity modifier, etc⁷⁵.



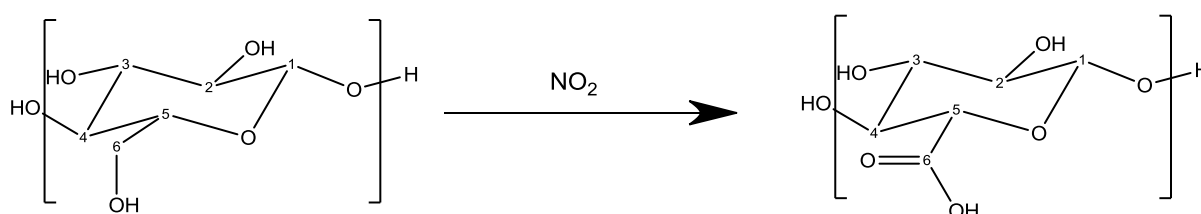
Scheme 2. Cellulose etherification – General synthesis.

II.4.3. Cellulose oxidation

The hydroxyl groups of cellulose can be oxidized in different functions depending on the type of alcohol (primary or secondary) and the selected reagent. Thus, hydroxyl groups can be turned in aldehydes, ketones, or carboxylic acids. Several oxidative reagents are commonly employed such as periodate^{76–78}, nitrogen oxide⁷⁹, TEMPO oxidation (2,2,6,6-tetramethylpiperidine-N-oxyl)^{80,81}, or peroxides. Oxidized cellulose finds applications in various fields such as agriculture, cosmetic, paper industry, and pharmaceuticals and biomedical field for its biocompatibility and bioresorbability^{82,83}.

- Nitrogen oxide

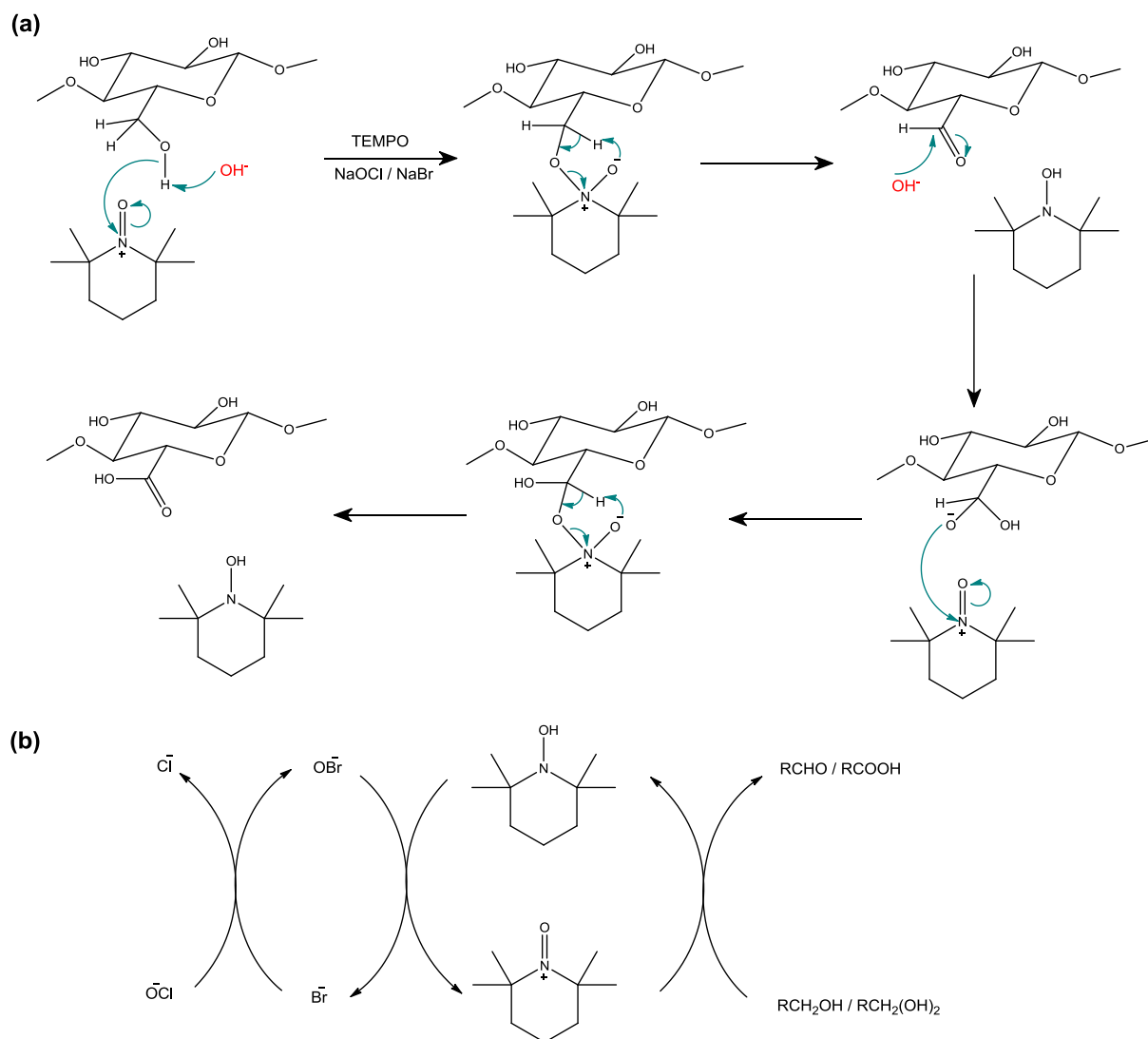
Nitrogen dioxide (NO_2) oxidizes selectively the primary alcohol in C_6 position into a carboxylic acid (**Scheme 3**). This method of oxidation is industrially used to confer bioresorbability. This reaction can lead to several side processes (*e.g.* decrystallization, nitration, etc.) and side reactions can occur such as the oxidation of secondary alcohols into ketones, the cleavage of the $\text{C}_2\text{-C}_3$ bond, the formation of aldehyde groups, of the incomplete oxidation of the C_6 hydroxyl group to a aldehyde function⁸⁴. A concentrated media can increase the amount of carboxyl content⁸⁵.



Scheme 3. Oxidation of the primary alcohol in C_6 position with NO_2 reagent.

- TEMPO-mediated oxidation

The global chemical reaction scheme is similar to the previous one, with the detailed mechanism of oxidation presented in **Scheme 4(a)**. In contrast to the oxidation with nitrogen oxide, the TEMPO-mediated oxidation allows a highly selective oxidation of the primary alcohol in C₆ position into a carboxyl group, making this method one of the most studied in cellulose application. De Nooy *et al.*⁸⁰ were the first to report this selective oxidation condition twenty years ago. This process leads to a fast reaction rate and a modest yield of polysaccharide degradation is obtained. Indeed, when performed under basic conditions, some cellulose depolymerization can occur by β -elimination^{86–88}. The carboxylic acid arising from TEMPO oxidation is a convenient intermediate for the subsequent grafting of functional molecules or macromolecules^{89,90}. Then, TEMPO reagent can be regenerated *in situ* by several oxidant like *m*-chlorobenzoic acid, copper salt, or more frequently, sodium bromide and sodium hypochlorite (**Scheme 4(b)**). Moreover, this reaction can be suitable as treatment surface for the individualization of cellulose microfibrils⁹¹.

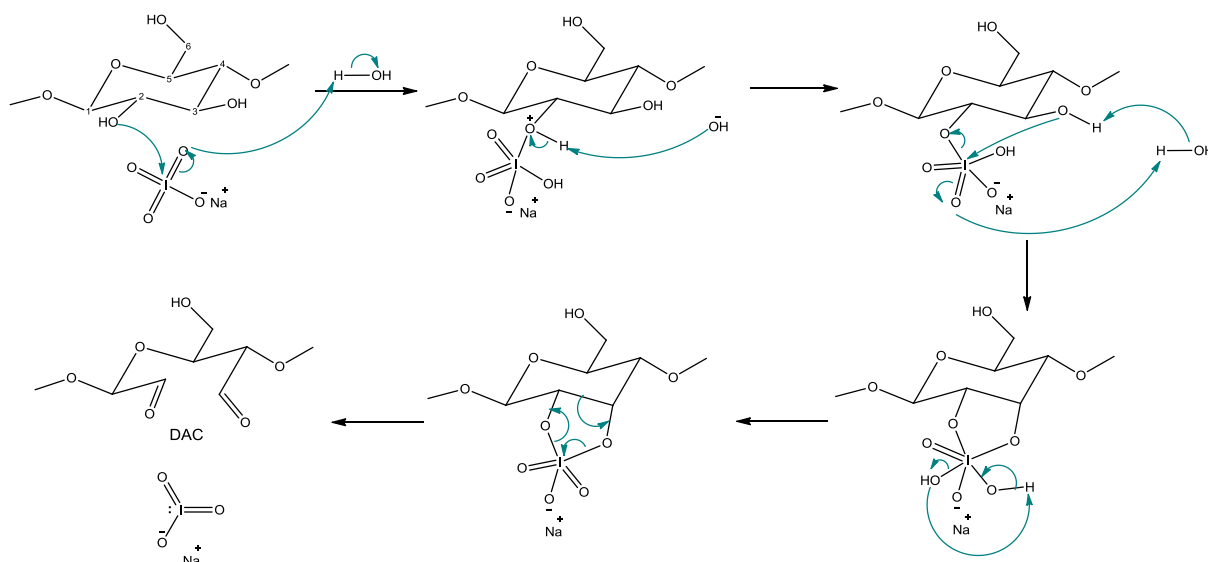


Scheme 4. (a) Regioselective TEMPO oxidation of the C6 primary alcohol into carboxylate group with a cyclic transition state – (b) catalytic cycle of TEMPO regeneration using NaOCl/NaBr as stoichiometric oxidant⁹².

- Periodate oxidation

The periodate oxidation is the only cellulose chemical modification method that selectively opens the glucose ring. The metaperiodate structure allows a selective oxidation of the two vicinal secondary alcohol in C₂ and C₃ position into aldehyde, by a bond cleavage. The general mechanism of the ring opening oxidation which implies the formation of iodine bridge between the C₂ and C₃ alcohols is described in **Scheme 5**. This oxidation method is heterogeneous since the sodium (*meta*)periodate salt is soluble in water, while cellulose is dispersed in water. The product obtained with this reaction is called dialdehyde cellulose (DAC). This periodate oxidation is characterized by a degree of oxidation (DO). The DO represents the

average number of aldehyde function introduced per AGU. The maximum DO which can be obtained is 2, corresponding to a fully oxidized DAC, where each oxidized AGU possesses two aldehyde functions. Consequently, a DO of 1 results in the half of the hydroxyl groups oxidized. Kim *et al.*⁷⁶ showed that the oxidation of microfibrils results in a decrease of its crystallinity.



Scheme 5. Periodate oxidation mechanism of vicinal hydroxyl groups of cellulose by C₂–C₃ cleavage.

III. From lignocellulosic biomass to furanic building blocks and polymers

Due to its considerable diversity, lignocellulosic biomass offers many possible routes for the elaboration of platform molecules for green chemistry or for application as biofuels²⁶. However, because of its structure complexity, the use of lignocellulosic biomass for building-blocks chemical generation requires the extraction and purification of these raw materials. Several techniques of extraction exist in the literature^{93–95}. The separation of lignin/cellulose/hemicellulose biomacromolecules is a complex process, usually accomplished by hydrolysis. For example, cellulose extraction is performed by enzymatic hydrolysis, giving glucose molecules while the extraction of lignin and/or hemicellulose is performed by acidic or basic hydrolysis. Lignin and hemicellulose do not possess the same stability depending on the pH. Indeed, hemicellulose is soluble in acidic environment (pH = 1-2) while a basic media (pH = 10-12) is required to solubilize lignin.

After hydrolysis of cellulose and hemicellulose, the resulting pentoses (xylose, arabinose...) or hexoses (fructose, glucose, mannose...) can undergo a series of reactions to generate a multitude of platform molecules. Carbohydrates are particularly interesting because they are

considered as the most important natural alternative resource of carbon in regards to oil and coal⁹⁶. The main reactions involved in the process of sugars conversion are described below:

- Fermentative conversion of carbohydrate into several acids (*e.g.* lactic, succinic, glutamic), but also into ethanol, butanol, or CO₂^{93,97,98}.
- Hydrogenolysis reactions which result in the cleavage of C-C and C-O bonds of carbohydrates by hydrogen and allow direct access to valuable chemicals such as alkanes, alcohols, and polyols like methanol, glycerol, or erythritol⁹⁹.
- Dehydration reaction of carbohydrates into a great variety of furan derivatives compounds such as furfural (FF) or 5-hydroxymethylfurfural (HMF)⁹⁶ (**Figure 6**).

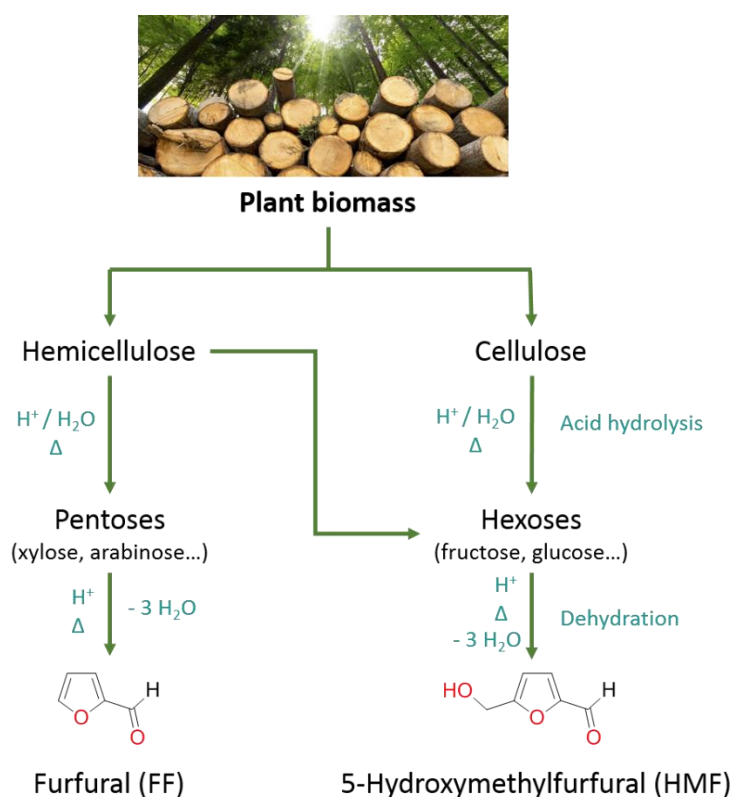


Figure 6. Production of furfural and 5-hydroxymethylfurfural from plant biomass.

This last strategy of dehydration pathway has required much effort and attention these last decades, particularly in the case of furanic compounds. These compounds are considered to have a great potential for the design of fuels and chemicals. A recent review of Bozell *et al.*¹⁰⁰ revisits the famous classification of US Department of Energy¹⁰¹, describing the high potential of furfural (FF) and 5-hydroxymethylfurfural (HMF) as part of the “Top 10+4” interesting compounds.

The HMF possesses a high potential demand^{93,102} because of its high ability to generate new green building block as shown in **Figure 7**. For polymers, 2,5-furandicarboxylic acid (FDCA) is able to replace terephthalic or isophthalic acids in the design of polyamides, polyesters, and polyurethanes¹⁰³.

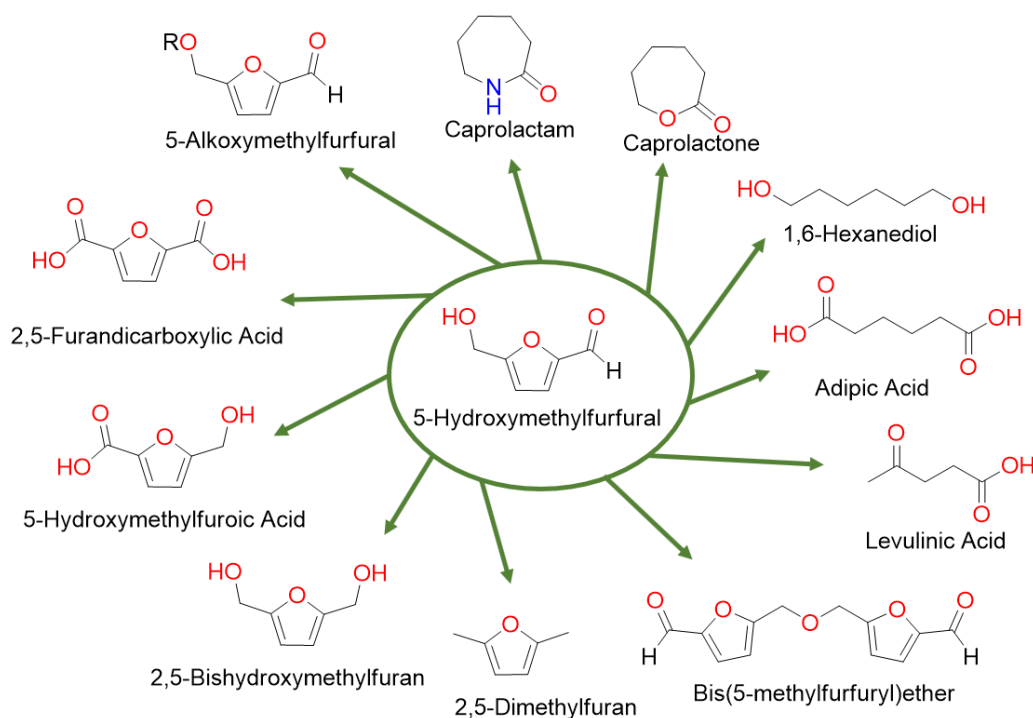


Figure 7. Building block molecules obtained from 5-hydroxymethylfurfural (HMF)⁹⁶.

Furfural (FF) represents another very important building block obtained from biorefinery, being the precursor of several high potential molecules as shown in **Figure 8**. FF is obtained from pentose (mainly xylose from agricultural waste) through an acidic hydrolysis undergoing a triple dehydration^{93,103}. FF can also be obtained from petro-based compounds, but such a synthesis pathway is not economically viable. The chemistry of FF is continuously developing. The most frequent derivatization of FF is for the preparation of furfuryl alcohol (FA).

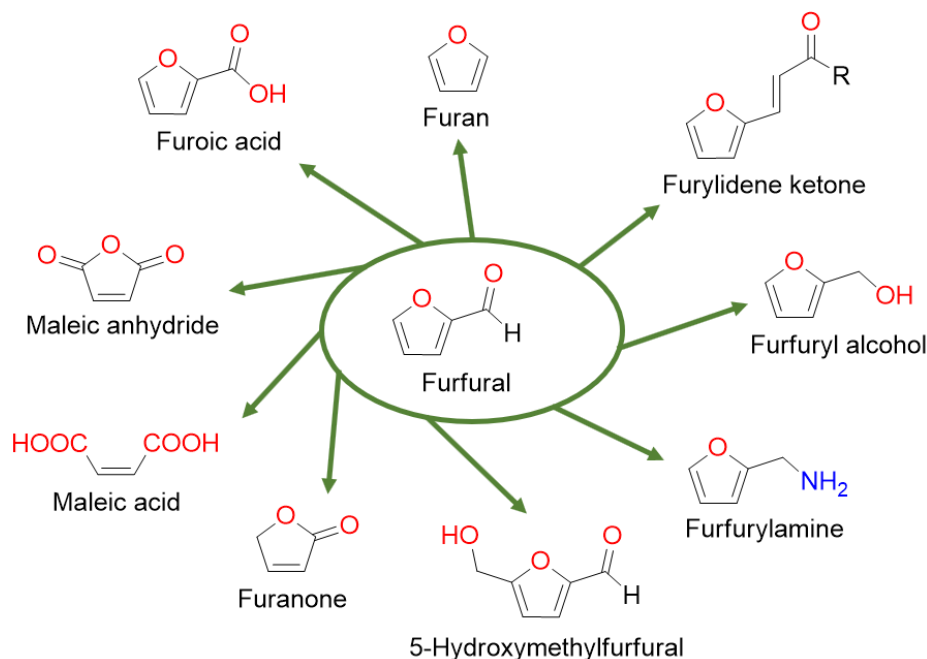


Figure 8. Primary products directly synthesized from furfural (FF)^{93,104}.

III.1. Furfuryl alcohol

III.1.1. Synthesis of furfuryl alcohol

The furfuryl alcohol (FA) is one of the most important building blocks generated from FF. Nowadays, the FF is used as extraction agent, as solvent, or as starting compound for the production of biofuels^{104,105}; however, 85 % of its worldwide production is converted in FA¹⁰⁶. This high conversion is due to the multitude of industrial applications, particularly because of its ability to polymerize.

Industrially, the FA is directly obtained by catalytic hydrogenation of FF *via* two possible ways of reduction: reduction in vapor phase or in liquid phase^{93,107}. In liquid phase, the reduction requires high pressures and temperatures. These drastic experimental conditions favorize the formation of side-products resulting of the furanic ring opening. In vapor phase, the possibility to use a catalyst increases the selectivity. The selectivity depends on the catalyst used which can lead to either FA, or secondary products such as 2-methylfuran and tetrahydrofurfuryl alcohol.

For 50 years, the catalyst used for these both pathways is Adkins catalyst (CuCr-based catalyst) with a maximum yield of 98 %. Today, the use of other catalysts like Cu/MgO, Cu/Ca/SiO₂, or Pt/TiO₂/SiO₂ is preferred because of their lower toxicity. Some alloys of Fe-Ni-B or Mo-Co-B

can also be used for dehydration of FF in liquid phase. These two examples of alloys are very interesting as they present a yield of 100 % at a temperature of 100 °C and a pressure of 1 MPa⁹³.

III.1.2. Properties, reactivity, and applications

Besides its great potential as a renewable “building block”, the furanic ring of furfuryl alcohol (FA) possesses a very peculiar chemical behavior, which is often different from their thiophene and pyrrole homologues. The dienic character of FA is more important while furan heterocycle possesses a lower aromaticity¹⁰⁸. Concerning FA stereochemistry, Barsberg *et al.*¹⁰⁹ have shown the preponderance of two conformers on a total of five at room temperature. This assertion has been completed by the work of Araujo-Andrade *et al.*¹¹⁰ who have fruitfully explored the energy barrier for FA conformational isomerization, highlighting *in fine* three stable conformations instead of five.

Nevertheless, FA is a carcinogenic, cytotoxic, and neurotoxic compound^{111,112}. FA is a yellowish liquid at ambient temperature presenting the following physical properties:

- Molar mass = 98.1 g.mol⁻¹
- Melting point = -29 °C
- Boiling point = 170 °C (1 atm)
- Density = 1.135 g.mL⁻¹ (at 20 °C)
- Dipole moment = 1.9 D

By the furan moieties and the presence of hydroxymethyl groups, FA is miscible in water, in various organic solvents (ether, ketone), and in low molecular weight alcohols. As a result, FA is commonly used as a wetting agent or as solvent^{108,113} and co-solvent¹¹⁴. Because of the presence of the hydroxymethyl group, the FA reactivity is close to classical primary alcohols, which means that FA can be subject to oxidation, esterification, etherification, etc.¹¹³ leading to various furanic derivatives. The FA furan ring reactivity has been exhaustively investigated for the design of new generation of lignocellulosic biofuels. As an example, catalytic hydrogenation reactions lead to produce promising gasoline components such as 2-methylfuran or 2-methyltetrahydrofuran¹¹⁵.

Concerning the FA behavior into acido-basic media, FA is relatively stable in basic environment, while it forms a highly reactive carbenium ion under acidic conditions. In diluted acidic media, the furanic ring opens and leads to aliphatic carboxylic acids^{116,117}. Previous studies pointed out the ability of FA to lead to levulinic acid^{118,119}, a green building-block used

as precursor for various products (γ -valerolactone, alkane derivatives,...)¹²⁰⁻¹²². In strong acidic conditions, the FA forms a very reactive carbocation and can then polymerize into poly(furfuryl alcohol) (PFA), a thermoset matrix.

Nowadays, the elaboration of PFA is the main industrial use of FA. Unlike the monomer, PFA thermoset is not toxic. PFA can be used in various applications:

- For wood industry, for reinforcement^{123,124} or adhesives^{125,126}
- As binders¹²⁷, for several applications such as porous materials for methane storage¹²⁸
- For corrosion and fire-resistant materials^{108,129,130}
- For sand consolidation for foundry molds^{131,132}.

PFA is also considered as a preferential polymer precursor for the elaboration of advanced material like carbon electrodes¹³³, carbon nanospheres¹³⁴, batteries¹³⁵, or membranes (gas separation^{136,137}, water desalination¹³⁸). This thermoset is also used in the formulation of composites in combination with natural fibers (lignin¹³⁹, cellulose¹⁴⁰, kenaf¹⁴¹), clays⁵³, silica¹⁴², or tannin¹⁴³. PFA is considered as a sustainable alternative of phenolic resins for wood impregnation and wood marine application.

As PFA presents lower chemical hazard than its monomer, it explains why the physico-chemical knowledge of the polymerization pathway is of high significance for production of stable resins.

III.1.3. From furfuryl alcohol to poly(furfuryl alcohol): polymerization mechanism

The polymerization of furfuryl alcohol occurs in acidic conditions. Mechanistic studies have been investigated using different acid catalysts:

- Brönsted acids: phosphoric acid¹⁴⁴, sulfuric acid¹⁴⁵
- Organic acids: *p*-toluene sulfonic acid^{146,147}, maleic anhydride^{148,149}, trifluoroacetic acid¹⁵⁰
- Lewis acid: TiCl₄¹⁵¹, SnCl₄¹⁵¹, ZnCl₂¹²⁹, iodine^{152,153}.

The FA polymerization is an exothermic reaction which proceeds *via* a complex mechanism which can be mostly discriminated in two steps.

In liquid phase, the first step is induced by the acid catalyst. It consists in the condensation of a hydroxymethyl group on the C₅ position of another FA molecule associated with dehydration. This was proposed by Dunlop and Peters¹¹³ in 1953 and was later confirmed by other studies¹⁵¹.

In consequence of these condensation reactions, furan rings are connected by methylene bridges generating linear oligomers and prepolymers¹⁰³ (**Figure 9(a)**). In a lesser extent, it can be noticed that the formation of a dimethylether bridge between two furan rings can also occur by a head-to-head condensation. Although, the amount of such structure is very small¹⁵⁴ because this structure tends to revert to methylene linkage with the loss of formaldehyde¹⁵⁵. As illustrated in **Figure 9(b)**, chromophores with highly conjugated sequences are generated by successive release of hydride and proton^{108,151}.

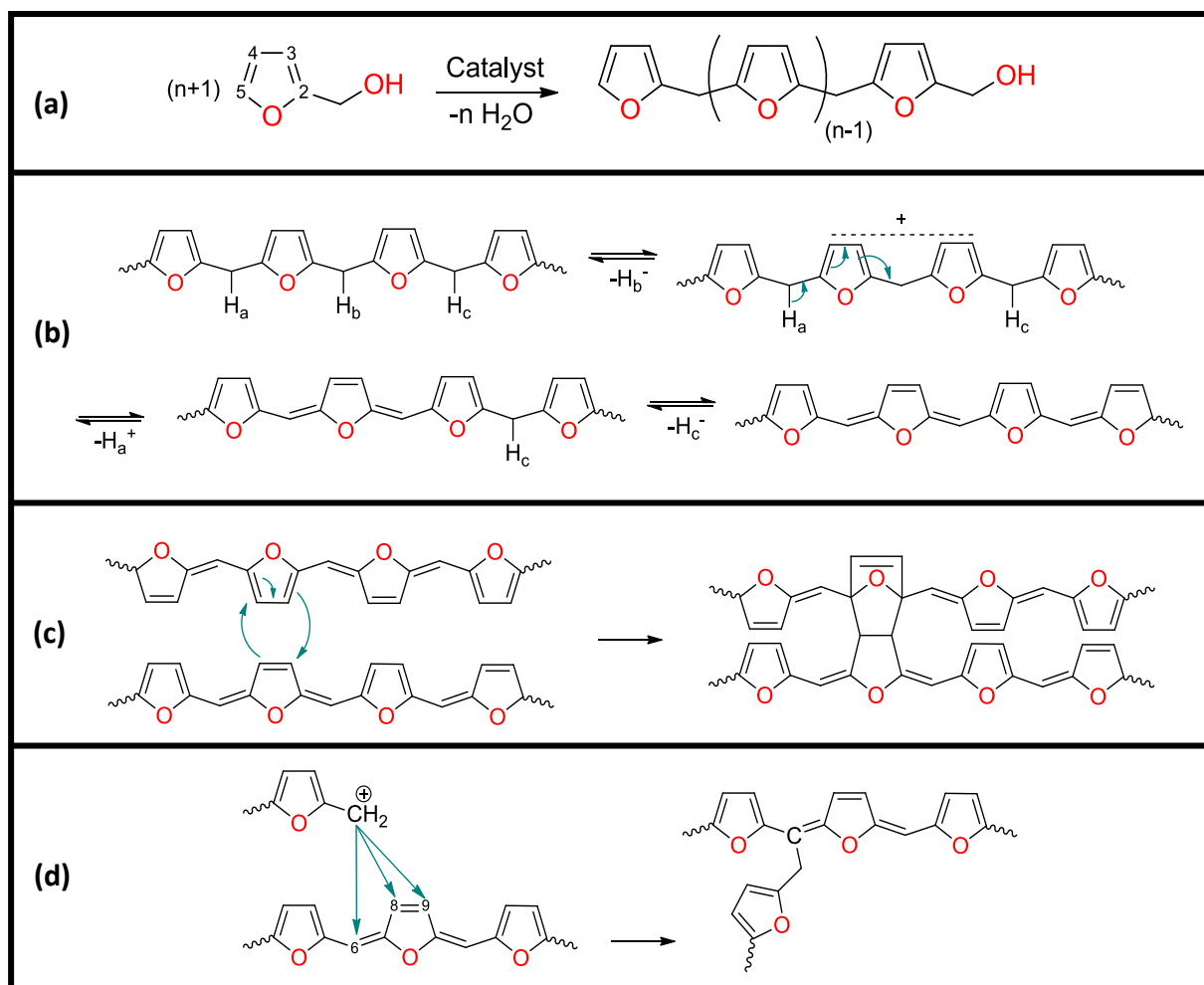


Figure 9. Polymerization of FA: **(a)** oligomerization through acid catalyzed polycondensation; **(b)** formation of conjugated sequences; **(c)** cross-linking by Diels-Alder cycloadditions; **(d)** potential cross-linking by electrophilic addition.

After completion of oligomerization, the second step starts. The linear oligomers cross-link to form the final 3-D network. Two possible pathways can be observed:

- Electrophilic additions of conjugated sequences as illustrated in **Figure 9(d)** have been suggested by Maciel *et al.*¹⁵⁶ and deepened by other authors^{147,152,157}. Through an

ab-initio modelling study, Montero *et al.*¹⁵⁸ highlighted a preferential electrophilic attack on the C₆ rather than C₈ or C₉ positions.

- Diel-Alder cycloadditions occur between the furan rings (diene) and the dihydrofuranic cycles (dienophile) as presented in **Figure 9(c)**. Choura *et al.*¹⁵¹ argued this mechanism by a deep study based on model molecules and demonstrate that this pathway is the most favorable for PFA cross-link.

It is also noteworthy that during the first step of polymerization, ring opening reactions can occur within the oligomers (**Figure 10**). Conley *et al.*¹⁵⁵ highlighted the presence of these γ -diketonic sequences by IR. However, more recent studies by spectroscopy^{151,159} or by theoretical calculations¹⁶⁰ demonstrate that there is only a few amount of the ring opening reactions. As demonstrated in a recent study, side reactions can be enhanced in presence of polar protic solvent, thus, decreasing significantly the degree of cross-link^{161,162}.

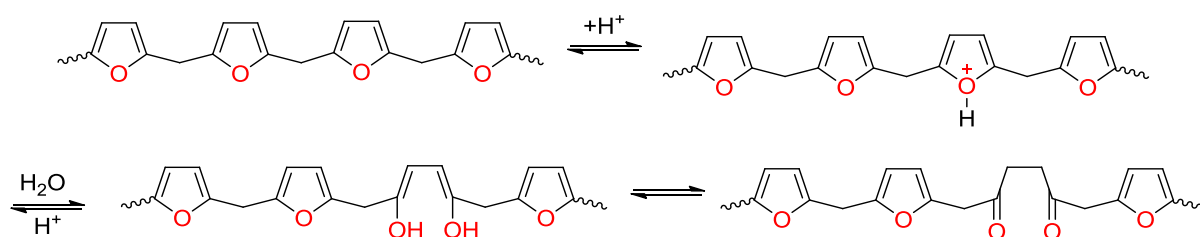


Figure 10. Side reaction of furanic ring-opening during FA polymerization.

The overall kinetic of FA polymerization has been investigated by liquid chromatography (LC)¹⁵³ or gel permeation chromatography (GPC)¹⁴⁵, revealing a complex mechanism. However, these techniques are limited by the physico-chemical modifications such as the decrease of the medium polarity (from polar FA to apolar PFA), and the high increase of viscosity during the polycondensation, and especially during cross-linking. To overcome these problems, DSC studies have been performed. This technique seems to be more adapted for kinetic analyses of polymerization as the measurement of heat flow variation is still possible on the entire range of reaction despite the high variation of viscosity.

The first investigation based on DSC data using ‘classical’ kinetic method have been performed in 1979 by Milkovic *et al.*¹⁴⁶, revealing a multi-step mechanism varying with both the temperature and the extent of cure. But in the case of a complex mechanism, the ‘classical’ empirical kinetic methods based on a reaction model are not relevant. In order to have an overall understanding of the polymerization process of FA, Guigo *et al.*¹⁴⁹ used advanced isoconversional methods^{163,164}, giving access to the apparent activation energy calculated for each extent of conversion, without the need of a reaction model for the polymerization

mechanism. This ‘model-free’ method, associated to rheological data and applied to the PFA cross-linking reaction, has been very powerful to discriminate each variation of the apparent activation energy during the entire polymerization process, and supplying another contribution on reactivity understanding of polycondensation and cross-linking.

IV. References

- (1) Moon, R. J.; Martini, A.; Nairn, J.; Simonsen, J.; Youngblood, J. Cellulose Nanomaterials Review: Structure, Properties and Nanocomposites. *Chem. Soc. Rev.* **2011**, *40* (7), 3941.
- (2) Chaffey, N. An Introduction to Plant Structure and Development. Plant Anatomy for the Twenty-First Century. *Ann. Bot.* **2011**, *108* (3), vi–vii.
- (3) Parambath Kanoth, B.; Claudino, M.; Johansson, M.; Berglund, L. A.; Zhou, Q. Biocomposites from Natural Rubber: Synergistic Effects of Functionalized Cellulose Nanocrystals as Both Reinforcing and Cross-Linking Agents via Free-Radical Thiol–ene Chemistry. *ACS Appl. Mater. Interfaces* **2015**, *7* (30), 16303–16310.
- (4) Sun, Y.; Cheng, J. Hydrolysis of Lignocellulosic Materials for Ethanol Production: A Review. *Bioresour. Technol.* **2002**, *83* (1), 1–11.
- (5) Payen, A. *Comptes rendus* **1839**, *8*, 51.
- (6) Brongniart, A.; Pelouze, T.; Dumas, A. Rapport Sur Un Mémoire de M. Payen, Relatif à La Composition de La Matière Ligneuse. In *Comptes rendus hebdomadaires des séances de l'Académie des Sciences*; **1839**; p 51.
- (7) Nechyporchuk, O.; Belgacem, M. N. Production of Cellulose Nanofibrils: A Review of Recent Advances. *Ind. Crops Prod.* **2016**, *93*, 2–25.
- (8) Klemm, D.; Heublein, B.; Fink, H.-P.; Bohn, A. Cellulose: Fascinating Biopolymer and Sustainable Raw Material. *Angew. Chemie Int. Ed.* **2005**, *44* (22), 3358–3393.
- (9) Varshney, V. K.; Naithani, S. Chemical Functionalization of Cellulose Derived from Nonconventional Sources. In *Cellulose Fibers: Bio- and Nano-Polymer Composites*; Springer Berlin Heidelberg, **2011**; 43–60.
- (10) Kumar, V.; Dhall, P.; Kumar, R.; Kumar, A. Bioconversion of Lignocellulosic Biomass for Bioethanol Production. In *Biofuels Production*; John Wiley & Sons, **2013**; 85–118.
- (11) Wohler, J.; Bergensträhle-Wohler, M.; Berglund, L. A. Deformation of Cellulose Nanocrystals: Entropy, Internal Energy and Temperature Dependence. *Cellulose* **2012**, *19* (6), 1821–1836.
- (12) Altaner, C. M.; Thomas, L. H.; Fernandes, A. N.; Jarvis, M. C. How Cellulose Stretches: Synergism between Covalent and Hydrogen Bonding. *Biomacromolecules* **2014**, *15* (3), 791–798.
- (13) Isikgor, F. H.; Becer, C. R. Lignocellulosic Biomass: A Sustainable Platform for the Production of Bio-Based Chemicals and Polymers. *Polym. Chem.* **2015**, *6* (25), 4497–4559.
- (14) McNamara, J. T.; Morgan, J. L. W.; Zimmer, J. A Molecular Description of Cellulose Biosynthesis. *Annu. Rev. Biochem.* **2015**, *84*, 895–921.
- (15) Saxena, I. M.; Brown, R. M.; JR. Cellulose Biosynthesis: Current Views and Evolving Concepts. *Ann. Bot.* **2005**, *96* (1), 9–21.
- (16) Delmer, D. P. Cellulose Biosynthesis. *Annu. Rev. Plant Physiol.* **1987**, *38* (1), 259–290.
- (17) Brown, R. M. Cellulose Microfibril Assembly and Orientation: Recent Developments. *J. Cell Sci. Suppl.* **1985**, *2*, 13–32.
- (18) Finaev, D. Some Aspects of Cellulose Biosynthesis. *Biol. Plant.* **2007**, *51* (3), 407–413.

- (19) O’sullivan, A. C. Cellulose: The Structure Slowly Unravels. *Cellulose* **1997**, 4 (3), 173–207.
- (20) Beg, Q. K.; Kapoor, M.; Mahajan, L.; Hoondal, G. S. Microbial Xylanases and Their Industrial Applications: A Review. *Appl. Microbiol. Biotechnol.* **2001**, 56 (3–4), 326–338.
- (21) Saha, B. C. Hemicellulose Bioconversion. *J. Ind. Microbiol. Biotechnol.* **2003**, 30 (5), 279–291.
- (22) De Jong, E.; Gosselink, R. J. A. Lignocellulose-Based Chemical Products. In *Bioenergy research: advances and applications*; Elsevier, **2014**; Vol. 18, 277.
- (23) Huffman, F. G. Uronic Acids. In *Encyclopedia of Food Sciences and Nutrition*; Academic Press,; 5890–5896.
- (24) Scheller, H. V.; Ulvskov, P. Hemicelluloses. *Annu. Rev. Plant Biol.* **2010**, 61 (1), 263–289.
- (25) Agbor, V. B.; Cicek, N.; Sparling, R.; Berlin, A.; Levin, D. B. Biomass Pretreatment: Fundamentals toward Application. *Biotechnol. Adv.* **2011**, 29 (6), 675–685.
- (26) Kamm, B.; Kamm, M.; Schmidt, M.; Hirth, T.; Schulze, M. Lignocellulose-Based Chemical Products and Product Family Trees. In *Biorefineries-Industrial Processes and Products*; Wiley-VCH Verlag GmbH, **2008**, 97–149.
- (27) Abdel-Hamid, A. M.; Solbiati, J. O.; Cann, I. K. O. Insights into Lignin Degradation and Its Potential Industrial Applications. *Adv. Appl. Microbiol.* **2013**, 82, 1–28.
- (28) Ke, J.; Laskar, D. D.; Chen, S. Biodegradation of Hardwood Lignocellulosics by the Western Poplar Clearwing Borer, *Paranthrene Robiniae* (Hy. Edwards). *Biomacromolecules* **2011**, 12 (5), 1610–1620.
- (29) Belgacem, M. N.; Gandini, A. *Monomers, Polymers and Composites from Renewable Resources*; Elsevier, **2008**.
- (30) Azadi, P.; Inderwildi, O. R.; Farnood, R.; King, D. A. Liquid Fuels, Hydrogen and Chemicals from Lignin: A Critical Review. *Renew. Sustain. Energy Rev.* **2013**, 21, 506–523.
- (31) Zogaj, X.; Nimtz, M.; Rohde, M.; Bokranz, W.; Romling, U. The Multicellular Morphotypes of Salmonella Typhimurium and Escherichia Coli Produce Cellulose as the Second Component of the Extracellular Matrix. *Mol. Microbiol.* **2001**, 39 (6), 1452–1463.
- (32) Stromme, M.; Mihranyan, A.; Ek, R. What to Do with All These Algae? *Mater. Lett.* **2002**, 57 (3), 569–572.
- (33) Pecoraro, É.; Manzani, D.; Messaddeq, Y.; Ribeiro, S. J. L. Bacterial Cellulose from Glucanacetobacter Xylinus: Preparation, Properties and Applications. In *Monomers, Polymers and Composites from Renewable Resources*; Elsevier, **2008**; 369.
- (34) Biermann, C. J. *Handbook of Pulping and Papermaking*; Elsevier, **1996**.
- (35) Herrick, F. W.; Casebier, R. L.; Hamilton, J. K.; Sandberg, K. R. Microfibrillated Cellulose: Morphology and Accessibility. In *J. Appl. Polym. Sci.: Appl. Polym. Symp.*; **2012**; Vol. 37, 57–65.
- (36) Turbak, A. F.; Snyder, F. W.; Sandberg, K. R. Microfibrillated Cellulose, a New Cellulose Product: Properties, Uses, and Commercial Potential. *J. Appl. Polym. Sci. Appl. Polym. Symp.*; (United States) **1982**, 37.
- (37) Siró, I.; Plackett, D. Microfibrillated Cellulose and New Nanocomposite Materials: A Review. *Cellulose* **2010**, 17 (3), 459–494.
- (38) Henriksson, M.; Henriksson, G.; Berglund, L. A.; Lindström, T. An Environmentally Friendly

- Method for Enzyme-Assisted Preparation of Microfibrillated Cellulose (MFC) Nanofibers. *Eur. Polym. J.* **2007**, *43* (8), 3434–3441.
- (39) Lavoine, N.; Desloges, I.; Dufresne, A.; Bras, J. Microfibrillated Cellulose – Its Barrier Properties and Applications in Cellulosic Materials: A Review. *Carbohydr. Polym.* **2012**, *90* (2), 735–764.
- (40) Chinga-Carrasco, G. Cellulose Fibres, Nanofibrils and Microfibrils: The Morphological Sequence of MFC Components from a Plant Physiology and Fibre Technology Point of View. *Nanoscale Res. Lett.* **2011**, *6* (1), 417.
- (41) Siqueira, G.; Bras, J.; Dufresne, A.; Siqueira, G.; Bras, J.; Dufresne, A. Cellulosic Bionanocomposites: A Review of Preparation, Properties and Applications. *Polymers* **2010**, *2* (4), 728–765.
- (42) Iwamoto, S.; Kai, W.; Isogai, A.; Iwata, T. Elastic Modulus of Single Cellulose Microfibrils from Tunicate Measured by Atomic Force Microscopy. *Biomacromolecules* **2009**, *10* (9), 2571–2576.
- (43) Sakurada, I.; Nukushina, Y.; Ito, T. Experimental Determination of the Elastic Modulus of Crystalline Regions in Oriented Polymers. *J. Polym. Sci.* **1962**, *57* (165), 651–660.
- (44) Favier, V.; Chanzy, H.; Cavaille, J. Y. Polymer Nanocomposites Reinforced by Cellulose Whiskers. *Macromolecules* **1995**, *28* (18), 6365–6367.
- (45) Dufresne, A. Polysaccharide Nano Crystal Reinforced Nanocomposites. *Can. J. Chem.* **2008**, *86* (6), 484–494.
- (46) Dufresne, A.; Dufresne, Alain. Processing of Polymer Nanocomposites Reinforced with Polysaccharide Nanocrystals. *Molecules* **2010**, *15* (6), 4111–4128.
- (47) Habibi, Y.; Lucia, L. A.; Rojas, O. J. Cellulose Nanocrystals: Chemistry, Self-Assembly, and Applications. *Chem. Rev.* **2010**, *110* (6), 3479–3500.
- (48) Gray, D.; Gray, G., D. Recent Advances in Chiral Nematic Structure and Iridescent Color of Cellulose Nanocrystal Films. *Nanomaterials* **2016**, *6* (11), 213.
- (49) De France, K. J.; Hoare, T.; Cranston, E. D. Review of Hydrogels and Aerogels Containing Nanocellulose. *Chem. Mater.* **2017**, *29* (11), 4609–4631.
- (50) Xu, C.; Lv, Q.; Wu, D.; Wang, Z. Polylactide/Cellulose Nanocrystal Composites: A Comparative Study on Cold and Melt Crystallization. *Cellulose* **2017**, *24* (5), 2163–2175.
- (51) Wan, H.; Li, X.; Zhang, L.; Li, X.; Liu, P.; Jiang, Z.; Yu, Z.-Z. Rapidly Responsive and Flexible Chiral Nematic Cellulose Nanocrystal Composites as Multifunctional Rewritable Photonic Papers with Eco-Friendly Inks. *ACS Appl. Mater. Interfaces* **2018**, *10* (6), 5918–5925.
- (52) Natterodt, J. C.; Meesorn, W.; Zoppe, J. O.; Weder, C. Functionally Graded Polyurethane/Cellulose Nanocrystal Composites. *Macromol. Mater. Eng.* **2018**, *303* (6), 1700661.
- (53) Pranger, L.; Tannenbaum, R. Biobased Nanocomposites Prepared by In Situ Polymerization of Furfuryl Alcohol with Cellulose Whiskers or Montmorillonite Clay. *Macromolecules* **2008**, *41* (22), 8682–8687.
- (54) Qu, P.; Gao, Y.; Wu, G.; Zhang, L. Nanocomposites of Poly(Lactic Acid) Reinforced with Cellulose Nanofibrils. *BioResources* **2010**, *5* (3), 1811–1823.
- (55) Venkatesh, A.; Thunberg, J.; Moberg, T.; Klingberg, M.; Hammar, L.; Peterson, A.; Müller, C.; Boldizar, A. Cellulose Nanofibril-Reinforced Composites Using Aqueous Dispersed Ethylene-

- Acrylic Acid Copolymer. *Cellulose* **2018**, 25 (8), 4577–4589.
- (56) Phiri, J.; Johansson, L.-S.; Gane, P.; Maloney, T. A Comparative Study of Mechanical, Thermal and Electrical Properties of Graphene-, Graphene Oxide- and Reduced Graphene Oxide-Doped Microfibrillated Cellulose Nanocomposites. *Compos. Part B Eng.* **2018**, 147, 104–113.
- (57) Guo, W.; Wang, X.; Zhang, P.; Liu, J.; Song, L.; Hu, Y. Nano-Fibrillated Cellulose-Hydroxyapatite Based Composite Foams with Excellent Fire Resistance. *Carbohydr. Polym.* **2018**, 195, 71–78.
- (58) Niazi, M. B. K.; Jahan, Z.; Berg, S. S.; Gregersen, Ø. W. Mechanical, Thermal and Swelling Properties of Phosphorylated Nanocellulose Fibrils/PVA Nanocomposite Membranes. *Carbohydr. Polym.* **2017**, 177, 258–268.
- (59) Messiry, M. E. Morphological Analysis of Micro-Fibrillated Cellulose from Different Raw Materials for Fiber Plastic Composites. *J. Text. Sci. Eng.* **2014**, 04 (05), 1–8.
- (60) Kumode, M. M. N.; Bolzon, G. I. M.; Magalhães, W. L. E.; Kestur, S. G. Microfibrillated Nanocellulose from Balsa Tree as Potential Reinforcement in the Preparation of ‘Green’ Composites with Castor Seed Cake. *J. Clean. Prod.* **2017**, 149, 1157–1163.
- (61) Solikhin, A.; Murayama, K. Enhanced Properties of Poly(Vinyl Alcohol) Composite Films Filled with Microfibrillated Cellulose Isolated from Continuous Steam Explosion. *Int. J. Plast. Technol.* **2018**, 22 (1), 122–136.
- (62) He, X.; Fan, X.; Feng, W.; Chen, Y.; Guo, T.; Wang, F.; Liu, J.; Tang, K. Incorporation of Microfibrillated Cellulose into Collagen-Hydroxyapatite Scaffold for Bone Tissue Engineering. *Int. J. Biol. Macromol.* **2018**, 115, 385–392.
- (63) Alfthan, E.; de Ruvo, A.; Brown, W. Glass Transition Temperatures of Oligosaccharides. *Polymer* **1973**, 14 (7), 329–330.
- (64) Szcześniak, L.; Rachocki, A.; Tritt-Goc, J. Glass Transition Temperature and Thermal Decomposition of Cellulose Powder. *Cellulose* **2008**, 15 (3), 445–451.
- (65) Nordin, S. B.; Nyren, J. O.; Back, E. L. Note on Molten Cellulose Produced in a Laser Beam. *Sven. papperstidning* **1973**.
- (66) *Renewable Resources for Functional Polymers and Biomaterials*; Williams, P. A., Ed.; Polymer Chemistry Series; Royal Society of Chemistry: Cambridge, **2011**.
- (67) Ganster, J.; Fink, H.-P. Cellulose and Cellulose Acetate. In *Bio-Based Plastics*; Kabasci, S., Ed.; John Wiley & Sons, **2013**; 35–62.
- (68) Kamide, K.; Saito, M. Thermal Analysis of Cellulose Acetate Solids with Total Degrees of Substitution of 0.49, 1.75, 2.46, and 2.92. *Polym. J.* **1985**, 17 (8), 919–928.
- (69) Bao, C. Cellulose Acetate / Plasticizer Systems : Structure, Morphology and Dynamics, Université Claude Bernard - Lyon I, 2015.
- (70) Fischer, S.; Thümmel, K.; Volkert, B.; Hettrich, K.; Schmidt, I.; Fischer, K. Properties and Applications of Cellulose Acetate. *Macromol. Symp.* **2008**, 262 (1), 89–96.
- (71) Law, R. C. 5. Applications of Cellulose Acetate— 5.1 Cellulose Acetate in Textile Application. *Macromol. Symp.* **2004**, 208 (1), 255–266.
- (72) Huang, K.; Wang, B.; Cao, Y.; Li, H.; Wang, J.; Lin, W.; Mu, C.; Liao, D. Homogeneous Preparation of Cellulose Acetate Propionate (CAP) and Cellulose Acetate Butyrate (CAB) from Sugarcane Bagasse Cellulose in Ionic Liquid. *J. Agric. Food Chem.* **2011**, 59 (10), 5376–5381.

- (73) Coffey, D. G.; Bell, D. A.; Henderson, A. Cellulose and Cellulose Derivatives. In *Food Polysaccharides and Their Applications*; Stephen, A. M., Phillips, G. O., Williams, P. A., Eds.; 2006; pp 147–180.
- (74) Samaranayake, G.; Glasser, W. G. Cellulose Derivatives with Low DS. I. A Novel Acylation System. *Carbohydr. Polym.* **1993**, *22* (1), 1–7.
- (75) Fink, J. K. Polysaccharides. In *Handbook of Engineering and Specialty Thermoplastics*; John Wiley & Sons, **2011**; 69–108.
- (76) Kim, U.-J.; Kuga, S.; Wada, M.; Okano, T.; Kondo, T. Periodate Oxidation of Crystalline Cellulose. *Biomacromolecules* **2000**, *1* (3), 188–492.
- (77) Calvini, P.; Gorassini, A.; Luciano, G.; Franceschi, E. FTIR and WAXS Analysis of Periodate Oxycellulose: Evidence for a Cluster Mechanism of Oxidation. *Vib. Spectrosc.* **2006**, *40* (2), 177–183.
- (78) Fras, L.; Johansson, L.-S.; Stenius, P.; Laine, J.; Stana-Kleinschek, K.; Ribitsch, V. Analysis of the Oxidation of Cellulose Fibres by Titration and XPS. *Colloids Surfaces A Physicochem. Eng. Asp.* **2005**, *260* (1–3), 101–108.
- (79) Yackel, E. C.; Kenyon, W. O. The Oxidation of Cellulose by Nitrogen Dioxide. *J. Am. Chem. Soc.* **1942**, *64* (1), 121–127.
- (80) de Nooy, A. E. J.; Besemer, A. C.; van Bekkum, H. Highly Selective Nitroxyl Radical-Mediated Oxidation of Primary Alcohol Groups in Water-Soluble Glucans. *Carbohydr. Res.* **1995**, *269* (1), 89–98.
- (81) Tahiri, C.; Vignon, M. R. TEMPO-Oxidation of Cellulose: Synthesis and Characterisation of Polyglucuronans. *Cellulose* **2000**, *7* (2), 177–188.
- (82) Banker, G. S.; Kumar, V. Microfibrillated Oxycellulose. US5405953, April 11, **1995**.
- (83) Heinze, T.; Koschella, A.; Liebert, T.; Harabagiu, V.; Coseri, S. Cellulose: Chemistry of Cellulose Derivatization. In *The European Polysaccharide Network of Excellence (EPNOE)*; Springer, **2012**; 283–328.
- (84) McGee, P. A.; Fowler, W. F.; Taylor, E. W.; Unruh, C. C.; Kenyon, W. O. Investigation of the Properties of Cellulose Oxidized by Nitrogen Dioxide. V. Study of Mechanism of Oxidation in Presence of Carbon Tetrachloride. *J. Am. Chem. Soc.* **1947**, *69* (2), 355–361.
- (85) Zimnitsky, D. S.; Yurkshtovich, T. L.; Bychkovsky, P. M. Synthesis and Characterization of Oxidized Cellulose. *J. Polym. Sci. Part A Polym. Chem.* **2004**, *42* (19), 4785–4791.
- (86) Isogai, A.; Kato, Y. Preparation of Polyuronic Acid from Cellulose by TEMPO-Mediated Oxidation. *Cellulose* **1998**, *5* (3), 153–164.
- (87) de Nooy, A. E. J.; Besemer, A. C.; van Bekkum, H.; van Dijk, J. A. P. P.; Smit, J. A. M. TEMPO-Mediated Oxidation of Pullulan and Influence of Ionic Strength and Linear Charge Density on the Dimensions of the Obtained Polyelectrolyte Chains. *Macromolecules* **1996**, *29* (20), 6541–6547.
- (88) Fujisawa, S.; Isogai, T.; Isogai, A. Temperature and PH Stability of Cellouronic Acid. *Cellulose* **2010**, *17* (3), 607–615.
- (89) Araki, J.; Wada, M.; Kuga, S. Steric Stabilization of a Cellulose Microcrystal Suspension by Poly(Ethylene Glycol) Grafting. *Langmuir* **2000**, *17* (1), 21–27.
- (90) Azzam, F.; Heux, L.; Putaux, J.-L.; Jean, B. Preparation By Grafting Onto, Characterization, and

Properties of Thermally Responsive Polymer-Decorated Cellulose Nanocrystals.

Biomacromolecules **2010**, *11* (12), 3652–3659.

- (91) Saito, T.; Nishiyama, Y.; Putaux, J.-L.; Vignon, M.; Isogai, A. Homogeneous Suspensions of Individualized Microfibrils from TEMPO-Catalyzed Oxidation of Native Cellulose. *Biomacromolecules* **2006**, *7* (6), 1687–1691.
- (92) Eyley, S.; Thielemans, W. Surface Modification of Cellulose Nanocrystals. *Nanoscale* **2014**, *6* (14), 7764–7779.
- (93) Corma, A.; Iborra, S.; Velty, A. Chemical Routes for the Transformation of Biomass into Chemicals. *Chem. Rev.* **2007**, *107* (6), 2411–2502.
- (94) Carneiro, F.; Duarte, L. C.; Gírio, F. M. Hemicellulose Biorefineries: A Review on Biomass Pretreatments. *J. Sci. Ind. Res.* **2008**, *67* (11), 849–864.
- (95) Alvira, P.; Tomás-Pejó, E.; Ballesteros, M.; Negro, M. J. Pretreatment Technologies for an Efficient Bioethanol Production Process Based on Enzymatic Hydrolysis: A Review. *Bioresour. Technol.* **2010**, *101* (13), 4851–4861.
- (96) van Putten, R.-J.; van der Waal, J. C.; de Jong, E.; Rasrendra, C. B.; Heeres, H. J.; de Vries, J. G. Hydroxymethylfurfural, A Versatile Platform Chemical Made from Renewable Resources. *Chem. Rev.* **2013**, *113* (3), 1499–1597.
- (97) Wolin, M. J.; Miller, T. L. Carbohydrate Fermentation. In *Human Intestinal Microflora in Health and Disease*; Academic Press, **1983**; 147–165.
- (98) Lee, S. Y.; Park, J. H.; Jang, S. H.; Nielsen, L. K.; Kim, J.; Jung, K. S. Fermentative Butanol Production by Clostridia. *Biotechnol. Bioeng.* **2008**, *101* (2), 209–228.
- (99) Ruppert, A. M.; Weinberg, K.; Palkovits, R. Hydrogenolysis Goes Bio: From Carbohydrates and Sugar Alcohols to Platform Chemicals. *Angew. Chemie Int. Ed.* **2012**, *51* (11), 2564–2601.
- (100) Bozell, J. J.; Petersen, G. R. Technology Development for the Production of Biobased Products from Biorefinery Carbohydrates—the US Department of Energy’s “Top 10” Revisited. *Green Chem.* **2010**, *12* (4), 539.
- (101) Werpy, T.; Petersen, G. *Top Value Added Chemicals from Biomass: Volume I -- Results of Screening for Potential Candidates from Sugars and Synthesis Gas*; Golden, CO (United States), **2004**.
- (102) Bicker, M.; Kaiser, D.; Ott, L.; Vogel, H. Dehydration of D-Fructose to Hydroxymethylfurfural in Sub- and Supercritical Fluids. *J. Supercrit. Fluids* **2005**, *36* (2), 118–126.
- (103) Moreau, C.; Belgacem, M. N.; Gandini, A. Recent Catalytic Advances in the Chemistry of Substituted Furans from Carbohydrates and in the Ensuing Polymers. *Top. Catal.* **2004**, *27* (1–4), 11–30.
- (104) Mariscal, R.; Maireles-Torres, P.; Ojeda, M.; Sádaba, I.; López Granados, M. Furfural: A Renewable and Versatile Platform Molecule for the Synthesis of Chemicals and Fuels. *Energy Environ. Sci.* **2016**, *9* (4), 1144–1189.
- (105) Eseyin, Anthonia, E.; Steele, Philip, H.; Philip, H. S. An Overview of the Applications of Furfural and Its Derivatives. *Int. J. Adv. Chem.* **2015**, *3* (2), 42.
- (106) Gandini, A. Polymers from Renewable Resources: A Challenge for the Future of Macromolecular Materials. *Macromolecules* **2008**, *41* (24), 9491–9504.
- (107) Zeitsch, K. J. *The Chemistry and Technology of Furfural and Its Many By-Products*;

Elsevier, **2000**.

- (108) Gandini, A.; Belgacem, M. N. Furans in Polymer Chemistry. *Prog. Polym. Sci.* **1997**, *22* (6), 1203–1379.
- (109) Barsberg, S.; Berg, R. W. Combined Raman Spectroscopic and Theoretical Investigation of Fundamental Vibrational Bands of Furfuryl Alcohol (2-Furanmethanol). *J. Phys. Chem. A* **2006**, *110* (30), 9500–9504.
- (110) Araujo-Andrade, C.; Gómez-Zavaglia, A.; Reva, I. D.; Fausto, R. Conformers, Infrared Spectrum and UV-Induced Photochemistry of Matrix-Isolated Furfuryl Alcohol. *J. Phys. Chem. A* **2012**, *116* (9), 2352–2365.
- (111) Sujatha, P. S. Monitoring Cytotoxic Potentials of Furfuryl Alcohol and 2-Furyl Methyl Ketone in Mice. *Food Chem. Toxicol.* **2008**, *46* (1), 286–292.
- (112) Savolainen, H.; Pfäffli, P. Neurotoxicity of Furfuryl Alcohol Vapor in Prolonged Inhalation Exposure. *Environ. Res.* **1983**, *31* (2), 420–427.
- (113) Dunlop, A. P.; Peter, F. N. *The Furans*; Reinhold Publishing Corporation, **1953**.
- (114) Morawski, P.; Letcher, T. M.; Naicker, P. K.; Domańska, U. Liquid–Liquid Equilibria for Mixtures of (Furfuryl Alcohol + an Aromatic Hydrocarbon + an Alkane) at T = 298.15 K. *J. Chem. Eng. data* **2002**, *47* (6), 1453–1456.
- (115) Lange, J.-P.; van der Heide, E.; van Buijtenen, J.; Price, R. Furfural-A Promising Platform for Lignocellulosic Biofuels. *ChemSusChem* **2012**, *5* (1), 150–166.
- (116) Lange, J.-P.; van de Graaf, W. D.; Haan, R. J. Conversion of Furfuryl Alcohol into Ethyl Levulinate Using Solid Acid Catalysts. *ChemSusChem* **2009**, *2* (5), 437–441.
- (117) González Maldonado, G. M.; Assary, R. S.; Dumesic, J. A.; Curtiss, L. A. Acid-Catalyzed Conversion of Furfuryl Alcohol to Ethyl Levulinate in Liquid Ethanol. *Energy Environ. Sci.* **2012**, *5* (10), 8990.
- (118) Horvat, J.; Klaić, B.; Metelko, B.; Šunjić, V. Mechanism of Levulinic Acid Formation. *Tetrahedron Lett.* **1985**, *26* (17), 2111–2114.
- (119) van de Graaf, W. D.; Lange, J.-P. Process for the Conversion of Furfuryl Alcohol into Levulinic Acid or Alkyl Levulinate. US20070049771A1, March 1, **2007**.
- (120) González Maldonado, G. M.; Assary, R. S.; Dumesic, J.; Curtiss, L. A. Experimental and Theoretical Studies of the Acid-Catalyzed Conversion of Furfuryl Alcohol to Levulinic Acid in Aqueous Solution. *Energy Environ. Sci.* **2012**, *5* (5), 6981.
- (121) Bozell, J. J.; Moens, L.; Elliott, D. .; Wang, Y.; Neuenschwander, G. .; Fitzpatrick, S. .; Bilski, R. .; Jarnefeld, J. . Production of Levulinic Acid and Use as a Platform Chemical for Derived Products. *Resour. Conserv. Recycl.* **2000**, *28* (3–4), 227–239.
- (122) Pileidis, F. D.; Titirici, M.-M. Corrigendum: Levulinic Acid Biorefineries: New Challenges for Efficient Utilization of Biomass. *ChemSusChem* **2016**, *9* (6), 652–655.
- (123) Lande, S.; Westin, M.; Schneider, M. H. Eco-Efficient Wood Protection: Furfurylated Wood as Alternative to Traditional Wood Preservation. *Manag. Environ. Qual. An Int. J.* **2004**, *15* (5), 529–540.
- (124) Lande, S.; Westin, M.; Schneider, M. Development of Modified Wood Products Based on Furan Chemistry. *Mol. Cryst. Liq. Cryst.* **2008**, *484* (1), 1/[367]-12/[378].

- (125) Belgacem, M. N.; Gandini, A. Furan-Based Adhesives. In *Handbook of Adhesive Technology*; Marcel Dekker, **2003**; 615.
- (126) Dao, L. T.; Zavarin, E. Chemically Activated Furfuryl Alcohol-Based Wood Adhesives. I. The Role of Furfuryl Alcohol. *Holzforschung* **1996**, *50* (5), 470–476.
- (127) Toriz, G.; Arvidsson, R.; Westin, M.; Gatenholm, P. Novel Cellulose Ester-Poly(Furfuryl Alcohol)-Flax Fiber Biocomposites. *J. Appl. Polym. Sci.* **2003**, *88* (2), 337–345.
- (128) Machnikowski, J.; Kierzek, K.; Lis, K.; Machnikowska, H.; Czepirski, L. Tailoring Porosity Development in Monolithic Adsorbents Made of KOH-Activated Pitch Coke and Furfuryl Alcohol Binder for Methane Storage. *Energy & Fuels* **2010**, *24* (6), 3410–3414.
- (129) Sugama, T.; Kukacka, L. E. Effect of Zinc-Levulinic Acid Chelate Compounds Formed in Furfuryl Alcohol Polymer Concrete. *J. Mater. Sci.* **1982**, *17* (7), 2067–2076.
- (130) Varbanov, S.; Borissov, G. Furfuryl-Containing Tertiary Phosphine Oxides and Polymers Based on Some of Them. *Eur. Polym. J.* **1984**, *20* (2), 185–189.
- (131) Oliva-Teles, M. T.; Delerue-Matos, C.; Alvim-Ferraz, M. C. M. Determination of Free Furfuryl Alcohol in Foundry Resins by Chromatographic Techniques. *Anal. Chim. Acta* **2005**, *537* (1–2), 47–51.
- (132) Schmitt, C. R. Polyfurfuryl Alcohol Resins. *Polym. Plast. Technol. Eng.* **1974**, *3* (2), 121–158.
- (133) Ozaki, J.; Mitsui, M.; Nishiyama, Y.; Cashion, J. D.; Brown, L. J. Effects of Ferrocene on Production of High Performance Carbon Electrodes from Poly(Furfuryl Alcohol). *Chem. Mater.* **1998**, *10* (11), 3386–3392.
- (134) Ju, M.; Zeng, C.; Wang, C.; Zhang, L. Preparation of Ultrafine Carbon Spheres by Controlled Polymerization of Furfuryl Alcohol in Microdroplets. *Ind. Eng. Chem. Res.* **2014**, *53* (8), 3084–3090.
- (135) Lee, J.; Chen, Y.-M.; Zhu, Y.; Vogt, B. D. Fabrication of Porous Carbon/TiO₂ Composites through Polymerization-Induced Phase Separation and Use As an Anode for Na-Ion Batteries. *ACS Appl. Mater. Interfaces* **2014**, *6* (23), 21011–21018.
- (136) Yong-Rong Dong; Norikazu Nishiyama; Yasuyuki Egashira; Ueyama, K. H₂-Selective Carbon Membranes Prepared from Furfuryl Alcohol by Vapor-Phase Synthesis. *Ind. Eng. Chem. Res.* **2007**, *46* (12), 4040–4044.
- (137) He, L.; Li, D.; Wang, K.; Suresh, A. K.; Bellare, J.; Sridhar, T.; Wang, H. Synthesis of Silicalite-Poly(Furfuryl Alcohol) Composite Membranes for Oxygen Enrichment from Air. *Nanoscale Res. Lett.* **2011**, *6* (1), 637.
- (138) He, L.; Li, D.; Zhang, G.; Webley, P. A.; Zhao, D.; Wang, H. Synthesis of Carbonaceous Poly(Furfuryl Alcohol) Membrane for Water Desalination. *Ind. Eng. Chem. Res.* **2010**, *49* (9), 4175–4180.
- (139) Guigo, N.; Mija, A.; Vincent, L.; Sbirrazzuoli, N. Eco-Friendly Composite Resins Based on Renewable Biomass Resources: Polyfurfuryl Alcohol/Lignin Thermosets. *Eur. Polym. J.* **2010**, *46* (5), 1016–1023.
- (140) Motaung, T. E.; Gqokoma, Z.; Linganiso, L. Z.; Hato, M. J. The Effect of Acid Content on the Poly(Furfuryl Alcohol)/Cellulose Composites. *Polym. Compos.* **2016**, *37* (8), 2434–2441.
- (141) Deka, H.; Misra, M.; Mohanty, A. Renewable Resource Based “All Green Composites” from Kenaf Biofiber and Poly(Furfuryl Alcohol) Bioresin. *Ind. Crops Prod.* **2013**, *41*, 94–101.

- (142) Zarbin, A. J. ; Bertholdo, R.; Oliveira, M. A. F. . Preparation, Characterization and Pyrolysis of Poly(Furfuryl Alcohol)/Porous Silica Glass Nanocomposites: Novel Route to Carbon Template. *Carbon N. Y.* **2002**, *40* (13), 2413–2422.
- (143) Szczurek, A.; Fierro, V.; Thébault, M.; Pizzi, A.; Celzard, A. Structure and Properties of Poly(Furfuryl Alcohol)-Tannin PolyHIPes. *Eur. Polym. J.* **2016**, *78*, 195–212.
- (144) Wewerka, E. M. An Investigation of the Polymerization of Furfuryl Alcohol with Gel Permeation Chromatography. *J. Appl. Polym. Sci.* **1968**, *12* (7), 1671–1681.
- (145) Mokoena, T. T.; Ddamba, W. A. A.; Keikotlhaile, B. M. Gel Permeation Chromatography Study of the Kinetics of Condensation of Furfuryl Alcohol in THF Solution. *South African J. Chem.* **1999**, *52* (1), 2–7.
- (146) Milkovic, J.; Myers, G. E.; Young, R. A. Interpretation of Curing Mechanism of Furfuryl Alcohol Resins. *Cellul. Chem. Technol.* **1979**, *13* (5), 651–672.
- (147) Principe, M.; Ortiz, P.; Martínez, R. An NMR Study of Poly(Furfuryl Alcohol) Prepared with p-Toluenesulphonic Acid. *Polym. Int.* **1999**, *48* (8), 637–641.
- (148) Philippou, J. L.; Zavarin, E. Differential Scanning Calorimetric and Infra-Red Spectroscopic Studies of Interactions between Lignocellulosic Materials, Hydrogen Peroxide, and Furfuryl Alcohol. *Holzforschung* **1984**, *38* (3), 119–126.
- (149) Guigo, N.; Mija, A.; Vincent, L.; Sbirrazzuoli, N. Chemorheological Analysis and Model-Free Kinetics of Acid Catalysed Furfuryl Alcohol Polymerization. *Phys. Chem. Chem. Phys.* **2007**, *9* (39), 5359.
- (150) González, R.; Martínez, R.; Ortiz, P. Polymerization of Furfuryl Alcohol with Trifluoroacetic Acid: The Influence of Experimental Conditions. *Die Makromol. Chemie* **1992**, *193* (1), 1–9.
- (151) Choura, M.; Belgacem, N. M.; Gandini, A. Acid-Catalyzed Polycondensation of Furfuryl Alcohol: Mechanisms of Chromophore Formation and Cross-Linking. *Macromolecules* **1996**, *29* (11), 3839–3850.
- (152) González, R.; Figueroa, J. M.; González, H. Furfuryl Alcohol Polymerisation by Iodine in Methylene Chloride. *Eur. Polym. J.* **2002**, *38* (2), 287–297.
- (153) González, R.; Rieumont, J.; Figueroa, J. M.; Siller, J.; González, H. Kinetics of Furfuryl Alcohol Polymerisation by Iodine in Methylene Dichloride. *Eur. Polym. J.* **2002**, *38* (2), 281–286.
- (154) Choura, M.; Belgacem, N. M.; Gandini, A. The Acid-Catalyzed Polycondensation of Furfuryl Alcohol: Old Puzzles Unravelling. *Macromol. Symp.* **1997**, *122* (1), 263–268.
- (155) Conley, R. T.; Metil, I. An Investigation of the Structure of Furfuryl Alcohol Polycondensates with Infrared Spectroscopy. *J. Appl. Polym. Sci.* **1963**, *7* (1), 37–52.
- (156) Maciel, G. E.; Chuang, I.-S.; Myers, G. E. Carbon-13 NMR Study of Cured Furfuryl Alcohol Resins Using Cross Polarization and Magic-Angle Spinning. *Macromolecules* **1982**, *15* (4), 1218–1220.
- (157) Chuang, I. S.; Maciel, G. E.; Myers, G. E. Carbon-13 NMR Study of Curing in Furfuryl Alcohol Resins. *Macromolecules* **1984**, *17* (5), 1087–1090.
- (158) Montero, A. L.; Montero, L. A.; Martínez, R.; Spange, S. Ab Initio Modelling of Crosslinking in Polymers. A Case of Chains with Furan Rings. *J. Mol. Struct. THEOCHEM* **2006**, *770* (1–3), 99–106.
- (159) Kim, T.; Jeong, J.; Rahman, M.; Zhu, E.; Mahajan, D. Characterizations of Furfuryl Alcohol

Oligomer/Polymerization Catalyzed by Homogeneous and Heterogeneous Acid Catalysts. *Korean J. Chem. Eng.* **2014**, *31* (12), 2124–2129.

- (160) Kim, T.; Assary, R. S.; Marshall, C. L.; Gosztola, D. J.; Curtiss, L. A.; Stair, P. C. Acid-Catalyzed Furfuryl Alcohol Polymerization: Characterizations of Molecular Structure and Thermodynamic Properties. *ChemCatChem* **2011**, *3* (9), 1451–1458.
- (161) Falco, G.; Guigo, N.; Vincent, L.; Sbirrazzuoli, N.; FA Polymerization Disruption by Protic Polar Solvents. *Polymers* **2018**, *10* (5), 529.
- (162) Falco, G.; Guigo, N.; Vincent, L.; Sbirrazzuoli, N. Opening Furan for Tailoring Properties of Bio-Based Poly(Furfuryl Alcohol) Thermoset. *ChemSusChem* **2018**, *11* (11), 1805–1812.
- (163) Vyazovkin, S.; Sbirrazzuoli, N. Isoconversional Kinetic Analysis of Thermally Stimulated Processes in Polymers. *Macromol. Rapid Commun.* **2006**, *27* (18), 1515–1532.
- (164) Vyazovkin, S. *Isoconversional Kinetics of Thermally Stimulated Processes*; Springer International Publishing: Cham, 2015.

Chapter V

Microfibrillar cellulose: a suitable filler
for bio-based composites within a
poly(furfuryl alcohol) matrix

I. Introduction	173
II. Experimental section	175
II.1. Chemical materials	175
II.2. FTIR Spectroscopy	175
II.3. Transmission Electronic Microscopy (TEM)	175
II.4. Differential Scanning Calorimetry (DSC)	175
II.5. Dynamic Mechanical Analysis (DMA)	176
II.6. Thermogravimetric Analysis (TGA)	176
II.7. Cellulose oxidation	176
II.8. Determination of the degree of oxidation (DO)	176
II.9. Material preparation	177
III. Results and Discussions	179
III.1. FTIR analysis	179
III.2. DSC measurements of FA polymerization in presence of MFC	180
III.3. Microscopic morphology characterization by TEM	182
III.4. Thermo-mechanical properties investigation by DMA	184
III.5. Thermal properties investigated by TGA	188
IV. Conclusion	189
V. References	191
VI. Supplementary Information	194

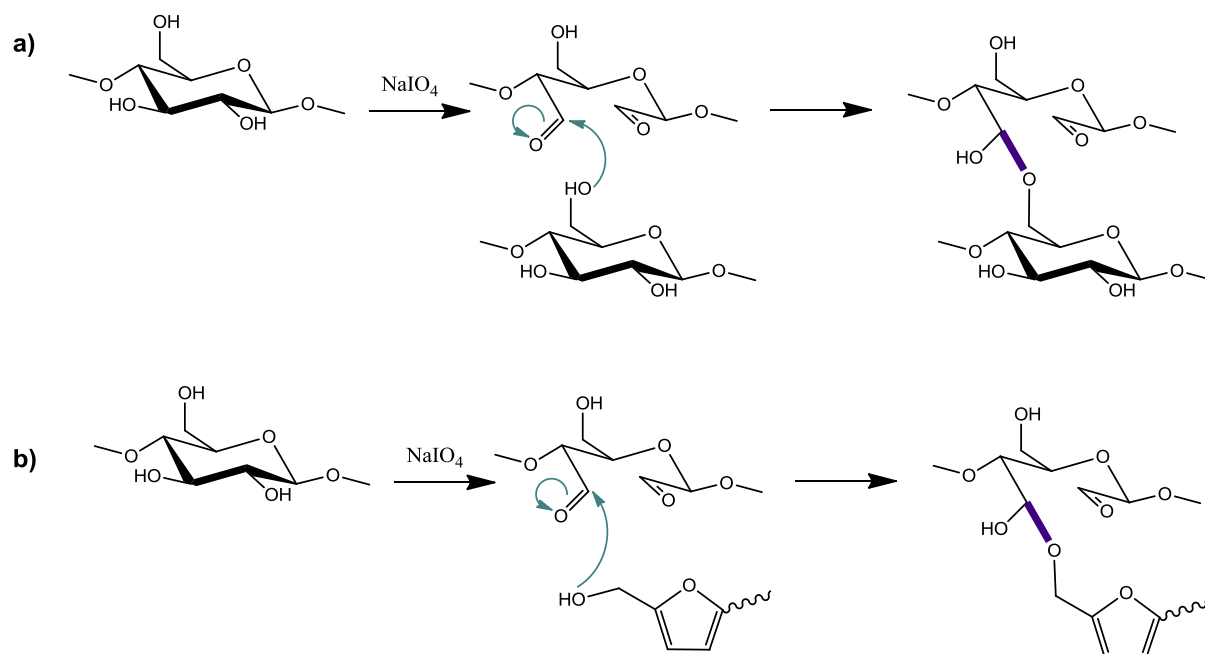
I. Introduction

This chapter aims at the preparation of composites. Composite materials are made up of reinforcing material and matrix, bonded together into a whole, where the polymer matrix transfers load to the fibers so that the load is uniformly distributed. For the reinforcement, or filler, natural fibers present attractive technical, economical, and environmental advantages such as low cost, high disposability, high renewability, biodegradability, and low energy consumption¹⁻⁴. Among a wide variety of possible fillers, cellulose is often used as reinforcing material, either as microcrystalline cellulose (MCC)⁵⁻⁷, as nanocrystals which can be obtained from MCC⁸⁻¹⁰, or as microfibrillar cellulose (MFC)¹¹⁻¹³. MFC is gaining a lot of interest as it presents, besides the general advantages of cellulose, outstanding mechanical properties due to their weight-to-strength ratio.

Due to these outstanding properties, cellulose fibers from different sources (wood, flax, jute, sisal, etc.) are being widely used for the processing of composites and bio-based composites. Different matrices have been studied such as poly(ϵ -caprolactone)¹⁴, polylactic acid (PLA)¹⁵, polyethylene¹⁶, bio-epoxy¹⁷, etc. Research gains also interest at increasing the compatibility between the filler and the matrix as it has often been observed a weak interfacial adhesion between the two components, being a major drawback of such eco-composites¹⁸, which may lead to inefficient stress transfer. Regarding another polymer matrix and in order to prepare fully bio-based composites, furfuryl alcohol (FA) is a monomer easily obtained from furfural, which polymerizes into poly(furfuryl alcohol) (PFA). The polymerization of FA into PFA has already been studied from a kinetic point of view of chemical polymerization mechanism¹⁹⁻²⁴. Among the wide range of industrial applications of FA (such as foundry molds, corrosion and fire resistant materials...), it is also widely used for wood reinforcement²⁵. It has been observed that the FA can react with hemicellulose and lignin during polymerization, but do not react with pristine cellulose^{26,27}. Up to now and to the best of our knowledge, only few articles are dedicated to the preparation of PFA/cellulose composites, and authors agreed that the cellulose increased the toughness of PFA^{28,29}. Though, Motaung *et al.*³⁰, despite the same observation, have concluded that there was a need to increase the compatibility between the PFA matrix and the filler.

This study aims at combining PFA with modified MFC in order to increase their compatibility, using different ratios of MFC. MFC was modified using sodium metaperiodate, generating a so-called dialdehyde cellulose (DAC), with vicinal reactive aldehyde groups. These reactive aldehyde groups react with hydroxymethyl groups of MFC to form a hemiacetal linkage. In

presence of FA, the aldehyde functions of DAC could react with the primary alcohol of FA in order to functionalize the DAC with furans. There is then a competitive reaction with the primary hydroxyl group on C₆ which can also react with the aldehyde functions (**Scheme 1**). After polymerization of FA, interpenetrated network of PFA and MFC could be created.



Scheme 1. Competitive reactions of hemiacetalisation between DAC and **a)** hydroxyl group of MFC; **b)** hydroxyl groups of FA.

II. Experimental section

II.1. Chemical materials

Microfibrillar cellulose (MFC) was kindly supplied by the *Centre de Recherche des Macromolécules Végétales (CERMAV)*, as a suspension at 2 wt % in water. Sodium metaperiodate, hydroxylamine hydrochloride, sodium hydroxide, furfuryl alcohol (FA, 98 %), and maleic anhydride (MA, ≥ 99.0 %) were purchased from Sigma Aldrich and used as received without further purification. Chlorohydric acid at 37 % was purchased from Carl Roth.

II.2. FTIR Spectroscopy

FTIR technique was employed to evaluate the eventual reactions between FA and oxidized MFC. For this purpose, a Perkin Elmer Spectrum BX II Spectrophotometer was employed in Attenuated Total Reflectance (ATR) mode using a diamond crystal and Spectrum software. Each spectrum was recorded with a 4 cm^{-1} resolution and 64 scans co-addition.

II.3. Transmission Electronic Microscopy (TEM)

The observation and characterization of internal morphology of materials were performed by transmission electron microscopy (TEM). This technique allowed the visualization of the MFC dispersion within the cross-linked PFA matrix. The images were recorded on a JEOL JEM 1400 microscope equipped with a SIS Morada camera and Olympus software, operated at an accelerating voltage of 100 kV. The samples were cut in sections of about 90 nm thick, using a Reichert Ultracut E power tome X ultramicrotome equipped with a diamond knife. The samples were negatively stained with 4 % uranyl acetate for 30 minutes.

II.4. Differential Scanning Calorimetry (DSC)

DSC measurements were performed on a Mettler-Toledo DSC1 equipped with STAR[®] software. This apparatus has a very high sensitivity due to its heat flux ceramic sensor FRS5 (with 56 thermocouples Au-Au/Pd). Temperature and enthalpy calibrations are performed by using Indium ($T_m = 156.56\text{ °C}$) and Zinc ($T_m = 419.52\text{ °C}$) standards. Samples of about 10 mg were placed in 30 μL stainless steel crucibles covered with gold-plated membranes, to avoid any evaporation. Samples were heated from 0 to 250 °C at $10\text{ K}\cdot\text{min}^{-1}$ under air atmosphere.

II.5. Dynamic Mechanical Analysis (DMA)

DMA analyses were performed on a Mettler-Toledo DMA 1 with STAR[®] software. The samples of a dimension of 5 mm long, 5 mm width, and 1 mm thick were submitted to a traction in non-isothermal mode (heating rate of 2 K.min⁻¹) from -100 °C to 250 °C, with a frequency of 1 Hz and an oscillation amplitude of 5 μm (0.033 %) in auto-tension mode.

II.6. Thermogravimetric Analysis (TGA)

Thermogravimetric measurements were performed on a TGA 851[°] from Mettler-Toledo. The microbalance has a precision of ± 0.1 μg. Samples of about 15 mg were placed into 70 μL alumina pans. Samples were heated at 5 K.min⁻¹ from 25 °C to 700 °C under air flow of 50 mL.min⁻¹.

II.7. Cellulose oxidation

Several oxidized MFC samples were produced with increasing the degree of oxidation (DO). In a typical oxidation treatment, 1 g of MFC was suspended in 100 mL of distilled water and stirred during 20 min. Then, 1.72 g of sodium metaperiodate was added to the suspension and the mixture was put into dark to minimize side reactions. The oxidation was proceeded at room temperature under magnetic stirring for 8 h, 16 h, 24 h, or 72 h. At the end of the oxidation period, the oxidized MFC suspension was centrifuged several times at 9,000 rpm for 10 min. After each centrifugation step, the supernatant was removed, and the pellet was re-dispersed in distilled water. Thus, 5 to 6 cycles of centrifugation were performed. At each cycle, the conductivity of the supernatant was monitored, and when it reached a value close to the one of distilled water (~0.9 μS.cm⁻¹) it was estimated that all the excess of sodium periodate was washed away, and the sample was then considered ready for subsequent processing. After the last centrifugation cycle, the MFC suspension was re-dispersed in water. The products were kept never dried at 5 °C. Aliquots were dried overnight at 60 °C under vacuum to estimate the dry mass of the products. The obtained products were referred as dialdehyde cellulose (DAC). Because of heterogeneous reaction, it has been assumed that the obtained samples were composed of two components: native non-oxidized cellulose, and fully oxidized chains³¹.

II.8. Determination of the degree of oxidation (DO)

Different methods exist to determine the DO of oxidized MFC such as titration or by ¹³C CP-MAS solid-state NMR. These methods have been compared and it has been concluded

that the more accurate method was by solid-state NMR³¹. However, this method could not have been applied for this work.

The carbonyl group content of the DAC, and thus the DO, was determined following the titrimetric method of Zhao *et al.*³², so-called the oximation titration. Each available carbonyl group is supposed to react with hydroxylamine hydrochloride to lead to an oxime and HCl. Thus, the HCl can be titrated by an alkali solution. Here, 25 mL of a solution of hydroxylamine hydrochloride at 0.25 M was adjusted to a pH of 3.2. Then, approximately 100 mg of oxidized MFC was added to the solution and stirred at room temperature for 2 h. The reaction mixture was titrated back to pH = 3.2 with a standardized solution of NaOH at 0.01 N. The weight of titrated oxidized MFC was determined precisely after centrifugation by drying aliquots. A blank titration was performed with the starting non-oxidized MFC.

The DO was calculated as follow:

$$DO = \frac{[(V_{NaOH\ sample} - V_{NaOH\ blank}) \cdot C_{NaOH} \cdot M_{AGU}]}{m_{DAC\ (dry\ basis)}}$$

where $V_{NaOH\ sample}$ and $V_{NaOH\ blank}$ correspond to the volumes (in mL) of NaOH solution to obtain the back titration to pH = 3.2 of respectively DAC and non-oxidized MFC, C_{NaOH} is the concentration of the NaOH solution, M_{AGU} is the molecular weight of one anhydroglucose unit (AGU), which is $162\ g \cdot mol^{-1}$, and $m_{DAC\ (dry\ basis)}$ is the weight on dry basis (in mg) of the DAC sample. The calculated DO for each oxidation was the mean value of three replicates. Thus, the DOs obtained for MFC oxidized for 8, 16, 24, and 72 h were respectively of 0.2, 0.4, 0.6, and 1.5.

II.9. Material preparation

Different materials were prepared starting from different mixtures between furfuryl alcohol (FA) and oxidized MFC. A reference sample of neat matrix was prepared from a mixture of FA and 2 wt% maleic anhydride (MA) as acid catalyst to initiate the homopolymerization reaction of FA. Different composites were prepared from FA and MFC, using different ratios and different DOs (**Table 1**). After oxidation, the obtained MFC was suspended in water. The suspension was filtered on a Büchner Funnel with addition of FA to never let dry the MFC. This would lead to an exchange of solvents and finally to a suspension of MFC in FA. FTIR analysis was performed to confirm that all water was removed from the MFC/FA suspension. The suspension was homogenized by ultrasonication and then filtered to the desired ratio (in wt%) of MFC in FA. The ratio was estimated in function of the dry mass of the MFC sample.

Then, 2 wt% of MA (regarding the mass of FA) was added and the mixture was heated for pre-polymerization.

Table 1. PFA/MFC composites prepared for further analyses.

PFA/MFC samples	DO = 0.2	DO = 0.4	DO = 0.6	DO = 1.5
Ratio of MFC in FA	8 %	8 %	1% - 4% - 8% - 15%	8 %

All samples were pre-polymerized in a polytetrafluoroethylene (PTFE) round-bottomed flask equipped with a magnetic stirrer and a reflux condenser. The mixture was first heated to 90 °C for 30 min to dissolve the MA and put in contact the reactants. The reflux condenser avoided the evaporation of FA before the beginning of the pre-polymerization. Then, the mixture was heated to 100 °C and the temperature was increased by 10 °C every 30 min to finally reach a highly viscous resin. Usually, the mixtures for composites preparations were heated to 120 °C, while the reference sample of neat PFA matrix reached the adequate viscosity at 130 °C.

After pre-polymerization, each sample was put in a silicon mold, placed in a PTFE mold and polymerized by compression molding for 2 h at 160 °C, with a pressure of 10 bars. This step completed the polymerization and led to a solid material. It was important to perform this polymerization step by compression molding as polycondensation reactions is releasing water. This would lead to trapped water within the sample thus creating bubbles during curing. Such defects may impact the final mechanical and thermal properties of the materials. Finally, after cooling to room temperature, the materials were unmolded, and a final step of post-curing was performed in an oven, at 180 °C for 2 h and 230 °C for 3 h, to achieve complete cross-link and release residual unreacted FA monomer.

III. Results and Discussions

III.1. FTIR analysis

Preliminary FTIR analyses were performed to check branching between oxidized MFC and FA which would lead to a covalent hemiacetal linkage as presented in **Scheme 1b**. For this purpose, a small amount of oxidized MFC (at DO = 0.6 and DO = 1.5) impregnated with FA was washed several time with ethanol to remove any excess of non-reacted FA and was then dried under vacuum. FTIR analyses aimed at pointing out characteristic bands of FA after ethanol washings.

FTIR spectra are depicted in **Figure 1** and the spectra were normalized to 1 with the highest band at 1015 cm^{-1} . At DO = 0.6, weak bands appeared at 1504 cm^{-1} and 748 cm^{-1} , respectively attributed to the C=C stretching and C-H out of plane deformation of furan rings. The maximal DO that can be obtained is 2 for complete oxidation of AGU. Thus, at DO = 0.6, the MFC was oxidized at 30 %, while at DO = 1.5, MFC was oxidized at 75 %. Though, MFC oxidized at DO = 0.6 contains only 30 % of aldehyde functions. To verify this result, the same experiment was performed with MFC oxidized at DO = 1.5, containing 75 % of aldehyde functions. This should lead to higher content of branched FA. Indeed, the spectrum of MFC at DO = 1.5 which was impregnated with FA showed stronger peaks at 1504 cm^{-1} and 748 cm^{-1} , characteristics of furanic rings. This could confirm the eventual reaction between the aldehyde function of DAC and the primary alcohol of FA. FTIR spectra were normalized regarding the C-O bond at 1022 cm^{-1} . Comparing the ratios between the bands around 1400 cm^{-1} and the C-O band at 1022 cm^{-1} , it was observed that as the bands around 1400 cm^{-1} were lower in presence of FA, it should imply that the amount of C-O was increased due to the addition of FA. This could also confirm the presence of branched FA on MFC.

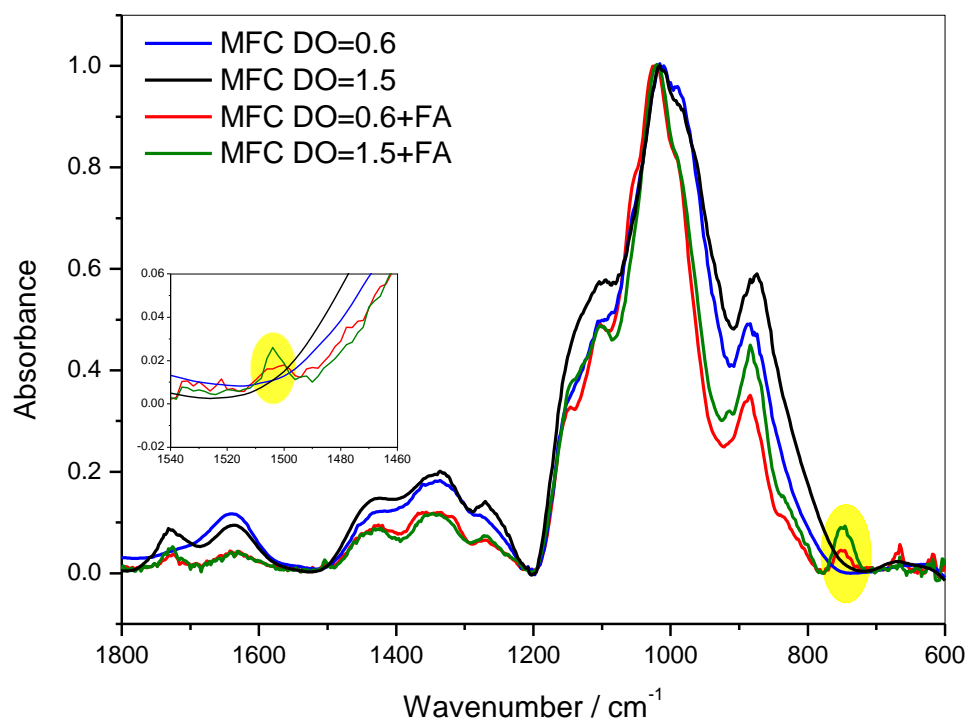


Figure 1. FTIR spectra of MFC at DO = 0.6, MFC at DO = 1.5, MFC at DO = 0.6 reacted with FA, and MFC at DO = 1.5 reacted with FA. Peaks characteristic to furan rings are highlighted.

III.2. DSC measurements of FA polymerization in presence of MFC

DSC measurements were performed to follow-up the global polymerization of FA in presence of MFC at a ratio of 8 %. DSC thermograms are presented in **Figure 2** and compared to the one of the reference FA/MA system. The polymerization of FA catalyzed with 2 wt% of MA presented a sharp peak centered at 113 °C with an enthalpy of 61.1 kJ.mol⁻¹. It is interesting to note that the introduction of MFC shifted the polymerization reaction to higher temperatures as the peak temperature after addition of unmodified MFC was observed at 129 °C. The oxidation of MFC kept increasing the polymerization temperature until a temperature of 152 °C for FA with MFC at DO = 0.6. The presence of MFC within the FA delayed the polymerization reaction, as it may hinders the formation of the carbocation. Indeed, MFC possesses strong ability to form hydrogen bonds which can protect the hydroxyl group from further reaction. In the same idea, this has already been observed with the use of solvent as it may form solvation spheres around the hydroxyl group³³, or with silica³⁴. However, when the MFC was highly

oxidized to reach a DO of 1.5, the polymerization temperature of FA was observed at a temperature close to the average value of the other samples, at 135 °C (**Table 2**). At such a high DO, the MFC is highly amorphous and the H-bonds network appeared to be strong enough to still delay the polymerization compared to the FA/MA reference system. However, at DO = 1.5, the resulting DAC is very reactive, and it may also form its own network. The final material should be more related to a copolymer than to a composite.

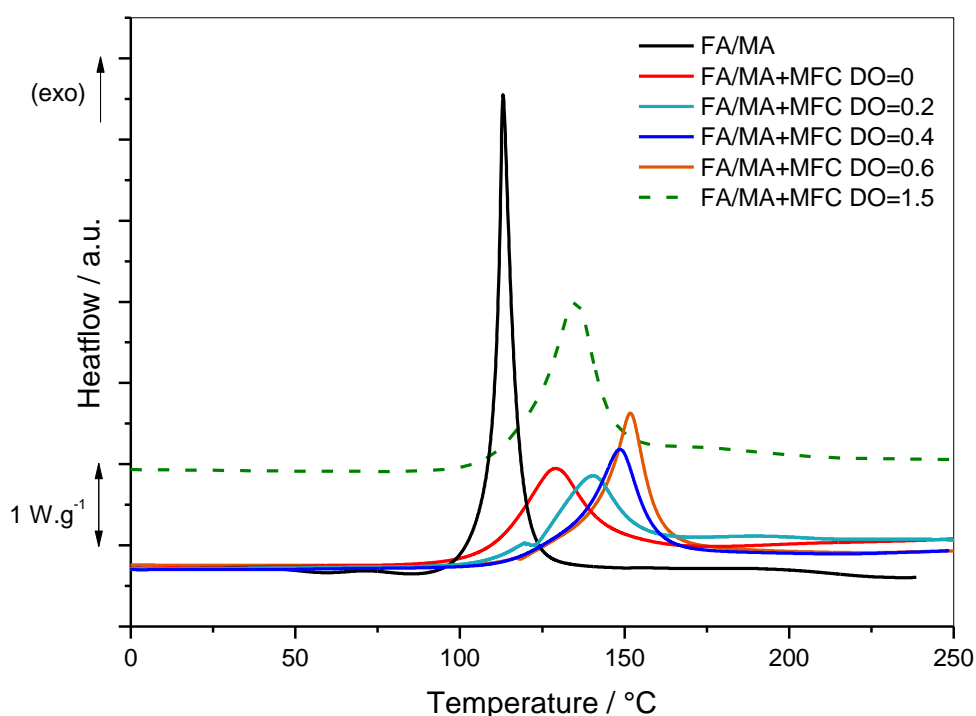


Figure 2. DSC thermograms of FA/MA (100/2), and FA/MA/MFC (100/2/8) composites preparation.

As mentioned in previous study²⁶, FA does not react with pristine cellulose, thus the temperature range of polymerization should correspond to the one of FA. This is the case for crystalline cellulose as it is not reactive at all. However, MFC contains some amorphous fractions leading to higher reactivity than crystalline cellulose. The peaks of polymerization when MFC was introduced were lower and wider, which implies a lower reactivity. This can also be due to the hindrance due to the impregnation of MFC and the initial increase of viscosity. Moreover, the enthalpy of polymerization varied in presence of oxidized MFC, as the amorphous fractions may interact with FA and modify the polymerization reaction. DSC data are summarized in **Table 2** where enthalpy values are normalized regarding the molar mass of FA. The overall enthalpy of polymerization of FA was about 61.1 kJ.mol⁻¹ and was observed to decrease to 50.8 kJ.mol⁻¹ with addition of MFC, due to its reinforcing effect. The enthalpy

continued to decrease with oxidation of MFC until the DO of 0.6 where the enthalpy reached about 41.7 kJ.mol⁻¹. This decrease of the enthalpy was observed as the presence of oxidized MFC as this filler might hinder the overall polymerization reaction. Indeed, with increasing DO, FA molecules are likely to be more engaged into hemiacetals formation which lead to a decrease of the enthalpy since less FA will participate to FA polymerization. However, when MFC is almost fully amorphous (DO = 1.5), the enthalpy of polymerization of FA was observed to be at around 60 kJ.mol⁻¹, close to the enthalpy of polymerization of neat FA. With highly oxidized MFC, the microfibrils are almost completely amorphous. At this DO, the polymerization could more easily be performed as almost no crystalline fractions were present to hinder the reactivity between FA molecules. Moreover, side reactions could occur between DAC and FA increasing the enthalpy of polymerization.

Table 2. DSC data of polymerization reaction of FA and MFC/FA (8 wt%) preparations.

Sample	ΔH (kJ.mol ⁻¹) ^[a]	T_p (°C) ^[b]
FA + 2 wt% MA	61.1 ± 2.4	113
FA/MA/MFC DO=0	50.8 ± 2.0	129
FA/MA/MFC DO=0.2	49.5 ± 1.9	140
FA/MA/MFC DO=0.4	43.9 ± 1.8	149
FA/MA/MFC DO=0.6	41.7 ± 1.7	152
FA/MA/MFC DO=1.5	59.9 ± 2.4	135

^[a] Enthalpy of polymerization. ^[b] Temperature at maximum of polymerization.

III.3. Microscopic morphology characterization by TEM

The dispersion of the MFC inside the PFA matrix was characterized by TEM. First, the morphology of the MFC was analyzed at the same ratio of MFC in FA but with MFC at different DOs. The TEM images are shown in **Figure 3**. Each composite at a ratio of 8 % of MFC in FA was analyzed: with unmodified MFC (DO = 0), with DAC at a DO of 0.2, 0.4, 0.6, and 1.5. It is worthy to note that the MFC kept their microfibrillar structure until a DO of 0.6, which is in adequation with previous studies³⁵; however, the preparation with DAC at a DO of 1.5 did not present any sign of remaining fibrils and was similar to what was observed for the neat PFA matrix. After an oxidation of 72 h to reach a DO of 1.5, the MFC was oxidized at 73 % and became highly amorphous. No MFC structure was observed which confirmed the absence of

crystalline fractions. Thus, at DO = 1.5, the compatibility between the PFA matrix and the DAC was strongly increased, to reach a perfectly homogeneous copolymer.

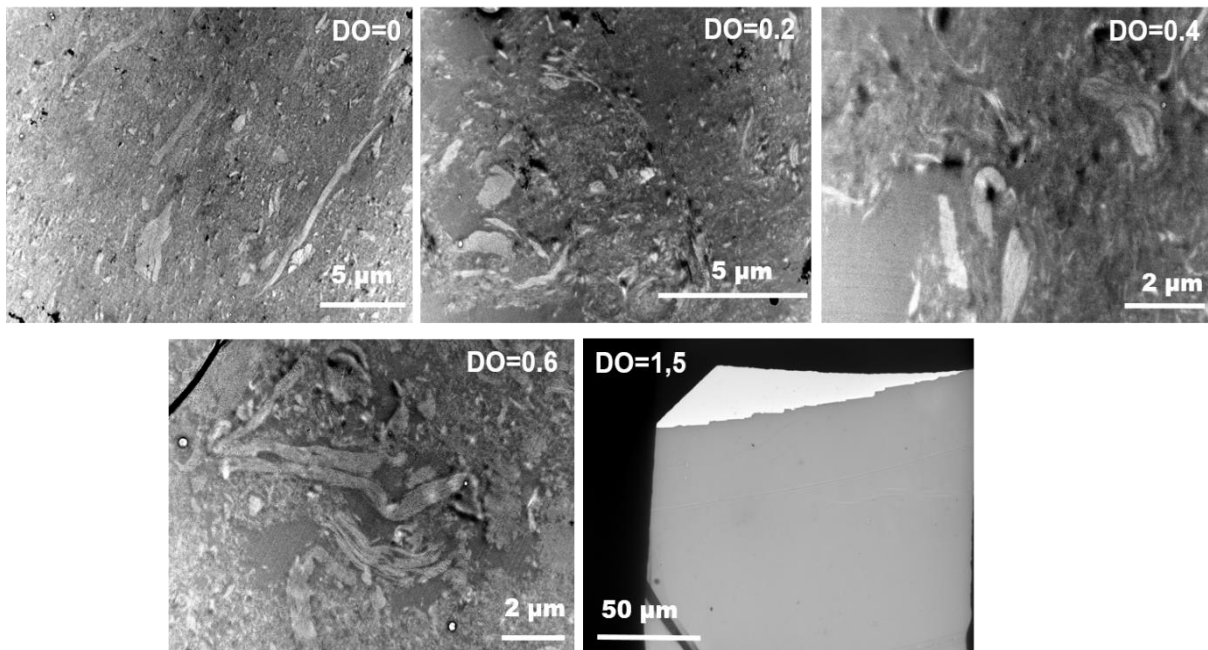


Figure 3. TEM micrographs at 8 % of MFC in FA for composites with unmodified MFC, DAC with DO = 0.2, DO = 0.4, DO = 0.6, and DO = 1.5.

To evaluate the most suitable ratio of MFC in FA to prepare the composites, preliminary observations were performed at a given DO. At low ratios of 1 and 4 %, the composite presented a heterogeneous morphology with DAC aggregated in some parts of the matrix. At the highest ratio of 15 %, the composite presented a high concentration of MFC which formed a dense network of microfibrils, reaching percolation. Finally, the 8 % ratio seemed to be the most adequate as the composite presented a homogeneous dispersion of the microfibrils, which may then lead to a good interaction between the MFC filler and the PFA matrix.

TEM images in **Figure 4** were obtained for DO = 0.6. For the highest DO of 1.5, the ratio did not have an influence on the microscopical aspect as images were similar to the one presented in **Figure 3**. Thus, as mentioned previously, the term composite was used to designate the materials prepared from MFC at DO = 0 to DO = 0.6, while the materials prepared from MFC at DO = 1.5 were closer to copolymers, hence, will not be considered further in the study.

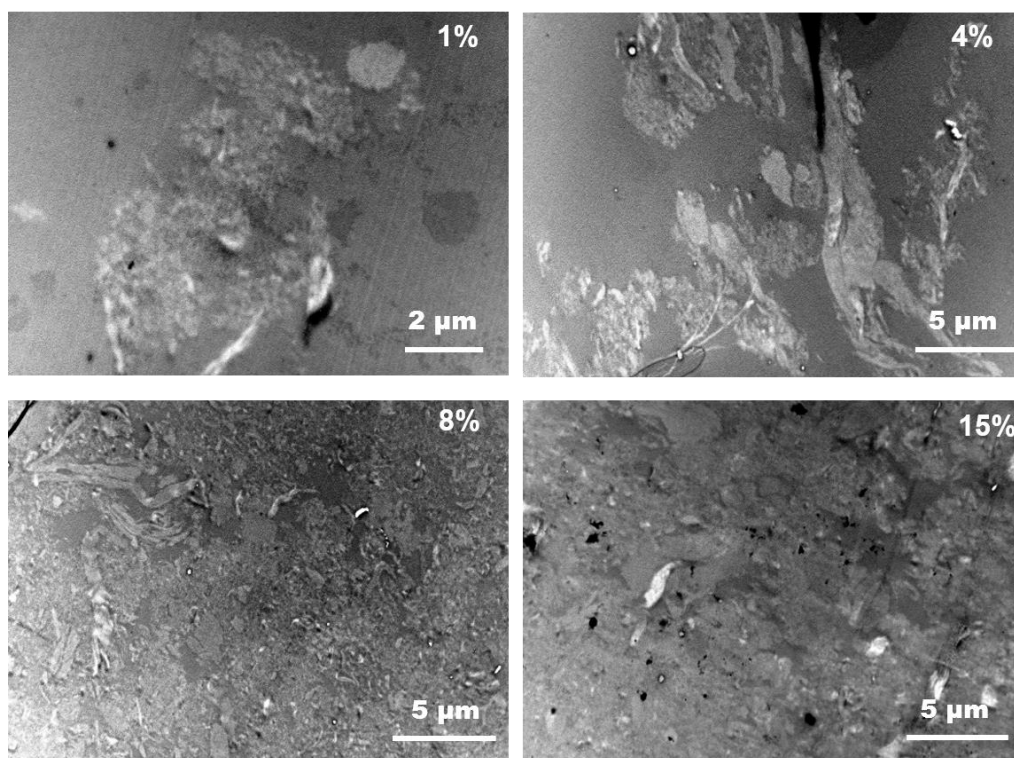


Figure 4. TEM micrographs at DO = 0.6 with 1 %, 4 %, 8 %, and 15 % of MFC in FA.

III.4. Thermo-mechanical properties investigation by DMA

The study focused on the effect of the DO at a ratio of 8 % of MFC in FA. After polymerization and post-curing, the mechanical properties were investigated by DMA. The evolution of the storage modulus (E') and the $\tan \delta$ for each sample are respectively depicted in **Figure 5a)** and **Figure 5b)**. For all the systems, E' decreased from about 30 to 180 °C, with a more important diminution for the neat PFA. This transition is commonly attributed to the glass transition, from the glassy state to the rubbery state of the polymer (or composite).

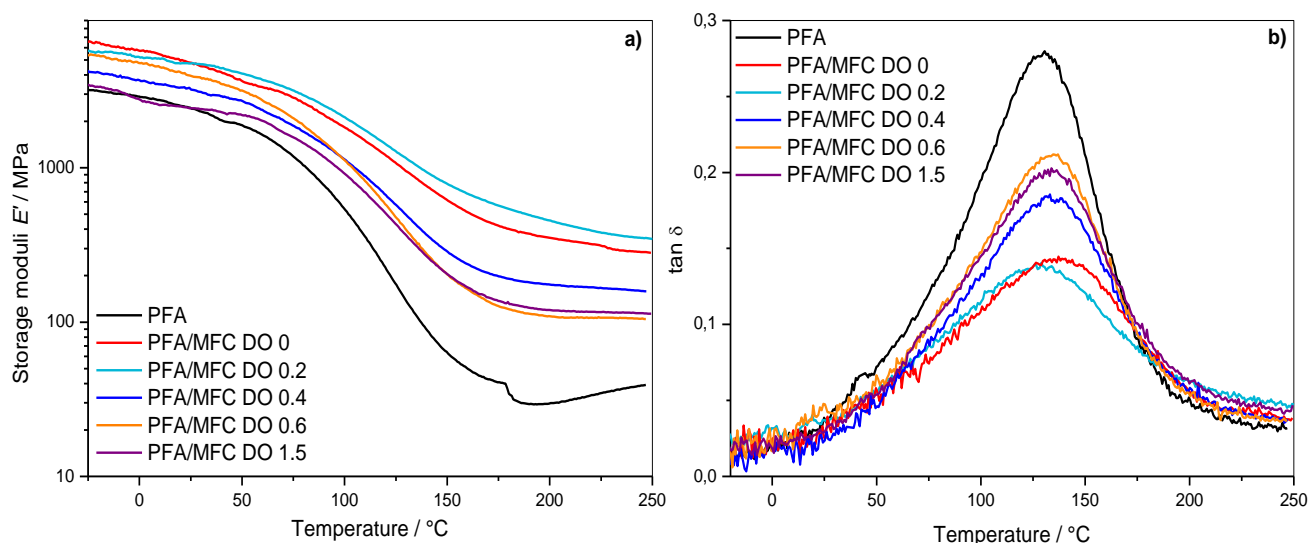


Figure 5. DMA thermograms of neat PFA matrix and composites at 8 % of MFC in FA from MFC at DO = 0, 0.2, 0.4, 0.6, 1.5. **a)** Evolution of the storage moduli and **b)** Evolution of $\tan \delta$.

When the rubbery state was reached, an increase of the storage modulus E' of the neat PFA matrix in the rubbery state was observed, starting around 180-200 °C which corresponds to the post curing temperatures for PFA. This increase has already been studied by Falco *et al.* and was attributed to the final cross-link reactions in the solid-state not observed by DSC, which is a technique more appropriate for the study of the firsts reactions in the liquid²³. Interestingly, the composites did not present an increase for E' although all samples were cured with the same thermal treatment. Thus, the presence of MFC created a network within the PFA matrix, increasing the rigidity in the rubbery state in comparison with the neat matrix. Moreover, it could be noticed that all the E' moduli for the composites were higher than E' for the neat matrix for the whole temperature range (**Table 3**), confirming the strong reinforcement effect of MFC^{36,37}.

The composites prepared with unmodified MFC and MFC oxidized at the lowest DO of 0.2 presented close storage moduli with the highest values (respectively of 5,718 and 5,180 MPa at 0 °C). Essentially for unmodified MFC, or slightly oxidized, there is strong MFC/MFC interactions due to the high H-bonding network within the microfibrils leading to higher elastic modulus on the whole temperature range. Such result has also been observed for composites with biopolyamide³⁷. The modification of the MFC had an influence on the thermo-mechanical properties of the resultant composites. Indeed, the oxidation of MFC decreased the storage modulus of the composite compared to the composite with unmodified MFC. This is especially highlighted in the rubbery state. As the DO of the MFC increased, the content of amorphous

parts in MFC was increased which consequently decreased the rigidity of MFC. Thus, as the DAC content increased, the composite presented more MFC/PFA interactions over MFC/MFC interactions, as the thermo-mechanical behavior of the composite tended to the behavior of neat PFA. The PFA/MFC copolymer prepared from MFC at DO = 1.5 showed the lowest storage modulus in the glassy state among the composites, with a value of E' close to the neat matrix (2,780 MPa). This is due to the high amorphization of MFC, which decreased the rigidity compared to the other composites. However, the evolution of E' for this copolymer was not the lowest for the whole temperature range of analysis. Indeed, from a temperature of 145 °C, the storage modulus for PFA/MFC at DO = 1.5 crossed the storage moduli of the composite prepared from MFC at DO = 0.6 and remained close to that latter E' . The final E' value obtained at the glassy state was about 120 °C, slightly higher than that of DO = 0.6.

The temperature dependence of $\tan \delta$ presented in **Figure 5b)** shows that the incorporation of MFC decreased the magnitude of $\tan \delta$ peak. The lowest $\tan \delta$ peak was observed for the composite prepared with unmodified MFC. This may imply a high densification of the network along with a lower mobility of the polymer chains. Thus, this confirmed the reinforcement effect of the MFC increasing the rigidity of the composites and lowering the energy dissipation in the material. As shown in **Figure 5b)**, the magnitude of $\tan \delta$ was increased with oxidation of MFC. This confirmed the observation of the E' variation in the rubbery state: the higher amplitude of the $\tan \delta$ peak reflected a higher chain mobility due to the increase of amorphous parts with oxidation. However, the oxidation of MFC only slightly increased the glass transition temperature. Moreover, as for the observations on the evolution of E' , the evolution of $\tan \delta$ for the copolymer PFA/MFC DO = 1.5 showed very similar profile to the one of the composite from MFC at DO = 0.6. Such similarity between the copolymer and the composite PFA/MFC DO=0.6 would indicate that from MFC oxidized at DO = 0.6, the corresponding composite would reach optimal conditions. Then, from this optimum, further oxidation would not have important influence on the thermo-mechanical properties.

Table 3. DMA data for neat PFA and PFA/MFC composites.

Sample	E' at 0 °C (MPa) ^[a]	E' at 200 °C (MPa) ^[b]	T_α (°C) ^[c]
PFA	2,870	29.8	130
PFA/MFC DO=0	5,718	351.7	138
PFA/MFC DO=0.2	5,180	454.5	127
PFA/MFC DO=0.4	3,690	174.9	135
PFA/MFC DO=0.6	4,770	108.9	135
PFA/MFC DO=1.5	2,780	119.9	135

^[a] Storage moduli in the glassy plateau. ^[b] Storage moduli in the rubbery plateau. ^[c] Glass transition temperature at the maximum of $\tan \delta$ peak (α relaxation).

Regarding the thermo-mechanical properties of different composites prepared from the same DO but at a different ratio, complementary DMA were performed for composites prepared from oxidized MFC at DO = 0.6 at 1, 4, 8, and 15 % of MFC in FA. Corresponding mechanical spectra are depicted in **Figure 6**. Composites at 4 and 8 % of MFC in FA showed intermediate behaviors. Indeed, the composite with only 1 % of MFC presented very similar behavior to the neat PFA, showing a slight increase the storage modulus but no influence on the evolution of the $\tan \delta$. On the opposite, it is noteworthy that a higher increase of the MFC content went with a strong influence on the final properties of the corresponding composite. Indeed, the incorporation of 15 % of MFC within the composite increased the storage modulus to 4,865 MPa in the glassy state, which is close to E' of the composite at 8 %. However, the evolution of E' did not show a definite transition, as it kept decreasing almost linearly to reach 900 MPa at 250 °C. This was also reflected on the evolution of $\tan \delta$. The composite at 15 % of MFC presented a very low and wide peak, roughly estimated from 30 to 250 °C. The width of the peak did not allow to determine properly a maximum. Thus, it can be assumed that at high concentration of MFC, the composite presents a high degree of percolation of the MFC network, hindering the relaxation of the PFA matrix.

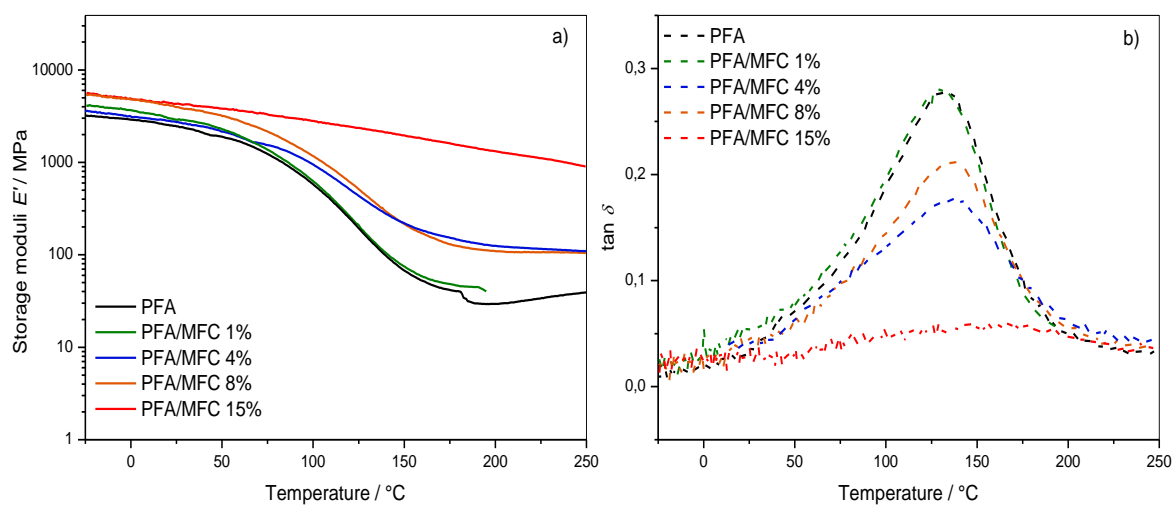


Figure 6. DMA thermograms of neat PFA matrix and composites at different ratios of MFC in FA from MFC at DO = 0.6. **a)** Evolution of the storage moduli and **b)** Evolution of $\tan \delta$.

III.5. Thermal properties investigated by TGA

The thermo-mechanical analyses showed that the incorporation of MFC within the PFA matrix highly increased the storage modulus both in the glassy state and the rubbery state. The effect can be counterbalanced by initial oxidation of MFC which decreased the reinforcement effect due to amorphization of the cellulose. It was then interesting to evaluate the effect of the addition of MFC on the thermal properties of the materials. First analyses were performed to evaluate the effect of the DO at a given ratio of MFC in FA (8 %) (**Figure 7**). The neat PFA matrix presented already a high thermal stability with a temperature at 5 % of mass loss ($T_{5\%}$) of 372 °C. The addition of MFC within the matrix decreased the thermal stability of about 30 °C, with a negligible influence of the DO. Moreover, no mass loss was observed below 300 °C, as the PFA protected the MFC from thermal degradation. Indeed, the thermal degradation of neat DAC 0.6 appeared to start around 200 °C, though no thermal degradation was observed in this temperature range for the composites.

The derivative of thermal degradation showed several steps of decomposition. The first step presented a maximum at 374 °C for neat PFA, and at 345 °C for PFA/MFC composites. This first step was attributed to the formation of alkylfurans due to the scission of both methylene and methyne links, as presented in previous study³⁸. This step occurred faster and at lower temperatures for the composites as it also included the thermal degradation of MFC. The second step occurred at 600 °C for PFA and at 575 °C for PFA/MFC composites. This step was

attributed to the scission of furanic links to form ketonic volatile compounds. Finally, the oxidation of the char which presented a maximum at 705 °C for the neat PFA seemed to be more convoluted in the case of the composites. Complementary TGA analyses were performed at the same DO to evaluate the effect of the ratio (Supplementary Information, **Figure S1**). The thermal stability decreased as the MFC content increased, with a decrease of 50 °C from PFA/MFC at 1 % to PFA/MFC at 15 %. Indeed, as the MFC content increased, the amount of amorphous parts was consequently increased reducing the thermal stability.

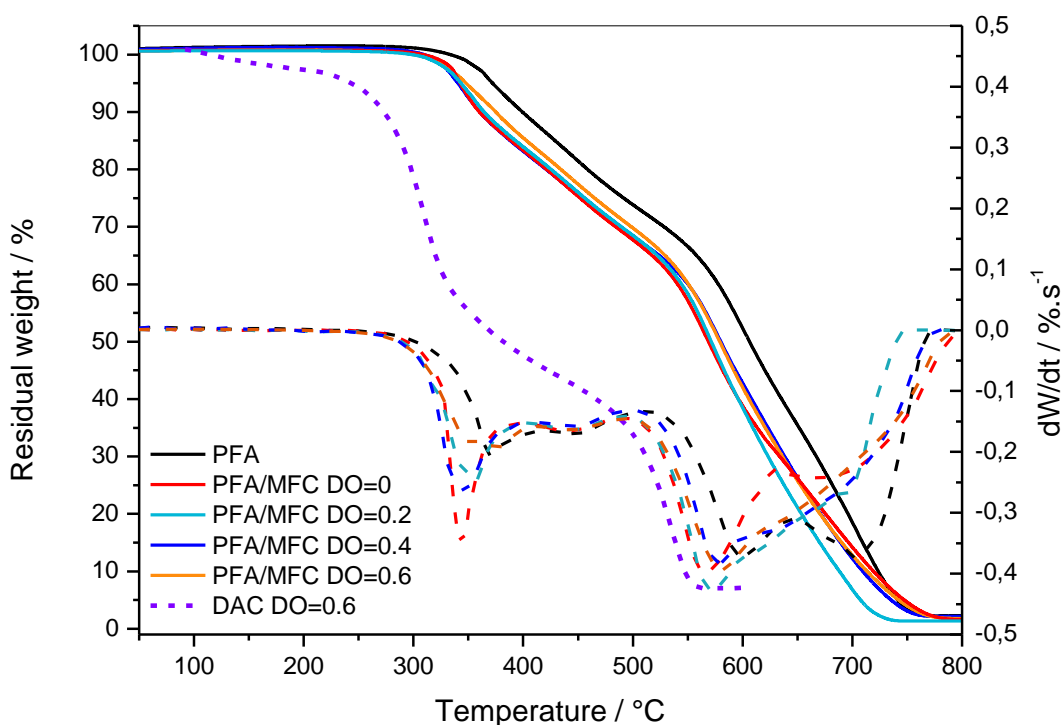


Figure 7. Thermogram analyses for neat PFA and PFA/MFC composites at 8 %. Right axis: TG curves (full lines) – Left axis: DTG curves (dotted lines).

IV. Conclusion

Composites were prepared from a PFA matrix reinforced with MFC. MFC was modified by oxidation to increase the compatibility between the matrix and the filler. Different composites were processed using MFC at different DOs (unmodified, DO = 0.2, 0.4, 0.6, and 1.5) to evaluate the variation of the general properties when increasing the dialdehyde content. For complementary analyses, another set of composites was prepared by varying the ratio of MFC at a given DO. Through modification of MFC by oxidation, reactive aldehyde functions were generated. These aldehyde groups can create hemiacetal linkage by reactions with adjacent

hydroxymethyl groups, either with MFC or with FA monomer. Potential hemiacetal linkage has been confirmed by FTIR analyses which confirmed the presence of furan groups on aliquots of oxidized MFC impregnated with FA. TEM analyses allowed to determine that the ratio of 8 % presented the most adequate dispersion of MFC within the PFA matrix, thus, this ratio was selected to evaluate the thermo-mechanical properties by varying the DO. DMA of composites at a ratio of 8 % showed a high increase of the rigidity compared to the neat PFA matrix, as the storage moduli of the composites were higher than the modulus of PFA during the whole temperature range. More specifically, the storage modulus of PFA showed an increase in the rubbery state typical of cross-linking reactions in the solid state. This increase was not observed for the composites confirming the reinforcing effect of MFC which increased the rigidity. Moreover, the values of E' decreased when increasing the DO, and thus the DAC content, as the composite presented more PFA/MFC interactions over MFC/MFC interactions. Furthermore, it was observed that the amplitude of $\tan \delta$ decreased for the composites, confirming the reinforcement effect of MFC which increased the rigidity and lowered the energy dissipation in the material. In addition, the increase of amorphous fractions with oxidation increased the chain mobility as the $\tan \delta$ amplitude increased with the DO. Finally, the introduction of MFC within the PFA matrix only slightly decreased the thermal stability, as the PFA already presented a high thermal stability.

V. References

- (1) Herrera-Franco, P. .; Valadez-González, A. Mechanical Properties of Continuous Natural Fibre-Reinforced Polymer Composites. *Compos. Part A Appl. Sci. Manuf.* **2004**, 35 (3), 339–345.
- (2) Saba, N.; Tahir, P. M.; Jawaid, M. A Review on Potentiality of Nano Filler/Natural Fiber Filled Polymer Hybrid Composites. *Polymers (Basel)*. **2014**, 6 (8), 2247–2273.
- (3) Ahad, N. A.; Mohd Radzi, N. F. H.; Sadli, N. S.; Seng, T. J. Comparing Various Type of Natural Fibers as Filler in TPU: Mechanical Properties, Morphological and Oil Absorption Behavior. *MATEC Web Conf.* **2017**, 97, 01062/1-01062/7.
- (4) Rol, F.; Belgacem, M. N.; Gandini, A.; Bras, J. Recent Advances in Surface-Modified Cellulose Nanofibrils. *Prog. Polym. Sci.* **2018**.
- (5) Wang, B.; Nie, K.; Xue, X.; Lin, F.; Li, X.; Xue, Y.; Luo, J. Preparation of Maleic Anhydride Grafted Polybutene and Its Application in Isotactic Polybutene-1/Microcrystalline Cellulose Composites. *Polymers* **2018**, 10 (4), 393.
- (6) Cao, Z.; Lu, Y.; Zhang, C.; Zhang, Q.; Zhou, A.; Hu, Y.; Wu, D.; Tao, G.; Gong, F.; Ma, W.; Liu, C. Effects of the Chain-Extender Content on the Structure and Performance of Poly(Lactic Acid)-Poly(Butylene Succinate)-Microcrystalline Cellulose Composites. *J. Appl. Polym. Sci.* **2017**, 134 (22).
- (7) Spoljaric, S.; Genovese, A.; Shanks, R. A. Polypropylene–microcrystalline Cellulose Composites with Enhanced Compatibility and Properties. *Compos. Part A Appl. Sci. Manuf.* **2009**, 40 (6–7), 791–799.
- (8) Bondeson, D.; Kvien, I.; Oksman, K. Strategies for Preparation of Cellulose Whiskers from Microcrystalline Cellulose as Reinforcement in Nanocomposites. In *Cellulose Nanocomposites: Processing, Characterization, and Properties*; Kristiina Oksman, Mohini Sain, Eds.; ACS Symposium Series, **2006**; 10–25.
- (9) Oksman, K.; Mathew, A. P.; Bondeson, D.; Kvien, I. Manufacturing Process of Cellulose Whiskers/Poly(lactic Acid) Nanocomposites. *Compos. Sci. Technol.* **2006**, 66 (15), 2776–2784.
- (10) Elanthikkal, S.; Francis, T.; Sangeetha, C.; Unnikrishnan, G. Cellulose Whisker-Based Green Polymer Composites. In *Handbook of Composites from Renewable Materials*; Vijay Kumar Thakur Manju Kumari Thakur Michael R. Kessler, Ed.; John Wiley & Sons, Inc.: Hoboken, **2017**; 461–494.
- (11) Mbarki, K.; Boumbimba, R. M.; Sayari, A.; Elleuch, B. Influence of Microfibers Length on PDLA/Cellulose Microfibers Biocomposites Crystallinity and Properties. *Polym. Bull.* **2018**, 1–19.
- (12) Solikhin, A.; Murayama, K. Enhanced Properties of Poly(Vinyl Alcohol) Composite Films Filled with Microfibrillated Cellulose Isolated from Continuous Steam Explosion. *Int. J. Plast. Technol.* **2018**, 22 (1), 122–136.
- (13) Suryanegara, L.; Nugraha, R. A.; Achmadi, S. S. Improvement of Thermal and Mechanical Properties of Composite Based on Poly(lactic Acid) and Microfibrillated Cellulose through Chemical Modification. *IOP Conf. Ser. Mater. Sci. Eng.* **2017**, 223 (1), 012032.

- (14) Lo Re, G.; Spinella, S.; Boujemaoui, A.; Vilaseca, F.; Larsson, P. T.; Adås, F.; Berglund, L. A. Poly(ϵ -Caprolactone) Biocomposites Based on Acetylated Cellulose Fibers and Wet Compounding for Improved Mechanical Performance. *ACS Sustain. Chem. Eng.* **2018**, *6* (5), 6753–6760.
- (15) Johari, A. P.; Kurmvanshi, S. K.; Mohanty, S.; Nayak, S. K. Influence of Surface Modified Cellulose Microfibrils on the Improved Mechanical Properties of Poly (Lactic Acid). *Int. J. Biol. Macromol.* **2016**, *84*, 329–339.
- (16) Guilhen, A.; Gadioli, R.; Fernandes, F. C.; Waldman, W. R.; Aurelio De Paoli, M. High-Density Green Polyethylene Biocomposite Reinforced with Cellulose Fibers and Using Lignin as Antioxidant. *J. Appl. Polym. Sci.* **2017**, *134* (35), 45219.
- (17) Barari, B.; Omrani, E.; Dorri Moghadam, A.; Menezes, P. L.; Pillai, K. M.; Rohatgi, P. K. Mechanical, Physical and Tribological Characterization of Nano-Cellulose Fibers Reinforced Bio-Epoxy Composites: An Attempt to Fabricate and Scale the ‘Green’ Composite. *Carbohydr. Polym.* **2016**, *147*, 282–293.
- (18) Eichhorn, S. J.; Young, R. J. Composite Micromechanics of Hemp Fibres and Epoxy Resin Microdroplets. *Compos. Sci. Technol.* **2004**, *64* (5), 767–772.
- (19) Choura, M.; Belgacem, M.N.; Gandin, A. Acid-Catalyzed Polycondensation of Furfuryl Alcohol: Mechanisms of Chromophore Formation and Cross-Linking. *Macromolecules* **1996**, *29* (11), 3839–3850.
- (20) Choura, M.; Belgacem, M.N.; Gandini, A. The Acid-Catalyzed Polycondensation of Furfuryl Alcohol: Old Puzzles Unravelling. *Macromol. Symp.* **1997**, *122* (1), 263–268.
- (21) Guigo, N.; Mija, A.; Vincent, L.; Sbirrazzuoli, N. Chemorheological Analysis and Model-Free Kinetics of Acid Catalysed Furfuryl Alcohol Polymerization. *Phys. Chem. Chem. Phys.* **2007**, *9* (39), 5359.
- (22) Zavaglia, R.; Guigo, N.; Sbirrazzuoli, N.; Mija, A.; Vincent, L. Complex Kinetic Pathway of Furfuryl Alcohol Polymerization Catalyzed by Green Montmorillonite Clays. *J. Phys. Chem. B* **2012**, *116* (28), 8259–8268.
- (23) Falco, G.; Guigo, N.; Vincent, L.; Sbirrazzuoli, N. FA Polymerization Disruption by Protic Polar Solvents. *Polymers* **2018**, *10* (5), 529.
- (24) Falco, G.; Guigo, N.; Vincent, L.; Sbirrazzuoli, N. Opening Furan for Tailoring Properties of Bio-Based Poly(Furfuryl Alcohol) Thermoset. *ChemSusChem* **2018**, *11* (11), 1805–1812.
- (25) Lande, S.; Westin, M.; Schneider, M. Development of Modified Wood Products Based on Furan Chemistry. *Mol. Cryst. Liq. Cryst.* **2008**, *484* (1), 1/[367]-12/[378].
- (26) Nordstierna, L.; Lande, S.; Westin, M.; Karlsson, O.; Furó, I. Towards Novel Wood-Based Materials: Chemical Bonds between Lignin-like Model Molecules and Poly(Furfuryl Alcohol) Studied by NMR. *Holzforschung* **2008**, *62* (6), 709–713.
- (27) Guigo, N.; Mija, A.; Vincent, L.; Sbirrazzuoli, N. Eco-Friendly Composite Resins Based on Renewable Biomass Resources: Polyfurfuryl Alcohol/Lignin Thermosets. *Eur. Polym. J.* **2010**, *46* (5), 1016–1023.
- (28) Pranger, L.; Tannenbaum, R. Biobased Nanocomposites Prepared by In Situ Polymerization of Furfuryl Alcohol with Cellulose Whiskers or Montmorillonite Clay.

Macromolecules **2008**, *41* (22), 8682–8687.

- (29) Pranger, L. A.; Nunnery, G. A.; Tannenbaum, R. Mechanism of the Nanoparticle-Catalyzed Polymerization of Furfuryl Alcohol and the Thermal and Mechanical Properties of the Resulting Nanocomposites. *Compos. Part B Eng.* **2012**, *43* (3), 1139–1146.
- (30) Motaung, T. E.; Gqokoma, Z.; Linganiso, L. Z.; Hato, M. J. The Effect of Acid Content on the Poly(Furfuryl) Alcohol/Cellulose Composites. *Polym. Compos.* **2016**, *37* (8), 2434–2441.
- (31) Leguy, J. Periodate Oxidation of Cellulose for Internal Plasticization and Materials Design, Grenoble Alpes, 2018.
- (32) Zhao, H.; Heindel, N. D. Determination of Degree of Substitution of Formyl Groups in Polyaldehyde Dextran by the Hydroxylamine Hydrochloride Method. *Pharm. Res.* **1991**, *08* (3), 400–402.
- (33) Kim, T.; Assary, R. S.; Kim, H.; Marshall, C. L.; Gosztola, D. J.; Curtiss, L. A.; Stair, P. C. Effects of Solvent on the Furfuryl Alcohol Polymerization Reaction: UV Raman Spectroscopy Study. *Catal. Today* **2013**, *205*, 60–66.
- (34) Bosq, N.; Guigo, N.; Falco, G.; Persello, J.; Sbirrazzuoli, N. Impact of Silica Nanoclusters on Furfuryl Alcohol Polymerization and Molecular Mobility. *J. Phys. Chem. C* **2017**, *121* (13), 7485–7494.
- (35) Codou, A.; Guigo, N.; Heux, L.; Sbirrazzuoli, N. Partial Periodate Oxidation and Thermal Cross-Linking for the Processing of Thermoset All-Cellulose Composites. *Compos. Sci. Technol.* **2015**, *117*, 54–61.
- (36) Kalia, S.; Dufresne, A.; Cherian, B. M.; Kaith, B. S.; Avérous, L.; Njuguna, J.; Nassiopoulos, E. Cellulose-Based Bio- and Nanocomposites: A Review. *Int. J. Polym. Sci.* **2011**, *2011*, 1–35.
- (37) Leszczyńska, A.; Stafin, K.; Pagacz, J.; Mičušík, M.; Omastova, M.; Hebda, E.; Pielichowski, J.; Borschneck, D.; Rose, J.; Pielichowski, K. The Effect of Surface Modification of Microfibrillated Cellulose (MFC) by Acid Chlorides on the Structural and Thermomechanical Properties of Biopolyamide 4.10 Nanocomposites. *Ind. Crops Prod.* **2018**, *116*, 97–108.
- (38) Guigo, N.; Mija, A.; Zavaglia, R.; Vincent, L.; Sbirrazzuoli, N. New Insights on the Thermal Degradation Pathways of Neat Poly(Furfuryl Alcohol) and Poly(Furfuryl Alcohol)/SiO₂ Hybrid Materials. *Polym. Degrad. Stab.* **2009**, *94* (6), 908–913.

VI. Supplementary Information

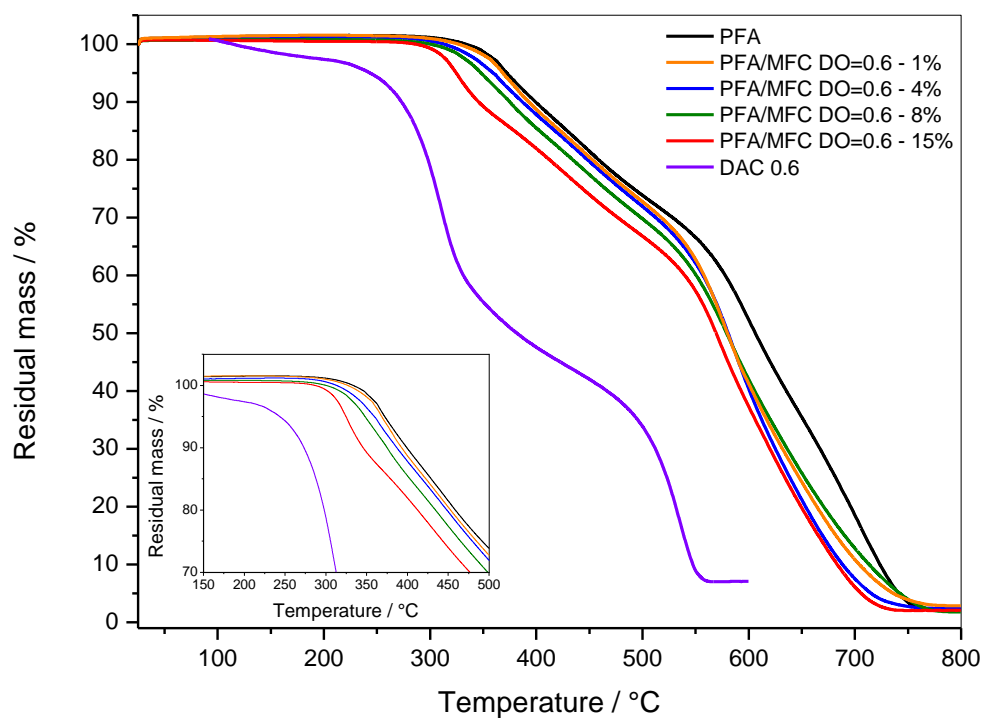


Figure S1. Thermogram analyses for neat PFA and PFA/MFC composites at different ratios for DO = 0.6.

Chapter VI

Hydrophobization of thermoset-like all cellulose composites

I. Introduction	197
II. Experimental section	200
II.1. Characterization techniques	200
II.1.1. Liquid state NMR	200
II.1.2. FTIR spectroscopy	200
II.1.3. Scanning electron microscopy (SEM)	200
II.1.4. Water contact angle	200
II.1.5. Dynamical mechanical analysis (DMA)	200
II.2. Chemical materials	201
II.3. Preparation of 5,5'-dihydroxymethyl furoin (DHMF)	201
II.3.1. Characterization by ^1H NMR	202
II.3.2. Characterization by FTIR	203
II.4. Processing of the reinforced All Cellulose Composites	204
III. Results and Discussions	206
III.1. Structural characterization	206
III.1.1. FT-IR characterization	206
III.1.2. Macroscopic and microscopic morphologies of the thermosets ACCs	208
III.2. Moisture sensitivity	211
III.3. Thermo-mechanical properties of the composites by DMA	215
IV. Conclusion	219
V. References	220
VI. Supplementary Information	222

I. Introduction

This work is based on the preparation and modification of thermoset-like all-cellulose composites (ACCs). Alternative routes for environmentally friendly composites focused on so-called single polymer composites or self-reinforced polymer composites. This concept, introduced about four decades ago by Capiati and Porter¹, is about homocomposites, self-reinforced, or homogeneous composites. Both matrix and filler are from the same material. Thus, all-cellulose composite is a fully cellulose based composite which presents good mechanical properties, no fiber-matrix compatibility issues. It may present various forms (*e.g.* films, sheets, or laminates) with the advantage of biodegradability²⁻⁵. Initial work on the development of ACCs performed by Nishino *et al.* succeeded to a combination of trends towards natural fiber reinforcement and single polymer composites⁶. Herein, the preparation was based on the difference of solubility between the cellulose matrix and the reinforcing cellulose fibers in lithium chloride/N,N-dimethylacetamide (LiCl/DMAc) through the pre-treatment. A solution of dissolved pre-treated cellulose pulp in LiCl/DMAc has been used to impregnate untreated rami fibers, followed by a coagulation in methanol and drying. Such composites presented significant expectations as a bio-based and biodegradable material with excellent mechanical performance. Another strategy for the preparation of all-cellulose composites relies on cellulose derivatization: a thermoplastic cellulose matrix can be formed by benzylation^{7,8}, oxypropylation⁹, or esterification^{10,11}. These derivatized ACCs showed mechanical properties similar to those of cellulose-based composites with synthetic thermoplastic polymers, and presented in general physical properties five to ten times lower than those of non-derivatized ACCs¹².

Among the numerous possibilities of cellulose modification, modification by periodate oxidation allows also to deal with the problem of rigidity by introducing additional mobility to the backbone. This oxidation method is characterized by the selective oxidation of the hydroxyl groups in C₂ and C₃ position into aldehydes, through a ring-opening of the glucose cycle. In the field of material development, cellulose modified through periodate oxidation was proposed as a platform for further modification¹³⁻¹⁵ and hydrogel¹⁶ or aerogel cross-linking¹⁷.

Even in the form of ACC, cellulose is very moisture sensitive. However, current literature is rare on the moisture sensitivity behavior of ACC. These composites are pure cellulosic material, thus, they can undergo a decomposition in presence of moisture leading to a lower strength and modification in the physical structure with reduction of their service-life⁴. In a very recent

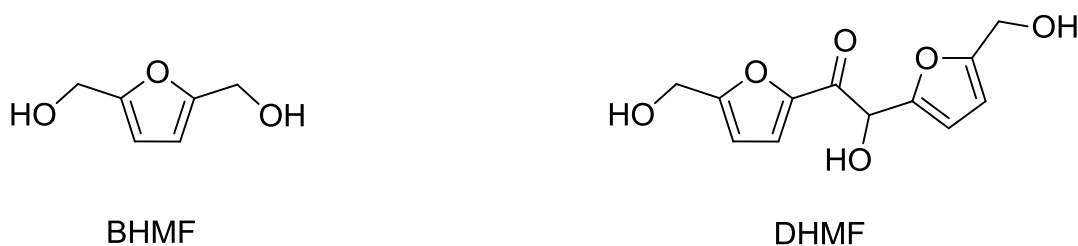
paper, Adak *et al.*¹⁸ started to investigate the moisture uptake and water absorbency of ACCs to improve their performances.

The present work proposes a solution to enhance the moisture resistance of ACCs using furanic derivatives to reinforce the cellulose matrix.

Neat ACCs were prepared using a single source of cellulose. Derivatization was proceeded on part of it to yield an *in situ* thermosetting-prone matrix which can be heat-processed with the remaining underivatized part of the sample. This concept was patented in 1963 by Battista *et al.*¹⁹ as the authors have highlighted the potential of ACCs resulting from partially oxidized microcrystalline cellulose.

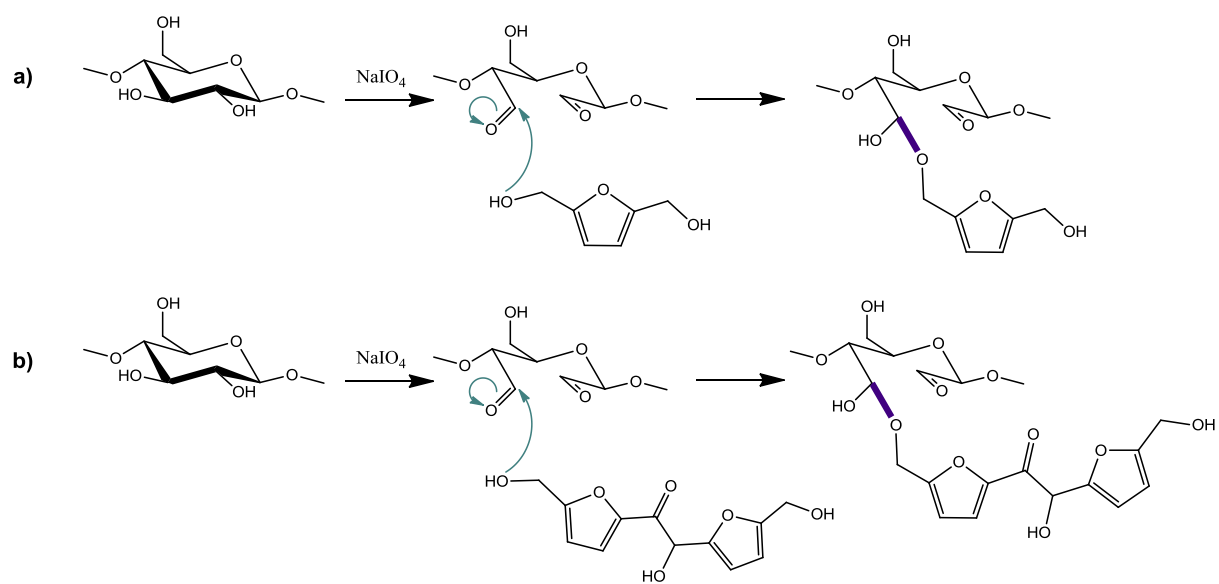
In this work, periodate oxidation of microfibrillar cellulose (MFC) was performed. In a former paper dealing with the periodate oxidation of similar MFC¹⁵, authors have defined time-depending conditions where limited oxidation took place only at the surface of the MFC. As described in **Scheme 1a)** of the previous chapter, the periodate oxidation led to a glycosyl ring opening with the formation of two aldehyde groups at the C₂ and C₃ positions. The resulting carbonyl moieties were found to be very reactive, leading to a recombination with adjacent unreacted primary –OH groups forming hemiacetals with 5 to 8-member fused rings¹⁵.

As furan ring presents a certain hydrophobicity, furanic derivatives can be used to increase the moisture resistance of ACCs. To this end, two different furanic compounds were used: a first compound with one furanic ring, the 2,5-bis(hydroxymethyl)furan (BHMF); and another with two furanic rings, the 5,5'-dihydroxymethyl furoin (DHMF). Their chemical structures are depicted in **Scheme 1**.



Scheme 1. Chemical structure of BHMF and DHMF.

After oxidation, the introduction of a slight excess of furanic compounds containing primary alcohols may induce competitive reactions as these compounds can also react with the aldehyde functions of oxidized MFC, as shown in **Scheme 2**. Thus, the furanic derivative can have a reinforcement effect, increasing the rigidity of the sample thanks to the furan rings, and through a more important H-bonds network.



Scheme 2. Competitive reactions to hemiacetalisation between MFC: **a)** with BHMf, and **b)** with DHMF.

II. Experimental section

II.1. Characterization techniques

II.1.1. Liquid state NMR

NMR spectra were recorded in deuterated chloroform (CDCl_3) or in deuterated dimethylsulfoxide (DMSO d_6) on a Bruker AVANCE III HD spectrometer operating at 400.17 MHz for ^1H . Experiments were recorded with a flip angle of 30° , and using sequences provided by Bruker. The spectrometer was equipped with the following probe: PA BBO 400S1 BBF-H-D-05 Z. The residual solvent signal at 7.26 ppm has been used as standard reference for CDCl_3 , while the standard reference for DMSO d_6 was taken with the peak at 2.26 ppm.

II.1.2. FTIR spectroscopy

FT-IR technique was used in this chapter section for the characterization of the product of synthesis, and the final thermosets ACCs. For this purpose, a Bruker tensor 27 equipped with a nitrogen-cooled MCT detector, in ATR mode with diamond crystal and OPUS software was used. Each spectrum was recorded with 4 cm^{-1} resolution and 64 scans co-addition.

II.1.3. Scanning electron microscopy (SEM)

The fracture morphologies of the ACCs samples were investigated by Scanning electron microscopy (SEM) with a Jeol JSM-6700F SEM at an accelerating voltage of 3 kV. Prior to observation, samples were cut to produce fresh surface, and coated with platinum.

II.1.4. Water contact angle

The surface wettability was determined using a DSA30 goniometer (Kruss) and the software “Drop Shape Analysis System”. 2 μL of water droplets were placed on samples, and samples were observed with a camera. The apparent contact angles (θ) were taken at the triple point of the solid-liquid-vapor interface.

II.1.5. Dynamical mechanical analysis (DMA)

DMA analyses were performed on a Mettler-Toledo DMA 1 with STAR[®] software. The samples of a dimension of 5 mm long, 5mm width, and 0.1-0.3 mm thick were submitted to a traction in non-isothermal mode (heating rate of $2\text{ K}\cdot\text{min}^{-1}$) from $-170\text{ }^\circ\text{C}$ to $250\text{ }^\circ\text{C}$ (samples may break before that temperature), with a frequency of 1 Hz and an oscillation amplitude of $5\text{ }\mu\text{m}$ (0.033 %) in auto-tension mode.

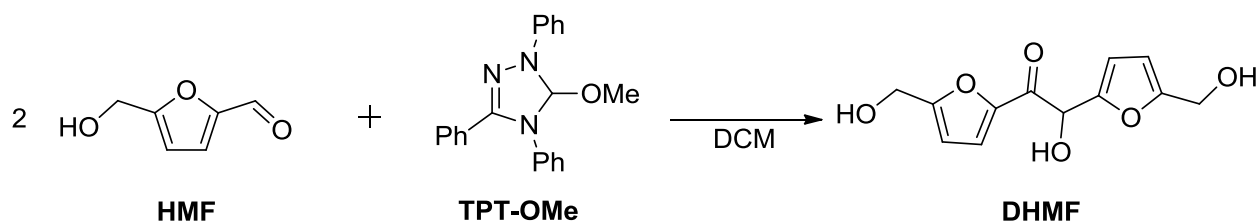
II.2. Chemical materials

Microfibrillar cellulose (MFC) was kindly supplied by the *Centre de Recherche des Macromolécules Végétales (CERMAV)*, as a suspension at 2 wt % in water. Sodium metaperiodate, hydroxylamine hydrochloride, benzoyl chloride, thionyl chloride (SOCl₂), aniline, triethylamine (Et₃N), phenylhydrazine, acetic acid (HOAc), acetic anhydride (Ac₂O), formic acid, sodium methanolate (NaOMe), and all the solvents were purchased from Sigma Aldrich and used without further purification. 2,5-bis(hydroxymethyl)furan (BHMF, purity: 97 %) and 5-hydroxymethylfurfural (HMF, purity ≥ 97 %) were purchased from Carbosynth and used as received.

II.3. Preparation of 5,5'-dihydroxymethyl furfural (DHMF)

DHMF was synthesized from hydroxymethylfurfural (HMF) according to previous literature^{20,21}. The conversion of HMF to DHMF is a highly selective synthesis that can be performed at 40 °C for less than 1 hour (about 40 minutes) in dichloromethane (DCM), and under nitrogen atmosphere. The reactant used to convert HMF into DHMF was the 5-Methoxy-1,3,4-triphenyl-4,5-dihydro-1H-1,2,4-triazoline (TPT-OMe) that was not found to be commercially available and was synthesized followed Enders *et al.*²² procedure. Synthesis description and structural characterization by ¹H NMR (**Figure S2**) of TPT-OMe are presented in Supplementary Information at the end of the chapter.

The synthesis route of DHMF was performed as described by Mou *et al.*²³ who modified the initial literature procedure²⁰. Reaction scheme is described in **Scheme 3**. To a round-bottomed flask equipped with a stirring bar and a reflux condenser, was added HMF (30.14 g, 0.24 mol), TPT-OMe (0.8 g, 2.4 mmol), and DCM, then the vessel was sealed under nitrogen atmosphere. The reaction mixture was heated to 40 °C for 40 min and a solid precipitated. After cooling down to room temperature, the solid was isolated by filtration, rinsed with DCM, and dried under vacuum overnight at ambient temperature. DHMF (21.38 g, 85 %) was then obtained as a yellow thin powder.



Scheme 3. Synthesis of difuranic polyol DHMF from HMF.

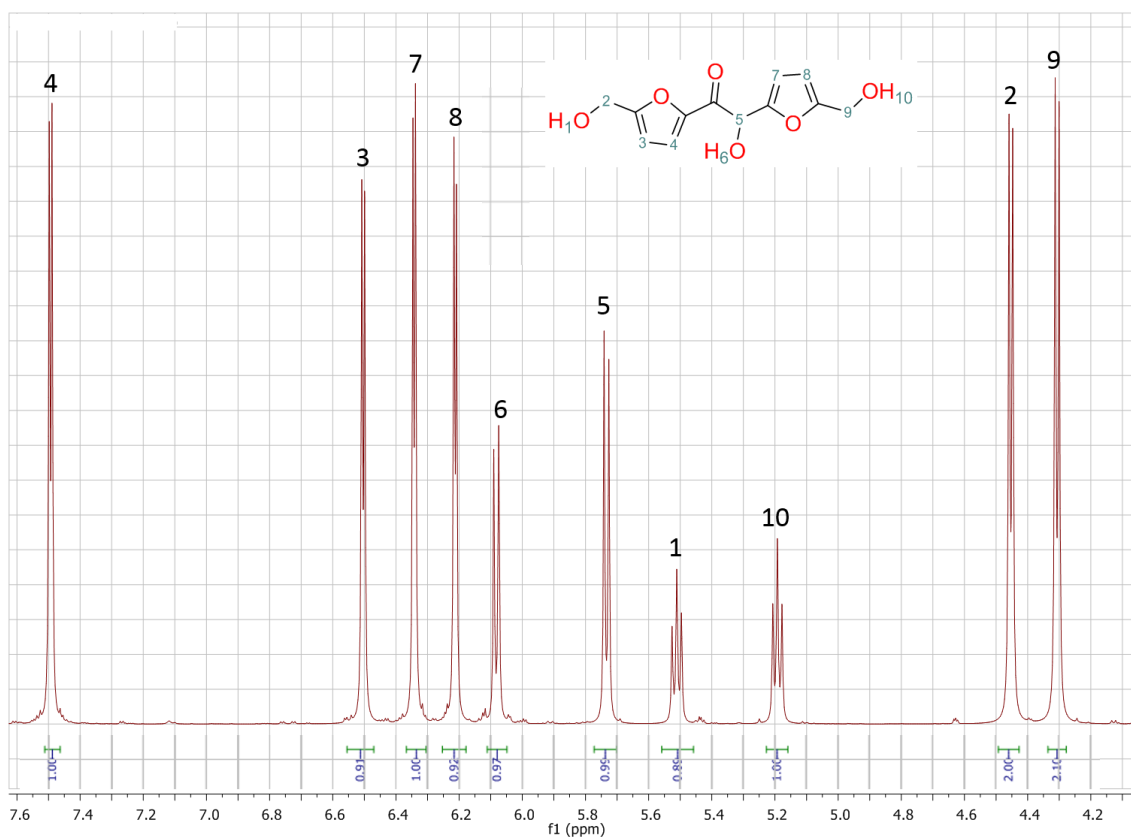
II.3.1. Characterization by ^1H NMR

Figure 1. ^1H NMR spectrum of the final product of synthesis: DHMF (solvent: DMSO d_6).

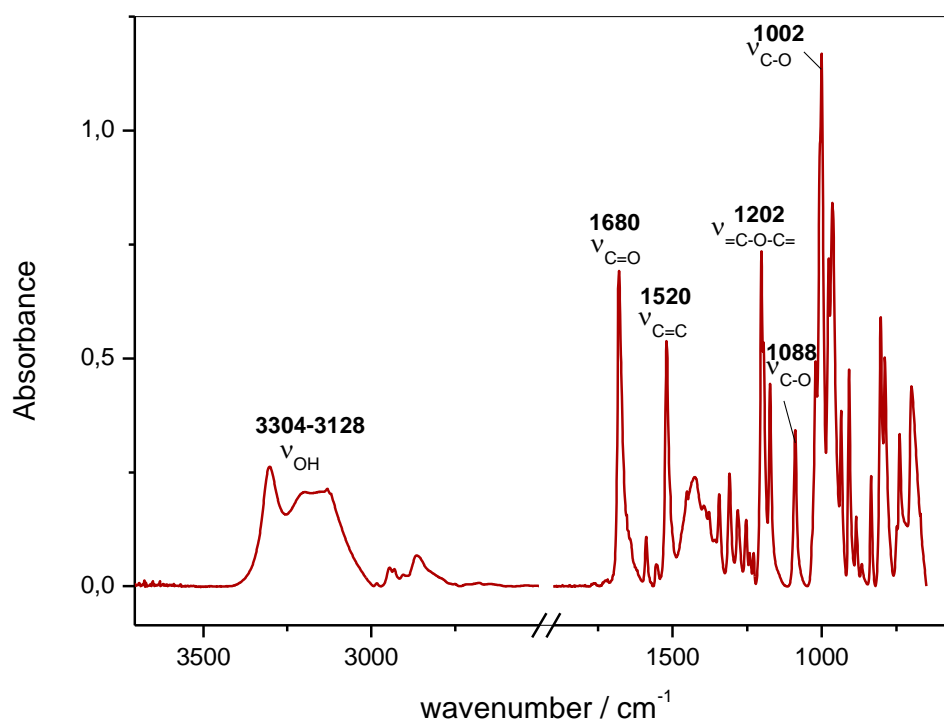
The spectrum exhibited the characteristic peaks of the DHMF which confirmed the structure of the synthesized product. As the molecule is not symmetric, each proton of the furan rings appeared individually as doublets. The most deshielded furanic proton [4] at $\delta = 7.49$ ppm was taken arbitrarily as integration reference and set for 1 H. Thus, the others furanic proton atoms at $\delta = 6.50$, 6.34, and 6.21, respectively attributed to protons [3,7,8], integrated for 0.91, 1.00, and 0.92 H respectively ($I_{\text{th}} = 1.00$ H each). The lateral CH_2 at $\delta = 4.46$ and 4.31 ppm presented signals as doublets with respective values of $I_{\text{exp}} [2] = 2.00$ H and $I_{\text{exp}} [9] = 2.10$ H ($I_{\text{th}} = 2.00$ H each), while the CH^*-OH [5] presented a doublet at $\delta = 5.74$ ppm with an experimental integration of 0.99 H ($I_{\text{th}} = 1.00$ H). Finally, the proton [6] of the alcohol function in β of the ketone was the most deshielded and appeared as a doublet at $\delta = 6.09$ ppm with an integration value of 0.97 H ($I_{\text{th}} = 1.00$ H), while lateral alcohol protons [1] and [10] appeared as triplets at respectively $\delta = 5.51$ and 5.19 ppm and showed respective integration values of 0.89 H and 1.00 H ($I_{\text{th}} = 1.00$ H each). All values are summarized in **Table 1**.

Table 1. ^1H NMR data of DHMF.

Chemical shift (ppm)	Assignment	$I_{\text{experimental}}$	$I_{\text{theoretical}}$
4.31	$\text{CH}_2\text{-OH}$ [9]	2.10 H	2.00 H
4.46	$\text{CH}_2\text{-OH}$ [2]	2.00 H	2.00 H
5.19	$\text{CH}_2\text{-OH}$ [10]	1.00 H	1.00 H
5.51	$\text{CH}_2\text{-OH}$ [1]	0.89 H	1.00 H
5.74	CH-OH [5]	0.99 H	1.00 H
6.09	CH-OH [6]	0.97 H	1.00 H
6.21 / 6.34 / 6.50 / 7.49	Furan-H [4,3,7,8]	0.92 / 1.00 / 0.91 / Ref. 1.00 H	1.00 / 1.00 / 1.00 / 1.00 H

II.3.2. Characterization by FTIR

The chemical structure of the final product of synthesis was also confirmed by ATR-IR spectroscopy. The corresponding spectrum is depicted in **Figure 2**.

**Figure 2.** FTIR spectrum of DHMF.

The presence of alcohol functions was confirmed by the wide band at 3304-3128 cm^{-1} corresponding to the O–H stretching. The carbonyl (C=O) stretching of the conjugated ketone function was unambiguously assigned to the strong peak at 1680 cm^{-1} . The furan rings were confirmed by the C=C stretching at 1520 cm^{-1} , the =C–O–C= ring vibration at 1202 cm^{-1} , and the C–H out of plane deformation of the furan rings at 812 and 738 cm^{-1} . Moreover, the weak band at 1588 cm^{-1} can be attributed to the C=C stretching for 2,5-disubstituted furan rings. Finally, the medium peak at 1088 cm^{-1} was attributed to the C–O stretching of the secondary alcohol, and the strong peak observed at 1002 cm^{-1} was attributed to the C–O stretching of the primary alcohols of the hydroxymethyl groups. These main observations are summarized in **Table 2**.

Table 2. Assignments of major bands on FTIR spectrum of DHMF.

Assignment	Wavenumber (cm^{-1})
O–H stretching	3304 – 3128
C=O stretching conjugated with C=C	1680
C=C stretching 2,5-disubst. furan ring	1588
C=C stretching furan ring	1520
=C–O–C= stretching furan ring	1202
C–O stretching secondary alcohol	1088
C–O stretching primary alcohol / =C–O–C= stretching furan ring	1002
C–C–C in-plane bending furan ring	908
C–H out of plane deformation furan ring	812
C–H out of plane deformation furan ring	738
O–H out of plane deformation	698

II.4. Processing of the reinforced All Cellulose Composites

Neat ACCs and reinforced ACCs were processed by heat compression molding to form thin films. After oxidation, the obtained DAC were re-dispersed in water using an ultra-turrax at 10,000 rpm for 30 sec, in order to obtain a homogeneous suspension. Reinforced ACCs were prepared by addition of 1.1 equivalent of BHMF or DHMF to DAC before homogenization with ultra-turrax.

The maximal DO that can be obtained is 2 for complete oxidation of AGU. Thus, at DO = 0.6, the MFC was oxidized at 30 %, while at DO = 1.5, MFC was oxidized at 75 % meaning that

the structure contained respectively 30 % and 75 % of aldehyde functions. BHMF and DHMF were added regarding the amount of aldehyde groups. Thus, the addition of 1.1 equivalent of furanic derivative (regarding the aldehyde functions) corresponds to the addition of 33 % and 83% respectively for $DO = 0.6$ and $DO = 1.5$.

After removing the excess of water, about 1 g of DAC was poured into a rectangular silicon mold with lateral sizes of 27 and 72 mm and a height of 30 mm, itself placed into a polytetrafluoroethylene (PTFE) mold. The PTFE mold was then heated to 100 °C and compression was progressively increased to reach 15 bars for 2 h to induce drying and cross-linking. This process resulted in the formation of isotropic ACC materials with a thickness of about 0.1-0.3 mm. **Figure 3** shows the different steps of the compression-molding process.

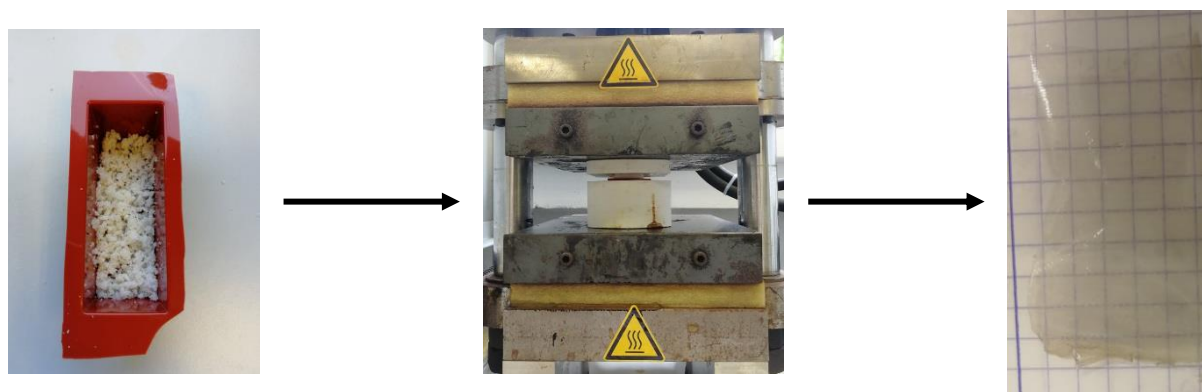


Figure 3. Different steps of the preparations of ACC thermoset. From left to right: silicon mold containing oxidized MFC, compression molding, and final ACC sample after drying (from MFC at $DO=1.5$).

In total, six samples were prepared: three samples with MFC oxidized at $DO = 0.6$ to obtain one neat ACC, one ACC reinforced with BHMF, and one ACC reinforced with DHMF; and three other equivalent samples with MFC oxidized at $DO = 1.5$ (**Table 3**).

Table 3. Different ACC samples prepared from DAC at $DO = 0.6$ and $DO = 1.5$.

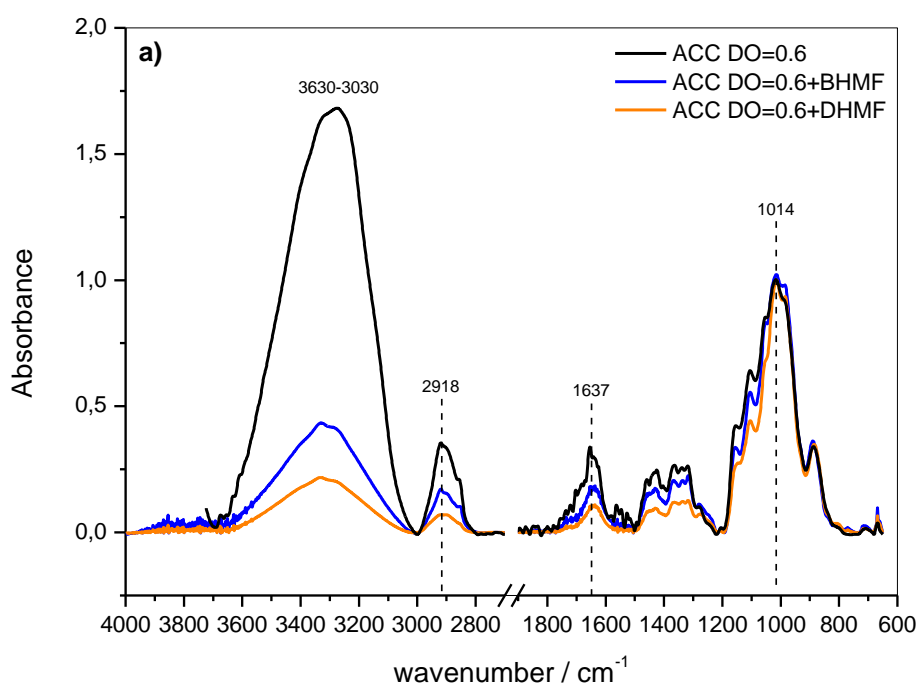
DO	Sample		
	0.6	Neat ACC	ACC + 33 % BHMF
1.5	Neat ACC	ACC + 83 % BHMF	ACC + 83 % DHMF

III. Results and Discussions

III.1. Structural characterization

III.1.1. FT-IR characterization

In order to find interactions between the furanic compound and the cellulosic ACC matrix, the ACC samples were investigated by FTIR and the corresponding spectra are depicted in **Figure 4a)** for samples at DO = 0.6. A strong -OH band was observed for neat ACC at 3630-3030 cm^{-1} . By comparing the height ratio of -OH stretching band over -CH stretching band at 2918 cm^{-1} , it could be observed that the intensity of the -OH stretching band was twice lower in presence of the furanic derivatives. It can be assumed from this observation that the furanic cross-linkers strongly interferes with the H-bonding network by increasing the network density. At 1637 cm^{-1} , a weak band was observed for all the samples. This band has often been observed for cellulosic materials and was attributed to the adsorbed water²⁴. It is interesting to observe that the intensity of this band was decreased with the introduction of furanic derivatives, with the lowest intensity for the ACC prepared with DHMF, which contains two furan rings. This can be a first indication of the hydrophobic effect of this compound. As ACC at DO = 0.6 is only modified at 30 %, the presence of a furanic compound within the ACC did not seem to present other significant modifications of the chemical structure.



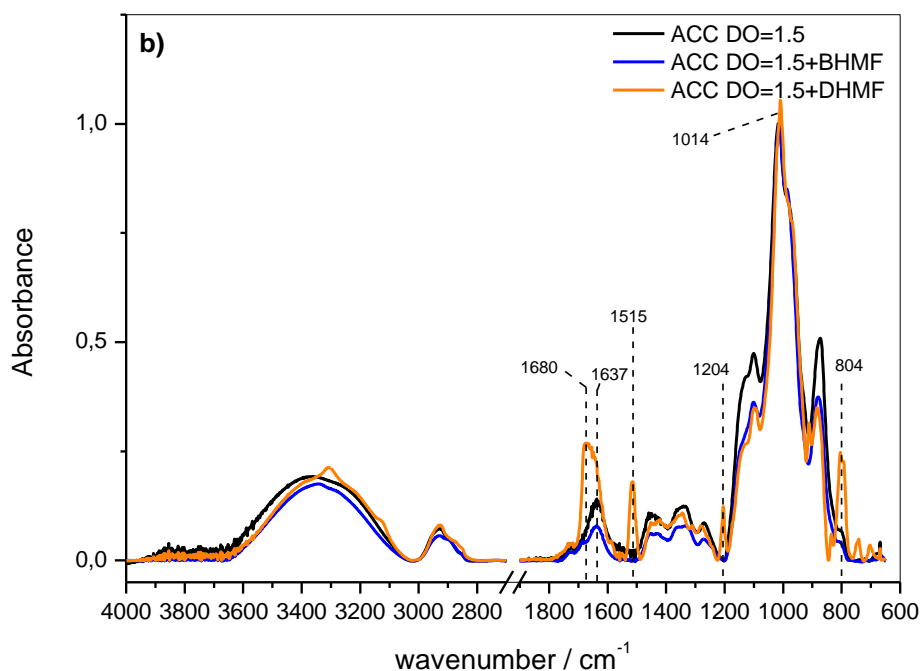


Figure 4. FTIR spectra of ACC samples at **a)** DO = 0.6 and **b)** DO = 1.5.

FTIR spectra of ACC samples at DO = 1.5 are depicted in **Figure 4b)**. ACC samples at DO = 1.5 presented a higher concentration of BHMF and DHMF, as the chemical modification of MFC led to 75 % of aldehydes. This would facilitate observations regarding the presence of the furanic compounds. At such high degree of modification, the MFC is highly amorphous with a larger amount of OH functions oxidized into aldehydes, thus reducing the intensity of the corresponding -OH peak. As the intensities of the -OH band were relatively close for the three samples, it was easier to note a slight shift of the -OH band to lower wavenumbers in presence of BHMF and DHMF, which may indicate a lower amount of free -OH that can be due to moisture. Moreover, the peak at 1637 cm^{-1} characteristic to the adsorbed water was decreased in presence of BHMF due to lower adsorbed moisture, while the peak was increased and shifted to 1680 cm^{-1} in presence of DHMF. This shift was then due to the presence of conjugated ketone in the structure. Other peaks corresponding to the furanic backbone were evidenced: mainly at 1515 cm^{-1} , 1204 cm^{-1} , and 804 cm^{-1} .

More generally, the band at 1428 and 1338 cm^{-1} were respectively attributed to the $-\text{CH}_2$ scissoring and $-\text{OH}$ bending vibrations. The absorption bands at 1104 and 1053 cm^{-1} correspond to the vibration of the C-O-C glycosidic linkage²⁵, while the band at 1156 cm^{-1} can be attributed to the antisymmetric stretching of the C-O bridge of cellulose²⁴, while the C-O band at 1014 cm^{-1} is attributed to the stretching of the hydroxymethyl groups, as well as the $=\text{C}-\text{O}-\text{C}=\text{C}$

symmetric stretching of furan rings. The sharp small peak at 884 cm^{-1} was commonly attributed to the C–H rocking vibrations²⁶. The data are summarized in **Table 4**. Regarding the ratio of the C–O band at 1014 cm^{-1} over the C–H rocking band at 884 cm^{-1} , a difference was however noticed for the peak at 1014 cm^{-1} as its intensity is increased on presence of DHMF which can be due to the additional C–O stretching of the furanic rings, to supplementary hydroxymethyl groups and C–O bonds from DHMF, or to eventual hemiacetal linkage between MFC and DHMF, as these bonds present a stretching vibration in this area.

Table 4. Assignment of major bands on FTIR spectra of ACCs at DO = 0.6.

Assignment	Wavenumber (cm^{-1})
O–H stretching	3630-3030
C–H stretching	2918
C=O stretching conjugated	1680
Water adsorption	1637
C=C stretching furan ring	1515
–CH ₂ scissoring	1428
–OH bending	1338
=C–O–C= stretching furan ring (asym)	1204
C–O–C stretching glycosydic linkage	1104 – 1053
C–O bridge antisymmetric stretching	1156
C–O stretching primary alcohol / =C–O–C= stretching furan ring (sym)	1014
C–H rocking	884
C–H out of plane deformation furan ring	804

III.1.2. Macroscopic and microscopic morphologies of the thermosets ACCs

A photography for each ACC sample resulting from the compression molding is displayed in **Figure 5**. In a previous study, Codou *et al.*²⁷ compared the effect of the DO on the optical transparency and noticed that the transparency of ACCs were increasing with the DO. At a DO of 0.6, which is considered as an intermediate DO, NMR data indicated that there was still a significant amount of pristine cellulose, responsible of the opacity of the sample. Authors noticed that the newly formed amorphous oxidized cellulose acts like an interfacial glue between the remaining unoxidized microfibrils, thus, decreasing the light scattering of the sample. When the oxidized part increases, the sample gains in homogeneity and displays a

better transparency, which is observed with ACC sample from MFC oxidized at 1.5 which is totally transparent (**Figure 3** right image).

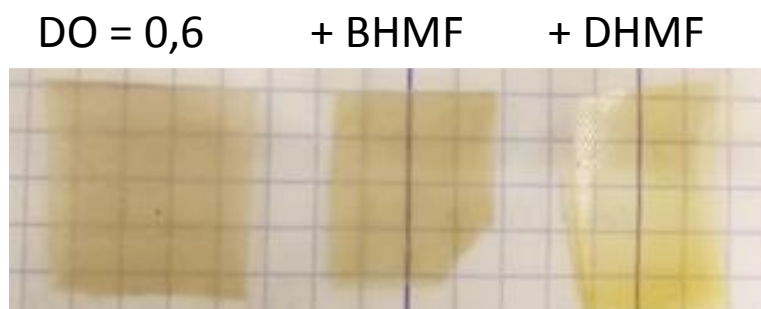


Figure 5. Photograph of the samples after compression molding. From left to right: neat ACC at DO=0.6.

However, the pristine cellulose is white while the ACC obtained from oxidized MFC present a yellowish color. This effect is often observed in the case of cellulose oxidation as the occurrence of numerous carbonyl groups induces the development of chromophores, responsible of the yellowing of the ACC^{28,29}. The incorporation of furanic compound within the ACC increases the yellowing of the sample. This is moderated in the case of BHMF as shown in **Figure 5**. It becomes more yellow with DHMF as this compound contains two furanic rings, which one presents a higher delocalization of its electrons with a conjugated ketone.

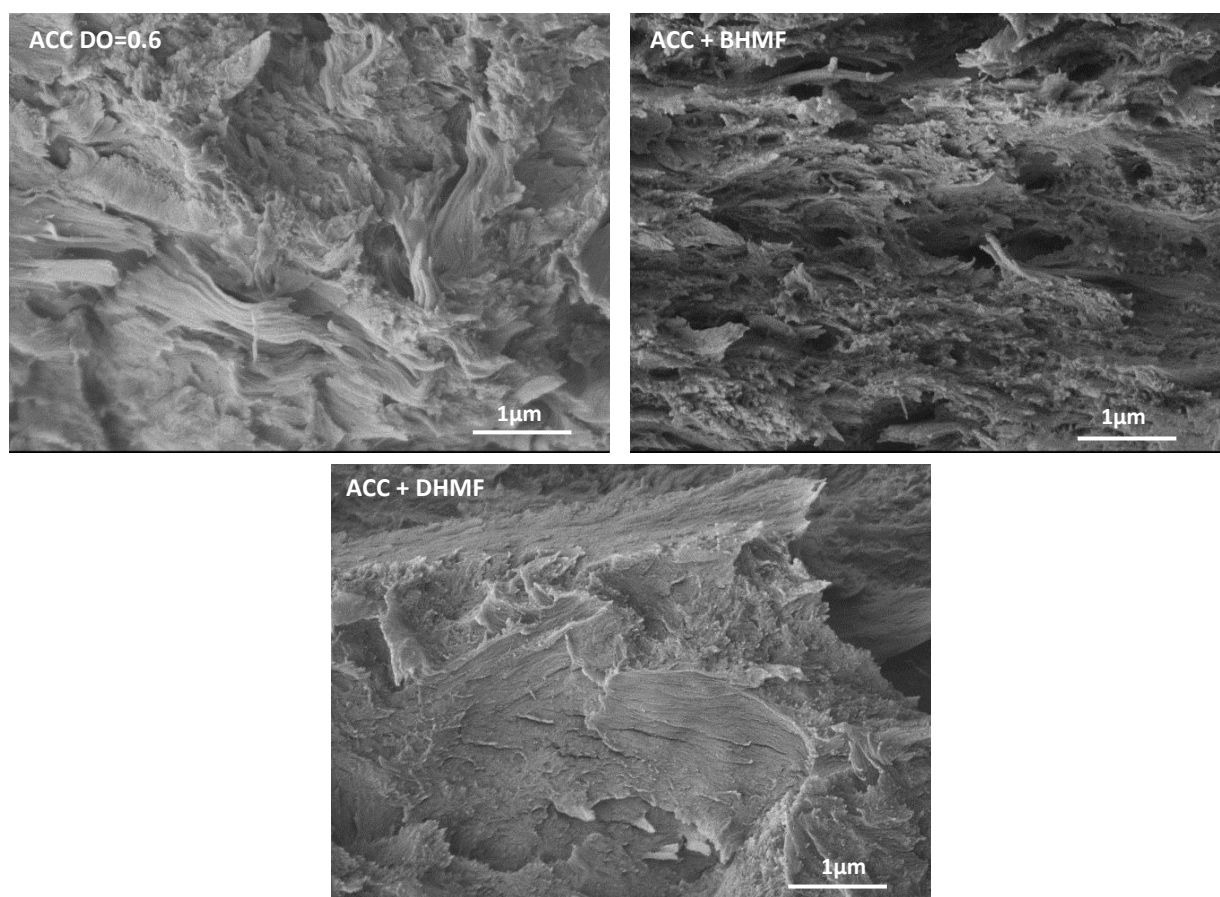


Figure 6. SEM micrographs of the fractures of ACCs samples at DO 0.6: neat ACC, ACC with BHMF, and ACC with DHMF.

The SEM images displayed in **Figure 6** of the fractures of the three ACC samples at DO = 0.6 show a good homogeneity of the ACCs. Moreover, the presence of the furanic compound within the microfibrils seemed to increase the compactness in the final ACC, especially in the presence of DHMF.

SEM micrographs for samples at DO = 1.5 are displayed in **Figure 7**. At DO = 1.5 the MFC is highly amorphous and the sample of neat ACC showed already a good homogeneity with a smooth surface. However, this sample showed some cracking and seemed to inflate at some parts. The inflation of this sample was finally due to the interactions with the electron beam. The introduction of the furanic derivatives seemed to bring roughness to the material with a coherent alignment of the network. Moreover, the ACC sample at DO = 1.5 with BHMF presented some defects like small holes as microfibrils could have been ripped during the sample fracture.

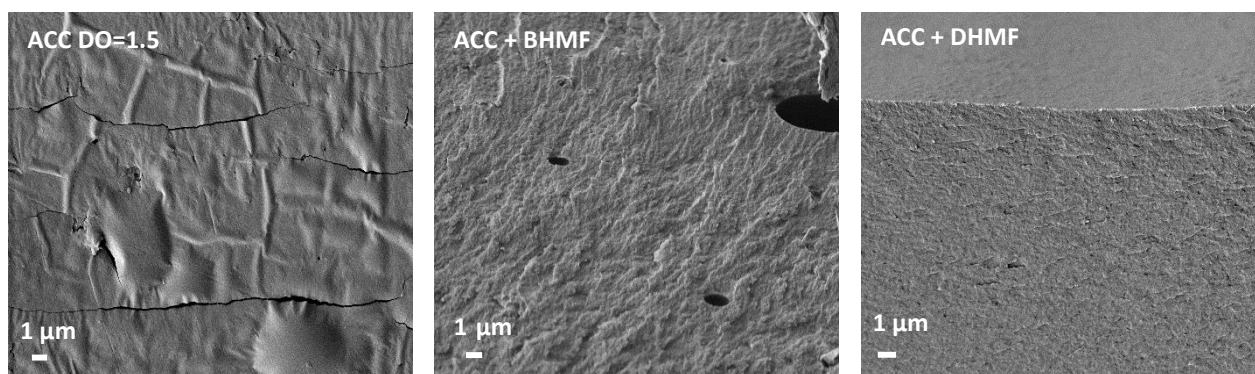


Figure 7. SEM micrographs of the fractures of ACCs samples at DO 1.5: neat ACC, ACC with BHMF, and ACC with DHMF.

III.2. Moisture sensitivity

The water contact angles were measured for each sample with a goniometer to evaluate the potential hydrophobic property brought by the furanic cross-linkers. Pictures of the water drops are depicted in **Figure 8**. A surface material is considered hydrophilic when the contact angle (θ) is below 90° , hydrophobic when $\theta \geq 90^\circ$, and superhydrophobic when $\theta \geq 150^\circ$.

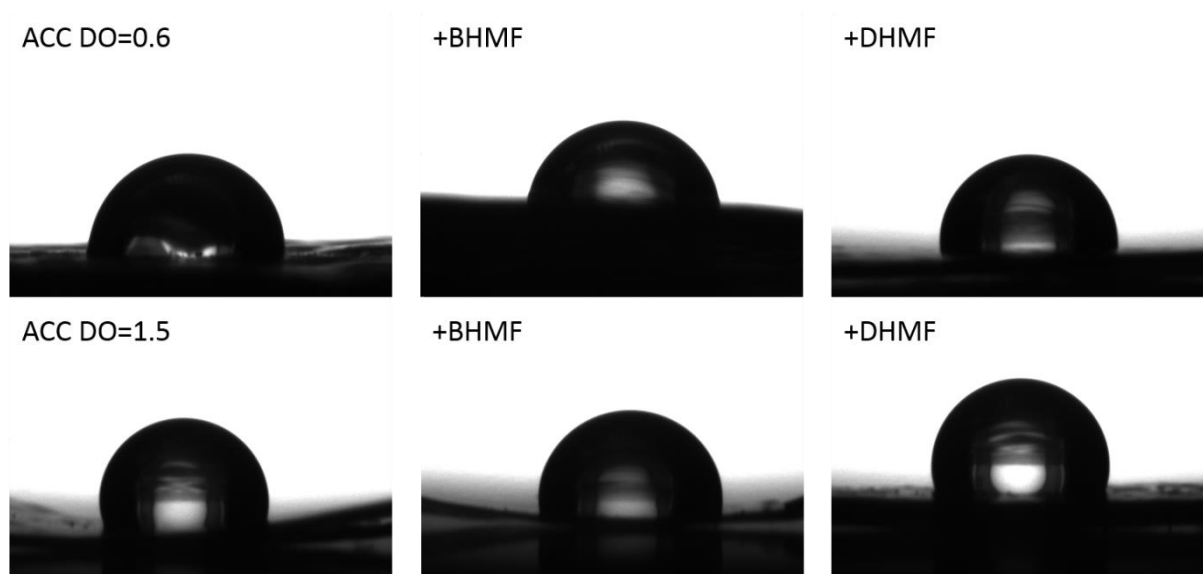


Figure 8. Water drops on the surface of each ACC sample.

Considering the values of the obtained contact angle summarized in **Table 5**, it appeared that neat ACC sample at DO = 0.6 could be considered as hydrophilic as it presented a contact angle of 85° . The incorporation of BHMF did not present a significant effect as the contact angle was very close (87°), indicating also a hydrophilic material. In the presence of DHMF within the structure, the contact angle was increased to reach 92° , leading to a hydrophobic material.

ACC samples at DO = 1.5 showed a more important hydrophobic behavior compared to samples at DO = 0.6, even for neat ACC due to the high amorphization of the MFC and lower -OH content. Again, the presence of BHMF did not impact the hydrophobicity as the water contact angle was very close to the neat ACC at DO = 1.5. It is interesting to note the strong increase of hydrophobicity brought by the DHMF as the surface contact angle was observed at 117°. Such increase of the contact angle correlates with SEM observations, as the presence of furanic derivatives increased the roughness of the ACC. Indeed, the presence of rugosity may also increase the surface contact angle of water drops³⁰. Thus, the presence of furan rings actually increased the hydrophobicity of ACCs.

Table 5. Water contact angle for each ACC sample.

Sample	$\theta_{\text{water}} (^{\circ})$	Sample	$\theta_{\text{water}} (^{\circ})$
ACC DO = 0.6	85	ACC DO = 1.5	104
ACC DO = 0.6 + BHMF	87	ACC DO = 1.5 + BHMF	101
ACC DO = 0.6 + DHMF	92	ACC DO = 1.5 + DHMF	117

Additional experiment was performed to measure the water intake of each ACC sample by soaking samples into water and measuring the mass over time. The evolution of the water intake over time are depicted in **Figure 9a)** and **Figure 9b)** the ACC samples at DO = 0.6 and DO = 1.5 respectively. For both DOs, the water intake was strongly increased during the first 30 hours, with no significant effect from BHMF. Indeed, neat ACC samples and ACCs containing BHMF showed similar behavior. At DO = 0.6, the addition of DHMF seemed to slightly hamper the water intake ability as the maximum was reached almost 100 h later. After soaking into water for 120 h, ACC samples at DO = 0.6 have adsorbed the larger part of water, *i.e.* around 90 % for neat ACC and ACC containing BHMF, while the presence of DHMF lowered that quantity to about 80 %. From 120 h, the water intake slightly increases for several hours until it finally reached a maximum and did no longer evolved. The effect of the furanic cross-linkers was more relevant at higher DO. For neat ACC at DO = 1.5 and ACC containing BHMF, the experiment could not be continued further respectively 58 and 82 hours as the samples were dissolved into water. After reaching a maximum of water absorption, the sample mass of ACC containing BHMF started to decrease. Indeed, at high DO, cellulose is highly amorphous and becomes soluble in water. The addition of DHMF within the structure strongly influenced the water absorption ability of the corresponding material. Thus, for ACC containing over 80 % of DHMF, the water absorption increased slower, reaching only 45 % after 82 h, as

the two other samples were solubilized. After a progressive increase of the water absorption, a maximum was finally reached after 200 h in water. Then, the sample mass decreased as the sample started to dissolve limiting further measurements.

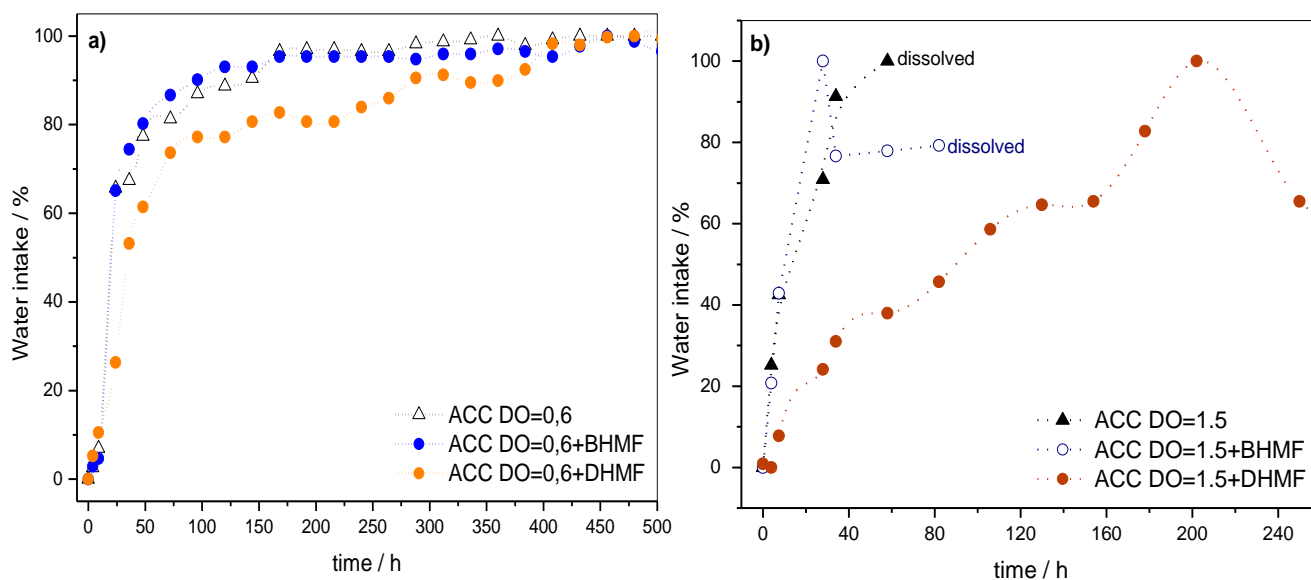


Figure 9. Water intake diagram for the ACC samples at **a)** DO = 0.6 and **b)** DO = 1.5.

It was interesting to notice that for analyses performed until now, the presence of BHMF did not show a strong impact as it did not bring particular hydrophobicity and it did not hamper the water intake neither. From a dimensional point of view, the distance between two aldehyde functions was estimated at about 4.7 Å (**Figure 10a**). The *inter*-distance between the lateral oxygen atoms of hydroxymethyl groups was estimated at about 6.3 Å (**Figure 10b**). However, considering a rotation around the axe of C_a–C_b bond, the oxygen noted O₁ would undergo this rotation and take place of the noted H_a, leading to an *inter*-atomic distance of 5.1 Å. In these conditions, as the theoretical distance between carbonyl groups of DAC and the distance between hydroxyl groups of BHMF are very close, it can be assumed that BHMF can preferentially undergo *intra*-hemiacetal linkage *i.e.* in the same chain. In the case of *intra* linkage the *inter*-chain cross-linking is then limited. On the contrary, DHMF presented a bigger structure (**Figure 10c**) with an *inter*-atomic distance between lateral hydroxyl groups estimated at about 8.6 Å. This would rather lead to *inter*-linkages between DAC. These inter chains' cross-links are able to reinforce the material. The *intra* and *inter*-hemiacetal linkage obtained with BHMF and DHMF respectively are schematized on **Figure 10 1)** and **2)**.

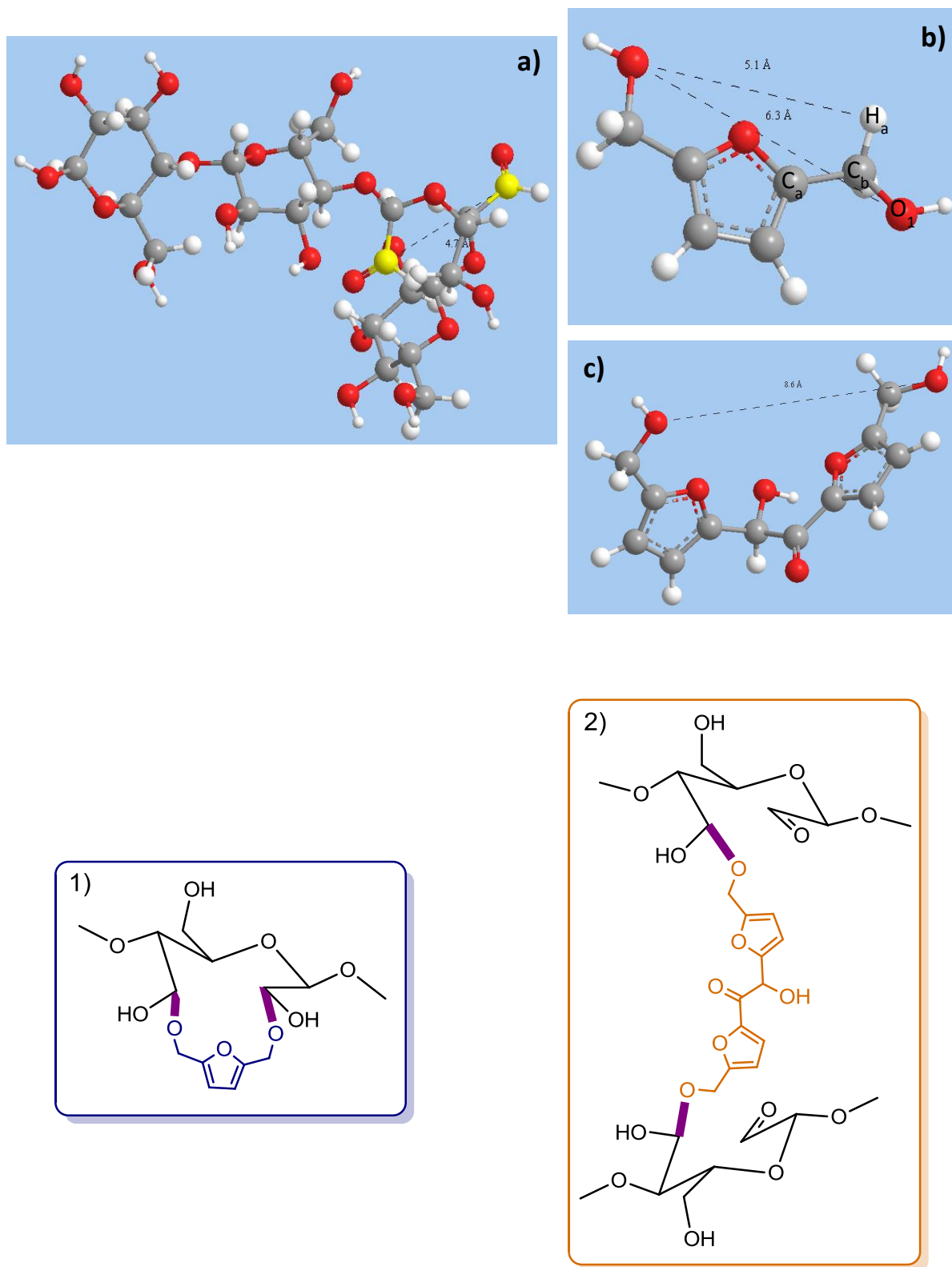


Figure 10. Top: Model estimation of the inter-atomic distance between **a)** carbonyl functions of DAC, **b)** hydroxymethyl oxygens of BHMF, and **c)** hydroxymethyl oxygens of DHMF – **Bottom: 1)** BHMF linear *intra*-hemiacetal linkage, **2)** DHMF cross-linked *inter*-hemiacetal linkage.

III.3. Thermo-mechanical properties of the composites by DMA

The first three samples of ACC prepared from MFC oxidized at a DO of 0.6 were investigated by DMA (**Figure 11**) to evaluate the mechanical properties and the relaxation processes of the materials.

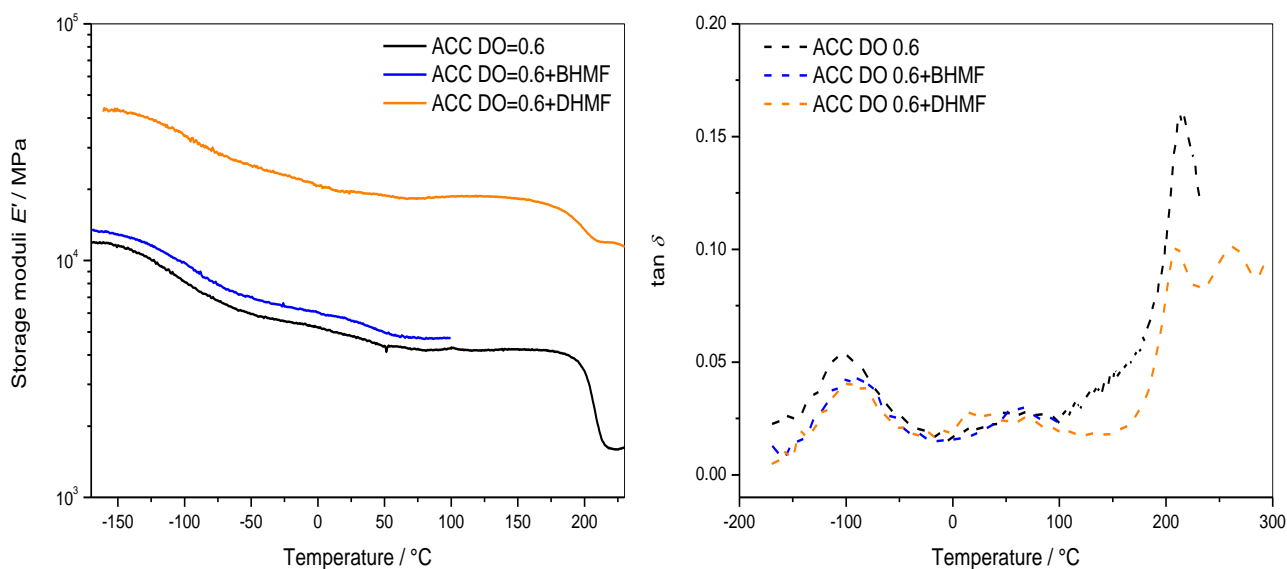


Figure 11. DMA thermograms of ACC at a DO of 0.6 (black), and ACC reinforced with BHMf (blue) and DHMF (orange) – **a**) Evolution of the storage moduli E' and **b**) Evolution of $\tan \delta$.

As a first observation of the variation of the storage moduli, it is noticed that the presence of DHMF within the oxidized microfibrillar structure highly increased the E' values *i.e.* the stiffness of the material. On the other hand, the presence of BHMf which contains one furan ring slightly increased the storage modulus (taken at 0 $^{\circ}\text{C}$) from about 5.2 GPa for the neat ACC at DO = 0.6, to 6.1 GPa for the ACC containing BHMf. The presence of DHMF increased the storage modulus to a much higher value of 20.7 GPa. The addition of furan rings as *inter*-chains cross-linkers brings rigidity and consequently the stiffness of the ACC. Through the observation of the evolution of $\tan \delta$, the ACCs presented three relaxations, which may be attributed to α , β , and γ relaxations, from higher to lower temperatures. The γ relaxation observed at -100 $^{\circ}\text{C}$ appeared to be specific of the ACC and independent of the cross-linker. The relaxations at low temperature are still a matter of controversy. Montès *et al.*³¹ suggested that the relaxation observed at the lowest temperature, at -123 $^{\circ}\text{C}$ which is close to the relaxation observed in **Figure 11**, was attributed to the γ relaxation of amorphous cellulose. Later, Kaminski *et al.*³² associated this γ relaxation to the rotation of the hydroxymethyl group ($\text{CH}_2\text{-OH}$). Previous

studies also noticed that the γ relaxation was not shifted with modification of the DO³³, which indicates that the *intra-* or *inter-*molecular hemiacetal cross-links did not affect the mobility of untouched hydroxymethyl groups. Montès *et al.* also observed a β relaxation close to the γ relaxation. This β relaxation was then observed to be moisture dependent, as it was shifted to higher temperatures after water removal by thermal treatment. For the ACC samples presented in **Figure 11**, the β relaxation was observed at 60 °C for both neat ACC and ACC containing BHMF, while the ACC thermoset containing DHMF presented a β relaxation at about 18 °C (**Table 6**). The amplitude of this relaxation was very low. The glycosyl ring opening of cellulose is followed by different possibilities of hemiacetal recombination mainly with the hydroxymethyl groups¹⁵, which is likely to give more mobility to the cellulosic main chain. However, these *intra-* or *inter-*chain hemiacetal formations are in competition with the hemiacetal formation with the hydroxyl groups of BHMF or DHMF. Thus, the cycles may remain open, but the mobility was reduced by the furan rings which bring rigidity to the structure.

The main relaxation usually associated to the glass transition temperature (T_g), the α relaxation (T_α), was observed at much higher temperatures. The T_g seemed to be only slightly shifted to lower temperatures in presence of the furanic cross-linker, from 213 °C to the neat ACC to 210 °C for the ACC containing DHMF. Unfortunately, the T_α of ACC containing BHMF could not have been evaluated as the sample broke before the end of the measurement. It is noteworthy that the α relaxation of the neat ACC presented a broad shoulder which was not present in the presence of DHMF in the structure, leading to a thinner, but also a lower peak. Such difference in the shape of the T_α peak may remain in the higher cross-linked and organized structure due to the presence of DHMF within the ACC, as the two furanic rings may induce a more compact and organized structure.

Table 6. Thermo-mechanical data for ACC samples at DO = 0.6.

	ACC DO = 0.6	ACC DO = 0.6 + BHMF	ACC DO = 0.6 + DHMF
E' at 0 °C (GPa)	5.2	6.1	20.7
T_γ	-100	-100	-100
T_β	60	60	18
T_α	213	-	210

For ACC samples prepared from highly oxidized MFC at DO = 1.5, the presence of a furanic cross-linker did not seem to have a strong influence on the final thermo-mechanical properties.

As presented in **Figure 12**, the storage modulus in the glassy state was slightly decreased when the furanic ring content was increased. Indeed, E' value at $-150\text{ }^{\circ}\text{C}$ was decreased from 4.6 GPa for neat ACC at $\text{DO} = 1.5$, to 3.9 GPa for ACC containing BHMF, and to 3.5 GPa for ACC containing DHMF. Then, the moduli for the three samples became identical from $-70\text{ }^{\circ}\text{C}$. Regarding the evolution of $\tan \delta$, a weak but wide peak was observed and more significantly for neat ACC. This broad peak from -135 to $0\text{ }^{\circ}\text{C}$ may be attributed to the γ relaxation of amorphous cellulose. As the MFC is almost completely amorphous at $\text{DO} = 1.5$, the large amount of DAC (and thus reactive sites) may create a dense network reaching percolation. In such a heavy network of amorphous MFC, only the DHMF seemed to present an influence on the thermo-mechanical properties. Indeed, by forming *inter*-hemiacetal cross-links, the network could be modified, and the corresponding material presented a decrease in the storage modulus, (and an increase in $\tan \delta$), starting an α relaxation. This α relaxation did not reach completion as the sample broke before the end of the experiment.

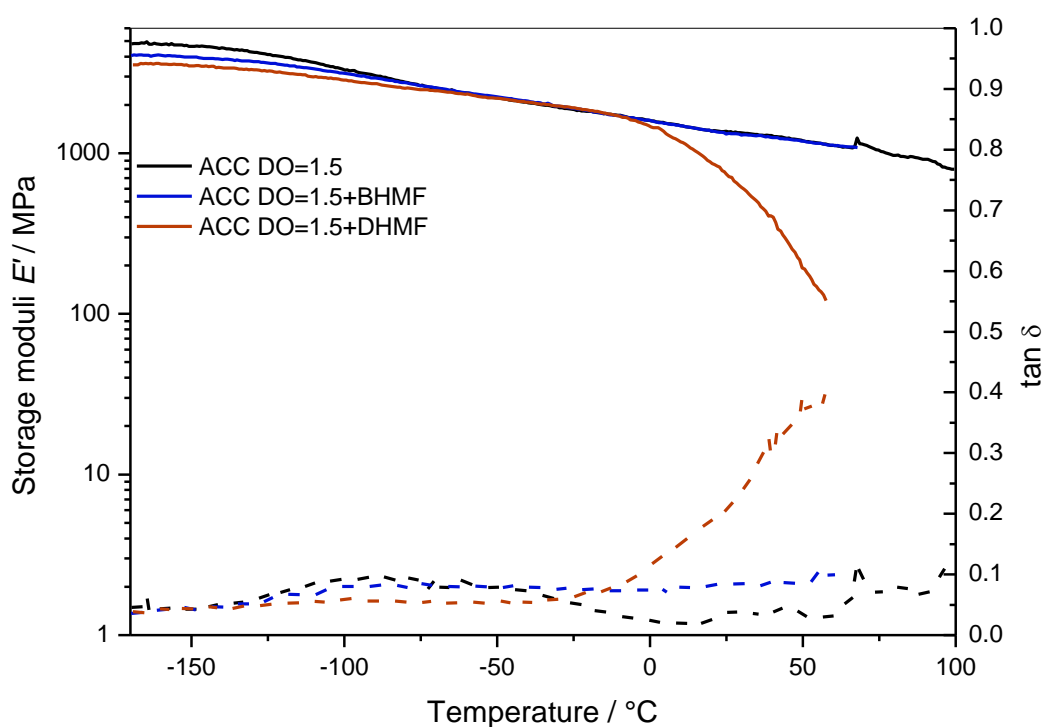


Figure 12. DMA thermograms of ACC at a DO of 1.5 (black), and ACC reinforced with BHMF (blue) and DHMF (orange) – Left axis: Evolution of the storage moduli E' (full lines), Right axis: Evolution of $\tan \delta$ (dotted lines).

Preliminary DSC experiments were conducted to confirm the α relaxation and to confirm that this phenomenon was not due to melting. Corresponding DSC data are depicted in Supplementary Information (**Figure S7**). DSC thermograms did not show any thermal event between 0 and 50 °C. If the evolution of E' and $\tan \delta$ for the ACC DO = 1.5+DHMF was due to a melting, it should have been observed at the same temperatures in DSC as this thermal event is independent of the heating rate. Moreover, no melting of residual BHMF ($T_m = 73$ °C) or DHMF ($T_m = 132$ °C) was observed, which confirmed that the furanic compounds are branched with covalent linkage. However, later melting was observed in DSC around 100 °C that may be due to the evaporation of water, before thermal degradation. On the second scan, a T_g was indeed observed, around 80 °C in presence of DHMF, confirming the DMA observations. However, these DSC preliminary DSC results need to be developed.

IV. Conclusion

The study focused on the preparation of two series of ACCs from MFC oxidized at DO = 0.6 and 1.5. The aim of this study was to increase the moisture resistance of ACC by increasing the hydrophobicity. Indeed, as ACCs are prepared from a single source of cellulose, they present a high moisture sensitivity due to the hydroxyl groups. Thus, two different furanic derivatives were introduced within the ACC network as the furan ring presented hydrophobicity: BHMF presented one furanic ring, and DHMF presented two furanic rings. DHMF was first synthesized from HMF and characterized. Preliminary FTIR analyses showed that at DO = 0.6, the presence of the furanic compounds increased the H-bonding network density. Moreover, a slight shift of the -OH band indicated a lower free -OH content in presence of the furanic derivatives. This observation could be a preliminary indication of the diminution of moisture in presence of BHMF and DHMF. Water contact angles were measured to evaluate the hydrophobicity of each sample. As interesting results, the goniometry did not show particular hydrophobization from BHMF, as for water intake experiments. However, DHMF successfully increased the hydrophobicity of ACC, reaching a contact angle of 117 °C for the ACC at DO = 1.5 containing DHMF. The hydrophobicity of a material can also be characterized by a rough surface. Indeed, SEM analyses showed that the presence of the furanic derivatives increased the roughness of ACC at DO = 1.5. Through thermo-mechanical analyses by DMA, the presence of DHMF within ACC at DO = 0.6 seemed to highly increase the stiffness, from 5.2 GPa for neat ACC to 20.7 GPa in presence of DHMF. The furanic compounds had also the role of cross-linker as they can modify the ACC network. Thus, the rigid structure of furan rings of DHMF increased rigidity and induced a more organized structure. In this study, the DHMF can be more assimilated to a cross-linker as it formed *inter*-hemiacetal cross-link, in opposition to BHMF which can tend to form *intra*-hemiacetal linkage. Such results were in adequation with SEM analyses of the samples at DO = 0.6, as the presence of DHMF led to a better compactness. However, the presence of BHMF and DHMF did not present a strong influence on the thermo-mechanical properties at DO = 1.5 as the cellulose is highly amorphous. Finally, as there was low difference between neat ACC and ACC containing BHMF, compared to the results with DHMF, it was suggested that such difference came from the size of the molecules. Indeed, BHMF can be small enough to create essentially *intra*-hemiacetal interactions, limiting its effect. On the contrary, DHMF could reinforce the material by the formation of *inter*-hemiacetal cross-links.

V. References

- (1) Capiati, N. J.; Porter, R. S. The Concept of One Polymer Composites Modelled with High Density Polyethylene. *J. Mater. Sci.* **1975**, *10* (10), 1671–1677.
- (2) Ma, H.; Zhou, B.; Li, H.-S.; Li, Y.-Q.; Ou, S.-Y. Green Composite Films Composed of Nanocrystalline Cellulose and a Cellulose Matrix Regenerated from Functionalized Ionic Liquid Solution. *Carbohydr. Polym.* **2011**, *84* (1), 383–389.
- (3) Adak, B.; Mukhopadhyay, S. A Comparative Study on Lyocell-Fabric Based All-Cellulose Composite Laminates Produced by Different Processes. *Cellulose* **2017**, *24* (2), 835–849.
- (4) Kalka, S.; Huber, T.; Steinberg, J.; Baronian, K.; Müssig, J.; Staiger, M. P. Biodegradability of All-Cellulose Composite Laminates. *Compos. Part A Appl. Sci. Manuf.* **2014**, *59*, 37–44.
- (5) Gindl, W.; Keckes, J. All-Cellulose Nanocomposite. *Polymer* **2005**, *46* (23), 10221–10225.
- (6) Nishino, T.; Matsuda, I.; Koichi, H. All-Cellulose Composite. *Macromolecules* **2004**, *37*, 7683–7687.
- (7) Lu, X.; Zhang, M. Q.; Rong, M. Z.; Shi, G.; Yang, G. C. Self-Reinforced Melt Processable Composites of Sisal. *Compos. Sci. Technol.* **2003**, *63* (2), 177–186.
- (8) Zhang, M. Q.; Rong, M. Z.; Lu, X. Fully Biodegradable Natural Fiber Composites from Renewable Resources: All-Plant Fiber Composites. *Compos. Sci. Technol.* **2005**, *65* (15–16), 2514–2525.
- (9) Gandini, A.; da Silva Curvelo, A. A.; Pasquini, D.; de Menezes, A. J. Direct Transformation of Cellulose Fibres into Self-Reinforced Composites by Partial Oxypropylation. *Polymer* **2005**, *46* (24), 10611–10613.
- (10) Matsumura, H.; Sugiyama, J.; Glasser, W. G. Cellulosic Nanocomposites. I. Thermally Deformable Cellulose Hexanoates from Heterogeneous Reaction. *J. Appl. Polym. Sci.* **2000**, *78* (13), 2242–2253.
- (11) Matsumura, H.; Glasser, W. G. Cellulosic Nanocomposites. II. Studies by Atomic Force Microscopy. *J. Appl. Polym. Sci.* **2000**, *78* (13), 2254–2261.
- (12) Huber, T.; Müssig, J.; Curnow, O.; Pang, S.; Bickerton, S.; Staiger, M. P. A Critical Review of All-Cellulose Composites. *J. Mater. Sci.* **2012**, *47* (3), 1171–1186.
- (13) Sirviö, J. A.; Visanko, M.; Heiskanen, J. P.; Liimatainen, H. UV-Absorbing Cellulose Nanocrystals as Functional Reinforcing Fillers in Polymer Nanocomposite Films. *J. Mater. Chem. A* **2016**, *4* (17), 6368–6375.
- (14) Suopajarvi, T.; Sirviö, J. A.; Liimatainen, H. Cationic Nanocelluloses in Dewatering of Municipal Activated Sludge. *J. Environ. Chem. Eng.* **2017**, *5*, 86–92.
- (15) Guigo, N.; Mazeau, K.; Putaux, J.-L.; Heux, L. Surface Modification of Cellulose Microfibrils by Periodate Oxidation and Subsequent Reductive Amination with Benzylamine: A Topochemical Study. *Cellulose* **2014**, *21* (6), 4119–4133.
- (16) Yang, X.; Bakaic, E.; Hoare, T.; Cranston, E. D. Injectable Polysaccharide Hydrogels

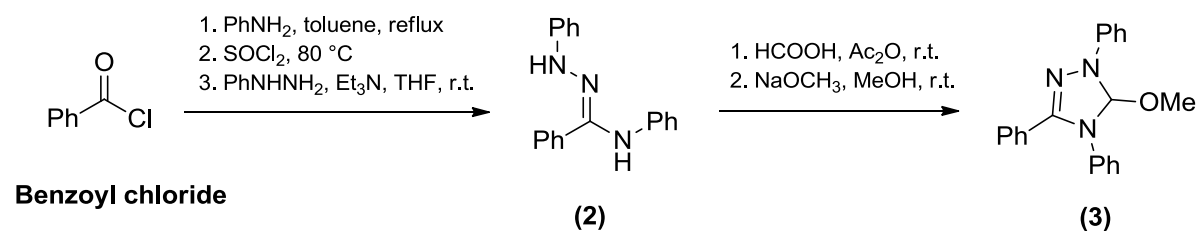
- Reinforced with Cellulose Nanocrystals: Morphology, Rheology, Degradation, and Cytotoxicity. *Biomacromolecules* **2013**, *14* (12), 4447–4455.
- (17) Yang, X.; Cranston, E. D. Chemically Cross-Linked Cellulose Nanocrystal Aerogels with Shape Recovery and Superabsorbent Properties. *Chem. Mater.* **2014**, *26* (20), 6016–6025.
- (18) Adak, B.; Mukhopadhyay, S. All-Cellulose Composite Laminates with Low Moisture and Water Sensitivity. *Polymer* **2018**, *141*, 79–85.
- (19) Battista, O. A.; Fleck, E. G. J.; Neumann, E. W. Oxidation Derivatives of Cellulose Crystallite Aggregates. US3111513, **1963**.
- (20) Liu, D. (D. J. .; Zhang, Y.; Chen, E. Y.-X. Organocatalytic Upgrading of the Key Biorefining Building Block by a Catalytic Ionic Liquid and N-Heterocyclic Carbenes. *Green Chem.* **2012**, *14* (10), 2738.
- (21) Mou, Z.; Feng, S. (Kelvin); Chen, E. Y. X. Bio-Based Difuranic Polyol Monomers and Their Derived Linear and Cross-Linked Polyurethanes. *Polym. Chem.* **2016**, *7* (8), 1593–1602.
- (22) Enders, D.; Breuer, K.; Kallfass, U.; Balensiefer, T. Preparation and Application Of 1,3,4-Triphenyl-4,5-Dihydro-1 H -1,2,4-Triazol-5-Ylidene, A Stable Carbene. *Synthesis* **2003**, *2003* (08), 1292–1295.
- (23) Mou, Z.; Feng, S. (Kelvin); Chen, E. Y. X. Bio-Based Difuranic Polyol Monomers and Their Derived Linear and Cross-Linked Polyurethanes. *Polym. Chem.* **2016**, *7* (8), 1593–1602.
- (24) Maheswari, C. U.; Reddy, K. O.; Muzenda, E.; Guduri, B. R.; Rajulu, A. V. Extraction and Characterization of Cellulose Microfibrils from Agricultural Residue-Cocas Nucifer L. *Biomass and Bioenergy* **2012**, *46*, 555–563.
- (25) Geng, Z. C.; Sun, R. C.; Sun, X. F.; Lu, Q. Comparative Study of Hemicelluloses Released during Two-Stage Treatments with Acidic Organosolv and Alkaline Peroxide from *Caligonum Monogolicum* and *Tamarix Spp.* *Polym. Degrad. Stab.* **2003**, *80* (2), 315–325.
- (26) Senthil Muthu Kumar, T.; Rajini, N.; Reddy, K. O.; Rajulu, A. V.; Siengchin, S.; Ayrimis, N. All-Cellulose Composite Films with Cellulose Matrix and Napier Grass Cellulose Fibril Fillers. *Int. J. Biological Macromol.* **2018**, *112*, 1310–1315.
- (27) Codou, A.; Guigo, N.; Heux, L.; Sbirrazzuoli, N. Partial Periodate Oxidation and Thermal Cross-Linking for the Processing of Thermoset All-Cellulose Composites. *Compos. Sci. Technol.* **2015**, *117*, 54–61.
- (28) Mosca Conte, A.; Pulci, O.; Knapik, A.; Bagniuk, J.; Del Sole, R.; Lojewska, J.; Missori, M. Role of Cellulose Oxidation in the Yellowing of Ancient Paper. *Phys. Rev. Lett.* **2012**, *108* (15), 158301.
- (29) Lewin, M. Oxidation and Aging of Cellulose. *Macromol. Symp.* **1997**, *118* (1), 715–724.
- (30) Mortier, C.; Darmanin, T.; Guittard, F. 3,4-Ethylenedioxy pyrrole (EDOP) Monomers with Aromatic Substituents for Parahydrophobic Surfaces by Electropolymerization. *Macromolecules* **2015**, *48* (15), 5188–5195.

- (31) Montès, H.; Mazeau, K.; Cavaillé, J. Y. Secondary Mechanical Relaxations in Amorphous Cellulose. *Macromolecules* **1997**, *30* (22), 6977–6984.
- (32) Kaminski, K.; Kaminska, E.; Ngai, K. L.; Paluch, M.; Włodarczyk, P.; Kasprzycka, A.; Szeja, W. Identifying the Origins of Two Secondary Relaxations in Polysaccharides. *J. Phys. Chem. B* **2009**, *113* (30), 10088–10096.
- (33) Codou, A. La Cellulose et Le Poly(Ethylene 2,5-Furandicarboxylate) Comme Précurseurs Biosourcés de Matériaux Thermoplastiques et Thermodurcissables : Les Transitions Physiques Des Biopolymères et l'élaboration Des Composites, Nice, 2015.

VI. Supplementary Information

• Synthesis and characterization of TPT-OMe

The reactant is also synthesized as it was not found commercially available. For this purpose, a multi-step synthesis summarized in **Scheme S1** was performed.



Scheme S1. Synthesis route from the preparation of TPT-OMe from benzoyl chloride.

For the first step, a three-necked round-bottomed flask equipped with a mechanical stirrer, a reflux condenser, and a dropping funnel, was charged with benzoyl chloride (5.62 g, 0.04 mol) and toluene. The flask was placed in an ice bath and aniline (3.73 g, 0.04 mol) was added dropwise over 30 min under vigorous stirring and a colorless solid precipitated. After complete addition, the cooling bath was removed and replaced by an oil bath which was heated to 135 °C to reach a gentle reflux. The reaction mixture was then heated for 16 h. After this time, most of precipitated disappeared and the reaction mixture was cooled to room temperature. Then, SOCl₂ (14.27 g, 0.12 mol) was quickly added to the solution and the reaction mixture was heated to 80 °C for 7 h under vigorous stirring to lead to a yellow solution. Once the mixture was cooled to room temperature, volatiles (toluene and residual SOCl₂) were removed under vacuum. Crude imidoyl chloride was then obtained as a yellow viscous oil. This crude product was put back into the three-necked flask and dissolved in tetrahydrofuran (THF). A solution of Et₃N (6.07 g, 0.06 mol) in THF was added through the dropping funnel, then, phenylhydrazine (4.33 g, 0.04 mol) was also added dropwise at room temperature under mechanical stirring. For this step, Enders *et al.* recommended to keep an ice bath ready to ensure an adequate reaction

control in case of sudden temperature increase⁶¹. After complete addition a yellow solution was obtained, and the mixture was stirred overnight at room temperature. The product was then concentrated at the rotary evaporator. The crude residue was treated with a 2 % aqueous solution of HOAc and heated to 70 °C until the oil solidified. The solid was then collected on a Büchner funnel, washed with water and with methanol and dried in air. **N-Phenylbenzamide phenylhydrazone (2)** was obtained as a colorless solid and used in the next step without further purification.

For the next step, a three-necked round-bottomed flask was again equipped with reflux condenser and mechanical stirrer. Acetic anhydride (100 mL) and concentrated formic acid (50 mL) were mixed and heated at 60 °C for 30 min then the mixture was cooled at room temperature. After cooling down, the solid product (2) (2.793 g, 0.009 mol) was slowly added and the mixture was stirred for 24 h at ambient temperature using a water bath. Then, the solvent was removed as completely as possible with the rotary evaporator to obtain a viscous yellow/orange oil.

The following step which consisted in the isolation of the triazolium salt could be avoided. In such case, the obtained residue previously obtained was dissolved in methanol and cooled to 0 °C for 1 h. A solution at 30 % of NaOMe in methanol was then added dropwise under stirring at 0 °C. After complete addition, the reaction mixture was stirred in an ice bath until the formation of a precipitate, for a duration of about 5 h. The precipitate was collected on a Büchner funnel and rinsed with methanol to lead to beige colored crystals, the **5-Methoxy-1,3,4-triphenyl-4,5-dihydro-1H-1,2,4-triazoline (TPT-OMe) (3)**. Despite the meticulous synthesis procedure, the desired product was obtained with a low yield of 25 %.

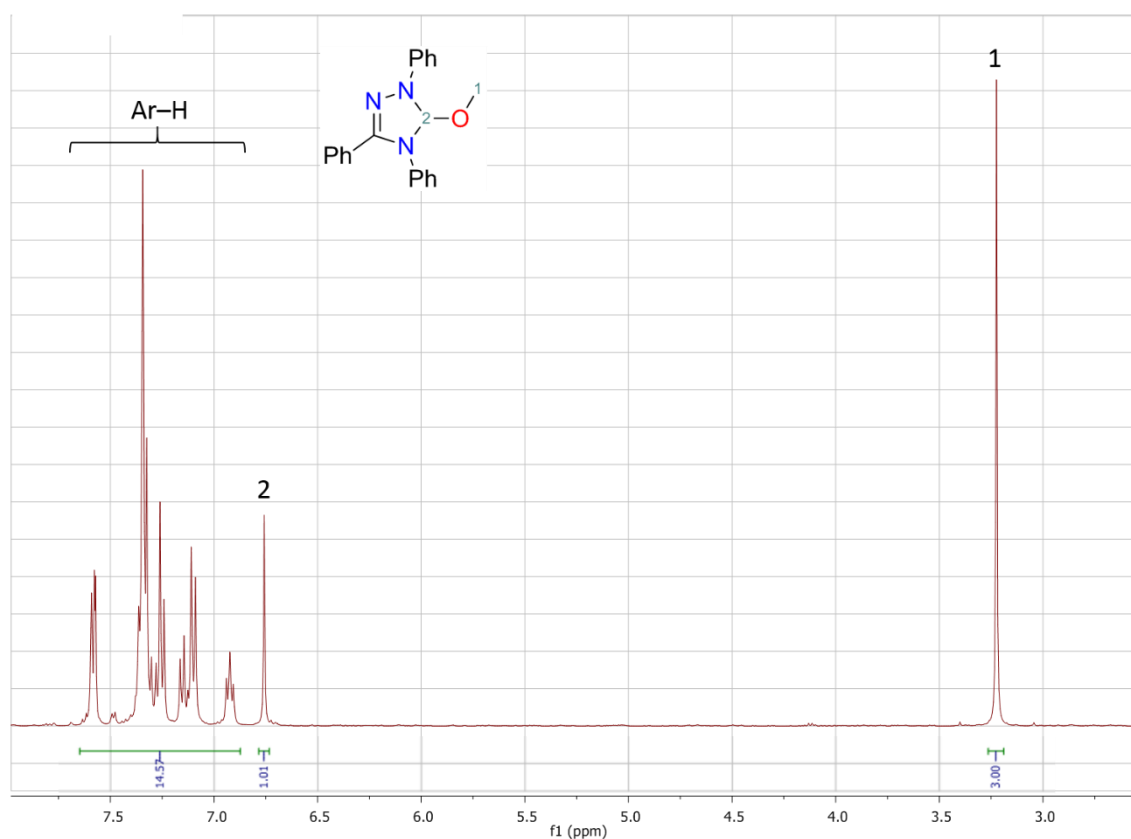


Figure S2. ^1H NMR spectrum of the synthesized TPT-OMe (solvent: CDCl_3).

The product of this synthesis which is used as reactant for the next step. The structure of TPT-OMe was confirmed with the ^1H NMR spectrum depicted in **Figure S2**. The singlet signal attributed to $\text{O}-\text{CH}_3$ was taken as integration reference and set for 3 H. The $-\text{CH}$ proton of the triazolone ring appeared as a singlet at $\delta = 6.76$ ppm with an integration of 1.01 H ($I_{\text{th}} = 1.00$ H). Finally, the protons of the aromatic rings [Ar-H] presented a signal at $\delta = 6.92 - 7.59$ ppm which integrated for 14.57 H which is close to the expected theoretical integration of 15.00 H. As deuterated chloroform was used for the analysis, its related peak appeared with the signal of aromatic protons at $\delta = 7.26$ ppm, but the integration could be performed without considering the peak of the solvent.

- Thermal characterization of BHMf and DHMF

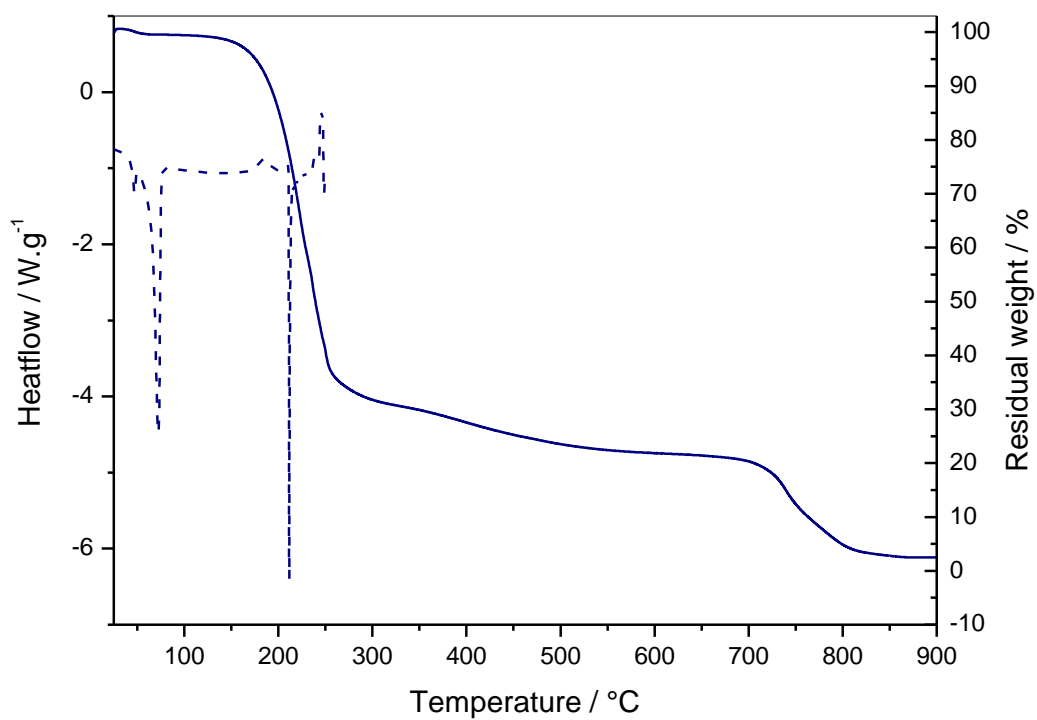


Figure S3. Characterization of commercially available BHMf. Left axis: DSC thermogram (dotted line) – Right axis: TGA thermogram (full line).

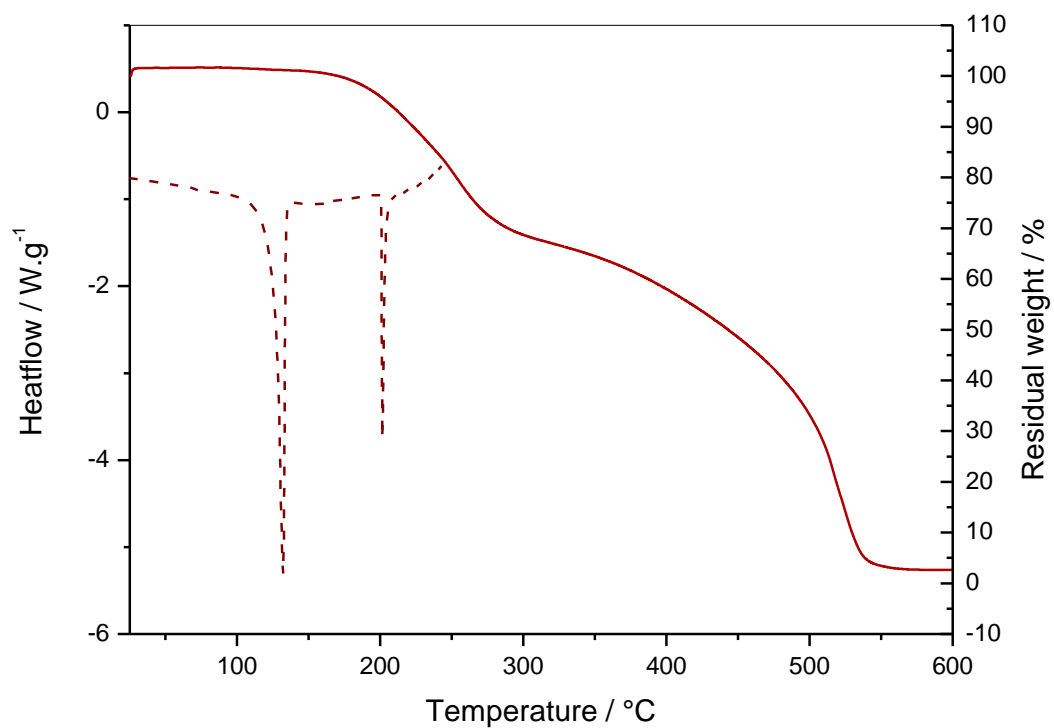


Figure S4. Characterization of synthesized DHMF. Left axis: DSC thermogram (dotted line) – Right axis: TGA thermogram (full line).

- Thermal characterization of ACC samples

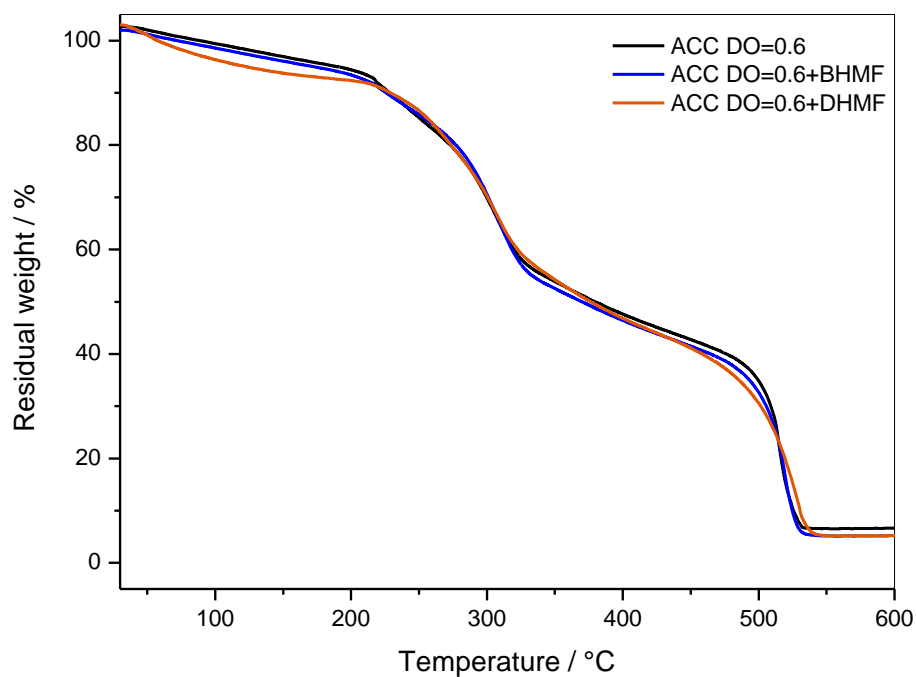


Figure S5. TGA thermograms of ACC samples at DO = 0.6 (10 K.min⁻¹, air atmosphere).

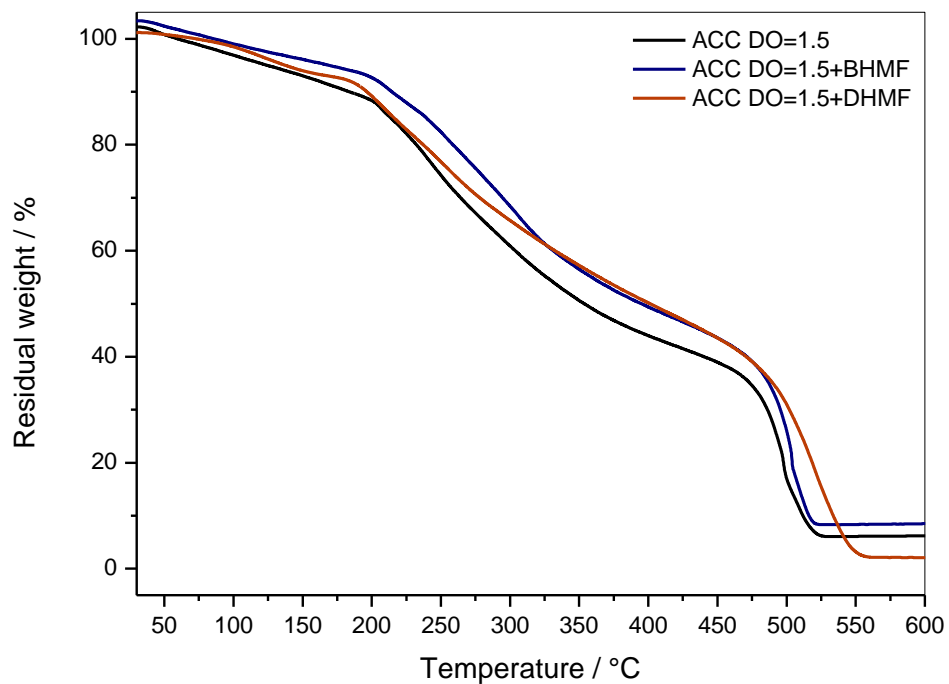


Figure S6. TGA thermograms of ACC samples at DO = 1.5 (10 K.min⁻¹, air atmosphere).

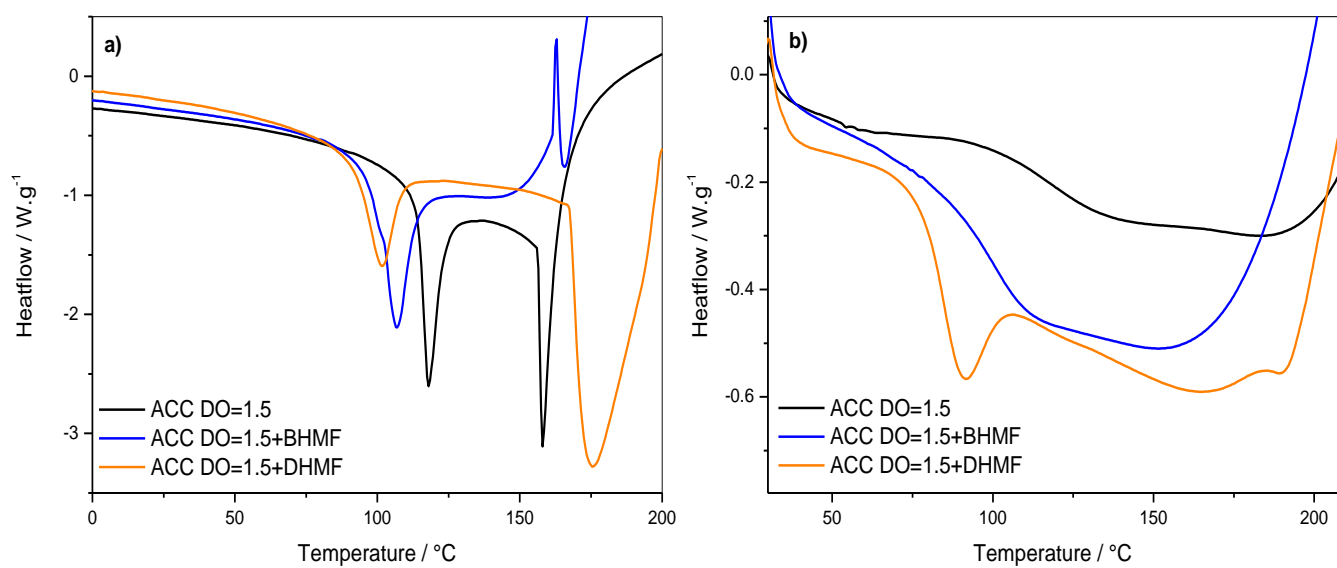


Figure S7. DSC thermograms of ACC samples at DO = 1.5. **a)** First scan, **b)** Second scan. DSC performed at 30 K.min⁻¹ under air atmosphere.

General Conclusion

In the face of the environmental concern, plant oil and lignocellulosic biomass gain a lot of interest as starting materials for the development of polymeric materials from natural and renewable resources. Among these resources, cardanol and cellulose were the main focus of the work of this thesis. Thus, the first part was dedicated to cardanol-based polybenzoxazines for a greener thermoset matrix, while the second part was focused on fully bio-based composites using dialdehyde cellulose.

The first study described in the **Chapter II** of the manuscript treated about the preparation of three PBZ materials. After synthesis and characterization of the monomers, reactivity and final properties were compared to evaluate the effect of the alkyl side chain of cardanol, as it has attracted a lot of attention in the field of PBZ. From a petro-based di-phenol BZ to a bio-based di-cardanol BZ and with an intermediate asymmetric card-phenol BZ, different aspects of the properties brought by this alkyl side chain have been studied. Cardanol induced a lower reactivity, as well as a lower glass transition temperature. The introduction of a long aliphatic side chain hindered the polymerization reaction and increased the flexibility of the final polymer. Moreover, the side chain of cardanol moieties seemed to importantly modify the H-bonding network within the polymer, which played a major role for the high performances of PBZ materials. Indeed, from a strong network of either *inter* or *intra*-H bonds for poly(di-phenol), the presence cardanol hindered the formation of *inter*-H bonding, thus favorizing the formation of *intra*-molecular H-bonds. The formation of *intra*-molecular H-bonds would lead to six-membered rings which highly stabilized the structure. Indeed, as the first step of thermal degradation is the Mannich bridge cleavage, the H-bonds reorganization due to the aliphatic chain of cardanol delayed this degradation step to much higher temperatures. Finally, the asymmetric structure seemed to present the better compromise, with an intermediate reactivity, a relatively high T_g , and one cardanol moiety appeared to be sufficient to highly increase the thermal stability.

Furthermore, the bio-based content can be improved using a bio-based amine. By replacing EDA by an aromatic amine, the rigid aromatic structure could counterbalance the flexibility brought by the alkyl side chain of cardanol.

The **Chapter III** focused on the kinetic analysis of the polymerization reaction of di-phenol BZ monomer, using advanced isoconversional analysis. This kinetic follow-up allowed to determine the evolution of the apparent activation energy and to highlight the various rate-limiting steps. Three main steps were observed in adequation with the literature: the first

step attributed to the autocatalytic ring opening reaction, a second step of aromatic electrophilic substitution, and finally a third rearrangement step. Final cross-linking continued to occur in the solid state with a nearly constant activation energy. It was interesting to observe that the apparent activation energy values of the polymerization depended on the heating rate. At low heating rate the reactions took time to occur and required more energy to reach completion, while high temperatures were reached faster at high heating rates though reactions required lower energies. However, an autocatalytic reaction should be reflected through a decrease of the activation energy. This was not the case for non-isothermal analyses as several reactions seemed to occur simultaneously and so the autocatalytic step was not the rate limiting step in non-isothermal conditions, as highlighted by advanced isoconversional analysis. To separate the reaction mechanisms, complementary isothermal analyses were performed. Considering isothermal analyses at relatively low temperature, a decrease in the E_a was finally observed which was in adequation with an autocatalytic reaction in this case. Thus, it was concluded that the autocatalytic step could be the rate-limiting step in isothermal conditions at the very beginning of the reaction. This would also confirm the hypothesis that the reactions of polymerization do not occur in the same way either proceeding in non-isothermal or isothermal mode. Moreover, the first reactions could successfully be separated in isothermal mode. However, the E_a dependencies showed a very complex mechanism that still need to be further investigated. The different variations in E_a were successfully correlated with different thermo-mechanical analyses such as rheology, DMA, or TGA. Nevertheless, complementary analyses can be required to follow-up the chemical modification, in a structural point of view. Though, it can be interesting to complete the study with complementary RAMAN or FTIR spectroscopy equipped with heating mode. Kinetic follow-up should also be performed on cardanol-based monomer to evaluate how the aliphatic side chain modify the polymerization pathway, in comparison with this di-phenol reference.

The second part treated about dialdehyde cellulose-based composites. The **Chapter V** aimed at the preparation of several PFA/MFC composites. It was interesting to modify the MFC through oxidation as literature presented a lack in compatibility between PFA and crystalline cellulose. Thus, the study focused on the influence of the DOs and ratios of DAC within a PFA matrix. In general, the introduction of MFC increased the rigidity of the material. MFC created a strong network within the PFA thus leading to high increase in rigidity. The preparation of fully bio-based composites from PFA and MFC successfully led to materials with a strong reinforcement effect of MFC, which also lowered the energy dissipation in the material. A

higher DO reflects a higher DAC content and thus a larger amount of amorphous fractions. Thus, by increasing the DAC content, the composite presented more PFA/MFC interactions over MFC/MFC interactions leading to a better compatibility between the matrix and the filler. MFC showed a high potential to reinforce the PFA matrix. However, PFA is known to be a brittle matrix and further mechanical tests such as impact tests or tensile tests could be interesting to complete this study and determine if the presence of MFC increase the toughness of the material, and how it behaves depending on the amorphous fractions.

Finally, the **Chapter VI** of this thesis focused on all cellulose composites prepared by chemical modification of a single source of cellulose. The aim of this chapter focused on the inherent hydrophilic behavior of cellulose. To perform more stable ACC materials, the influence of two different furanic cross-linkers were studied on ACCs at different DOs. Morphological observations that at DO = 0.6, the furanic cross-linkers increased the compactness, correlated with DMA as the DHMF highly increased the rigidity of the material and induced a more organized structure. The incorporation of furanic cross-linkers aimed particularly at increasing the hydrophobicity of the ACC material. Water contact angles were measured and indicated that the furanic compounds, and particularly DHMF, successfully increased the hydrophobicity of the material. This result was confirmed by water intake experiment. However, as BHMF, which possesses only one furan ring, it did not seem to have an important influence on the general properties of the ACC, and it could be assumed that the BHMF presented a small structure that would mainly react between *intra*-molecular DAC, in opposition to DHMF which took place through *inter*-molecular reactions and such position allowed to increase its influence. To confirm that the cross-linkers create a covalent hemiacetal linkage with DAC, complementary structural analyses by ^{13}C CP-MAS NMR can be performed. Moreover, the effect of DHMF on mechanical properties should also be investigation by tensile tests.